Order Number 9325174

Radiation transport in cloudy and aerosol loaded atmospheres

Kylling, Arve, Ph.D.

University of Alaska Fairbanks, 1992

U·M·I
300 N. Zeeb Rd.
Ann Arbor, MI 48106

RADIATION TRANSPORT IN CLOUDY AND AEROSOL LOADED ATMOSPHERES

A

THESIS

Presented to the Faculty

of the University of Alaska Fairbanks

in Partial Fulfillment of the Requirements

for the Degree of

DOCTOR OF PHILOSOPHY

By

Arve Kylling , Cand. Scient.

Fairbanks, Alaska

December 1992

RADIATION TRANSPORT IN CLOUDY AND AEROSOL LOADED ATMOSPHERES

by

Arve Kylling

RECOMMENDED:

Dr. Glenn E. Shaw

Dr. Wilford F. Weeks

Dr. Manfred H. Rees

Dr. Roger W. Smith

Dr. Knut Stamnes, Chairman, Advisory Committee

Dr. John L. Morack, Head, Physics Department

APPROVED:

Dr. Paul B. Reichardt, Dean, College of Natural Sciences

Dr. Edward C. Murphy, Chancellor's Faculty Associate for Graduate Studies

11 December 1992

Date

Abstract

The equation for radiation transport in vertical inhomogeneous absorbing, scattering, and emitting atmospheres is derived from first principles. It is cast in a form amenable to solution, and solved using the discrete ordinate method. Based on the discrete ordinate solution a new computationally efficient and stable two–stream algorithm which accounts for spherical geometry is developed.

The absorption and scattering properties of atmospheric molecules and particulate matter is discussed. The absorption cross sections of the principal absorbers in the atmosphere, H_2O, CO_2 and O_3, vary erratically and rapidly with wavelength. To account for this variation, the correlated–k distribution method is employed to simplify the integration over wavelength necessary for calculation of warming/cooling rates.

The radiation model, utilizing appropriate absorption and scattering cross sections, is compared with ultraviolet radiation measurements. The comparison suggests that further experiments are required.

Ultraviolet (UV) and photosynthetically active radiation (PAR) is computed for high and low latitudes for clear and cloudy skies under different ozone concentrations. An ozone depletion increases UV–B radiation detrimental to life. Water clouds diminish UV–B, UV–A and PAR for low surface albedos and increase them for high albedos. The relative amount of harmful UV–B increases on overcast days. The daily radiation doses exhibit small monthly variations at low latitudes but vary by a factor of 3 at high latitudes.

Photodissociation and warming/cooling rates are calculated for clear skies, aerosol loaded atmospheres, and atmospheres with cirrus and water clouds. After major volcanic explosions aerosols change O_3 and NO_2 photodissociation rates by 20%. Both aged aerosols and cirrus clouds have little effect on photodissociation rates. Water clouds increase ($\sim$ 100%) photodissociation rates that are sensitive to visible radiation above the cloud.

Solar warming rates vary by 50% in the stratosphere due to changing surface albedo. Water clouds have a similar effect. The net effect of cirrus clouds is to warm the troposphere and the stratosphere. Only extreme volcanic aerosol loadings affect the terrestrial warming rate, causing warming below the aerosol layer and cooling above it. Aerosols give increased solar warming above the aerosol layer and cooling below it.

Contents

Abstract iii

List of Figures viii

List of Tables xvi

Acknowledgements xvii

1 Introduction 1

2 Radiation transport in the earth's atmosphere 6

2.1 The radiative transfer equation 6

2.1.1 Spherical geometry 7

2.1.2 The streaming term pertinent to the calculation of mean intensities 10

2.1.3 The source term 12

2.1.4 The one dimensional radiative transfer equation 13

2.1.5 Layering of the atmosphere 15

2.2 Discrete ordinate solution 15

2.2.1 Homogeneous solution 16

Homogeneous solution in the two–stream approximation. 18

2.2.2 Inhomogeneous solution 19

Inhomogeneous exponential–linear solution in the two–stream approximation. 23

The ϱ, $X_0(\mu_i)$ and $X_1(\mu_i)$ coefficients in Eq. 2.54 24

2.2.3 Boundary conditions 25

2.3 Verification of the solution method 27

2.3.1 Results pertinent to the mono-directional beam pseudo-source 27

2.4 Summary 28

3 Optical properties of the atmosphere 30

3.1 Molecular absorption of radiation 31
3.1.1 The Schrödinger equation 31
3.1.2 First–order perturbation theory 32
3.1.3 Fermi's golden rule 33
3.1.4 The Hamiltonian and the absorption rate 34
3.1.5 The absorption cross section in the electric dipole approximation 35
3.1.6 The correlation function and the fluctuation–dissipation theorem 37
3.1.7 Impact approximation and the Lorentz line shape 39
3.1.8 Doppler broadening and the Voigt function 42
3.1.9 The HITRAN database and line–by–line calculations 44
3.1.10 The correlated–k distribution method 45
3.2 The absorption and scattering of light by small particles 48
3.2.1 Maxwell equations for periodic fields 50
3.2.2 Solutions to the vector wave equations 51
3.2.3 Solutions of coefficients from boundary conditions 51
3.2.4 Cross sections 53
3.2.5 An approximate scheme for Mie theory calculations for water clouds 55
3.2.6 Rayleigh scattering 55
3.3 Summary 56
4 Photodissociation rates 57
4.1 The continuity equation and photochemical processes 57
4.1.1 Definition of the photodissociation rate. 59
4.2 The solar spectrum, cross sections and quantum yields 61
4.3 Comparison of the radiation transport model with experiment 63
4.3.1 Model description 65
4.3.2 Model results and discussion 65
4.3.3 Summary of comparison of radiation model with experiment 73
4.4 Calculation of photodissociation rates 74
4.4.1 The accuracy of photodissociation rates with number of streams 76
4.4.2 The importance of spherical geometry in twilight conditions 76
4.5 Summary 77
5 Biologically active radiation, water cloud effects 81

5.1 Introduction 81
5.2 Model description 83
5.3 Results and discussion 84
5.3.1 UV–B, UV–A and PAR fluxes 84
5.3.2 UV–B/PAR, UV–A/PAR and UV–B/UV–A ratios 87
5.3.3 Daily UV–B, UV–A and PAR irradiances 92
5.4 Summary 94
6 Warming/cooling rates 96
6.1 Definition of warming/cooling rates 96
6.2 Cooling rates 99
6.2.1 Sample calculation, CO_2 in the 5000–5050 cm^{-1} region 100
6.2.2 H_2O cooling rate 103
6.2.3 CO_2 cooling rate 106
6.2.4 O_3 cooling rate 108
6.2.5 Note on the correlated–k distribution method 110
6.3 Warming rates 111
6.3.1 O_3, O_2 and NO_2 warming rates 112
6.3.2 H_2O warming rate 113
6.4 Summary 115
7 The radiative effects of clouds and aerosols 117
7.1 Cloud and aerosol models 117
7.1.1 Water cloud model 118
7.1.2 Cirrus cloud model 118
7.1.3 Aerosol models 119
7.2 Photodissociation rates 120
7.2.1 Surface albedo effects 122
7.2.2 The effects of clouds and aerosols 124
7.3 Warming/cooling rates 129
7.3.1 Surface albedo effects 130
7.3.2 The effects of clouds and aerosols 132
7.4 The radiative effects of clouds and aerosols on chemistry and dynamics 137
7.5 Summary 143

8 Summary and suggestions for further work 145

A The existence of the α coefficient for thermal radiation 149

List of Figures

2.1 The geometric setting. Note that in Fig. 2.1b the directional vector Ω has been parallel shifted to have its starting point at the surface of the earth (dotted sphere in Fig. 2.1a). 8

2.2 The division of the atmosphere into L adjacent homogeneous layers. 15

2.3 a)The Planck function integrated over the spectral range 300–800 cm^{-1} giving approximately a T^4 dependence (solid line) and the different approximations to it; constant (dotted line), linear (dashed line). Both the quadratic and the exponential–linear approximations are indistinguishable from the Planck function itself. b) The Planck function integrated over a narrow frequency range in the Wien limit (2702.99–2703.01 cm^{-1}). The solid line represents the Planck function, and the different approximations to it are the constant (dotted line), linear (dashed line), the quadratic (dash–dotted line) and the exponential–linear (dot–dot–dot–dashed line). c) The Planck function integrated over a narrow frequency range in the Rayleigh–Jeans limit (1.0–2.0 cm^{-1}). The solid line represents the Planck function, the dotted line is the constant approximation. The linear, the quadratic and the exponential–linear approximations coincide with the Planck function itself. 21

2.4 a) The beam pseudo-source for $\theta = \arccos \mu_0 = 70°$ (solid line) and the linear (dashed line) and the exponential-linear (dash-dashed line) approximations to it. b) The mean diffuse intensity, arbitrary units. c) The relative error for the different approximations. d)–f):Same as in a)–c), but for $\theta = \arccos \mu_0 = 85°$. Note that in f) the error for the linear approximation is so large that it is off the graph. 29

3.1 In the bottom row is shown the CO_2 cross section as calculated by GENLN2 for the Mc–Clatchey midlatitude–arctic summer atmosphere at ground level, and the cross section sorted in ascending order. The middle and top row give the cross section at 10.0 km and 20.0 km respectively and the corresponding $\sigma_p(g)$. The plus signs indicate the gaussian quadrature points (10 in this example) used to perform the integral over wavelength; see chapter 6 for details. 47

3.2 Same as in Fig. 3.1, but with the cross sections in the two upper panels sorted by the same mapping as used for sorting the ground level (bottom panel). The non–monotonic behaviour of the sorted cross sections in the two upper panels demonstrates the breakdown of the correlation assumption. 49

4.1 The solar flux at the top of the atmosphere is shown in a). The feature at 121.6 *nm* is the Lyman–α line (the data are from Nicolet (1989)). Figs. b)–h) show the absorption cross sections for O_3, O_2, H_2O, CO_2, CH_4, N_2O, NO_2, N_2O_5, CCl_4, HNO_3, HNO_4, HCl, HOCl, H_2O_2, OCS, H_2CO, OClO, Cl_2O_2, HOBr, $BrONO_2$, $ClNO_3$, CH_3Br, CCl_2O, CClFO, CF_2O, CH_3Cl, CH_3CCl_3, CFC–11, CFC–12, CFC–22, CFC–113, CFC–114, CFC–115, Halon 1211 and Halon 1301. The data are from DeMore et al. (1990) and the references therein. 62

4.2 The ratio of the scattered to the direct radiation at 40 km altitude. The thick solid line is the empirical curve of HM, their Figure 11, while the thin line represents results of our model calculations. 64

4.3 The direct flux above the atmosphere and at 40 km altitude. The thin lines are the calculated fluxes while the thick solid lines are experimental data taken from Figure 1 of HM. 66

4.4 The direct flux above the atmosphere and at 40 km altitude. The thin lines are the calculated fluxes while the thick solid line are experimental data taken from Figure 12 of HM. 67

4.5 The scattered solar flux for four ($\theta = 130.0°$, $\theta = 138.4°$, $\theta = 93.0°$ and $\theta = 48.4°$) of the six viewing directions of the experiment by HM (shown as thick lines). The modelled data (thin lines) have been corrected to take into account the instrument aperture of 0.0474 steradians. This figure should be compared with Figure 5 of HM. 71

4.6 The modelled scattered solar flux as a function of wavelength and polar angle. The wavelength resolution is as in WMO (1986) and the angular resolution is 6°. 73

4.7 Figs. a)–c) show different photodissociation rates for a clear, Rayleigh scattering atmosphere with a solar zenith angle $\theta = 40°$. The density and temperature profiles are taken from the subarctic summer model atmosphere (Anderson et al. 1987) and the ground albedo $A_g = 0.0$. 75

4.8 The mean intensity at different altitudes and the relative error between the two–stream algorithm and a 16–stream calculation. The dotted line in the top panel is the solar flux incident on the earth's atmosphere. The sub–arctic summer atmosphere (Anderson et al. 1987) was used with a solar zenith angle of 40° and a ground albedo of $A_g = 0.0$. 78

4.9 The single scattering albedo as a function of altitude for different wavelengths. Same atmospheric conditions as in Fig. 4.8. 79

4.10 Rate coefficients for the processes $O_3 + h\nu \rightarrow O_2 + O(^3P)$ (solid line) and $O_3 + h\nu \rightarrow O_2 + O(^1D)$ (dotted line) as calculated by the 2–stream method together with the error in the rates relative to a 16–stream calculation. The atmospheric conditions are the same as in Fig. 4.8. 79

4.11 a) Photodissociation rates calculated in plane-parallel geometry for solar zenith angles of 70, 80, 85, 86, 87, 88 and 89 degrees. b) shows the same rates in spherical geometry. Finally c) shows results for angles between 85° and 95 ° in 1° steps using spherical geometry. The sub–arctic summer atmosphere (Anderson et al. 1987) was used and the ground albedo is $A_g = 0.0$ 80

5.1 UV–B (a, d, g, j, m), UV–A (b, e, h, k, n) and PAR (c, f, i, l, o) for a clear sky with 350.0 DU (solid line), clear sky with 262.5 DU (dotted line), water cloud with 350.0 DU (dashed line) and water cloud with 262.5 DU (dash-dotted line). Results for the 1st of May (a, b, c), June (d, e, f), July (g, h, i), August (j, k, l) and September (m, n, o) are displayed for 26° N and 78° N. The ground albedo is $A_g = 0.2$. . . . 85

5.2 UV–B (a, d, g, j, m), UV–A (b, e, h, k, n) and PAR (c, f, i, l, o) for a clear sky with 350.0 DU (solid line), clear sky with 262.5 DU (dotted line), water cloud with 350.0 DU (dashed line) and water cloud with 262.5 DU (dash-dotted line). Results for the 1st of May (a, b, c), June (d, e, f), July (g, h, i), August (j, k, l) and September (m, n, o) are displayed for 26° N and 78° N. The ground albedo is $A_g = 0.95$. . . 86

5.3 UV–B/PAR (a, d, g, j, m), UV–A/PAR (b, e, h, k, n) and UV–B/UV–A (c, f, i, l, o) for a clear sky with 350.0 DU (solid line), clear sky with 262.5 DU (dotted line), water cloud with 350.0 DU (dashed line) and water cloud with 262.5 DU (dash-dotted line). Results for the 1st of May (a, b, c), June (d, e, f), July (g, h, i), August (j, k, l) and September (m, n, o) are displayed for 26° N. The ground albedo is $A_g = 0.2$. 88

5.4 UV–B/PAR (a, d, g, j, m), UV–A/PAR (b, e, h, k, n) and UV–B/UV–A (c, f, i, l, o) for a clear sky with 350.0 DU (solid line), clear sky with 262.5 DU (dotted line), water cloud with 350.0 DU (dashed line) and water cloud with 262.5 DU (dash-dotted line). Results for the 1st of May (a, b, c), June (d, e, f), July (g, h, i), August (j, k, l) and September (m, n, o) are displayed for 26° N. The ground albedo is $A_g = 0.95$. 89

5.5 UV–B/PAR (a, d, g, j, m), UV–A/PAR (b, e, h, k, n) and UV–B/UV–A (c, f, i, l, o) for a clear sky with 350.0 DU (solid line), clear sky with 262.5 DU (dotted line), water cloud with 350.0 DU (dashed line) and water cloud with 262.5 DU (dash-dotted line). Results for the 1st of May (a, b, c), June (d, e, f), July (g, h, i), August (j, k, l) and September (m, n, o) are displayed for 78° N. The ground albedo is $A_g = 0.2$. 90

5.6 UV–B/PAR (a, d, g, j, m), UV–A/PAR (b, e, h, k, n) and UV–B/UV–A (c, f, i, l, o) for a clear sky with 350.0 DU (solid line), clear sky with 262.5 DU (dotted line), water cloud with 350.0 DU (dashed line) and water cloud with 262.5 DU (dash-dotted line). Results for the 1st of May (a, b, c), June (d, e, f), July (g, h, i), August (j, k, l) and September (m, n, o) are displayed for 78° N. The ground albedo is $A_g = 0.95$. 91

5.7 UV–B (a, d, g, j), UV–A (b, e, h, k) and PAR (c, f, i, l) doses for a clear sky with 350.0 DU (plus), clear sky with 262.5 DU (asterisk), water cloud with 350.0 DU (triangle) and water cloud with 262.5 DU (×). Results at latitudes 26° N (a–f) and 78° N (g–l) with ground albedos 0.20 (a–c, g–i) and 0.95 (d–f, j–l) are displayed. . 93

6.1 The temperature profile and profiles of CO_2 (solid line), O_3 (dotted line), H_2O (dashed line) and NO_2 (dashed–dotted line) for the midlatitude summer atmosphere (Anderson et al. 1987), used in the calculation of warming/cooling rates. 101

6.2 In the left panel is shown the cooling rate in the 5000–5050 cm^{-1} interval for the mid-latitude summer atmosphere (Anderson et al. 1987), thermal radiation only. The solid line represents the line–by–line calculation. Results are also shown for a 50–points (dotted line), 36–points (dashed line) and 10–points Gaussian approximation (dashed–dotted line). In the right panel the errors of the different approximations are displayed. 102

6.3 The H_2O cooling rate from line–by–line calculations (solid line) together with correlated–k distribution results with 50 point quadrature rule (dotted line), 36 points quadrature rule (dashed line) and 10 points quadrature rule (dashed–dotted line). The right panel shows the error made by the different correlated–k distribution approximations. 104

6.4 The CO_2 cooling rate from line–by–line calculations (solid line), together with correlated–k distribution results with 50 points quadrature rule (dotted line), 36 points quadrature rule (dashed line) and 10 points quadrature rule (dashed–dotted line). The stars are the results of Lacis and Oinas (1991) given at 5 km intervals. The right panel shows the error made by the different correlated–k distribution approximations. 107

6.5 The O_3 cooling rate from line–by–line calculations (solid line) together with correlated–k distribution results with 50 points quadrature rule (dotted line), 36 points quadrature rule (dashed line) and 10 points quadrature rule (dashed–dotted line). The stars are the results of Lacis and Oinas (1991) given at 5 km intervals. The right panel shows the error made by the different correlated–k distribution approximations. An explanation for the rather large errors around 5, 30 and 66 km is given in the text. 108

6.6 Individual cooling rates for H_2O (dotted line), CO_2 (dashed line) and O_3 (dashed–dotted line) together with the total cooling rate (solid line) for all three absorbers. 110

6.7 The O_3 (dotted line), O_2 (dashed line) and NO_2 (dashed–dotted line) warming rates and their total (solid line). Also shown is the relative contribution of each gas with altitude. Note that due to overlapping absorption, the total warming rate is less than the sum of the individual warming rates. 112

6.8 The H_2O near–infrared warming rate from line–by–line calculations (solid line) together with correlated–k distribution results with 50 point quadrature rule (dotted line), 36 point quadrature rule (dashed line) and 10 point quadrature rule (dashed–dotted line). The right panel shows the error associated with the different correlated–k distribution approximations. 114

7.1 The aerosol extinction at 550 nm from the Shettle and Fenn (1976) aerosol models. The solid line represents spring–summer conditions and the dashed line fall–winter conditions. 119

7.2 The wavelength dependence of the extinction and absorption coefficients, the asymmetry factor and the single scattering albedo used in the region 10–30 km for fresh volcanic (solid line), background (dotted line) and aged volcanic (dashed line) conditions. Also shown are the optical properties of the cirrus cloud model used (dashed–dotted line). From the Shettle and Fenn (1976) models. (1 amagat = 1 atm at STP) 121

7.3 The $O_3 + h\nu \rightarrow O(^3P) + O_2$ photodissociation rate for different solar zenith angles and surface albedos. The rightmost curve in each figure is for $A_g = 1.0$, the next to the left for $A_g = 0.75$ and so on in steps of 0.25 to $A_g = 0.0$. A midlatitude summer atmosphere (Anderson et al. 1987) was used in the calculation. 123

7.4 The $O_3 + h\nu \rightarrow O(^1D) + O_2$ photodissociation rate for solar zenith angles $\theta_0 = 30°, 60°$ and $85°$ and different surface albedos. The rightmost curve for each solar zenith angle is for $A_g = 1.0$, the next to the left for $A_g = 0.75$ and so on in steps of 0.25 to $A_g = 0.0$. A midlatitude summer atmosphere (Anderson et al. 1987) was used in the calculation. 124

7.5 The left column shows O_3, O_3^* and NO_2 photodissociation rates for a clear sky (solid line) and an atmosphere with a cirrus cloud (dotted line) and a water cloud (dashed line). The right column shows the % difference between the clear sky situation and the different cloud cases. As a model atmosphere, the midlatitude summer atmosphere (Anderson et al. 1987) was adopted. The surface albedo $A_g = 0.0$ and the solar zenith angle $\theta_0 = 30.0$. 126

7.6 The left column shows O_2, O_3, O_3^*, NO_2 and CCl_4 photodissociation rates for a clear sky (solid line) and different aerosol loadings; background volcanic (dotted line), moderate volcanic (dashed line), high volcanic (dashed–dotted line) and extreme volcanic (dot–dot–dot–dashed line). The right column shows the % difference between the clear sky and the different aerosol loadings. The model atmosphere, solar zenith angle and surface albedo are as in Fig. 7.5. Summer conditions were used for the aerosol loadings. 127

7.7 Instantaneous warming rates in the ultra–violet and the visible part of the spectrum, 116.3–730.0 nm, for different surface albedos. The rightmost curve in each figure is for $A_g = 1.0$, the next to the left for $A_g = 0.75$, and so on in steps of 0.25 to $A_g = 0.0$ for the leftmost curve. The midlatitude summer atmosphere (Anderson et al. 1987) was used in the calculations. 130

7.8 In the left column is shown the instantaneous solar and terrestrial warming rate for a clear sky (solid line), an atmosphere with background (dotted line), moderate volcanic (dashed line), high volcanic (dashed–dotted line) and extreme volcanic (dot–dot–dot–dashed line) aerosol content. The right column shows the difference between the clear sky and the different aerosol loaded atmospheres. The solar zenith angle was 30°, the surface albedo $A_g = 0.0$ and the midlatitude summer atmosphere was used (Anderson et al. 1987). 133

7.9 In the left column is shown the instantaneous solar and terrestrial warming rate for a clear sky (solid line), and atmosphere with a cirrus cloud (dotted line) and a water cloud (dashed line). The right column gives the difference between the clear sky warming rate and the cloudy sky warming rates. The surface albedo was $A_g = 0.0$, the solar zenith angle 30°, and the midlatitude summer atmosphere was used (Anderson et al. 1987). 134

7.10 Mid–july diurnally averaged warming rates (K/day) for solar ultraviolet and visible radiation (116.3–730.0 nm) for a clear Rayleigh scattering atmosphere. 136

7.11 The difference in the solar diurnal warming rate after introducing the background aerosol model. 138

7.12 The difference in the solar diurnal warming rate after introducing the extreme volcanic aerosol model. 139

7.13 The coupling between the three major mechanisms necessary to describe stratospheric and tropospheric chemistry. The mechanisms directly change the atmospheric properties inside the circles and they interact through changes in the atmospheric properties indicated by arrows. For further details, see the text. 140

List of Tables

4.1 Photochemical reactions of stratospheric interest that are included in the present model. The relevant cross sections (Fig. 4.1) and quantum yields are from DeMore et al. (1990) and the references therein. For the O_2 Schumann–Runge bands and for NO the parameterization of Allen and Frederick (1982) was used. The uncertainty is the combined uncertainty for cross sections and quantum yields. Examples of the different photodissociation rates are given in Fig. 4.7 60

4.2 Atmospheric profile used in the radiation calculations. 70

6.1 The different molecules included in the radiation model, the spectral interval included for each molecule and the sources for the cross sections used to calculate their optical properties. 105

7.1 The seasonal and latitudinal characteristics of the AFGL model atmospheres, Anderson et al. (1987). 137

7.2 The response of photodissociation, solar warming and terrestrial cooling rates to increases (↑), decreases (↓) or introduction (+) of some atmospheric properties. An increase in the rates is indicated by ↑ and a decrease by ↓. If two symbols appear in the same column then the first symbol refers to the region above the cloud or aerosol layer and the second to the region below. The magnitude and sign of the changes may be different for atmospheric conditions not considered in this work. . 143

Acknowledgements

I would like to give my most sincere thanks to Knut Stamnes for neverending support, encouragement and guiding through my years at Gee Wiz, for giving me freedom to do what I wanted to, where I wanted to, and for helping me through cold Fairbanks winters and the occasional volcanic eruption; Fred Rees for stimulating discussions on and criticism of the present and other works, and for saving me many long cold walks home during the winter of 89; Willy Weeks, Roger Smith and Glenn Shaw for constructive criticism of this work; Dave Edwards for letting me hack on his cleverly made GENLN2 program; Mt. Redoubt for teaching me who is the strongest; KSUA for rocking me through many long and lonely hours; Alascom for providing some real–time, no–touch contact between me and Karen (actually Alascom should thank me, you should have seen those bills); 'Gutan på taket' at the Auroral Observatory, Tromsø, for letting me do things on their computers, and for sharing their insight in science, computers, and ... ; the National Aeronautics and Space Administration for economical support through grant NAGW–2165; the Norwegian Council on Science and Technology (NTNF) for economical support; Dirk Lummerzheim for very seldom being in Fairbanks when I was, I very much appreciated the cabin and all that came along; Mr. Hu for tables of numbers, red salmons and odd buffet lunches; Ivar Isaksen at the University of Oslo for paying a crossing of the North Pole, that is, by air; The Norwegian Space Agency for paying another one; Leiv Veseth and Øystein Lie–Svendsen for constructive criticism of Chapter 3. And to the rest of you who have made me smile, whether in Fairbanks, Tromsø or somewhere else, thanks too.

Thanks to Karen for giving me what science never can.

This document was typeset using LaTeX(thanks to Richard Honrath for the thesis.sty file). The computer programs used in this work are available for anyone interested (my e–mail address is arve@kaja.gi.alaska.edu). They are written in stoneage FORTRAN 77 with a few extensions from the committee–made–not–yet–available FORTRAN 90 (I'm writing this in the fall of 92). Figures were made with tgif and IDL, the latter has the one major drawback that it is not in the public domain. And if I was to do it all over again, I would use C, take time off to go to rock concerts and love the same woman.

... and nothing else matters ...

Chapter 1

Introduction

Accurate knowledge of the radiation field in the troposphere and the stratosphere is of paramount interest because the radiation field determines the photodissociation rates of the various gases involved in ozone chemistry and because the radiative warming/cooling rate, in part, determines the temperature structure and consequently the dynamical behavior of the troposphere and the stratosphere.

At present, clouds and aerosols may be said to be the least understood features of our atmosphere. Clouds and aerosols are known to play a significant role in determining the earth's climate and they may be key ingredients in several mechanisms that have kept the climate and the composition of the atmosphere surprisingly stable as long as life has existed on earth (Lovelock 1979). Several questions may be asked about clouds and aerosols: how do they form, what is their concentration, what are their optical properties and how do they affect the radiation field? In this work the last of these questions is addressed by investigating the impact of clouds and aerosols on tropospheric and stratospheric photodissociation and warming/cooling rates.

The photodissociation rate $J(z)$ at altitude z is proportional to the probability of molecules absorbing an incident photon, the absorption cross section $\sigma(\lambda)$, the probability for dissociation $q(\lambda)$, and the number of incident photons integrated over all wavelengths

$$J(z) = 4\pi \int \overline{I(z,\lambda)} q(\lambda)\sigma(\lambda)\, d\lambda. \tag{1.1}$$

Here the mean intensity $\overline{I(z,\lambda)}$ is in the units of no. photons per cm^2, s and nm. The factor 4π follows from the definition of the mean intensity $\overline{I(z,\lambda)}$; see chapter 2. The integration over wavelength extends typically from 120 to 700 nm to encompass all major photodissociation processes.

For a rigorous derivation of expression 1.1, see chapter 4.

The temperature change $\frac{\partial T}{\partial t}$ in a small volume element due to radiative processes, i.e., the warming/cooling rate, is directly proportional to the amount of radiation entering the volume minus the emitted radiation, in units[1] of W/m^2. The amount absorbed and emitted is further proportional to the density $n(z)$ of absorbing gases and their respective absorption cross sections $\sigma_{abs}(\lambda)$. Thus the net warming/cooling rate may be written (see chapter 6 for a more rigorous derivation)

$$\frac{\partial T(z)}{\partial t} = \frac{4\pi n(z)}{c_p \rho_m(z)} \int \sigma_{abs}(\lambda)[\overline{I(z,\lambda)} - B(T(z),\lambda)]d\lambda. \tag{1.2}$$

Here $B(T,\lambda)$ is the Planck function, c_p the specific heat at constant pressure, and ρ_m the mass density of air. The integration extends over all wavelengths λ in the solar as well as the terrestrial spectrum. Typically, solar or shortwave radiation ($\lambda < 4\mu m$) is absorbed and leads to warming, while for longwave or terrestrial radiation ($\lambda > 4\mu m$) emission dominates so that cooling prevails.

To quantify photodissociation rates one must identify the different photochemical processes of importance. Further, the relevant absorption cross sections and quantum yields must be measured. Finally, one must be able to calculate the radiation field in the atmosphere under a variety of different conditions. In this work focus is on the last of these problems. Reviews of relevant photodissociation rates and calculation procedures are given by Turco (1975) and Brasseur and Solomon (1986). While Turco (1975) only included the effect of absorption in his calculations, Luther and Gelinas (1976) focused on the effects and importance of Rayleigh scattering and varying ground albedo using a multiple scattering radiation model. Madronich (1987) pointed out that due to the use of wrong radiometric quantities, 'a fraction of the recent atmospheric chemistry literature contains improperly calculated rates of photodissociation'. He further showed that clouds may affect photodissociation rates, while Pollack et al. (1976) concluded that aerosols apparently have little influence on ozone photodissociation rates. Rayleigh scattering is nearly isotropic while clouds and aerosols may exhibit strong forward scattering. Strongly peaked scattering requires careful treatment and more advanced radiation models than those typically used in photochemical models, cf. e.g., Isaksen et al. (1977).

[1] To convert from no. photons/$cm^2 s\ nm$ to $W/m^2 nm$, note that each photon has the energy $e(\lambda) = h\nu = hc/\lambda$. Letting $I_1(\lambda)$ be in the units of $W/m^2 nm$ and $I_2(\lambda)$ in no. photons/$cm^2 s\ nm$, then

$$I_2(\lambda) = \frac{1}{e(\lambda) \times 10^4} I_1(\lambda) = \frac{\lambda}{1.9864 \times 10^{-12}} I_1(\lambda)$$

where λ is in nanometers.

Many atmospheric species exhibit strong diurnal variations of concentration and height distribution. To model them, accurate photodissociation rates at all solar zenith angles are needed. Furthermore, the most dramatic recent changes in ozone have been observed in polar regions where large solar zenith angles typically occur. This implies that a plane–parallel model is inadequate; the earth's curvature cannot be neglected. Photolysis of various key species are known to play an important role in the ozone chemistry in the polar regions. Thus, any realistic model for calculating photolysis rates must account for spherical effects, as demonstrated by Lary and Pyle (1991a,b).

The mean intensity is needed for calculating both photodissociation and warming/cooling rates, cf. Eqs. 1.1–1.2. A fast and accurate two–stream algorithm have been developed (Kylling, Stamnes and Tsay 1992), based on the general DISORT algorithm of Stamnes et al. (1988). This two–stream algorithm incorporates all the advanced features of the DISORT algorithm including the δ–M transformation to handle strongly peaked phase functions (Wiscombe 1977). Furthermore it has been extended to include spherical geometry (Dahlback and Stamnes 1990, Kylling and Stamnes 1992), and may be applied to both the solar and the terrestrial spectrum. It is thus well suited to calculate the radiation field for most atmospheric conditions and will be described and used in this work.

Typically, the absorption cross sections of atmospheric gases important for photodissociation and warming/cooling rate calculations vary rapidly, erratically, and by several orders of magnitude over small wavelength intervals. Furthermore, the optical properties of the gases vary with pressure and/or temperature. Thus, the integration over wavelengths in Eqs. 1.1–1.2 either includes very lengthy and time consuming computations, or approximations must be invoked.

For the calculation of J–values and warming rates between 120 nm and 700 nm, i.e. from the far ultraviolet through the visible part of the spectrum, a set of absorption cross sections averaged over narrow wavelength intervals has been compiled, WMO (1986). This set will be used later in this study with minor modifications. In the solar infrared (0.7–$4.0\mu m$) and the terrestrial infrared (4.0–$\infty\mu m$) the complex absorption spectra of the most important radiatively active gases, H_2O, CO_2, and O_3, do not allow use of simple averaging procedures. 'Exact' line–by–line integrations, where each absorption line and its temperature and pressure dependence is accounted for, may be performed. But such calculations are very time consuming, and various approximations have thus been introduced. While the abundance of carbon dioxide is changing relatively slowly, water vapor and ozone concentrations vary rapidly. Hence the approximations must remain valid for varying gas concentrations. Various band models (Goody and Yung 1989) have been used for a

long time. Typically, they include calculations of the mean absorptivity for an absorption band containing a number of lines. Line strengths and widths based on measurements and theoretical work are used as input for the absorptivity and subsequent transmission calculations. Pressure and/or temperature dependence may be included for when the gas abundance is constant with altitude, e.g. carbon dioxide.

The nonuniform concentration of ozone has long posed a problem for using these approximate methods. Thus, while they may be used with care in pure tropospheric or stratospheric models, they are not suitable for situations requiring coupling between the troposphere and the stratosphere. Furthermore, multiple scattering can not be included. Therefore the effect of scattering from clouds and aerosols, which may also be important in the solar infrared, can not be accounted for. The correlated–k distribution method (Lacis and Oinas 1991) largely overcomes all of these problems. It may be described as a wide band method; that is, provided the scattering properties and the radiation sources (thermal and solar) are constant within a spectral region, it can be applied to this spectral region regardless of the complexity of the line spectrum. Multiple scattering may readily be incorporated within the framework of the correlated–k distribution model. Thus, scattering from clouds and aerosols may be included in a consistent way. The correlated–k distribution method will be used in connection with the radiation model (Kylling, Stamnes and Tsay 1992) to be developed in this work to study the effect of clouds and aerosols on photodissociation and warming/cooling rates in the troposphere and the stratosphere.

Aerosols may have a large effect on the climate. Stratospheric aerosols are mainly of volcanic origin. Their size distribution and hence their optical properties change with time after an eruption. Several studies have been undertaken to investigate the effects of recent large volcanic eruptions, e.g. Pollack et al. (1976) on Mt. Agung, Pollack and Ackerman (1983) on El Chichon and Hansen et al. (1992) on Mount Pinatubo. These studies have focused on effects at low and middle latitudes. Tropospheric aerosols are both of natural and anthropogenic (25–50 %) origin. In most cases aerosols leads to cooling, but in polar regions they may have a warming effect. Furthermore, they may change the photolysis rates important for ozone chemistry (Lary and Pyle 1991a,b; Michelangeli et al. 1989; 1992; Tsay and Stamnes, 1992). Clouds cover approximately 50–60 % of the earth's surface, thereby substantially changing its albedo from that of a clear sky situation. Both low and high level clouds affect the radiation field in the stratosphere. In this work a unified radiation model of the troposphere and the stratosphere (Kylling, Stamnes and Tsay 1992) will be used in connection with realistic cloud and aerosol models to investigate how clouds and aerosols

affect the radiation field in the troposphere and the stratosphere. Special attention will be paid to high–latitude phenomena where high ground albedo and low solar elevation may drastically alter the radiative balance.

To summarize: the main goal of this work is to construct a unified model for computing the radiation field in the troposphere and the stratosphere, and then to use this model to perform a study of the effects of tropospheric clouds and stratospheric aerosols on tropospheric and stratospheric photodissociation and warming/cooling rates. To achieve these goals the equation pertinent to radiation transport in a stratified atmosphere is derived and solved (Chapter 3). In Chapter 3 the various absorption and scattering cross sections as functions of wavelength and scattering angle are calculated. Next, in Chapter 4 the computation of photodissociation rates is discussed and the radiation model developed in this work is compared with experimental results. In Chapter 5 the model developed in the preceding chapters is used to study the effects of water clouds on damaging ultra–violet radiation and photosynthetic active radiation. Chapter 6 discusses the computation of warming/cooling rates for a clear sky using both 'exact' and approximate methods. In Chapter 7 the effect of tropospheric and stratospheric clouds and of aerosols on tropospheric and stratospheric warming/cooling and photodissociation rates is studied. Finally, in Chapter 8 the method and the results are summarized and possible extensions and applications of the model are indicated.

Chapter 2

Radiation transport in the earth's atmosphere

The earth's atmosphere is a highly inhomogeneous and constantly changing medium whose optical properties exhibit large fluctuations on both short and long spatial and temporal scales. Radiation transport in absorbing, emitting and scattering media of arbitrary shape and inhomogeneity, is a complex physical process. Starting with the Boltzmann equation the radiative transfer equation applicable to the Earth's atmosphere is derived. By assuming a stratified atmosphere, spherical shell geometry and focusing on the calculation of mean intensities, the radiative transfer equation is cast in a form amenable to solution. The resulting one–dimensional radiative transfer equation is solved by the discrete ordinate method. The importance of properly treating the altitude variation of internal radiation sources in the atmosphere, e.g. thermal emission, is discussed in some detail.

2.1 The radiative transfer equation

The photon distribution function $f(\mathbf{r}, \hat{n}, \nu, t)$ varies with location ($\mathbf{r}$), direction of propagation ($\hat{n}$), frequency (ν) and time (t). It is defined such that

$$f(\mathbf{r}, \hat{n}, \nu, t)\, c\, \hat{n} \cdot d\mathbf{S}\, d\Omega\, d\nu\, dt \tag{2.1}$$

represents the number of photons with frequency between ν and $\nu + d\nu$ crossing a surface element $d\mathbf{S}$ in direction $\hat{n}$ into solid angle $d\Omega$ in time dt (Stamnes 1986). The units of $f(\mathbf{r}, \hat{n}, \nu, t)$ are $cm^{-3}\ sr^{-1}\ Hz^{-1}$ and c is the speed of light. For dilute gases the temporal and spatial evolution

of the photon distribution function is described by the Boltzmann equation

$$\frac{\partial f}{\partial t} + \nabla_{\mathbf{r}}(\mathbf{v}\, f) + \nabla_{\mathbf{p}}(\mathbf{F}\, f) = Q(\mathbf{r}, \hat{n}, \nu, t) \tag{2.2}$$

where $\nabla_{\mathbf{r}}$ and $\nabla_{\mathbf{p}}$ are the divergence operators in configuration and momentum space, respectively. The photons may be subject to an external force $\mathbf{F}(\mathbf{r}, \hat{n}, \nu, t)$ and $Q(\mathbf{r}, \hat{n}, \nu, t)$ which represents the sources and sinks of photons due to collisions and/or 'true' production and loss. In the absence of relativistic effects $\mathbf{F} = 0$, and the photons propagate in straight lines with velocity $\mathbf{v} = c\ \hat{n}$ between collisions. Using the relation

$$\nabla_{\mathbf{r}}(\mathbf{v}\, f) = f\ \nabla_{\mathbf{r}}\mathbf{v} + \mathbf{v} \cdot \nabla f = \mathbf{v} \cdot \nabla f, \tag{2.3}$$

where $\mathbf{r}$ and $\mathbf{v}$ are independent variables, Eq. 2.2 may be written as

$$\frac{\partial f}{\partial t} + c\ (\hat{n} \cdot \nabla)\ f = Q(\mathbf{r}, \hat{n}, \nu, t) \tag{2.4}$$

where the $\mathbf{r}$ subscript on the gradient operator ∇ have been omitted. The differential energy associated with the photon distribution is

$$dE = c\ h\nu\ f\ \hat{n} \cdot d\mathbf{S}\ d\Omega\ d\nu\ dt. \tag{2.5}$$

The specific intensity of photons $I(\mathbf{r}, \hat{n}, \nu, t)$ is defined such that $(\hat{n} \cdot d\mathbf{S} = \cos\theta\ dS)$

$$dE = I(\mathbf{r}, \hat{n}, \nu, t)\, dS\ \cos\theta\ d\Omega\ d\nu\ dt. \tag{2.6}$$

Hence

$$I(\mathbf{r}, \hat{n}, \nu, t) = c\ h\nu\ f(\mathbf{r}, \hat{n}, \nu, t) \tag{2.7}$$

and Eq. 2.4 may be written in a steady state situation as

$$(\hat{n} \cdot \nabla)\ I(\mathbf{r}, \hat{n}, \nu) = h\nu\ Q(\mathbf{r}, \hat{n}, \nu). \tag{2.8}$$

2.1.1 Spherical geometry

The earth's atmosphere has the form of a spherical shell, hence the radiative transfer equation must be cast in a form applicable to spherical geometry. The components of the streaming term $(\hat{n} \cdot \nabla)$ in spherical geometry are (Rottmann 1960)

$$\begin{aligned} \hat{n} &= \cos\Phi \sin\Theta\ \mathbf{e}_x + \sin\Phi \sin\Theta\ \mathbf{e}_y + \cos\Theta\ \mathbf{e}_z \\ \nabla &= \mathbf{e}_r \frac{\partial}{\partial r} + \mathbf{e}_{\Theta_0} \frac{1}{r} \frac{\partial}{\partial \Theta_0} + \mathbf{e}_{\Phi_0} \frac{1}{r \sin\Theta_0} \frac{\partial}{\partial \Phi_0} \end{aligned}$$

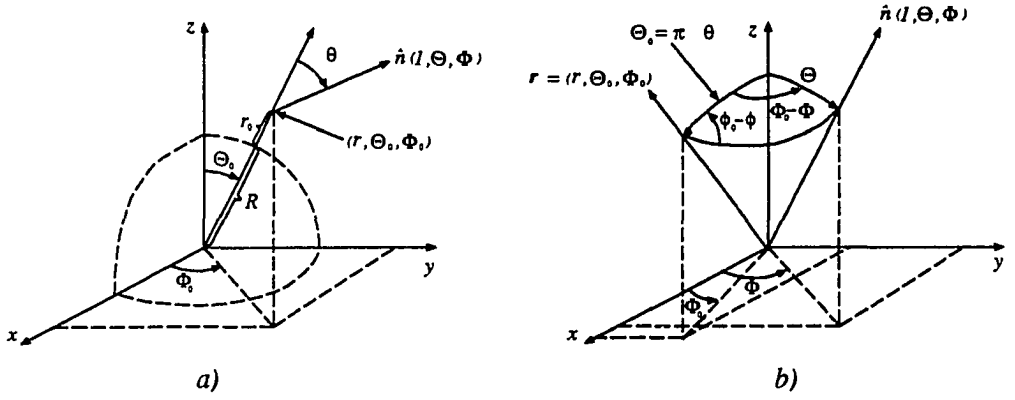

Figure 2.1: The geometric setting. Note that in Fig. 2.1b the directional vector Ω has been parallel shifted to have its starting point at the surface of the earth (dotted sphere in Fig. 2.1a).

where

$$\begin{aligned}
\mathbf{e}_r &= \sin\Theta_0\cos\Phi_0\,\mathbf{e}_x + \sin\Theta_0\sin\Phi_0\,\mathbf{e}_y + \cos\Theta_0\,\mathbf{e}_z \\
\mathbf{e}_\Theta &= \cos\Theta_0\cos\Phi_0\,\mathbf{e}_x + \cos\Theta_0\sin\Phi_0\,\mathbf{e}_y - \sin\Theta_0\,\mathbf{e}_z \\
\mathbf{e}_\Phi &= -\sin\Phi_0\,\mathbf{e}_x + \cos\Phi_0\,\mathbf{e}_y
\end{aligned}$$

and the angles are defined in Fig. 2.1. Taking the dot product of $\hat{n}$ and ∇ gives

$$\begin{aligned}
\hat{n}\cdot\nabla = {} & [\cos\Theta\cos\Theta_0 + \sin\Theta\sin\Theta_0\cos(\Phi_0-\Phi)]\tfrac{\partial}{\partial r} \\
& -\tfrac{1}{r}[\cos\Theta\sin\Theta_0 - \sin\Theta\cos\Theta_0\cos(\Phi_0-\Phi)]\tfrac{\partial}{\partial\Theta_0} \\
& -\tfrac{1}{r}\tfrac{\sin\Theta}{\sin\Theta_0}\sin(\Phi_0-\Phi)\tfrac{\partial}{\partial\Phi_0}.
\end{aligned} \tag{2.9}$$

For practical reasons it is preferable to refer the system of spherical coordinates to the local zenith direction. Thus, it is necessary to map the intensity from the set of global coordinates $(r,\Theta_0,\Phi_0,\Theta,\Phi)$ to the local set $(r,\mu_0,\phi_0,\mu,\phi)$, i.e.[1]

$$I(r,\Theta_0,\Phi_0,\Theta,\Phi) \longrightarrow I(r,\mu_0,\phi_0,\mu,\phi) \tag{2.10}$$

where

$$\mu \equiv \cos\theta \equiv \mathbf{e}_r\cdot\hat{n} = \cos\Theta\cos\Theta_0 + \sin\Theta\sin\Theta_0\cos(\Phi_0-\Phi) \tag{2.11}$$

[1] The global coordinates r, Θ_0 and Φ_0 denote a point in R^3, whereas Θ and Φ are the coordinates of a point on the unit sphere $\mathsf{S}^2 = \{x,y : x^2+y^2 = 1\}$, and similarly for the local coordinates. Hence both $I(r,\Theta_0,\Phi_0,\Theta,\Phi)$ and $I(r,\mu_0,\phi_0,\mu,\phi)$ are real-valued functions defined on $\mathsf{R}^3 \times \mathsf{S}^2$.

$$\mu_0 \equiv \cos\theta_0 \tag{2.12}$$

and the local polar (θ_0, θ) and azimuthal angles (ϕ_0, ϕ) are defined in Fig. 2.1. In view of Eq. 2.11 Eq. 2.9 may be rewritten as

$$\hat{n}\cdot\nabla = \mu\frac{\partial}{\partial r} + \frac{1}{r}\frac{\partial\mu}{\partial\Theta_0}\frac{\partial}{\partial\Theta_0} + \frac{1}{r\,\sin^2\Theta_0}\frac{\partial\mu}{\partial\Phi_0}\frac{\partial}{\partial\Phi_0}. \tag{2.13}$$

Since μ is a function of both Θ_0 and Φ_0

$$\begin{aligned}\frac{\partial}{\partial\Theta_0} &= \frac{\partial}{\partial\theta_0} + \frac{\partial\mu}{\partial\Theta_0}\frac{\partial}{\partial\mu}\\ \frac{\partial}{\partial\Phi_0} &= \frac{\partial\phi_0}{\partial\Phi_0}\frac{\partial}{\partial\phi_0} + \frac{\partial\mu}{\partial\Phi_0}\frac{\partial}{\partial\mu}\end{aligned}$$

and Eq. 2.13 becomes

$$\hat{n}\cdot\nabla = \mu\frac{\partial}{\partial r} + \frac{1}{r}\left[\left(\frac{\partial\mu}{\partial\Theta_0}\right)^2 + \frac{1}{\sin^2\theta_0}\left(\frac{\partial\mu}{\partial\Phi_0}\right)^2\right]\frac{\partial}{\partial\mu} + \frac{1}{r}\frac{\partial\mu}{\partial\Theta_0}\frac{\partial}{\partial\theta_0} + \frac{1}{r\,\sin^2\theta_0}\frac{\partial\mu}{\partial\Phi_0}\frac{\partial\phi_0}{\partial\Phi_0}\frac{\partial}{\partial\phi_0}. \tag{2.14}$$

Using Eq. 2.11 and some relationships from spherical trigonometry (Rottmann 1960)

$$\left[\left(\frac{\partial\mu}{\partial\Theta_0}\right)^2 + \frac{1}{\sin^2\theta_0}\left(\frac{\partial\mu}{\partial\Phi_0}\right)^2\right] = 1-\mu^2$$

$$\begin{aligned}\frac{\partial\mu}{\partial\Theta_0} &= -\cos\Theta\sin\Theta_0 + \sin\Theta\cos\Theta_0\cos(\Phi_0-\Phi) = -\sqrt{1-\mu^2}\cos(\phi_0-\phi)\\ \frac{\partial\mu}{\partial\Phi_0} &= -\sin\Theta\sin\Theta_0\sin(\Phi_0-\Phi) = -\sqrt{1-\mu^2}\sin\theta_0\sin(\phi_0-\phi)\\ \frac{\partial\phi_0}{\partial\Phi_0} &= \frac{\partial(\phi_0-\phi)}{\partial(\Phi_0-\Phi)} = \cos\theta_0\sin(\phi_0-\phi)\end{aligned}$$

the streaming term in spherical geometry referenced to the local zenith direction may finally be written as (Lenoble 1985)

$$\begin{aligned}\hat{n}\cdot\nabla &= \mu\frac{\partial}{\partial r} + \frac{1-\mu^2}{r}\frac{\partial}{\partial\mu}\\ &\quad + \frac{\sqrt{1-\mu^2}\sqrt{1-\mu_0^2}}{r}\left[\cos(\phi-\phi_0)\frac{\partial}{\partial\mu_0} + \frac{\mu_0}{1-\mu_0^2}\sin(\phi-\phi_0)\frac{\partial}{\partial(\phi-\phi_0)}\right].\end{aligned} \tag{2.15}$$

Note that in plane–parallel geometry only the first term in Eq. 2.15 is included. For a spherically symmetric atmosphere the second term must be added. The full expression is, as stated above, valid for an inhomogeneous spherical shell, i.e. a planetary atmosphere.

2.1.2 The streaming term pertinent to the calculation of mean intensities

Quite generally, the intensity may be expanded in a Fourier series

$$I(r,\mu_0,\phi_0,\mu,\phi)=\sum_{m=0}^{\infty}\{I_m^c(r,\mu_0,\mu)\cos m(\phi-\phi_0)+I_m^s(r,\mu_0,\mu)\sin m(\phi-\phi_0)\}. \qquad (2.16)$$

Combining Eq. 2.15 and Eq. 2.16 gives

$$\left\{\mu\frac{\partial}{\partial r}+\frac{1-\mu^2}{r}\frac{\partial}{\partial\mu}+\frac{\sqrt{1-\mu^2}\sqrt{1-\mu_0^2}}{r}\cos(\phi-\phi_0)\frac{\partial}{\partial\mu_0}\right\}I(r,\mu_0,\phi_0,\mu,\phi)$$
$$+\frac{\sqrt{1-\mu^2}\sqrt{1-\mu_0^2}}{r}\frac{\mu_0}{1-\mu_0^2}\sin(\phi-\phi_0)\sum_{m=0}^{\infty}\{-m\,I_m^c(r,\mu_0,\mu)\sin m(\phi-\phi_0)$$
$$+m\,I_m^s(r,\mu_0,\mu)\cos m(\phi-\phi_0)\}. \qquad (2.17)$$

Since only mean intensities are of interest in this work

$$\overline{I(r,\theta,\phi)}=\frac{1}{4\pi}\int_0^{2\pi}d\phi_0\int_0^{\pi}\sin\theta d\theta_0\,I(r,\theta_0,\phi_0,\phi,\theta)=\frac{1}{4\pi}\int_0^{2\pi}d\phi_0\int_{-1}^{1}d\mu_0\,I(r,\mu_0,\phi_0,\phi,\mu) \qquad (2.18)$$

Eq. 2.17 is averaged over azimuth to give

$$\mu\frac{\partial I_0^c(r,\mu_0,\mu)}{\partial r}+\frac{1-\mu^2}{r}\frac{\partial I_0^c(r,\mu_0,\mu)}{\partial\mu}+\frac{1}{2}\frac{\sqrt{1-\mu^2}\sqrt{1-\mu_0^2}}{r}\frac{\partial I_1^c(r,\mu_0,\mu)}{\partial\mu_0}$$
$$+\frac{1}{2}\frac{\sqrt{1-\mu^2}\sqrt{1-\mu_0^2}}{r}\frac{\mu_0}{1-\mu_0^2}I_1^c(r,\mu_0,\mu). \qquad (2.19)$$

In a stratified planetary atmosphere spherical effects, i.e. the angle derivatives, become important around sunrise and sunset. Thus, the first term in Eq. 2.19 is the dominant one and the other terms may be treated as perturbations. Using a perturbation technique suggested by Cannon (1984) to account for the spherical effects, Dahlback and Stamnes (1990) have shown that in a stratified atmosphere mean intensities may be calculated with sufficient accuracy for zenith angles less then 90° by including only the first term in Eq. 2.19, but using spherical geometry to compute the direct beam attenuation (see below). Hence, all angle derivatives will be ignored and the streaming term will simply be written as

$$\hat{n}\cdot\nabla=\mu\frac{\partial}{\partial r}. \qquad (2.20)$$

By ignoring all angle derivatives it has also been assumed that the medium varies only in the vertical direction, i.e. a stratified atmosphere. While neglecting angle derivatives is justified when treating the effect of the spherical shape of the atmosphere, these can not be neglected when the

inhomogeneity of the atmosphere is included. The atmosphere is highly inhomogeneous, both in the vertical and the horizontal, the latter variation being mostly due to clouds. While for a clear atmosphere it is a good approximation to assume that the medium is horizontally uniform, this is certainly not true for a cloudy atmosphere.

In, general clouds are inhomogeneous over a range of scale sizes, hence a realistic radiation model must be three dimensional and have high spatial resolution. Three dimensional models with mostly cubical clouds have been studied by several authors (McKee and Cox 1976, Wendling 1977, Davies 1978, Aida 1977, Harshvardham et al. 1981, Welch and Zdunkowski 1981a,b, Ellingson 1982, Bradley 1982), their major finding being the rather obvious result that finite clouds had lower albedos than plane–parallel clouds because of leakage of radiation out of the cloud sides. A general multi–dimensional formalism that includes arbitrary variability over many scale sizes, has been developed by Stephens (1988a,b). His results, so far, are qualitatively similar to the results from the cubical cloud models. Fractal descriptions of clouds are popular in the current research literature (Lovejoy et al. 1990, Gabriel et al. 1990, Davis et al. 1990). While fractals make *pictures* of clouds that look like clouds, there are, at the moment, no physical arguments leading to a fractal description of clouds. To quote Wiscombe (1983):

> ... measurements are the acid test of any model; it is not enough that a model simply 'looks' better. Perhaps a plane–parallel model taking proper account of vertical inhomogeneity will agree better with measurements than typical cubic cloud models with their spatially–invariant liquid water and drop distributions. Perhaps weighting plane–parallel albedos by the proper measure of cloudiness fraction will correctly predict the albedo of a patchy cloud field. But more importantly, our job is not to make our models as complicated as nature herself; it is to simplify and idealize, in order to gain understanding. Plane–parallel cloud modeling is an entirely acceptable way to do this. And, on a practical level, (a) we will never know, or want to know, the shape and size of every single cloud on Earth, and (b) plane–parallel clouds can be modeled with a level of spectral and angular detail unreachable in finite cloud models. Our job is to learn how to make simple adjustments to plane–parallel predictions to mimic patchiness, not to reject this very valuable modeling approach out of hand.

The search for a better understanding of radiation transport in inhomogeneous atmospheres is ongoing and many questions remain to be answered. For the development of models for studying quantities that depend on the radiation field, e.g. warming/cooling and photodissociation rates,

reliable and fast computational schemes are required. At the moment, only the plane–parallel approach has reached the state of development where it can safely be incorporated as a part of large models.

2.1.3 The source term

Having fixed the geometry and thus the streaming term in Eq. 2.8, attention is turned to the photon sources and sinks[2]

$$\begin{aligned} h\nu\, Q(r,\hat{n},\nu) = h\nu\, Q(r,\theta,\phi,\nu) \;=\; & -\beta^{ext}(r,\nu)\, I(r,\theta,\phi,\nu) \\ & +\frac{\beta^{sca}(r,\nu)}{4\pi}\int_0^{2\pi} d\phi' \int_0^{\pi} d\theta' p(r,\theta,\phi;\theta',\phi',\nu) I(r,\theta',\phi',\nu) \\ & +\beta^{abs}(r,\nu)\, B[T(r)]. \end{aligned} \tag{2.21}$$

The first term represents loss of radiation due to absorption and scattering out of the photon beam. The second term (multiple scattering term) describes the number of photons scattered into the beam from all other directions and, finally, the third term gives the amount of thermal radiation emitted in the frequency range between ν_1 and ν_2. The lower part of the Earth's atmosphere, may to a good approximation, be assumed to be in local thermodynamic equilibrium[3], thus the emitted radiation is proportional to the Planck function, $B[T(r)]$, integrated over the frequency or wavelength region of interest. Furthermore, by Kirchhoff's law the emissivity coefficient β^{emi} is equal to the absorption coefficient β^{abs}. The absorption, scattering and extinction coefficients are defined as (Stamnes 1986)

$$\beta^{abs}(r,\nu) = \sum_i \beta_i^{abs}(r,\nu), \qquad \beta_i^{abs}(r,\nu) = n_i(r)\sigma_i^{abs}(\nu) \tag{2.22}$$

$$\beta^{sca}(r,\nu) = \sum_i \beta_i^{sca}(r,\nu), \qquad \beta_i^{sca}(r,\nu) = n_i(r)\sigma_i^{sca}(\nu) \tag{2.23}$$

$$\beta^{ext}(r,\nu) = \beta^{abs}(r,\nu) + \beta^{sca}(r,\nu)$$

[2] For a derivation of the individual terms see e.g. Chandrasekhar (1960) or Cercignani (1975).

[3] The hypothesis of local thermodynamic equilibrium (LTE) makes the assumption that all thermodynamic properties of the medium are the same as their thermodynamic equilibrium (T.E.) values at the local T and density. Only the radiation field is allowed to depart from its T.E. value of $B[T(r)]$ and is obtained from a solution of the transfer equation. Such an approach is manifestly *internally inconsistent.* ... 'However, if the medium is subject only to *small* gradients over the mean free path a photon can travel before it is destroyed and thermalized by a collisional process, then the LTE approach is valid.' (adapted from Mihalas, p. 26, 1978)

where $n_i(r)$ is the density of the atmospheric molecule species i and $\sigma_i^{abs}(\nu)$ and $\sigma_i^{sca}(\nu)$ are the corresponding absorption and scattering cross sections. The phase function is defined as

$$p(r,\theta,\phi;\theta',\phi',\nu) = \frac{\sum_i \beta_i^{sca}(r,\nu) p_i(\theta,\phi;\theta',\phi',\nu)}{\sum_i \beta_i^{sca}(r,\nu)}$$

where the phase function for each species

$$p_i(\theta,\phi;\theta',\phi',\nu) = p_i(\cos\Theta,\nu) = \frac{\sigma_i^{sca}(\nu,\cos\Theta)}{\int_{4\pi} d\Omega\, \sigma_i^{sca}(\nu,\cos\Theta)}$$

and the scattering angle Θ is related to the local polar and azimuth angles through

$$\cos\Theta = \cos\theta\ \cos\theta' + \sin\theta\ \sin\theta'\ \cos(\phi-\phi').$$

The temperature profile, the densities and absorption and scattering cross sections are all needed to solve the radiative transfer equation. Temperatures and densities may readily be obtained from measurements or atmospheric models. In Chapter 3 is discussed how to obtain the required cross sections. The rest of this chapter is devoted to the solution of the one dimensional version of the radiative transfer equation 2.8.

2.1.4 The one dimensional radiative transfer equation

Above the streaming term and the source term in Eq. 2.8 were specified. Below the one dimensional radiative transfer equation will be cast in a form amenable to solution. Defining a single scattering albedo

$$\omega(r) = \omega(r,\nu) = \frac{\beta_i^{sca}(r,\nu)}{\beta_i^{ext}(r,\nu)} = \frac{\beta_i^{sca}(r,\nu)}{\beta_i^{abs}(r,\nu)+\beta_i^{sca}(r,\nu)}$$

and using Eqs. 2.20 and 2.21 the radiative transfer equation 2.8 may be written as

$$-\mu\frac{dI(r,\mu)}{\beta^{ext}dr} = I(r,\mu) - \frac{\omega(r)}{2}\int_{-1}^{1} d\mu' p(r,\mu,;\mu') I(r,\mu') - (1-\omega(r))B[T(r)] \qquad (2.24)$$

where all ϕ dependence have been integrated out. To reiterate, only the mean intensity given by Eq. 2.18, is of interest in this work. Assuming coherent (monochromatic) scattering all frequency dependence have also been suppressed.

The integro–differential equation 2.24 gives the azimuthally averaged intensity field when solved with appropriate boundary conditions, that is, the radiation incident at the bottom and the top of the atmosphere. At the bottom of the atmosphere the Earth partly reflects radiation and also

emits radiation as a quasi–black–body. At the top ($r = r_{top}$) a parallel beam of sunlight with magnitude I^0 in the direction μ_0 may be present

$$I(r_{top}, \mu) = I^0 \delta(\mu - \mu_0), \tag{2.25}$$

where $\delta(\mu - \mu_0)$ is the Dirac delta–function. It is akward to use a delta function for a boundary condition. However, a homogeneous differential equation with inhomogeneous boundary conditions may always be turned into an inhomogeneous differential equation with homogeneous boundary conditions. Since the integro–differential equation 2.24 is already inhomogeneous, the addition of another inhomogeneous term does not necessarily complicate the problem. Hence the intensity field is written as the sum of the direct and the scattered (or diffuse) radiation

$$I(r, \mu) = I^{dir}(r, \mu) + I^{sca}(r, \mu). \tag{2.26}$$

Inserting Eq. 2.26 into Eq. 2.24 it is seen that the direct beam satisfies

$$-\mu \frac{dI^{dir}(r, \mu)}{\beta^{ext} dr} = I^{dir}(r, \mu) \tag{2.27}$$

and the scattered intensity satisfies (the *sca* superscript is omitted)

$$\begin{aligned} -\mu \frac{dI(r, \mu)}{\beta^{ext} dr} &= I(r, \mu) - \frac{\omega(r)}{2} \int_{-1}^{1} d\mu' p(r, \mu; \mu') I(r, \mu') - (1 - \omega(r)) B[T(r)] \\ &\quad - \frac{\omega(r) I^0}{4\pi} p(r, \mu; \mu_0) e^{-ch(r, \mu_0)} \end{aligned} \tag{2.28}$$

where $ch(r, \mu_0)$ is the Chapman function describing the extinction path in a spherical atmosphere (Rees 1989, Dahlback and Stamnes, 1990)

$$ch(r_0, \mu_0) = \int_{r_0}^{\infty} \frac{\beta^{ext}(r, \nu)\, dr}{\sqrt{1 - \left(\frac{R + r_0}{R + r}\right)^2 (1 - \mu_0^2)}}. \tag{2.29}$$

Here R is the radius of the earth and r_0 the distance above the earth's surface. The direct beam is thus described by Beer's law

$$I^{dir}(r, \mu) = I^0 \, e^{-ch(r, \mu_0)}. \tag{2.30}$$

Defining an optical depth $d\tau = -\beta^{ext}(r) dr$ the equation for the diffuse radiation may be written as

$$\begin{aligned} \mu \frac{dI(\tau, \mu)}{d\tau} &= I(\tau, \mu) - \frac{\omega(\tau)}{2} \int_{-1}^{1} d\mu' p(\tau, \mu; \mu') I(\tau, \mu') - (1 - \omega(\tau)) B[T(\tau)] \\ &\quad - \frac{\omega(\tau) I^0}{4\pi} p(\tau, \mu; \mu_0) e^{-ch(\tau, \mu_0)}. \end{aligned} \tag{2.31}$$

The last term in the above equation is the direct beam pseudo–source.

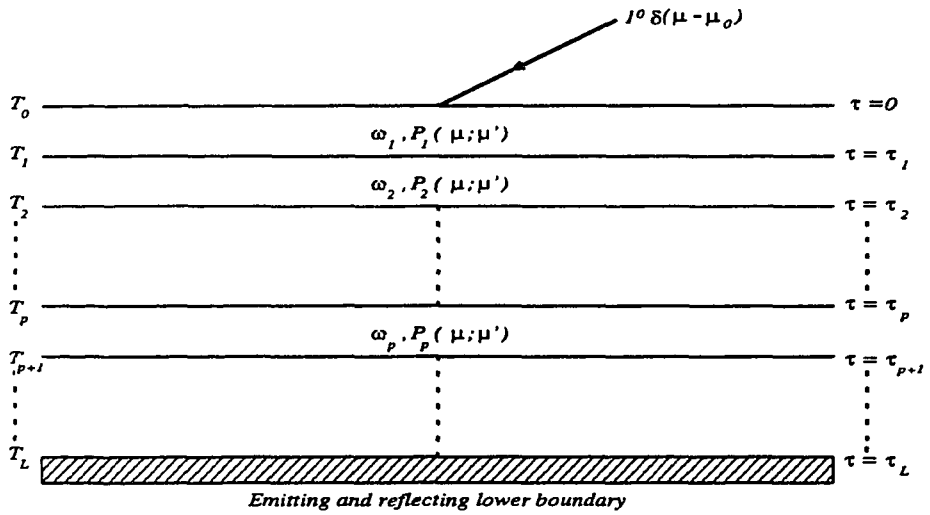

Figure 2.2: The division of the atmosphere into L adjacent homogeneous layers.

2.1.5 Layering of the atmosphere

The single scattering albedo, the phase function and the internal sources, the thermal source and the direct beam pseudo–source, are all functions of τ in an inhomogeneous atmosphere. To allow for this τ–dependence the atmosphere is divided into L adjacent homogeneous layers. In each layer the single scattering albedo and the phase function are taken be to constant, but are allowed to vary from layer to layer (see Fig. 2.2). The variation of the internal sources across a layer is taken into account by approximating the internal sources by an exponential-linear function in τ in each layer, see section 2.2.2. For each layer $\tau_{p-1} \leq \tau \leq \tau_p$, $p = 1, \cdots, L$ Eq. 2.31 is written as

$$\mu \frac{dI(\tau,\mu)}{d\tau} = I(\tau,\mu) - \frac{\omega}{2}\int_{-1}^{1} d\mu' p(\mu;\mu') I(\tau,\mu') - (1-\omega)B[T(\tau)] - \frac{\omega I^0}{4\pi} p(\mu;\mu_0) e^{-ch(\tau,\mu_0)}. \quad (2.32)$$

The coupling between adjacent layers is accounted for by requiring the intensity to be continuous across layer interfaces. In the following Eq. 2.32, which describes the diffuse radiation field in each homogeneous layer, will be solved.

2.2 Discrete ordinate solution

Numerous numerical methods exist for solving the integro-differential equation 2.32 (Lenoble 1985). In this work the discrete ordinate method as developed by Chandrasekhar (1960) and Stamnes and

collaborators (1988) will be used. The solution of the homogenous equation will first briefly be discussed. Next the inhomogeneous solution will be constructed and the importance of taking into account the variation with optical depth of the source terms in Eq. 2.32 will be discussed in some detail. The effects of polarization will be ignored as these are negligible (less than 0.1 %, Lacis and Hansen 1974) for the radiation quantities of interest in this study. However, a discrete ordinate solution of the radiative transfer equation for the 'polarization normal wave representation' has been presented by Kylling (1991). Weng (1992a,b) has developed a discrete ordinate solution for all the four components of the Stokes vector.

2.2.1 Homogeneous solution

The discrete ordinate approximation of the homogeneous part of Eq. 2.32 may be written (Chandrasekhar 1960)

$$\mu_i \frac{dI(\tau,\mu_i)}{d\tau} = I(\tau,\mu_i) - \sum_{\substack{j=-N \\ j\neq 0}}^{N} a_j D(\mu_i;\mu_j) I(\tau,\mu_j) \qquad i = \pm 1,\ldots,\pm N \tag{2.33}$$

where μ_i and a_i are quadrature points and weights (Gaussian quadrature is used), and

$$D(\mu_i;\mu_j) = \omega\, p(\mu_i;\mu_j).$$

The phase function is expanded in a series of $2N$ Legendre polynomials (valid for scattering by a central force field)

$$p(\mu_i;\mu_j) = \sum_{l=0}^{2N-1} (2l+1) g_l P_l(\mu_i) P_l(\mu_j)$$

where the phase function moments are given by

$$g_l = \frac{1}{2}\int_{-1}^{1} P_l(\cos\Theta) p(\cos\Theta) d(\cos\Theta).$$

For strongly forward-peaked phase functions the Delta-M method is utilized (Wiscombe 1977). Since the Delta-M transformation does not change the form of the radiative transfer equation (McKellar and Box 1981) the transformed quantities are not explicitly indicated below. The phase function satisfies the symmetry relations

$$\begin{aligned} p(\mu_i;\mu_j) &= p(-\mu_i;-\mu_j) \\ p(-\mu_i;\mu_j) &= p(\mu_i;-\mu_j). \end{aligned}$$

Using these symmetry relations Eq. 2.33 may be rewritten in matrix form as (Stamnes and Swanson 1981)

$$\frac{d}{d\tau}\begin{bmatrix} I^+ \\ I^- \end{bmatrix} = \begin{bmatrix} \alpha & \beta \\ -\beta & -\alpha \end{bmatrix}\begin{bmatrix} I^+ \\ I^- \end{bmatrix} \tag{2.34}$$

where

$$I^{\pm} = I(\tau, \pm\mu_i), \qquad i = 1, \ldots, N$$

and the $N \times N$ matrices α and β

$$\begin{aligned} \alpha_{ij} &= \frac{1}{\mu_i}\left[\delta_{ij} - a_j D(\mu_i;\mu_j)\right] = \frac{1}{\mu_i}\left[\delta_{ij} - a_j D(-\mu_i;-\mu_j)\right] \\ \beta_{ij} &= \frac{1}{\mu_i}\left[-a_j D(-\mu_i;\mu_j)\right] = \frac{1}{\mu_i}\left[-a_j D(\mu_i;-\mu_j)\right]. \end{aligned}$$

Here the fact have been used that Gaussian quadrature has the properties $\mu_{-i} = -\mu_i$ and $a_{-i} = a_i$. Seeking solutions to Eq. 2.34 of the form

$$I^{\pm} = g^{\pm}\, e^{-k\tau} \tag{2.35}$$

it is found that

$$\begin{bmatrix} -\alpha & -\beta \\ \beta & \alpha \end{bmatrix}\begin{bmatrix} g^+ \\ g^- \end{bmatrix} = k\begin{bmatrix} g^+ \\ g^- \end{bmatrix} \tag{2.36}$$

which is a standard algebraic eigenvalue problem of order $2N \times 2N$ determining the eigenvalues k and the eigenvectors $g^{\pm}$. Because of the special structure of the matrix in Eq. 2.36, the eigenvalues occur in pairs $(\pm k)$ and the order of the eigenvalue problem may be reduced by a factor 2 as follows (Stamnes and Swanson 1981). Rewriting Eq. 2.36 as

$$\begin{aligned} -\alpha g^+ - \beta g^- &= k g^+ \\ \beta g^+ + \alpha g^- &= k g^-. \end{aligned}$$

and adding and subtracting these two equations gives

$$(-\alpha + \beta)(g^+ - g^-) = k(g^+ + g^-) \tag{2.37}$$

$$(-\alpha - \beta)(g^+ + g^-) = k(g^+ - g^-). \tag{2.38}$$

Combining the two above equations gives

$$(\alpha - \beta)(\alpha + \beta)(g^+ + g^-) = k^2(g^+ + g^-)$$

which is an eigenvalue problem of order $N \times N$ determining the eigenvalues k and the eigenvectors $(g^+ + g^-)$; the eigenvectors $(g^+ - g^-)$ are determined from Eq. 2.38. The homogeneous solution of Eq. 2.32 for each homogeneous layer may thus be written as

$$I(\tau, \mu_i) = \sum_{\substack{j=-N \\ j\neq 0}}^{N} C_j g_j(\mu_i) e^{k_j \tau}, \qquad i = \pm 1, \ldots, \pm N \tag{2.39}$$

where the C_j's are constants of integration to be determined from the continuity and boundary conditions.

Homogeneous solution in the two–stream approximation. For $N = 1$ the popular two–stream approximation is obtained. Because analytic solutions may be written down for each layer, it is easy to implement. Furthermore it is computationally fast and of sufficient accuracy for many problems in atmospheric radiative transfer. For a review of different two–stream methods, see Meador and Weaver (1980). The two–stream solution presented below differs from previous approaches in that it accounts for spherical geometry both in the direct and the scattered intensity. For a complete discussion of the present two–stream approximation see Kylling, Stamnes and Tsay (1992).

Defining the asymmetry factor

$$g(\tau) = \frac{1}{2} \int_{-1}^{1} p(\tau, \cos\Theta) \cos\Theta \, d(\cos\Theta), \tag{2.40}$$

the backscatter probability is written as

$$\beta(\tau) = \frac{1}{2}(1 - 3g(\tau)\mu_1^2). \tag{2.41}$$

It describes the probability that a photon upon scattering will change direction from one hemisphere to the other. Solutions of the form

$$I^{\pm} = G^+(\pm\mu_1) e^{-k\tau} + G^-(\pm\mu_1) e^{k\tau} \tag{2.42}$$

are sought. Here

$$G^{\pm}(\pm\mu_1) = C^{\pm} g^{\pm}(\pm\mu_1). \tag{2.43}$$

and the $C^{\pm}$ are constants of integration. In the two–stream approximation the eigenvalue and eigenvectors are thus given by

$$k = \frac{1}{\mu_1} \sqrt{(1-\omega)(1-\omega+2\omega\beta)}. \tag{2.44}$$

$$g^+(-\mu_1) = g^-(+\mu_1) = 1 \tag{2.45}$$

$$g^+(+\mu_1) = g^-(-\mu_1) = R \tag{2.46}$$

where

$$R = \frac{g^+(+\mu_1)}{g^+(-\mu_1)} = \frac{g^-(-\mu_1)}{g^-(+\mu_1)} = \frac{\sqrt{1-\omega+2\omega\beta} - \sqrt{1-\omega}}{\sqrt{1-\omega+2\omega\beta} + \sqrt{1-\omega}}. \tag{2.47}$$

Some care must be exercised when choosing the quadrature angle μ_1 in the two–stream approximation. Possible choices for the quadrature rule include Gaussian full–range quadrature based on the interval [-1, 1] or half–range (double–Gaussian) quadrature based on the ranges [-1,0] and [0,1], separately. For general multi–stream algorithms it is preferable to use double Gaussian quadrature. However in the two stream approximation the double Gaussian quadrature ($\mu_1 = 0.5$) gives an unphysical backscattering ratio $\beta = 1/8$ for an asymmetry factor $g = 1$. The choice $\mu_1 = 1/\sqrt{3}$ (full–range Gaussian quadrature) gives the physically correct value $\beta = 0$. Since the mean intensity, and thus the flux divergence, is obtained by integrating over both hemispheres, the use of $\mu_1 = 1/\sqrt{3}$ is recommended for the calculation of mean intensities and flux divergences. For upward and downward fluxes, the choice $\mu_1 = 0.5$ may be preferable since accuracy to the maximum polynomial degree is then ensured for integrals over a single hemisphere.

2.2.2 Inhomogeneous solution

Both the thermal source and the direct beam pseudo–source vary with optical depth. For zenith angles less than approximately 75° curvature effects may be ignored in the direct beam pseudo–source, and it may be written in each layer as

$$Q^b(\tau, \mu) = \frac{\omega}{2} p(\mu, \mu_0) I^0 e^{-\tau/\mu_0} \tag{2.48}$$

hence exhibiting an exponential variation across the layer. The behavior of the thermal source depends upon the frequency range of interest. The Planck function in Eq. 2.21 is given by (Reif 1965)

$$B(T) = \int_{\nu_1}^{\nu_2} B_\nu(T)\, d\nu = \int_{\nu_1}^{\nu_2} \frac{2h\nu^3}{c^2} \frac{d\nu}{e^{\frac{h\nu}{kT}} - 1}. \tag{2.49}$$

Integrating over the entire spectrum ($\nu_1 = 0$, $\nu_2 = \infty$) gives the Stefan–Boltzmann law

$$B(T) = \sigma T^4 \tag{2.50}$$

where σ is the Stefan–Boltzmann constant. In the Wien limit ($h\nu \gg kT$)

$$B_\nu(T) = \frac{2h\nu^3}{c^3} e^{\frac{-h\nu}{kT}} \tag{2.51}$$

and

$$\int B_\nu(T)d\nu = \frac{2h\nu^4}{c^3} e^{\frac{-h\nu}{kT}} \left\{ \frac{kT}{h\nu} - 3\left(\frac{kT}{h\nu}\right)^2 + 6\left(\frac{kT}{h\nu}\right)^3 - 6\left(\frac{kT}{h\nu}\right)^4 \right\} + const \tag{2.52}$$

where only the first term inside the parentheses contributes since $h\nu \gg kT$. Hence, over some finite spectral range in the Wien limit, the Planck function is expected to have an exponential-linear dependence in $T(\tau)$. In the opposite limit $h\nu \ll kT$, the Rayleigh–Jeans limit,

$$B_\nu(T) = \frac{2h\nu^2 kT}{c^2} \tag{2.53}$$

gives a linear in $T(\tau)$ dependence of the Planck-function. Thus, in general a radiation problem with both isotropic (the thermal source) and anisotropic (the direct beam pseudo–source) internal sources that may vary both slowly and rapidly with optical depth must be solved. This variation, may in principle, be accomodated by subdividing the atmosphere into a sufficient number of layers, within each of which the source terms are taken to be constant. For rapidly varying sources the number of layers needed may be too large for this approach to be practically feasible, e.g. the computer time generally increases with the number of layers. However, by using a combination of analytical and numerical methods both slow and rapid variations of internal sources across a layer may be efficiently and accurately handled, (Kylling and Stamnes 1992). In each layer the source function is approximated by

$$Q(\tau, \mu) = e^{-\varrho\tau} \sum_{l=0}^{K} X_l(\mu)\tau^l \tag{2.54}$$

where ϱ and $X_l(\mu)$ are constants found by fitting the actual source to Eq. 2.54, as shown below.

Previous studies have used the constant ($K = 0$, $\varrho = 0$) and the linear ($K = 1$, $\varrho = 0$) optical depth approximation (Chandrasekhar 1960, Stamnes and Swanson 1981, Tsay et al. 1990, Wiscombe 1976). Kylling and Stamnes (1992) discussed the improvements obtained by invoking the quadratic ($K = 2$, $\varrho = 0$) and the exponential–linear ($K = 1$, $\varrho \neq 0$) optical depth approximations. In Fig. 2.3 the Planck function and the different approximations to it for different spectral regions are given. The exponential–linear approximation most closely resembles the Planck function in all the different cases shown and it will also best approximate the direct beam pseudo–source, cf. Eq. 2.48. Below a particular solution of the inhomogeneous radiative transfer equation 2.32, where the internal source is approximated by Eq. 2.54, is found.

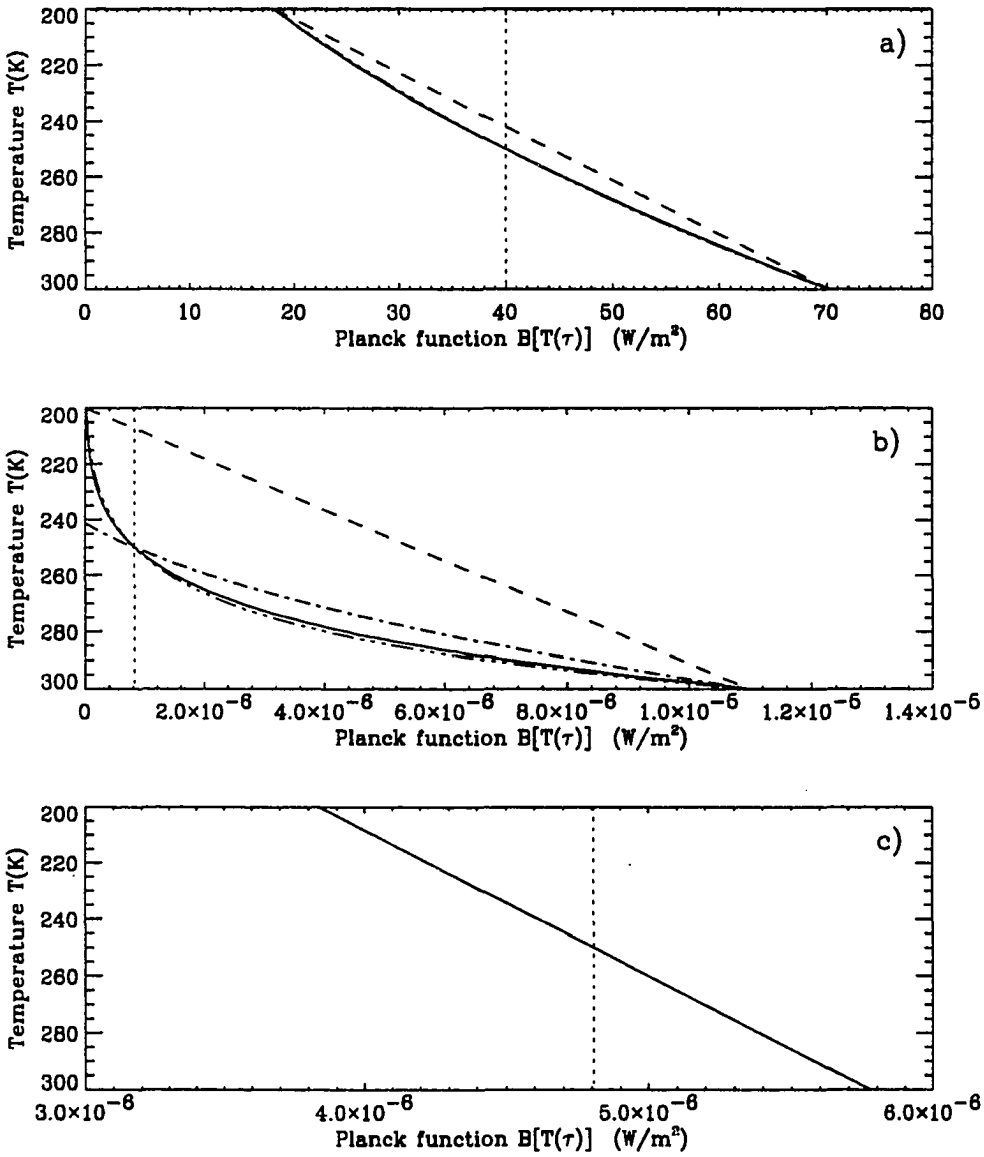

Figure 2.3: a)The Planck function integrated over the spectral range 300–800 cm^{-1} giving approximately a T^4 dependence (solid line) and the different approximations to it; constant (dotted line), linear (dashed line). Both the quadratic and the exponential–linear approximations are indistinguishable from the Planck function itself. b) The Planck function integrated over a narrow frequency range in the Wien limit (2702.99–2703.01 cm^{-1}). The solid line represents the Planck function, and the different approximations to it are the constant (dotted line), linear (dashed line), the quadratic (dash–dotted line) and the exponential–linear (dot–dot–dot–dashed line). c) The Planck function integrated over a narrow frequency range in the Rayleigh–Jeans limit (1.0–2.0 cm^{-1}). The solid line represents the Planck function, the dotted line is the constant approximation. The linear, the quadratic and the exponential–linear approximations coincide with the Planck function itself.

For a general anisotropic source $Q(\tau,\mu)$, the discrete version of the radiative transfer equation 2.32 is

$$\mu_i \frac{dI(\tau,\mu_i)}{d\tau} = I(\tau,\mu_i) - \sum_{\substack{j=-N \\ j\neq 0}}^{N} a_j D(\mu_i;\mu_j) I(\tau,\mu_j) - Q(\tau,\mu_i) \qquad i = \pm 1,\ldots,\pm N. \tag{2.55}$$

Insertion of Eq. 2.54 into Eq. 2.55 yields:

$$\mu_i \frac{dI(\tau,\mu_i)}{d\tau} = I(\tau,\mu_i) - \sum_{\substack{j=-N \\ j\neq 0}}^{N} a_j D(\mu_i;\mu_j) u(\tau,\mu_j) \quad - e^{-\varrho\tau} \sum_{l=0}^{K} X_l(\mu_i)\tau^l. \tag{2.56}$$

A particular solution to Eq. 2.56 is sought of the form

$$I(\tau,\mu_i) = e^{-\varrho\tau} \sum_{l=0}^{K} Y_l(\mu_i)\tau^l \tag{2.57}$$

where the $Y_l(\mu_i)$'s are coefficients to be determined. Substitution of Eq. 2.57 into Eq. 2.56 gives

$$\sum_{\substack{j=-N \\ j\neq 0}}^{N} \{\delta_{ij}(1+\varrho\mu_i) - a_j D(\mu_i;\mu_j)\} Y_K(\mu_j) \;=\; X_K(\mu_i) \tag{2.58}$$

$$\sum_{\substack{j=-N \\ j\neq 0}}^{N} \{\delta_{ij}(1+\varrho\mu_i) - a_j D(\mu_i;\mu_j)\} Y_l(\mu_j) \;=\; \mu_i(l+1)Y_{l+1}(\mu_i) + X_l(\mu_i) \tag{2.59}$$

$$l = K-1, K-2, \ldots, 0$$

which is a system of linear algebraic equations determining the $Y_l(\mu_i)$'s. In this work the relevant internal source is the sum of the thermal and the direct beam pseudo-source, cf. Eq. 2.32,

$$Q(\tau,\mu_i) = Q^t(\tau,\mu_i) + Q^b(\tau,\mu_i). \tag{2.60}$$

The internal thermal source is according to Eq. 2.32

$$Q^t(\tau,\mu) = Q^t(\tau) = (1-\omega)B[T(\tau)]. \tag{2.61}$$

The Planck source term is isotropic and may be approximated by:

$$B[T(\tau)] = e^{-\varrho_t\tau} \sum_{l=0}^{K} b_l \tau^l \tag{2.62}$$

according to Eq. 2.54. A particular solution is sought of the form

$$I^t(\tau,\mu_i) = (1-\omega)e^{-\varrho_t\tau} \sum_{l=0}^{K} Y_l^t(\mu_i)\tau^l. \tag{2.63}$$

The $Y_l^t(\mu_i)$ coefficients are determined by solving Eqs. 2.58-2.59 with $X_l(\mu_i) = (1-\omega)b_l$. For the direct beam pseudo–source

$$Q^b(\tau,\mu) = \frac{\omega}{2}p(\mu;\mu_0)I^0 e^{-ch(\tau,\mu_0)} \tag{2.64}$$

and the particular solution is again readily found from Eqs. 2.58–2.59. The general solution to Eq. (2.32) may then be written as

$$I(\tau,\mu_i) = \sum_{\substack{j=-N \\ j\neq 0}}^{N} C_j G_j(\mu_i)e^{k_j\tau} + e^{-\varrho_b\tau}\sum_{l=0}^{K} Y_l^b(\mu_i)\tau^l + e^{-\varrho_t\tau}\sum_{l=0}^{K} Y_l^t(\mu_i)\tau^l \tag{2.65}$$

where Y_l^b are the coefficients for the direct beam pseudo–source.

Inhomogeneous exponential–linear solution in the two–stream approximation. In the two–stream approximation the internal source in the exponential–linear approximation is written as

$$Q(\tau,\pm\mu_1) = e^{-\varrho\tau}(X_0(\pm\mu_1) + X_1(\pm\mu_1)\tau) \tag{2.66}$$

or

$$Q^{\pm}(\tau) = e^{-\varrho\tau}(X_0^{\pm} + X_1^{\pm}\tau). \tag{2.67}$$

Seeking a particular solution of the form

$$I^{\pm}(\tau) = e^{-\varrho\tau}(Y_0^{\pm} + Y_1^{\pm}\tau) \tag{2.68}$$

it is found

$$Y_1^{\pm} = \frac{\omega\beta X_1^{\pm} + (1-\omega+\omega\beta\mp\varrho\mu_1)X_1^{\pm}}{(1-\omega)(1-\omega+2\omega\beta)-(\varrho\mu_1)^2} \tag{2.69}$$

$$Y_0^{\pm} = \frac{\omega\beta Z_0^{\pm} + (1-\omega+\omega\beta\mp\varrho\mu_1)Z_0^{\pm}}{(1-\omega)(1-\omega+2\omega\beta)-(\varrho\mu_1)^2} \tag{2.70}$$

where

$$Z_0^{\pm} = X_0^{\pm} \pm \mu_1 Y_1^{\pm}. \tag{2.71}$$

Thus, in the two–stream approximation the complete solution to the radiative transfer equation is

$$I(\tau,\pm\mu_1) = C^+g^+(\pm\mu_1)e^{-k\tau} + C^-g^-(\pm\mu_1)e^{k\tau} + e^{-\varrho_b\tau}(Y_{b0}^{\pm} + Y_{b1}^{\pm}\tau) + e^{-\varrho_t\tau}(Y_{t0}^{\pm} + Y_{t1}^{\pm}\tau) \tag{2.72}$$

The boundary and continuity conditions are applied as in the general N–stream case.

The ϱ, $X_0(\mu_i)$ and $X_1(\mu_i)$ coefficients in Eq. 2.54. For $\varrho \neq 0$ Eq. 2.54 represents a set of non-linear equations determining ϱ and the $X_l(\mu)$ coefficients. This set of equations can not be readily solved for all values of K by analytical methods. However, for $K \leq 3$ analytic solutions exist and for $K = 1$ the exponential-linear approximation is arrived at. Knowing the internal source Q_i for each layer at the top, center and bottom, three equations to solve for the three unknown coefficients are ϱ, $X_0(\mu_i)$ and $X_1(\mu_i)$,

$$Q_0(\mu_i) = e^{-\varrho\tau_0}(X_0(\mu_i) + X_1(\mu_i)\tau_0) \tag{2.73}$$

$$Q_1(\mu_i) = e^{-\varrho\tau_1}(X_0(\mu_i) + X_1(\mu_i)\tau_1) \tag{2.74}$$

$$Q_2(\mu_i) = e^{-\varrho\tau_2}(X_0(\mu_i) + X_1(\mu_i)\tau_2) \qquad i = \pm 1, \ldots, \pm N. \tag{2.75}$$

The ϱ coefficient are forced to be angle independent by solving Eqs. 2.73-2.75 for one specific μ_i. The angular dependence is in the $X_l(\mu)$ coefficients. Assuming $\tau_1 = \frac{\tau_0+\tau_2}{2}$ the solution for ϱ, $X_0(\mu_i)$ and $X_1(\mu_i)$ is:

$$\varrho = \frac{2}{\tau_2 - \tau_0} \ln\left\{ \frac{Q_1(\mu_1)}{Q_2(\mu_1)} \pm \sqrt{\left(\frac{Q_1(\mu_1)}{Q_2(\mu_1)}\right)^2 - \frac{Q_0(\mu_1)}{Q_2(\mu_1)}} \right\} \tag{2.76}$$

$$X_1(\mu_i) = \frac{Q_2(\mu_i)e^{\varrho\tau_2} - Q_0(\mu_i)e^{\varrho\tau_0}}{\tau_2 - \tau_0} \tag{2.77}$$

$$X_0(\mu_i) = Q_0(\mu_i)e^{\varrho\tau_0} - X_1(\mu_i)\tau_0 \qquad i = \pm 1, \ldots, \pm N.$$

To calulate ϱ from Eq. 2.76 it is required that $Q_1^2 - Q_0Q_2 \geq 0$. It is shown in Appendix A that this is always the case when the internal source is the Planck function. For sources where $Q_2 > Q_1 > Q_0$ the (+) solution is used for ϱ and the (−) solution when $Q_2 < Q_1 < Q_0$. For source functions that decrease very rapidly with scattering depth, Q_2 (the source at the bottom) may be close or equal to zero. In this case $X_1(\mu_i)$ is set equal to 0, and

$$\varrho = \frac{2}{\tau_2 - \tau_0} \ln\left\{ \frac{Q_0(\mu_1)}{Q_1(\mu_1)} \right\} \tag{2.78}$$

$$X_0(\mu_i) = -Q_0(\mu_i)e^{\varrho\tau_0}. \tag{2.79}$$

If both Q_2 and Q_1 are close or equal to zero, $X_1(\mu_i)$ is set equal to 0 and $X_0(\mu_i) = Q_0(\mu_i)$ and $\varrho = \sqrt{(max/\tau_2)}$ where max is the largest number available on the computer.

When the absolute value of ϱ becomes large, numerical overflow problems may occur in either Eqs. 2.77- 2.78 or Eq. 2.65. The value of ϱ is most likely get large because $\tau_2 - \tau_0$ becomes small. For optically thin layers however, the linear approximation gives adequate results. Thus when the absolute value of ϱ is large enough to cause overflow, ϱ is set equal to 0 and the linear approximation is used.

2.2.3 Boundary conditions

The constants of integration C_j in Eq. 2.65 are found from the boundary and continuity conditions for the diffuse intensity. At the top boundary there is no incident diffuse intensity ($\mu \geq 0$)

$$I(\tau = 0, -\mu) = 0. \tag{2.80}$$

Furthermore, the intensities are required to be continuous across layer interfaces

$$I_p(\tau_p, \mu) \;=\; I_{p+1}(\tau_p, \mu) \qquad\qquad p = 1, \ldots, L-1. \tag{2.81}$$

At the bottom boundary is is assumed that the reflected flux is proportional to the incident flux, and that the Earth emits quasi–blackbody thermal radiation. Hence the total reflected flux is

$$\pi I(\tau_L, +\mu) = \pi\, \epsilon\, B[T(\tau_L)] + 2\pi\, A \int_0^1 \mu I(\tau_L, -\mu) d\mu + \mu_0\, A\, I^0 e^{-ch(\tau_L, \mu_0)} \tag{2.82}$$

where the albedo, A, gives the fraction of reflected light, and it has been assumed that the Earth reflects radiation isotropically (Lambert reflector). The emissivity $\epsilon = 1 - A$, by Kirchhoff's law. The first term on the right hand side is thermal radiation emitted by the Earth, the second term is reflection of downward diffuse radiation and the last term is due to reflection of the direct beam that has penetrated through the whole atmosphere.

Upon insertion of Eq. 2.65 into Eqs. 2.80–2.82 a system of linear algebraic equations determining the constants of integration C_j is obtained. However, to avoid overflow in Eq. 2.65 and, most importantly, numerical ill–conditioning when solving for the constants of integration, Eqs. 2.80–2.82, the scaling transformation discussed by Stamnes and Conklin (1984) is utilized. Since $k_{-j} = -k_j$, than $k_j > 0$ for all j.

$$C_{+j,p} = \tilde{C}_{+j,p} e^{k_{j,p}\tau_{p-1}} \tag{2.83}$$

$$C_{-j,p} = \tilde{C}_{-j,p} e^{-k_{j,p}\tau_p}. \tag{2.84}$$

Insertion of Eqs. 2.83–2.84 into Eq. 2.65 gives the intensity in layer p

$$I_p(\tau, \mu_i) = \sum_{j=1}^{N} \left\{ \tilde{C}_{-j,p} G_{-j,p}(\mu_i) e^{-k_{j,p}(\tau_p - \tau)} + \tilde{C}_{+j,p} G_{+j,p}(\mu_i) e^{-k_{j,p}(\tau - \tau_{p-1})} \right\} + R_p(\tau, \mu_i), \tag{2.85}$$

$$i = \pm 1, \ldots, \pm N, \quad p = 1, \ldots, L$$

where

$$R_p(\tau, \mu_i) = e^{\varrho_b \tau} \sum_{l=0}^{K} Y_l^b(\mu_i) \tau^l + e^{\varrho_t \tau} \sum_{l=0}^{K} Y_l^t(\mu_i) \tau^l$$

and all the exponentials in the homogeneous solution have negative arguments, as they should, to avoid numerical overflow. The discrete version of the boundary and continuity conditions Eqs. 2.80–2.82 is

$$I_1(0,-\mu_i) = 0 \qquad i=1,\ldots,N.$$

$$I_p(\tau_p,\mu_i) = I_{p+1}(\tau_p,\mu_i) \qquad i=\pm1,\ldots,\pm N, \quad p=1,\ldots,L-1. \tag{2.86}$$

$$I_L(\tau_L,+\mu_i) = \epsilon\, B[T(\tau_L)] + 2A\sum_{j=1}^{N} a_j\mu_j I_L(\tau_L,-\mu_j) + \frac{\mu_0 A}{\pi} I_0 e^{-ch(\tau_L,\mu_0)} \tag{2.87}$$
$$i=1,\ldots,N.$$

Insertion of Eq. 2.65 into Eqs. 2.86–2.81 yields (Stamnes et al. 1988)

$$\sum_{j=1}^{N}\left\{\tilde{C}_{-j,1}G_{-j,1}(-\mu_i) + \tilde{C}_{+j,1}G_{+j,1}(-\mu_i)e^{-k_{j,1}\tau_1}\right\} = -R_1(0,\mu_i), \qquad i=1,\ldots,N, \tag{2.88}$$

$$\sum_{j=1}^{N}\left\{\tilde{C}_{-j,p}G_{-j,p}(\mu_i) + \tilde{C}_{+j,p}G_{+j,p}(\mu_i)e^{-k_{j,p}(\tau_p-\tau_{p-1})}\right.$$
$$\left. -\tilde{C}_{-j,p+1}G_{-j,p+1}(\mu_i)e^{-k_{j,p+1}(\tau_{p+1}-\tau_p)} - \tilde{C}_{+j,p+1}G_{+j,p+1}(\mu_i)\right\}$$
$$= R_{p+1}(\tau_p,\mu_i) - R_p(\tau_p,\mu_i), \tag{2.89}$$
$$i=\pm1,\ldots,\pm N, \quad p=1,\ldots,L-1$$

$$\sum_{j=1}^{N}\left\{\tilde{C}_{-j,L}r_{-j,L}(\mu_i) + e^{-k_{j,L}(\tau_L-\tau_{L-1})} + \tilde{C}_{+j,L}r_{+j,L}(\mu_i)\right\} = \gamma(\tau_L,\mu_i) \qquad i=1,\ldots,N \tag{2.90}$$

where

$$\gamma(\tau_L,\mu_i) = \epsilon\, B[T(\tau_L)] - R_L(\tau_L,\mu_i) + \frac{\mu_0 A}{\pi} I^0 e^{-ch(\tau_L,\mu_0)} + 2A\sum_{n=1}^{N} a_n\mu_n R_L(\tau_L,-\mu_n) \tag{2.91}$$

$$r_{j,L}(\mu_i) = G_{j,L}(\mu_i) - 2A\sum_{n=1}^{N} a_n\mu_n G_{j,L}(-\mu_n). \tag{2.92}$$

Eqs. 2.88–2.90 are a $(2N\times L)\times(2N\times L)$ system of linear algebraic equations from which the $2N\times L$ unknown coefficients $\tilde{C}_{j,p}$, $j=\pm1,\ldots,\pm N$, $p=1,\ldots,L$, are determined. To solve this system of equations, it is taken advantage of the fact that the coefficient matrix is a $(6N-1)$ diagonal band matrix (Stamnes and Conklin 1984).

The one dimensional radiative transfer equation 2.24 has thus been solved. The solution is given by the sum of the direct and the diffuse intensity (Eq. 2.26), where the direct intensity is given by Eq. 2.30 and the diffuse intensity by Eq. 2.65. The constants of integration are found by solving Eqs. 2.88–2.90.

2.3 Verification of the solution method

Complex numerical procedures as the one outlined above are difficult both to develop and to implement. Great care must be taken during implementation to assure that the numerical procedure is stable for any values and combinations of the input parameters, i.e. optical depth, single scattering albedo, phase function and boundary conditions. The homogeneous solution of the radiative transfer equation has been tested and verified in detail by Stamnes and Swanson (1981), Stamnes and Conklin (1984), Stamnes et al. (1992) and Tsay et al. (1990). The inhomogeneous solution in the exponential–linear approximation has been tested and verified by Kylling and Stamnes (1992), who present results pertinent to an internal thermal radiation source. Below, some of the results are presented for the direct beam pseudo–source to demonstrate the power of the exponential–linear approximation and the importance of properly treating the variation of internal sources within each of the layers into which the atmosphere is divided.

2.3.1 Results pertinent to the mono-directional beam pseudo-source

In Fig. 2.4 results are given for the mono-directional beam pseudo-source, Eq. 2.64 in the linear and the exponential–linear approximation for a single layer of optical depth $\tau = 1.0$. Only the diffuse radiation, as given by Eq. 2.65, is included in the results presented below. The diffuse radiation is calculated for beam angles of 70°, and 85°. At 70°, curvature effects are small and the beam pseudo-source exhibits essentially an exponential behavior which is nicely fitted with the exponential-linear approximation. The linear approximation gives unacceptably large errors, even for a medium with moderate optical depth, $\tau = 1.0$. At 85° curvature effects come into play and the beam pseudo-source falls off slower with optical depth than in a plane parallel medium. In this case the exponential-linear approximation overestimates the diffuse radiation by about 10%. But this is still much better than the linear approximation which overestimates the diffuse radiation by several hundred percent. Similar examples for an optical depth of $\tau = 10.0$ for a single layer were also investigated. The exponential-linear approximation behaves well for angles where curvature effects are negligible, but was off by $50 - 100\%$ for large zenith angles. The linear approximation overestimated the diffuse radiation by several orders of magnitude for large optical depths. When the direct beam is also included the error in the total intensity (Eq. 2.26), will be less than for the diffuse intensity alone. However, for cloudy atmospheres large optical depths are often encountered and the diffuse intensity prevails.

2.4 Summary

The equation pertinent to radiation transport in the Earth's atmosphere has been derived from the Boltzmann equation. Assuming a stratified spherical atmosphere the radiative transfer equation was cast in a form amenable to solution. The discrete ordinate method was employed to solve the resulting one–dimensional radiative transfer equation for the azimuthally averaged radiation field. It is given as the sum of the direct, Eq. 2.30, and the scattered (diffuse), Eq. 2.65, intensity, cf. Eq. 2.26. The solution allows us to compute the intensity field at any optical depth in the medium. Furthermore, the computer time is independent of the optical thickness of the atmosphere, and the algorithm is unconditionally stable for an arbitrarily large number of quadrature angles and arbitrarily large optical depths.

The main concern here has been to outline a numerical scheme to calculate the mean intensity

$$\overline{I_\nu(\tau)} = \frac{1}{2}\int_{-1}^{1} I(\tau,\mu,\nu)d\mu \tag{2.93}$$

since that is the quantity of interest when calculating photodissociation and warming/cooling rates. For completeness, it is noted that the flux F and the flux divergence $\frac{dF}{d\tau}$ is also readily calculated by the above procedure

$$F_\nu(\tau) = 2\pi\int_{-1}^{1} \mu I(\tau,\mu,\nu)d\mu \tag{2.94}$$

and

$$\frac{dF_\nu(\tau)}{d\tau} = 4\pi(1-\omega)(\overline{I} - B). \tag{2.95}$$

The latter relationship is obtained by integrating Eq. 2.24 over the polar angle.

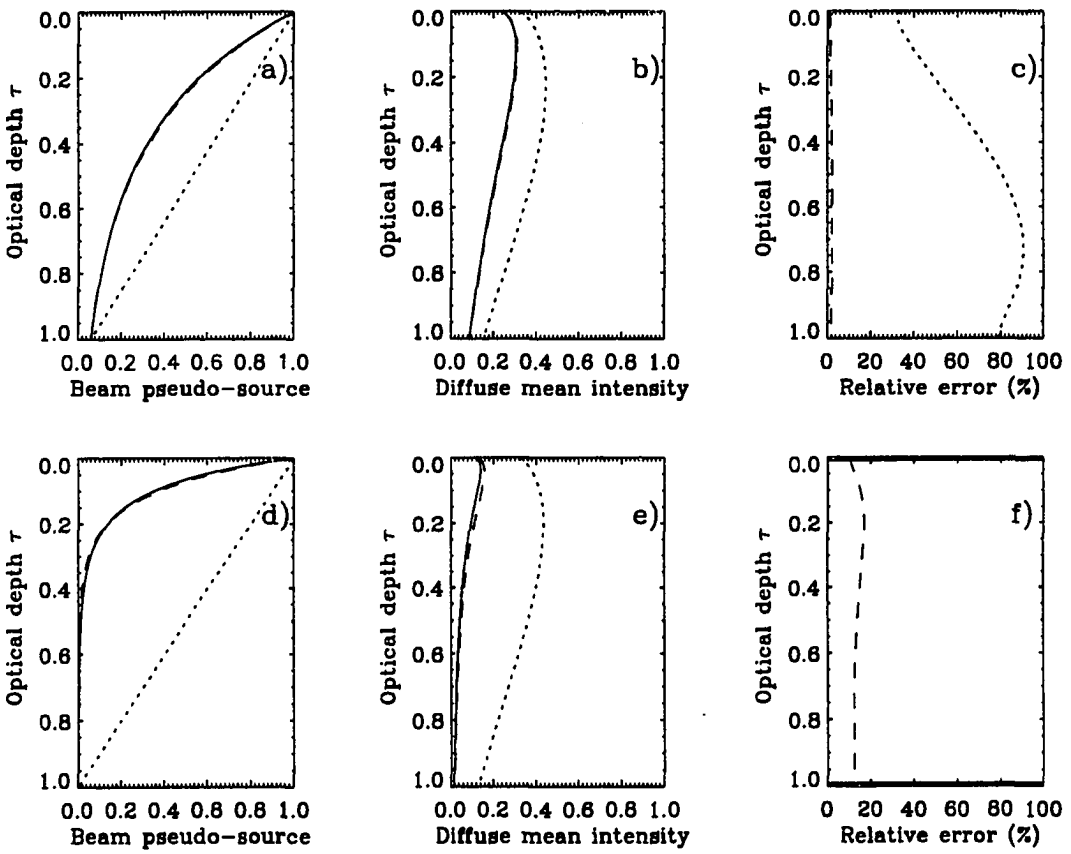

Figure 2.4: a) The beam pseudo-source for $\theta = \arccos \mu_0 = 70°$ (solid line) and the linear (dashed line) and the exponential-linear (dash-dashed line) approximations to it. b) The mean diffuse intensity, arbitrary units. c) The relative error for the different approximations. d)–f):Same as in a)–c), but for $\theta = \arccos \mu_0 = 85°$. Note that in f) the error for the linear approximation is so large that it is off the graph.

Chapter 3

Optical properties of the atmosphere

To calculate the radiation field in the earth's atmosphere, the absorption and scattering cross sections for the molecules and aerosols in question are needed. In general, these cross sections vary both with pressure and temperature. Furthermore, they may vary rapidly and erratically with wavelength. In order to accurately calculate quantities pertinent to modelling of the chemistry and dynamics of the atmosphere, e.g. warming/cooling and photodissociation rates, all these variations should be accounted for. However, detailed calculations are too time consuming to be of any practical use for many types of studies. Therefore approximate schemes must be utilized.

The first section is devoted to the calculation of molecular absorption cross sections. Using quantum theory it is briefly reviewed how molecules absorb radiation in the electric dipole approximation. Next this knowledge is combined with a high resolution molecular absorption data base to calculate detailed absorption cross sections as a function of pressure, temperature and wavenumber. These detailed cross sections are used as a benchmark for developing an approximate scheme based on the so–called correlated–k distribution technique.

In the second section the absorption and scattering amplitudes of radiation impinging upon homogeneous spheres representing molecules, water droplets and aerosols, are calculated. Assuming that the radiation is made up of monochromatic plane waves, the absorption and scattering amplitudes are calculated from Mie–theory. These absorption and scattering amplitudes are subsequently used to develop approximate cross sections for absorption and scattering of water droplets

(clouds) and aerosols. A parameterization scheme is utilized to simplify the use of these calculations. Finally, Rayleigh scattering, i.e. scattering by molecules, is briefly discussed.

3.1 Molecular absorption of radiation[1]

The absorption cross section σ_{abs} for N photons incident on a molecule is defined as

$$\sigma_{abs} = \frac{\text{net rate of absorption of photons}}{\text{incident photon flux}} = \frac{(dW/dt)_{abs}}{(Nc/\mathcal{V})} \tag{3.1}$$

where c is the speed of light and $N/\mathcal{V}$ is the density of photons per unit volume. In order to calculate the net rate of absorption of photons the behavior of molecules in the presence of photons, i.e. an electromagnetic field, must be studied. Generally, both the molecule and the electromagnetic radiation field must be quantized. However, interested here are in the macroscopic properties of the electromagnetic field of the earth's atmosphere, it suffices to describe it classically[2].

3.1.1 The Schrödinger equation

The state of the molecule is described by a wave function $\psi(\mathbf{r}_a, \mathbf{r}_1, \ldots, \mathbf{r}_n, t)$, where $\mathbf{r}_a$ represents all the internal coordinates of the molecule and the $\mathbf{r}_i$'s are the positions of the n surrounding molecules (perturbers). The probability of finding the molecule in the volume element between $\mathbf{r}_a$ and $\mathbf{r}_a + d\mathbf{r}_a$ is, as usual, $\psi^*\psi d\mathbf{r}_a$. The evolution of the wave function is described by the Schrödinger equation (see e.g. Baym 1969)

$$H|\psi\rangle = i\hbar\frac{\partial}{\partial t}|\psi\rangle \tag{3.2}$$

where the total Hamiltonian of the system is

$$H \equiv H(t) = H^0 + H^{int}(t). \tag{3.3}$$

Here H^0 is the Hamiltonian of the unperturbed molecule and $H^{int}(t)$ represents the interaction between the molecule and the radiation field, and between the molecule and the perturbers. Before

[1] Part of the exposition presented in this section is standard material in any advanced book on quantum mechanics. It is included in order to develop a complete picture of the physical processes involved in radiation transport in a planetary atmosphere, and of the approximations necessary to obtain a solveable problem.

[2] A macroscopic (or strong) field (or source) is understood to be 'the average of a field (or source) over a volume that is large compared to the volume occupied by a single atom or molecule' (Jackson 1975). The theory of the interaction between a quantum mechanical molecule and a classical electromagnetic field is labeled semiclassical. It has been shown that a semiclassical treatment of absorption gives the same result as the full quantum theory also for weak fields. This is not true for emission where the effect of spontaneous emission must be included (Dirac 1958, p. 246).

describing the Hamiltonian in detail, the average transition rate of the molecule going from state $|i\rangle$ to state $|f\rangle$ is calculated. It is noted that all time–dependence of the Hamiltonian lies in $H^{int}(t)$ and furthermore that the strength of H^{int} relative to H^0 allows H^{int} to be treated as a perturbation. Using first order perturbation theory, Fermi's golden rule is dereived for the transition rate.

3.1.2 First–order perturbation theory

The eigenstates (stationary states) $|\phi_j\rangle$ of the unperturbed molecule are given by the time–independent Schrödinger equation

$$H^0|\phi_j\rangle = E_j|\phi_j\rangle. \tag{3.4}$$

The time evolution is described by

$$H^0|\psi_j\rangle = i\hbar\frac{\partial}{\partial t}|\psi_j\rangle. \tag{3.5}$$

Since the eigenstates of H^0 form a complete set

$$|\psi_j(\mathbf{r},t)\rangle = e^{-iE_jt/\hbar}|\phi_j(\mathbf{r})\rangle. \tag{3.6}$$

A general state of the system may always be expanded in terms of the eigenstates

$$|\psi(\mathbf{r},t)\rangle = \sum_j d_j(t)e^{-iE_jt/\hbar}|\phi_j(\mathbf{r})\rangle. \tag{3.7}$$

The expansion coefficients $d_j(t)$ are functions of t because of the time dependence in H^{int}. The equation for the evolution of $d_j(t)$ is found upon insertion of Eq. 3.7 into Eq. 3.2

$$i\hbar\sum_j \dot{d}_j e^{-iE_jt/\hbar}|\phi_j\rangle = H^{int}(t)\sum_j d_j e^{-iE_jt/\hbar}|\phi_j\rangle \tag{3.8}$$

where the dot has the usual meaning of a time derivative. Operating on Eq. 3.8 with $\langle\phi_f|e^{iE_ft/\hbar}$ gives

$$i\hbar\dot{d}_f = \sum_j\langle\phi_f|H^{int}(t)|\phi_j\rangle e^{i\omega_{fj}t}d_j(t) \tag{3.9}$$

where

$$\omega_{fj} = \frac{E_f - Ej}{\hbar}. \tag{3.10}$$

It is assumed that at $t = 0$ the system is in a state $|\psi_i\rangle$, i.e. $d_j(0) = \delta_{ji}$. To the zeroth order Eq. 3.9 then becomes (recalling that H^{int} is treated as a perturbation),

$$\dot{d}_f = 0 \tag{3.11}$$

as expected. To the first order the equation for d_f reads

$$\dot{d}_f = -\frac{i}{\hbar}\langle\phi_f|H^{int}(t)|\phi_i\rangle e^{i\omega_{fi}t} \tag{3.12}$$

which has the solution

$$d_f(t) = \delta_{fi} - \frac{i}{\hbar}\int_0^t \langle\phi_f|H^{int}(t')|\phi_i\rangle e^{i\omega_{fi}t'}dt'. \tag{3.13}$$

As it stands, Eq. 3.13 represents the amplitude for a transition from state $|\phi_i\rangle$ to state $|\phi_f\rangle$ in time t.

3.1.3 Fermi's golden rule

Next the time dependence of H^{int} is discussed. Since the radiation field is periodic its time variation may be represented by

$$H^{int}(t) = H^{int}e^{-i\omega t}. \tag{3.14}$$

Insertion of Eq. 3.14 into Eq. 3.13 gives ($i \neq f$)

$$d_f(t) = -\frac{i}{\hbar}\int_{-T/2}^{T/2}\langle\phi_f|H^{int}|\phi_i\rangle e^{i(\omega_{fi}-\omega)t'}dt' \tag{3.15}$$

where the molecule is exposed to the radiation field from $t = -T/2$ to $t = T/2$. In the case discussed here, the perturbation is obviously allowed to persist, hence one may let $\mathbf{T} \rightarrow \infty$ in Eq. 3.15 to get[3]

$$d_f(t) = -\frac{2\pi i}{\hbar}\langle\phi_f|H^{int}|\phi_i\rangle\delta(\omega_{fi} - \omega). \tag{3.16}$$

The probability for the transition $i \rightarrow f$ is

$$P_{i\rightarrow f} = d_f(t)d_f^*(t) = \frac{4\pi^2}{\hbar^2}|\langle\phi_f|H^{int}|\phi_i\rangle|^2\delta(\omega_{fi} - \omega)\delta(\omega_{fi} - \omega). \tag{3.17}$$

[3] One of the ways of writing the Dirac δ-function is

$$\delta(x' - x) = \frac{1}{2\pi}\int_{-\infty}^{\infty} dk\, e^{ik(x'-x)}$$

and the average transition rate[4]

$$\left(\frac{dW}{dt}\right)_{i\to f} = \frac{P_{i\to f}}{T} = \frac{2\pi}{\hbar}|\langle\phi_f|H^{int}|\phi_i\rangle|^2\delta(E_f - E_i - \hbar\omega). \tag{3.18}$$

Eq. 3.18 is called Fermi's golden rule; below it will be used to write down an expression for the absorption cross section.

3.1.4 The Hamiltonian and the absorption rate

For a single electron, i.e. the electron involved in the absorption process, moving in an external electromagnetic field the Hamiltonian is given by (see e.g. Goldstein 1980, p. 346)

$$H = \frac{1}{2m}(\mathbf{p} - \frac{e}{c}\mathbf{A})^2 + e\phi + V(\mathbf{r}) = H^0 + H^{int} \tag{3.19}$$

where

$$H^0 = \frac{|\mathbf{p}|^2}{2m} + V(\mathbf{r}_1, \ldots, \mathbf{r}_n) \tag{3.20}$$

$$H^{int} = -\frac{e}{2mc}(\mathbf{p}\cdot\mathbf{A} + \mathbf{A}\cdot\mathbf{p}) + \frac{e^2}{2mc}\mathbf{A}\cdot\mathbf{A} + e\phi, \tag{3.21}$$

$\mathbf{p}$ is the momentum operator and $V(\mathbf{r}_1, \ldots, \mathbf{r}_n)$ describes the potentials from other molecules (perturbers). This term will be ignored for the moment. It will be discussed later in connection with the line shape of the transition, i.e. the frequency shift in the transition caused by collisions with other molecules. The electromagnetic field is invariant under gauge transformations of the scalar potential ϕ and the vector potential $\mathbf{A}$. It is most convenient to work in the Coulomb or transverse gauge (see e.g. Jackson, 1975, p. 220–222)

$$\nabla\cdot\mathbf{A} = 0. \tag{3.22}$$

The scalar potential satisfies the Poisson equation

$$\nabla^2\phi = -4\pi\rho \tag{3.23}$$

where ρ is the charge density. Eq. 3.23 have the solution

$$\phi(\mathbf{r}, t) = \int \frac{\rho(\mathbf{r}', t)}{|\mathbf{r} - \mathbf{r}'|} d^3\mathbf{r}' \tag{3.24}$$

[4]The product of δ–functions in Eq. 3.17 is handled as follows

$$\delta\delta = \lim_{T\to\infty} \delta(\omega_{fi} - \omega)\frac{1}{2\pi}\int_{-T/2}^{T/2} dt\, e^{i(\omega_{fi}-\omega)t} = \delta(\omega_{fi} - \omega)\lim_{T\to\infty}\frac{T}{2\pi}$$

since the δ–function in front of the integral vanishes unless $\omega_{fi} = \omega$.

Here no sources are present, hence $\phi = 0$. As noted above, the electromagnetic fields described by A are small compared with the 'atomic' fields, thus in H^{int} the second order term in A may be ignored. Thus

$$H^{int} = -\frac{e}{c}(\frac{\mathbf{p}}{2m} \cdot \mathbf{A} + \mathbf{A} \cdot \frac{\mathbf{p}}{2m}) = -\frac{e}{c}\int d\mathbf{r}\, \mathbf{j}(\mathbf{r}) \cdot \mathbf{A}(\mathbf{r},t) \tag{3.25}$$

where

$$\mathbf{j}(\mathbf{r}) = \sum_i \left(\frac{\mathbf{p}_i}{2m}\delta(\mathbf{r}-\mathbf{r}_i) + \delta(\mathbf{r}-\mathbf{r}_i)\frac{\mathbf{p}_i}{2m}\right) \tag{3.26}$$

is the paramagnetic current and $\delta(\mathbf{r}-\mathbf{r}_i)$ the density operator for the i'th molecule. Writing $\mathbf{A}(\mathbf{r},t)$ as a plane wave

$$\mathbf{A}(\mathbf{r},t) = \frac{1}{\sqrt{\mathcal{V}}}\left(\mathbf{A}_\mathbf{k} e^{i\mathbf{k}\cdot\mathbf{r}-i\omega t} + \mathbf{A}^*_\mathbf{k} e^{-i\mathbf{k}\cdot\mathbf{r}+i\omega t}\right) \tag{3.27}$$

Eq. 3.25 becomes

$$H^{int} = -\frac{e}{c}\frac{1}{\sqrt{\mathcal{V}}}\left(\mathbf{A}_\mathbf{k} \cdot \mathbf{j}_\mathbf{k} e^{-i\omega t} + \mathbf{A}^*_\mathbf{k} \cdot \mathbf{j}^*_\mathbf{k} e^{i\omega t}\right) \tag{3.28}$$

where

$$\mathbf{j}_\mathbf{k} = \int d\mathbf{r}\, e^{-i\mathbf{k}\cdot\mathbf{r}}\mathbf{j}(\mathbf{r}) = \sum_i \left(\frac{\mathbf{p}_i}{2m}e^{-i\mathbf{k}\cdot\mathbf{r}_i} + e^{-i\mathbf{k}\cdot\mathbf{r}_i}\frac{\mathbf{p}_i}{2m}\right). \tag{3.29}$$

Insertion of Eq. 3.28 in the golden rule, Eq. 3.18, gives the absorption transition rate between the two states $|\phi_i\rangle$ and $|\phi_f\rangle$

$$\left(\frac{dW}{dt}\right)_{i\to f} = \frac{2\pi}{\hbar}\frac{e^2}{\mathcal{V}c^2}|\mathbf{A}_\mathbf{k}|^2|\langle\phi_f|\mathbf{j}_\mathbf{k}\cdot\mathbf{i}|\phi_i\rangle|^2\delta(E_f - E_i - \hbar\omega). \tag{3.30}$$

where $\mathbf{i} = \dfrac{\mathbf{A}_\mathbf{k}}{|\mathbf{A}_\mathbf{k}|}$.

3.1.5 The absorption cross section in the electric dipole approximation

To develop an expression for the absorption cross section defined by Eq. 3.1 the magnitude of the vector potential must be related to the corresponding number of photons. The electric and magnetic fields are described by

$$\mathcal{E}(\mathbf{r},t) = -\frac{1}{c}\frac{\partial \mathbf{A}(\mathbf{r},t)}{\partial t} \tag{3.31}$$

$$\mathcal{H}(\mathbf{r},t) = \nabla \times \mathbf{A}(\mathbf{r},t). \tag{3.32}$$

The energy associated with the radiation field is

$$E = \int \frac{\mathcal{E}^2(\mathbf{r},t) + \mathcal{H}^2(\mathbf{r},t)}{8\pi} d\mathbf{r} = \frac{\omega^2}{2\pi c^2}|\mathbf{A}|^2 \tag{3.33}$$

where it has been summed over the two orthogonal directions of polarization. Since each photon has a frequency ω, the energy of the radiation field may also be written as

$$E = N\hbar\omega. \tag{3.34}$$

Combining Eq. 3.33 and Eq. 3.34 gives

$$|\mathbf{A}|^2 = \frac{N2\pi c^2\hbar}{\omega}. \tag{3.35}$$

Insertion of Eq. 3.35 into Eq. 3.30 gives the following expression for the absorption rate

$$\left(\frac{dW}{dt}\right)_{i\to f} = \frac{4\pi^2e^2}{\omega}\frac{N}{\mathcal{V}}|\langle\phi_f|\mathbf{j}_\mathbf{k}\cdot\mathbf{i}|\phi_i\rangle|^2\delta(E_f - E_i - \hbar\omega). \tag{3.36}$$

The net rate of absorption is given by the average over the levels of the difference between the rate at which the electromagnetic field is reduced by processes where a photon is destroyed and the molecule is promoted from state i to f ($E_f > E_i$), and the rate at which it is increased by the inverse process in which a photon is created and the transition is from f to i

$$\left(\frac{dW}{dt}\right)_{abs} = \frac{4\pi^2e^2}{\omega}\frac{N}{\mathcal{V}}\sum_{if}|\langle\phi_f|\mathbf{j}_\mathbf{k}\cdot\mathbf{i}|\phi_i\rangle|^2\delta(E_f - E_i - \hbar\omega)\times(P_i - P_f). \tag{3.37}$$

Here P_i and P_f are the occupation probabilities of the two levels. In thermal equilibrium these probabilities are given by the Boltzmann distribution

$$P_r = \frac{e^{-E_r/kT}}{\sum_s e^{-E_s/kT}}. \tag{3.38}$$

For the absorption cross section insertion of Eq. 3.37 in Eq. 3.1 gives

$$\sigma_{abs}(\omega) = \frac{4\pi^2e^2}{\omega c}\sum_{if}|\langle\phi_f|\mathbf{j}_\mathbf{k}\cdot\mathbf{i}|\phi_i\rangle|^2\delta(E_f - E_i - \hbar\omega)\times(P_i - P_f). \tag{3.39}$$

Next, use is made of the fact that the wavelengths of radiation from the infrared to the ultraviolet part of the spectrum are several orders of magnitude greater than the spatial extent of the electron orbits about the nucleus. Hence, to evaluate the matrix element

$$\langle\phi_f|\mathbf{j}_\mathbf{k}|\phi_i\rangle = \int d\mathbf{r}\, e^{-i\mathbf{k}\cdot\mathbf{r}}\langle\phi_f|\mathbf{j}(\mathbf{r})|\phi_i\rangle \tag{3.40}$$

a good approximation is to expand $e^{-i\mathbf{k}\cdot\mathbf{r}}$ around the position $\mathbf{r}_0$ of the nucleus

$$\begin{aligned}\langle\phi_f|\mathbf{j}_\mathbf{k}|\phi_i\rangle &= \int d\mathbf{r}\,[1-\mathbf{k}\cdot\mathbf{r}+\cdots]\langle\phi_f|\mathbf{j}(\mathbf{r})|\phi_i\rangle \\ &= \langle\phi_f|\mathbf{j}_0|\phi_i\rangle - i\langle\phi_f|\int d\mathbf{r}\,\mathbf{k}\cdot\mathbf{r}\,\mathbf{j}(\mathbf{r})|\phi_i\rangle+\cdots \end{aligned} \tag{3.41}$$

where the choice $\mathbf{r}_0 = \mathbf{0}$ has been made. From Eq. 3.29

$$\mathbf{j}_0 = \sum_i \frac{\mathbf{p}_i}{m} = \frac{\mathbf{P}}{m} = \frac{1}{i\hbar}[\mathbf{R}, H^0]. \tag{3.42}$$

Here $\mathbf{R} = \sum_i \mathbf{r}_i$ is the dipole moment operator, and the commutation relation $[\mathbf{r}_i, \mathbf{p}_i] = i\hbar$ has been used. In view of Eq. 3.42 the first term on the right-hand side of Eq. 3.41 may be written

$$\langle\phi_f|\mathbf{j}_0|\phi_i\rangle = \frac{1}{i\hbar}\langle\phi_f|\mathbf{R}H^0 - H^0\mathbf{R}|\phi_i\rangle = \frac{E_f - E_i}{i\hbar}\langle\phi_f|\mathbf{R}|\phi_i\rangle = -i\omega\mathbf{d}_{fi} \tag{3.43}$$

where $\omega = (E_f - E_i)/\hbar$ is the energy of the absorbed radiation and the off diagonal matrix element of the dipole operator $\mathbf{d}_{fi} = \langle\phi_f|\mathbf{R}|\phi_i\rangle$. Thus, to the lowest order in $\mathbf{k}\cdot\mathbf{r}$, the matrix element Eq. 3.40 is $-i\omega\mathbf{d}_{fi}$. Upon insertion of this expression in Eq. 3.39 the total absorption cross section in the electric dipole approximation is obtained,

$$\sigma_{abs}(\omega) = \frac{4\pi^2 e^2\omega}{c}\sum_{if} d_{fi}^2\,\delta(E_f - E_i - \hbar\omega)\times(P_i - P_f). \tag{3.44}$$

3.1.6 The correlation function and the fluctuation–dissipation theorem

As it stands Eq. 3.44 gives the absorption cross section in terms of the eigenstates of the coupled molecule–perturber system. Usually these eigenstates are not known and Eq. 3.44 is thus not particularly useful. However, as long as the perturbers have an appreciable effect, the absorption cross section may be calculated when written in terms of correlation functions (Van Vleck and Huber 1977). The correlation function associated with a time dependent quantity is the average $\langle f(t)f(t')\rangle$ taken over an ensemble of molecules so that all differences in phase and state are smoothed out. Following Van Vleck and Huber (1977) one may write

$$\begin{aligned}&\sum_{if} d_{fi}^2\,\delta(E_f - E_i - \hbar\omega)\times(P_i - P_f) \\ &\qquad = \sum_{if}|\langle\phi_f|\mathbf{r}|\phi_i\rangle|^2\delta(E_f - E_i - \hbar\omega)\times(P_i - P_f) \\ &= \sum_{if}\left(P_i\langle\phi_i|\mathbf{r}|\phi_f\rangle\langle\phi_f|\mathbf{r}|\phi_i\rangle - P_f\langle\phi_f|\mathbf{r}|\phi_i\rangle\langle\phi_i|\mathbf{r}|\phi_f\rangle\right)\delta(E_f - E_i - \hbar\omega)\end{aligned} \tag{3.45}$$

since $\langle\phi_f|\mathbf{r}|\phi_i\rangle = \langle\phi_i|\mathbf{r}|\phi_f\rangle^*$. Using the integral representation of the δ–function once again the right–hand side of Eq. 3.45 is rewritten as

$$\begin{aligned}
&\frac{1}{2\pi\hbar}\int_{-\infty}^{\infty} dt\, e^{-i\omega t}\sum_{i,f}\Big\{P_i\langle\phi_i|\mathbf{r}|\phi_f\rangle\langle\phi_f|e^{iE_it/\hbar}\mathbf{r}\,e^{-iE_ft/\hbar}|\phi_i\rangle \\
&\qquad\qquad -P_f\langle\phi_f|e^{iE_ft/\hbar}\mathbf{r}\,e^{-iE_it/\hbar}|\phi_i\rangle\langle\phi_i|\mathbf{r}|\phi_f\rangle\Big\} \\
&= \frac{1}{2\pi\hbar}\int_{-\infty}^{\infty} dt\, e^{-i\omega t}\sum_{i,f}\{P_i\langle\phi_i|\mathbf{r}|\phi_f\rangle\langle\phi_f|\mathbf{r}(t)|\phi_i\rangle - P_f\langle\phi_f|\mathbf{r}(t)|\phi_i\rangle\langle\phi_i|\mathbf{r}|\phi_f\rangle\} \\
&= \frac{1}{2\pi\hbar}\int_{-\infty}^{\infty} dt\, e^{-i\omega t}\left[\langle\mathbf{r}(0)\mathbf{r}(t)\rangle - \langle\mathbf{r}(t)\mathbf{r}(0)\rangle\right]. \qquad (3.46)
\end{aligned}$$

Here the symbolic identity $\sum_k |\phi_k\rangle\langle\phi_k| = 1$ has been used, with $\langle O\rangle$ refering to the average

$$\langle O\rangle = \sum_k P_k\langle\phi_k|O|\phi_k\rangle. \qquad (3.47)$$

$\mathbf{r}(t)$ is the dipole operator in the Heisenberg notation

$$\mathbf{r}(t) = e^{iHt/\hbar}\mathbf{r}\,e^{-iHt/\hbar}. \qquad (3.48)$$

In general, the two correlation functions $\langle\mathbf{r}(0)\mathbf{r}(t)\rangle$ and $\langle\mathbf{r}(t)\mathbf{r}(0)\rangle$ can not be equated. However, there is a relation between the Fourier transforms of them, referred to as the fluctuation–dissipation theorem (Huber and Van Vleck 1966)

$$\int_{-\infty}^{\infty} dt\, e^{-i\omega t}\langle\mathbf{r}(0)\mathbf{r}(t)\rangle = e^{\hbar\omega/kT}\int_{-\infty}^{\infty} dt\, e^{-i\omega t}\langle\mathbf{r}(t)\mathbf{r}(0)\rangle. \qquad (3.49)$$

Using Eq. 3.49 twice gives

$$\begin{aligned}
&\frac{1}{2\pi}\int_{-\infty}^{\infty} dt\, e^{-i\omega t}\left[\langle\mathbf{r}(0)\mathbf{r}(t)\rangle - \langle\mathbf{r}(t)\mathbf{r}(0)\rangle\right] = \frac{1}{2\pi}\left(1-e^{-\hbar\omega/kT}\right)\int_{-\infty}^{\infty} dt\, e^{-i\omega t}\langle\mathbf{r}(0)\mathbf{r}(t)\rangle \\
&\quad = \frac{1-e^{-\hbar\omega/kT}}{1+e^{-\hbar\omega/kT}}\frac{1}{2\pi}\int_{-\infty}^{\infty} dt\, e^{-i\omega t}\left[\langle\mathbf{r}(0)\mathbf{r}(t)\rangle + e^{-\hbar\omega/kT}\langle\mathbf{r}(0)\mathbf{r}(t)\rangle\right] \\
&= \tanh\left(\frac{\hbar\omega}{2kT}\right)\frac{1}{2\pi}\int_{-\infty}^{\infty} dt\, e^{-i\omega t}\langle\mathbf{r}(0)\mathbf{r}(t)+\mathbf{r}(t)\mathbf{r}(0)\rangle = \tanh\left(\frac{\hbar\omega}{2kT}\right)\mathcal{R}(\omega) \qquad (3.50)
\end{aligned}$$

where the symmetrized correlation function is

$$\mathcal{R}(\omega) = \frac{1}{2\pi}\int_{-\infty}^{\infty} dt\, e^{-i\omega t}\langle\mathbf{r}(0)\mathbf{r}(t)+\mathbf{r}(t)\mathbf{r}(0)\rangle. \qquad (3.51)$$

In terms of $\mathcal{R}(\omega)$ the absorption cross section Eq. 3.44 is

$$\sigma_{abs}(\omega) = \frac{8\pi^3e^2\omega}{h\,c}\tanh\left(\frac{\hbar\omega}{2kT}\right)\mathcal{R}(\omega). \qquad (3.52)$$

3.1.7 Impact approximation and the Lorentz line shape

Up to now it has barely been mentioned that other molecules (perturbers) surrounding the molecule in which the transition takes place, have a significant effect on the signature of the transition. Ignoring the perturbers gives a sharp absorption line. However, in a transition some of the energy involved may go to increase or decrease the total kinetic energy of the perturbers; hence the frequency of the absorbed light is distributed around the unperturbed value $(E_i - E_f)/\hbar$. In this work the approach of Baranger (1958a) is adopted to calculate the effect of the perturbers. His method is based on the impact approximation discussed in detail by Anderson (1949). Several simplifying assumptions are made, i.e. isolated lines and no degeneracy. For purposes of this work, however, the main results remain the same. For a more general theory, the reader is referred to Baranger (1958b,c) and for an overview to Cooper (1969).

Instead of calculating the correlation function directly, it is easier to consider its Fourier transform

$$\Phi(t) = \int_{-\infty}^{\infty} d\omega\, \mathcal{R}(\omega)\, e^{i\omega t}. \tag{3.53}$$

The correlation function $\mathcal{R}(\omega)$ is obtained from the inverse formula

$$\mathcal{R}(\omega) = \frac{1}{2\pi} \int_{-\infty}^{\infty} dt\, \Phi(t)\, e^{-i\omega t}. \tag{3.54}$$

Since $\mathcal{R}(\omega)$ must be real $\Phi(-t) = \Phi^*(t)$, hence $\Phi(t)$ is computed for positive t only and this condition is then used to determine it for negative values of t. It is assumed that the wave function $\phi(\mathbf{r}_a, \mathbf{r}_1, \ldots, \mathbf{r}_n)$ is the product of an internal wave function of the atom and a function of the center of mass coordinates of the perturbers

$$\phi(\mathbf{r}_a, \mathbf{r}_1, \ldots, \mathbf{r}_n) = \phi_a(\mathbf{r}_a)\phi_p(\mathbf{r}_1, \ldots, \mathbf{r}_n). \tag{3.55}$$

The perturbers are assumed not to interact with each other, but only with the molecule

$$\phi_p(\mathbf{r}_1, \ldots, \mathbf{r}_n) = \phi_1(\mathbf{r}_1) \cdots \phi_n(\mathbf{r}_n). \tag{3.56}$$

Furthermore, 'scalar addition' is assumed for the interaction potential V[5]

$$V(\mathbf{r}_1, \ldots, \mathbf{r}_n) = V(\mathbf{r}_1) + \cdots + V(\mathbf{r}_n). \tag{3.57}$$

If the back reaction of the atom on the perturber can be neglected, the probability P of finding the molecule in a state $|\phi(\mathbf{r}_a)\rangle$ and the surrounding molecules in $|\phi_1(\mathbf{r}_1) \cdots \phi_n(\mathbf{r}_n)\rangle$ is given by the

[5] All the assumptions made here may be removed according to Baranger (1958b,c).

product $P = P_m p$, where P_m refers to molecular states only, and p refers to perturbers only and is diagonal in the perturber coordinates.

Instead of summing over ω in Eq. 3.53, a change of variables is made, all final states k'_j are summed over and all initial states k_j averaged over. In view of Eq. 3.46 and the above assumptions

$$\begin{aligned}
\Phi(t) \sim\ & P_i \sum_{k_1 \ldots k_n} \sum_{k'_1 \ldots k'_n} d^2_{fi} p_{k_1} \cdots p_{k_n} |\langle \phi_{f k'_1} | \phi_{i k_1} \rangle|^2 \cdots |\langle \phi_{f k'_n} | \phi_{i k_n} \rangle|^2 \\
& \times e^{i[(E_i - E_f) + (\epsilon_1 - \epsilon'_1) + \cdots + (\epsilon_n - \epsilon'_n)]t/\hbar} \\
+\ & P_f \sum_{k_1 \ldots k_n} \sum_{k'_1 \ldots k'_n} d^2_{fi} p_{k_1} \cdots p_{k_n} |\langle \phi_{f k'_1} | \phi_{i k_1} \rangle|^2 \cdots |\langle \phi_{f k'_n} | \phi_{i k_n} \rangle|^2 \\
& \times e^{i[(E_f - E_i) + (\epsilon'_1 - \epsilon_1) + \cdots + (\epsilon'_n - \epsilon_n)]t/\hbar} \\
=\ & P_i d^2_{fi} e^{-i\omega_{fi} t} [\varphi_+(t)]^n + P_f d^2_{fi} e^{i\omega_{fi} t} [\varphi_-(t)]^n \qquad (3.58)
\end{aligned}$$

where

$$\varphi_\pm(t) = \sum_{kk'} p_k |\langle \phi_{f k'} | \phi_{i k} \rangle|^2 e^{\pm i(\epsilon - \epsilon')t/\hbar}. \qquad (3.59)$$

Because of our assumption of scalar addition $\varphi(t)$ refers to a single perturber, i.e. the perturbers affect the molecule independently, and the total frequency shift is the sum of individual shifts due to each perturber.

Most of the time the perturber is far away from the molecule and does not influence it, thus the line shape must consist mainly of a δ–function at the origin. A small correction of the order $\mathcal{V}^{-1}$, where $\mathcal{V}$ is the very large volume surrounding the molecule, must be included when the perturber happens to be close to the molecule. Thus $\varphi(t)$ must have the form

$$\varphi(t) = 1 - \frac{g(t)}{\mathcal{V}}. \qquad (3.60)$$

Defining n_0 to be the number of perturbers per unit volume ($n_0 = n/\mathcal{V}$) at some reference temperature and pressure, and raising Eq. 3.60 to the n'th power gives

$$\Phi(t) = e^{-n_0 g(t)}. \qquad (3.61)$$

To put $\varphi(t)$ in the form of Eq. 3.60 the Hamiltonian H^p of the perturber with the molecule in its initial and final state is introduced

$$H^p_i = K + V_i \qquad (3.62)$$

$$H^p_f = K + V_f. \qquad (3.63)$$

Here K is the kinetic energy of the perturber. Using Eq. 3.62–3.63 in Eq. 3.59 the final states are eliminated as follows

$$\varphi_{\pm}(t) = \sum_{kk'} p_k \langle \phi_{ik} | \phi_{fk'} \rangle e^{i\epsilon' t/\hbar} \langle \phi_{fk'} | \phi_{ik} \rangle e^{-i\epsilon t/\hbar} = \sum_{k} p_k \langle \phi_{ik} | e^{iH_f^p t/\hbar} e^{-iH_i^p t/\hbar} | \phi_{ik} \rangle. \tag{3.64}$$

Up to this point, the wave functions have been normalized to unity. For convenience, they are now normalized to the volume $\mathcal{V}$. Eq. 3.64 thus becomes

$$\varphi(t) = \sum_{k} p_k \frac{1}{\mathcal{V}} \langle \phi_{ik} | e^{iH_f^p t/\hbar} e^{-iH_i^p t/\hbar} | \phi_{ik} \rangle \tag{3.65}$$

Next $\varphi(t)$ is transformed by using the integral equation due to Feynman (1949)

$$e^{iH_f^p t/\hbar} e^{-iH_i^p t/\hbar} = 1 - i \int_0^t dt'\, e^{iH_f^p t'/\hbar} \Delta V\, e^{-iH_i^p t'/\hbar} \tag{3.66}$$

where

$$\Delta V = V_i - V_f = H_i - H_f. \tag{3.67}$$

Thus, Eq. 3.65 may be written as

$$\varphi(t) = 1 - \frac{i}{\mathcal{V}} \int_0^t dt\, e^{-i\epsilon t/\hbar} \sum_{k} p_k \langle \phi_{ik} | e^{iH_f^p t/\hbar} \Delta V | \phi_{ik} \rangle \tag{3.68}$$

and $g(t)$ identified as

$$g(t) = i \int_0^t dt\, e^{-i\epsilon t/\hbar} \sum_{k} p_k \langle \phi_{ik} | e^{iH_f^p t/\hbar} \Delta V | \phi_{ik} \rangle. \tag{3.69}$$

In Eq. 3.69 $\langle \phi_{ik} | e^{iH_f^p t/\hbar}$ is the result of propagating the wave $\langle \phi_{ik}|$ for time t with the Hamiltonian H_f^p. During this propagation the 'scattered' part of the wave function gradually changes and starts to look more like the 'scattered' part of $\langle \phi_{fk}|$, at least near the origin. At large distances, the 'scattered' wave is still that of $\langle \phi_{ik}|$, as long as t is finite. But since this has to be multiplied by $\Delta V|\phi_{ik}\rangle$, which vanishes at large distances, the matrix element $\langle \phi_{ik} | e^{iH_f^p t/\hbar} \Delta V | \phi_{ik} \rangle$ becomes practically equal to $\langle \phi_{fk} | e^{i\epsilon t/\hbar} \Delta V | \phi_{ik} \rangle$ for sufficiently large t [6]. Thus $g(t)$ becomes

$$g(t) \simeq i\, t \sum_{k} p_k \langle \phi_{fk} | \Delta V | \phi_{ik} \rangle \tag{3.70}$$

[6] This is the so-called impact approximation. It is equivalent to saying that the average collision is weak, or alternatively one may say that the time interval between strong collisions is much longer than the duration of such collisions.

Using this expression for $g(t)$ in Eq. 3.61 gives the symmetrized correlation function

$$\begin{aligned}\mathcal{R}(\omega) &= \frac{1}{2\pi}\int_{-\infty}^{\infty} dt\, e^{-i\omega t}\Phi(t) \\ &= \frac{1}{\pi}\sum_{if}\left\{\frac{\alpha_{fi}}{(\omega+\omega_{fi}+\Delta\omega_0)^2+\alpha_{fi}^2}+\frac{\alpha_{fi}}{(\omega-\omega_{fi}-\Delta\omega_0)^2+\alpha_{fi}^2}\right\} d_{fi}^2\times(P_i+P_f) \quad (3.71)\end{aligned}$$

where the half width at half maximum (HWHM) is

$$\alpha_{fi} = \frac{1}{2}n_0\sum_k p_k \Re\langle\phi_{fk}|\Delta V|\phi_{ik}\rangle \quad (3.72)$$

and the line shift is

$$\Delta\omega_0 = n_0\sum_k p_k \Im\langle\phi_{fk}|\Delta V|\phi_{ik}\rangle. \quad (3.73)$$

$\Re$ and $\Im$ refer to the real and imaginary parts respectively. The absorption cross section may thus be written as

$$\sigma_{abs}(\omega) = \frac{8\pi^3 e^2\omega}{3h\,c}\tanh\left(\frac{\hbar\omega}{2kT}\right)\sum_{if} S_{fi}(P_i+P_f)\{f_+ + f_-\} \quad (3.74)$$

where

$$f_\pm = \frac{1}{\pi}\frac{\alpha_{fi}}{(\omega\pm\omega_{fi}\pm\Delta\omega_0)^2+\alpha_{fi}^2} \quad (3.75)$$

and the line strength is defined by (Cooper 1967)

$$S_{fi} = \sum_{if,\mu=x,y,z}|\langle\phi_f|\mathbf{R}_\mu|\phi_i\rangle|^2 = 3\sum_{if}|\langle\phi_f|\mathbf{R}_z|\phi_i\rangle|^2. \quad (3.76)$$

The function $f_\pm$ (Eq. 3.75) is known as the Lorentz profile and is the line shape due to collisions by surrounding molecules, i.e. pressure broadening.

3.1.8 Doppler broadening and the Voigt function

The molecules in the lower atmosphere may be characterized by a kinetic temperature T, i.e. they have a Maxwellian velocity distribution. Thus in the observer's frame, each molecule has a velocity component along the line of sight and the intrinsic profile of that molecule will be frequency–shifted a corresponding amount. It is assumed that the processes producing the intrinsic profile of each molecule as given above, are uncorrelated with its velocity. Hence the profiles due to collision broadening and Doppler broadening may be superimposed as follows. With a Maxwellian velocity

distribution, the probability of finding a molecule with a line of sight velocity ξ between ξ and $d\xi$ is

$$P_D(\xi)d\xi = \frac{1}{\xi_0\sqrt{\pi}}e^{-\xi^2/\xi_0^2}d\xi \tag{3.77}$$

where $\xi_0 = \sqrt{\frac{2kT}{m}}$. Observing at frequency ω, an atom with velocity component ξ is absorbing at frequency $\omega[1-(\xi/c)]$ in its own frame and the absorption cross section for that molecule is $\sigma(\omega - \xi\omega/c)$. The total absorption cross section at frequency ω is thus given by the convolution integral

$$\sigma(\omega) = \int_{-\infty}^{\infty} \sigma(\omega - \xi\omega/c)P_D(\xi)d\xi. \tag{3.78}$$

Insertion of Eqs. 3.77–3.78 in Eq. 3.74 yields ($\Delta\omega_0 = 0$ for convenience)

$$\sigma(\omega) = \frac{8\pi^3e^2\omega}{3hc}\tanh\left(\frac{\hbar\omega}{2kT}\right)\sum_{if} S_{fi}(P_i + P_f)f(a,v) \tag{3.79}$$

where the normalised line shape is

$$f(a,v) = \frac{1}{\alpha_D}\frac{\sqrt{\ln 2}}{\pi}H(a,v) \tag{3.80}$$

and the Voigt function is

$$H(a,v) = \frac{a}{\pi}\int_{-\infty}^{\infty}\frac{e^{-t^2}}{(v-t)^2 + a^2}dt. \tag{3.81}$$

Here

$$\alpha_D = \frac{\omega_{fi}}{c}\sqrt{\frac{2\ln 2\, kT}{m}} \tag{3.82}$$

$$a = \sqrt{\ln 2}\,\frac{\alpha_L}{\alpha_D} \tag{3.83}$$

$$v = \sqrt{\ln 2}\,\frac{\omega + \omega_f i}{\alpha_D} \tag{3.84}$$

and $\alpha_L = \alpha_{fi}$ is given by Eq. 3.72. In deriving the Voigt function the approximation $\xi\omega/c = \xi\omega_{fi}/c$ has been made. For $a = 0$, i.e. pure Doppler broadening, $\alpha_L = 0$, and the line shape is a Doppler profile

$$f(0,v) = \frac{1}{\alpha_D}\frac{\sqrt{\ln 2}}{\pi}e^{-v^2}. \tag{3.85}$$

For $\alpha_D = 0$, e.g. pure Lorentz broadening, $a \to \infty, v \to \infty$,

$$f(a \to \infty, v \to \infty) = \frac{1}{\pi}\frac{\alpha_L}{(\omega - \omega_0)^2 + \alpha_L^2} \tag{3.86}$$

the line shape becomes a Lorentz profile, as expected.

Eq. 3.79 yields an expression for the absorption cross section that may be used for calculations pertinent to planetary atmospheres. It is this expression that will be used to calculate the absorption properties needed to characterize the radiation field in the earth's atmosphere.

3.1.9 The HITRAN database and line–by–line calculations

All the quantities going into Eq. 3.79 for the absorption cross section are not given above. It is still needed to specify the Lorentz half width at half maximum α_L, Eq. 3.72, and the line strength S_{fi}, Eq. 3.76. There are many industrial, military and scientific applications and investigations that require detailed knowledge of the transmission properties of the gases in the Earth's atmosphere. Extensive efforts have been made to measure and collect data which may be used as input to computer models such as the one described in this work, and in connection with remote sensing applications. The high–resolution transmission molecular absorption database (HITRAN, Rothman et al. (1987)), is such a compilation of absorption line parameters for the seven principal atmospheric absorbers (H_2O, CO_2, O_3, N_2O, CO, CH_4, O_2) and twenty–one additional molecular species. The line strength used in the HITRAN database is defined as

$$S_{if}^H(T_0) = \frac{8\pi^3}{3hc}\nu_{if}[1 - e^{-hc\nu_{if}/kT_0}]g_i I_a \frac{e^{-hcE_i/kT_0}}{Q(T_0)} R_{if} \cdot 10^{-36} \tag{3.87}$$

where ν_{if} is the resonant frequency of the line in units of cm^{-1}, E_i is the energy of the lower state of the transition in units of cm^{-1}, g_i is the nuclear spin partition sum, I_a is the natural isotopic abundance, $Q(T_0)$ the total internal partition sum and R_{if} is the transition probability in *Debye* units (1 *Debye* $= 10^{-18} e.s.u.\ cm$). All quantities are specified at the reference temperature $T_0 = 296K$, and must be adjusted according to the temperature T of the absorbing gas

$$S_{if}^H(T) = \frac{Q_r(T_0)Q_v(T_0)}{Q_r(T)Q_v(T)} \frac{e^{-hcE_i/kT}}{e^{-hcE_i/kT_0}} \frac{1 - e^{-hc\nu_{if}/kT}}{1 - e^{-hc\nu_{if}/kT_0}} S_{if}^H(T_0). \tag{3.88}$$

Here it is assumed that the rotational and vibrational parts of the partition function, $Q_r(T)$ and $Q_v(T)$, may be treated independently. The temperature dependence of $Q_r(T)$ is given by $(T/T_0)^j$, where $j = 1$ for linear molecules and 1.5 for non–linear molecules.

The Lorentz half width as given in the database is comprised of two components, the air–broadened half width due to air–absorber gas collisions, and the self–broadened half width due to collisions between absorber gas molecules. In terms of the reference temperature $T_0 = 296K$, the

half width at T is given by

$$\alpha_L(T) = \alpha_L(T_0)\left(\frac{T_0}{T}\right)^n \tag{3.89}$$

where the exponent n for the temperature dependence is given in the database.

Combining this information with Eq. 3.79, one may, in principle, calculate the absorption properties of an inhomogeneous atmosphere. However, the large number of absorption lines, (the 1986 edition of the HITRAN database contained 348043 entries between 0 and $17,900cm^{-1}$), makes the computation of absorption cross sections and the subsequent solution of the radiative transfer equation an impractical task. This is true, not only because of the large number of lines involved, but also because a very fine wavelength grid is required to resolve the shape of each line. For limited wavelength regions so–called line–by–line calculations are feasible, mostly in connection with remote sensing applications. Several line–by–line codes are in the public domain, e.g. FASCODE (Clough et al. 1981) and GENLN2 (Edwards 1988, 1992). Having been developed for remote sensing applications, their radiation transport algorithms are highly simplified, whereas the line shapes are often treated with a higher degree of sophistication than outlined above. The time consuming part of line–by–line codes is the calculation of the Voigt function, Eq. 3.81. Several algorithms exist for numerically evaluating this integral, see Edwards (1992) and references therein.

In this work GENLN2 together with the HITRAN database (1986 edition) was used to produce absorption cross sections using Eq. 3.79. These cross sections were used as input to the radiation transport algorithm described in Chapter 2 to produce benchmark results, and as starting values for developing an approximate scheme requiring fewer solutions of the radiative transfer equation. This approximation scheme is based on the correlated–k distribution method, described below.

3.1.10 The correlated–k distribution method[7]

The correlated–k distribution method (Lacis and Oinas 1991) is a technique for performing radiation calculations in inhomogeneous atmospheres by employing spectrally averaged data. For more than 50 years the accepted approach has been the use of spectral band models usually with the Curtis–Godson approximation for inhomogeneous atmospheres. A recent review of the different methods has been given Goody and Yung (1990), and will not be repeated here. An excellent brief description of the various methods is given by Andrews, Holton and Leovy (1987). While such

[7] In atmospheric science the letter k is often used for the absorption coefficient. The notation used here is different, but no reason is seen to add confusion by giving the correlated–k distribution method a name consistent with the notation used in this work.

approximate methods are computationally efficient, they are known to be inaccurate for gases for which the hydrostatic approximation is not applicable, e.g. ozone, and they can not be applied to scattering problems, e.g. atmospheres with clouds and/or aerosols. The correlated–k distribution overcomes these deficiencies by making fewer assumptions while still being computationally very fast. It may be described as a wide band method, that is, provided that the scattering properties and the radiation sources (thermal and solar) are constant within a spectral region $\Delta\omega$, it can be applied to this spectral region regardless of the complexity of the line spectrum.

Assuming that each layer of an inhomogenous atmosphere is homogeneous, (cf. the assumptions made in chapter 2 when solving the radiative transfer equation) the average value of the absorption cross section $\sigma_p(\omega)$ in the interval $\Delta\omega$ and layer p is

$$\begin{aligned}\overline{\sigma_p} &= \int_0^1 \sigma_p(\omega) d\left(\frac{\omega}{\Delta\omega}\right) = \int_0^\infty f_p(\sigma)\,\sigma\,d\sigma \\ &= \int_0^1 \sigma\, dg_p(\sigma) = \int_0^1 \sigma_p(g)\, dg. \end{aligned} \tag{3.90}$$

The first integral in Eq. 3.90 defines the mean of σ_p over the spectral interval $\Delta\omega$. The second integral is the mean written in terms of the distribution function $f_p(\sigma)$ in the p'th layer and spectral interval $\Delta\omega$. Defining a cumulative distribution

$$g_p(\sigma) = \int_0^\sigma f_p(\sigma')d\sigma' \tag{3.91}$$

gives the third integral form for the mean of $\sigma_p(\omega)$. By definition $g_p(\sigma)$ is a monotonic function of σ and the relationship between g and σ may thus be inverted. Hence, the fourth integral of the mean in Eq. 3.90 may be written, where $\sigma_p(g)$ represents the value of σ that corresponds to the independent variable g in the p'th layer. For a single layer the four integral forms are identical, however for an inhomogeneous atmosphere there are different σ and $g_p(\sigma)$ relationships for each layer and no single way for all layers to invert Eq. 3.91.

The importance of Eq. 3.90 is seen by comparing the first and fourth integral form of the mean of the absorption cross section. Whereas $\sigma(\omega)$ varies rapidly, erratically and by several orders of magnitude, $\sigma(g)$ is a smooth monotonic function, see Fig. 3.1. Thus, using the fourth integral form greatly decreases the number of points needed to calculate $\overline{\sigma_p}$ to a sufficient degree of accuracy.

The cumulative distribution $g_p(\sigma)$ may be calculated in different ways. Lacis and Oinas (1991) fitted Malkmus band model parameters to correlated–k distributions. In this work the approach of Goody et al. (1990) is adopted. Hence, $\sigma_p(g)$ is formed by sorting $\sigma(\omega)$ into bins such that it increases monotonically. Each bin has a width $\delta g_p = \delta\omega_p/\Delta\omega$, thus g_p spans the interval [0,1].

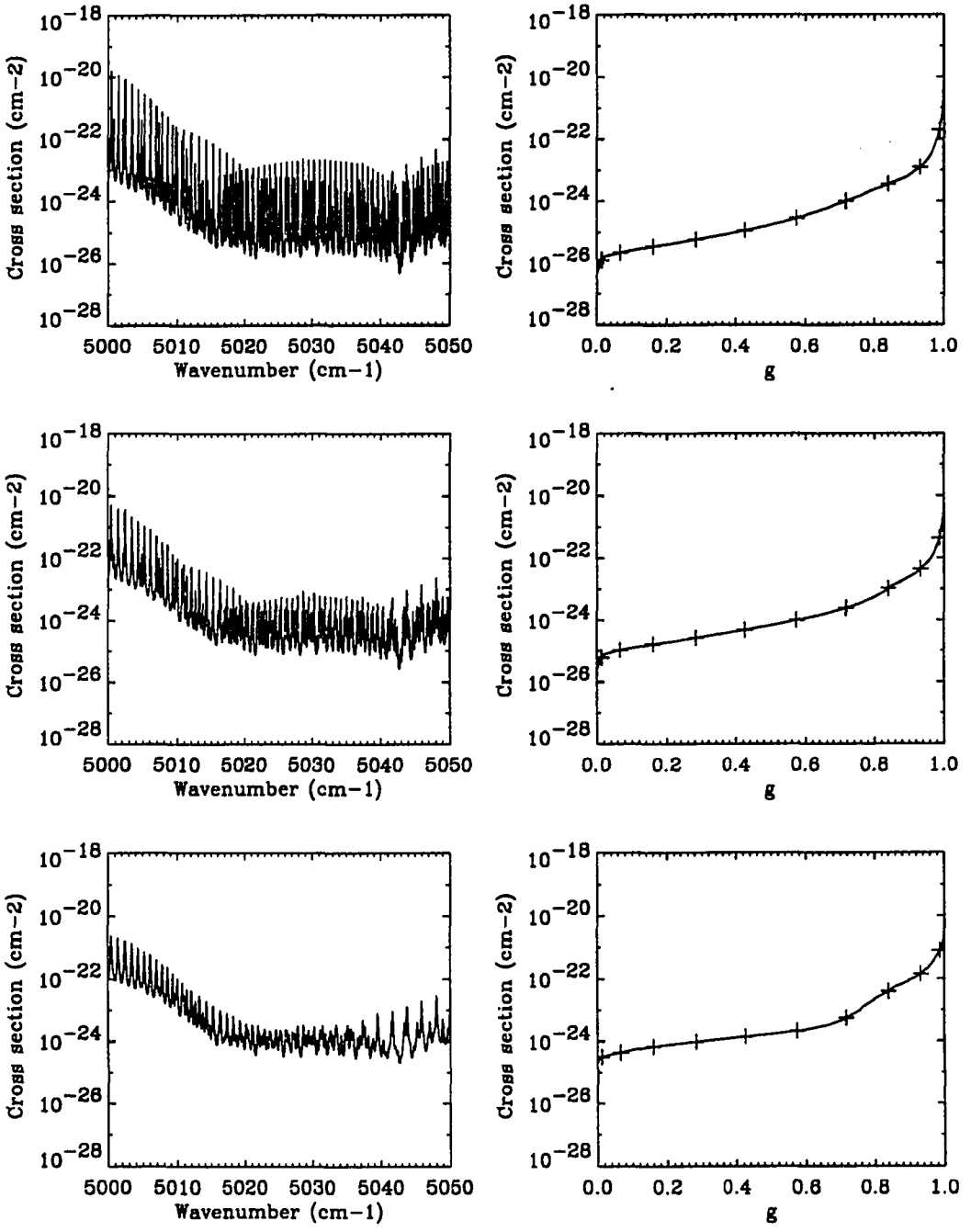

Figure 3.1: In the bottom row is shown the CO_2 cross section as calculated by GENLN2 for the Mc-Clatchey midlatitude-arctic summer atmosphere at ground level, and the cross section sorted in ascending order. The middle and top row give the cross section at 10.0 km and 20.0 km respectively and the corresponding $\sigma_p(g)$. The plus signs indicate the gaussian quadrature points (10 in this example) used to perform the integral over wavelength; see chapter 6 for details.

Fig. 3.1 shows the CO_2 cross section in the interval 5000–5050 cm^{-1} for different altitudes and the corresponding $\sigma_p(g)$. Each layer has been sorted individually to make sure $\sigma_p(g)$ is monotonically increasing. The changes in the line–profile due to pressure and temperature effects are readily seen.

The term 'correlated' refers to the assumption that the mapping that makes $\sigma_A(g)$ a monotonic function will also do this for the other layers $p \neq A$. For special cases like the weak–line limit, with small absorber amounts, and the strong–line limit, or for pressure broadened lines that are strongly absorbing, the correlated–k method may be proven to yield the correct result (Goody et al. 1990). In the general case numerical comparisons must be made with exact calculations to test the accuracy of the correlated–k distribution method. It is demonstrated in Fig. 3.2 that the correlation assumption is not generally correct. Here the mapping used for layer A to make $\sigma_A(g)$ a monotonic function is also used to calculate $\sigma_p(g)$ for the other layers, $p \neq A$. The error using the correlated–k distribution is mainly due to the non–monotonic behaviour of $\sigma_p(g)$ for the layers where $p \neq A$. However the error made is generally rather small for quantities integrated over large spectral intervals (Lacis and Oinas 1991, Goody et al. 1990). The accuracy of the correlated–k distribution as compared to accurate line-by-line calculations will be discussed in chapter 6 when discussing warming and cooling rates.

3.2 The absorption and scattering of light by small particles

The particles found in the earth's atmosphere show an extreme variability in both size and shape. To find the absorption and scattering properties of these particles it will be assumed that they are spherical, since for spheres of arbitrary size and refractive index, exact expressions may be found for the absorption and scattering cross sections[8]. Obviously the assumption that all particles in the air are spheres does not hold e.g. for ice crystals. However, 'Mie theory does provide a first order description of optical effects in nonspherical particles, and it correctly describes many small–particle effects that are not intuitively obvious' (Bohren and Huffmann, 1983). For a discussion of the applicability of the Mie theory see Bohren and Huffmann (1983).

[8]The solution to the problem of absorption and scattering of electromagnetic radiation by small spheres of arbitrary radius and refractive index is refered to as Mie theory. Gustav Mie solved this problem in 1908 but was not the first one to solve it (Bohren and Huffmann, 1983). The exposition of the Mie theory is given for completeness and is rather sketchy. For a rigourous treatment the reader is referred to the amusing presentation given by Bohren and Huffmann (1983).

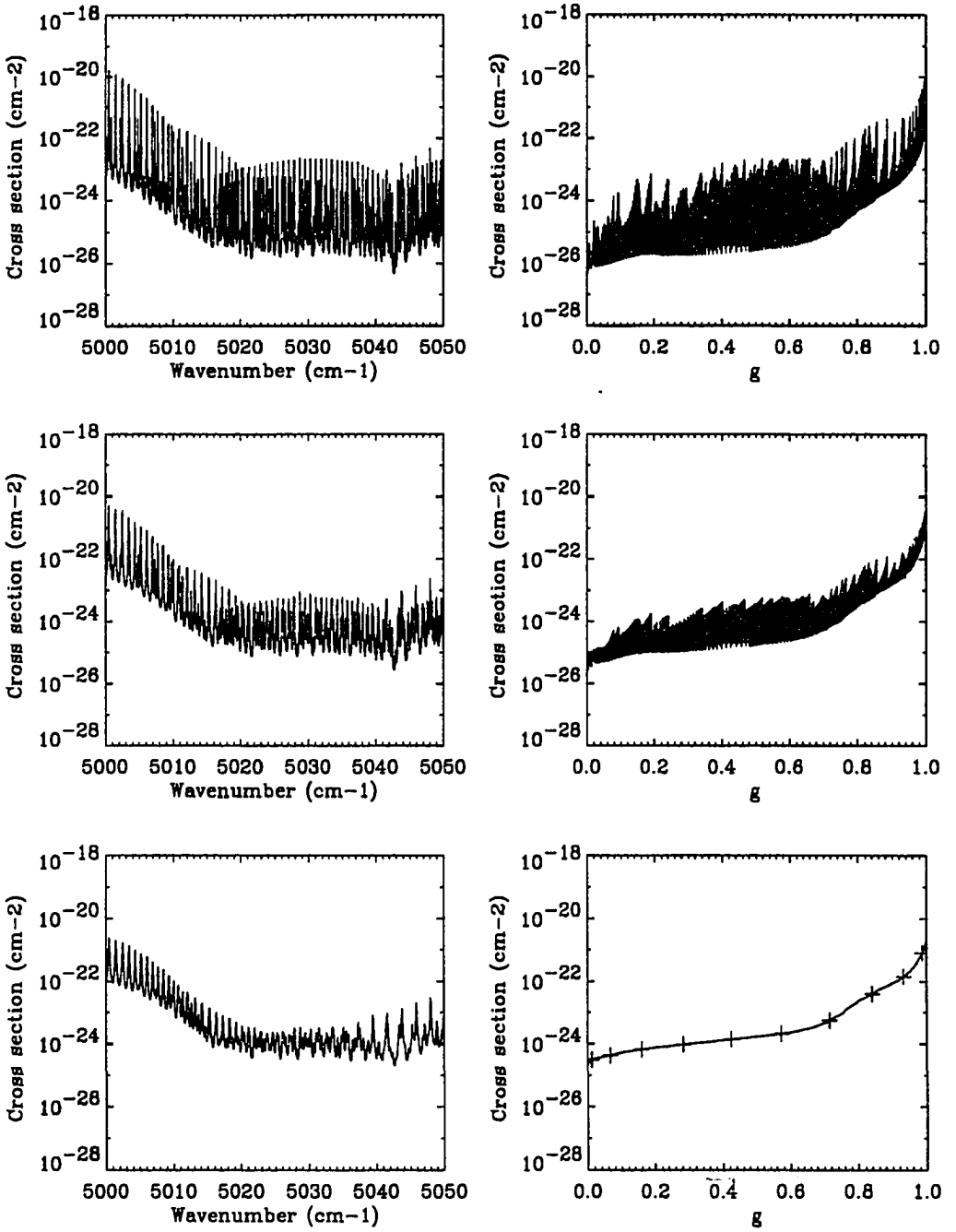

Figure 3.2: Same as in Fig. 3.1, but with the cross sections in the two upper panels sorted by the same mapping as used for sorting the ground level (bottom panel). The non-monotonic behaviour of the sorted cross sections in the two upper panels demonstrates the breakdown of the correlation assumption.

3.2.1 Maxwell equations for periodic fields

The electromagnetic field inside the particle is denoted by $\mathcal{E}_1, \mathcal{H}_1$, and $\mathcal{E}_2, \mathcal{H}_2$ is the field in the medium surrounding the particle. It is a superposition of the incident (i) and the scattered (s) field ($\mathcal{E}$ and $\mathcal{H}$ are vectors here and below)

$$\mathcal{E}_2 = \mathcal{E}_i + \mathcal{E}_s \tag{3.92}$$

$$\mathcal{H}_2 = \mathcal{H}_i + \mathcal{H}_s. \tag{3.93}$$

The incident electromagnetic field is written as a monochromatic, plane harmonic wave

$$\mathcal{E}_i = \mathcal{E}_0 \exp(-i\mathbf{k} \cdot \mathbf{x} - \omega t) \tag{3.94}$$

$$\mathcal{H}_i = \mathcal{H}_0 \exp(-i\mathbf{k} \cdot \mathbf{x} - \omega t). \tag{3.95}$$

The fields must satisfy the Maxwell equations (Bohren and Huffmann, 1983)

$$\nabla \cdot \mathcal{E} = 0 \tag{3.96}$$

$$\nabla \cdot \mathcal{H} = 0 \tag{3.97}$$

$$\nabla \times \mathcal{E} = i\omega\mu\mathcal{H} \tag{3.98}$$

$$\nabla \times \mathcal{H} = -i\omega\varepsilon\mathcal{E} \tag{3.99}$$

where μ is the permeability and ε the permitivity. Taking the curl of Eqs. 3.98–3.99, and using the vector identity

$$\nabla \times (\nabla \times \mathbf{A}) = \nabla(\nabla \cdot \mathbf{A}) - \nabla \cdot (\nabla \mathbf{A}) \tag{3.100}$$

gives

$$\nabla^2\mathcal{E} + k^2\mathcal{E} = 0 \tag{3.101}$$

$$\nabla^2\mathcal{H} + k^2\mathcal{H} = 0 \tag{3.102}$$

where $k^2 = \varepsilon\mu\omega^2$. The vector wave equations 3.101– 3.102 describe the electromagnetic field outside and inside the sphere. A sharp boundary is assumed between the particle and the medium. Requiring that the tangential components of $\mathcal{E}$ and $\mathcal{H}$ are continous across the interface, our boundary conditions are

$$[\mathcal{E}_s(\mathbf{r}_s) + \mathcal{E}_i(\mathbf{r}_s) - \mathcal{E}_1(\mathbf{r}_s)] \times \mathbf{e}_r = 0 \tag{3.103}$$

$$[\mathcal{H}_s(\mathbf{r}_s) + \mathcal{H}_i(\mathbf{r}_s) - \mathcal{H}_1(\mathbf{r}_s)] \times \mathbf{e}_r = 0. \tag{3.104}$$

Here $\mathbf{r}_s$ describes the surface of the spherical particle.

3.2.2 Solutions to the vector wave equations

The field vectors $\mathcal{E}$ and $\mathcal{H}$ satisfy the vector wave equations 3.101–3.102. To solve these equations two vector functions M and N are constructed

$$\mathbf{M} = \nabla \times (\mathbf{r}\psi) \tag{3.105}$$

$$\mathbf{N} = \frac{1}{k}\nabla \times \mathbf{M} \tag{3.106}$$

where ψ is a scalar function and r the radius vector. It can be shown that if ψ is a solution to the scalar wave equation

$$\nabla^2\psi + k^2\psi = 0 \tag{3.107}$$

then M and N satisfy the vector wave equation

$$\nabla^2\mathbf{A} + k^2\mathbf{A} = 0. \tag{3.108}$$

In spherical polar coordinates the scalar wave equation 3.107 is separable and has elementary solutions

$$\psi_{mn} = \begin{cases} \cos m\phi \\ \sin m\phi \end{cases} P_n^m(\cos\theta) z_n(kr) \tag{3.109}$$

where m and n are integers, $n \geq m \geq 0$, $P_n^m(\cos\theta)$ are the associated Legendre functions of degree n and order m, and z_n is any spherical Bessel function. If u and v are two solutions of the scalar wave equation and $\mathbf{M}_u$, $\mathbf{N}_u$, $\mathbf{M}_v$ and $\mathbf{N}_v$ the derived vector fields from Eqs. 3.105–3.106, then the Maxwell equations 3.98–3.99 are satisfied if

$$\mathcal{E} = \mathbf{M}_v - i\mathbf{N}_u \tag{3.110}$$

$$\mathcal{H} = -\frac{k}{\omega\mu}(\mathbf{M}_u + i\mathbf{N}_v). \tag{3.111}$$

3.2.3 Solutions of coefficients from boundary conditions

Assuming that the incident radiation is linearly polarized in the x–direction and with amplitude of unity, the incident field is written as

$$\mathcal{E}_i = e^{-ikz-i\omega t}\mathbf{e}_x \tag{3.112}$$

$$\mathcal{H}_i = e^{-ikz-i\omega t}\mathbf{e}_y. \tag{3.113}$$

Moving to spherical polar coordinates the incident fields may be written as in Eqs. 3.110–3.111 if[9]

$$u_i = e^{-i\omega t}\cos\phi\sum_{n=1}^{\infty} i^n \frac{2n+1}{n(n+1)} P_n^1(\cos\theta) j_n(kr) \tag{3.114}$$

$$v_i = e^{-i\omega t}\sin\phi\sum_{n=1}^{\infty} i^n \frac{2n+1}{n(n+1)} P_n^1(\cos\theta) j_n(kr) \tag{3.115}$$

where

$$j_n(\rho) = \sqrt{\frac{\pi}{2\rho}} J_{n+1/2}(\rho). \tag{3.116}$$

Here J_ν is the Bessel function of the first kind. Likewise the field inside the sphere can be represented by

$$u_1 = e^{-i\omega t}\cos\phi\sum_{n=1}^{\infty} \frac{k_1}{k} c_n i^n \frac{2n+1}{n(n+1)} P_n^1(\cos\theta) j_n(kr) \tag{3.117}$$

$$v_1 = e^{-i\omega t}\sin\phi\sum_{n=1}^{\infty} \frac{k_1}{k} d_n i^n \frac{2n+1}{n(n+1)} P_n^1(\cos\theta) j_n(kr) \tag{3.118}$$

where $k_1/k = N_1/N$ and N_1 and N are the refractive indices of the particle and medium, respectively. When writing down the incident field in the medium and in the particle, care was excercised when 'picking' the spherical Bessel function. These fields must be finite at the origin, and $j_n(kr)$ fulfills this requirement. The scattered field is, of course, an outgoing wave and is represented by

$$u_s = e^{-i\omega t}\cos\phi\sum_{n=1}^{\infty} a_n i^n \frac{2n+1}{n(n+1)} P_n^1(\cos\theta) h_n^{(1)}(kr) \tag{3.119}$$

$$v_s = e^{-i\omega t}\sin\phi\sum_{n=1}^{\infty} b_n i^n \frac{2n+1}{n(n+1)} P_n^1(\cos\theta) h_n^{(1)}(kr). \tag{3.120}$$

The quantities

$$h_n^{(1)}(\rho) = j_n(\rho) + i y_n(\rho) \tag{3.121}$$

and

$$y_n(\rho) = \sqrt{\frac{\pi}{2\rho}} Y_{n+1/2}(\rho) \tag{3.122}$$

are the spherical Hankel functions, where Y_ν is the Bessel function of the second kind.

[9] Because of the orthogonality properties of the cos and sin functions, only the $m = 1$ term will make a contribution when transforming from rectangular to spherical polar coordinates, see Bohren and Huffmann (1983) for details.

The coefficients a_n, b_n, c_n and d_n in Eqs. 3.117–3.120 are determined from the boundary conditions Eqs. 3.103–3.104, i.e.

$$a_n = \frac{\mu_1 m^2 j_n(mx)[xj_n(x)]' - \mu_1 m j_n(x)[mxj_n(mx)]'}{\mu_1 m^2 j_n(mx)[xh_n^{(1)}(x)]' - \mu_1 h_n^{(1)}(x)[mxj_n(mx)]'} \tag{3.123}$$

$$b_n = \frac{\mu_1 j_n(mx)[xj_n(x)]' - \mu_1 j_n(x)[mxj_n(mx)]'}{\mu_1 j_n(mx)[xh_n^{(1)}(x)]' - \mu_1 h_n^{(1)}(x)[mxj_n(mx)]'} \tag{3.124}$$

$$c_n = \frac{\mu_1 j_n(x)[xh_n^{(1)}(x)]' - \mu_1 h_n^{(1)}(x)[xj_n(x)]'}{\mu_1 j_n(mx)[xh_n^{(1)}(x)]' - \mu_1 h_n^{(1)}(x)[mxj_n(mx)]'} \tag{3.125}$$

$$d_n = \frac{\mu_1 j_n(x)[xh_n^{(1)}(x)]' - \mu_1 m h_n^{(1)}(x)[xj_n(x)]'}{\mu_1 m^2 j_n(mx)[xh_n^{(1)}(x)]' - \mu_1 h_n^{(1)}(x)[mxj_n(mx)]'}. \tag{3.126}$$

Here, the prime indicates differentation with respect to x of the argument in brackets. The size parameter, x, and the relative refractive index, m, are

$$x = ka = \frac{2\pi Na}{\lambda} \tag{3.127}$$

$$m = \frac{k_1}{k} = \frac{N_1}{N} \tag{3.128}$$

where a is the radius of the particle.

3.2.4 Cross sections

The absorption cross section has already been defined by Eq. 3.1. A similar expression applies for the scattering cross section. The magnitude and direction of the rate of transfer of electromagnetic energy at all points in space is given by the Poynting vector

$$\mathbf{S} = \mathcal{E} \times \mathcal{H}. \tag{3.129}$$

For time harmonic fields the time averaged Poynting vector is

$$< \mathbf{S} >= \frac{1}{2}\Re\{\mathcal{E} \times \mathcal{H}^*\} =< \mathbf{S}_i > + < \mathbf{S}_{sca} > + < \mathbf{S}_{ext} > \tag{3.130}$$

where

$$\mathbf{S}_i = \frac{1}{2}\Re\{\mathcal{E}_i \times \mathcal{H}_i^*\} \tag{3.131}$$

$$\mathbf{S}_{sca} = \frac{1}{2}\Re\{\mathcal{E}_{sca} \times \mathcal{H}_{sca}^*\} \tag{3.132}$$

$$\mathbf{S}_{ext} = \frac{1}{2}\Re\{\mathcal{E}_i \times \mathcal{H}_{sca}^* + \mathcal{E}_{sca} \times \mathcal{H}_i^*\}. \tag{3.133}$$

Here $\mathbf{S}_i$ is associated with the incident wave, $\mathbf{S}_{sca}$ the scattered wave and $\mathbf{S}_{ext}$ is the term that arises because of interaction between the incident and scattered waves. The net rate at which

electromagnetic energy crosses a surface A of an imaginary sphere of radius r surrounding the particle is

$$\left(\frac{dW}{dt}\right)_{abs} = -\int_A \mathbf{S}\cdot\mathbf{e}_r dA = -\left(\frac{dW}{dt}\right)_{sca} + \left(\frac{dW}{dt}\right)_{ext} \tag{3.134}$$

since the integral over $\mathbf{S}_i$ vanishes for a nonabsorbing medium. Using the above results for the incident and scattered fields, cf. Eqs. 3.112–3.115 and 3.119–3.120, the absorption and scattering cross sections may be written as

$$\sigma_{sca} = \frac{\left(\frac{dW}{dt}\right)_{sca}}{I_i} = \frac{2\pi}{k^2}\sum_{n=1}^{\infty}(2n+1)(|a_n|^2+|b_n|^2) \tag{3.135}$$

$$\sigma_{abs} = \sigma_{ext} - \sigma_{sca} \tag{3.136}$$

where

$$\sigma_{ext} = \frac{\left(\frac{dW}{dt}\right)_{ext}}{I_i} = \frac{2\pi}{k^2}\sum_{n=1}^{\infty}(2n+1)\Re\{a_n+b_n\} \tag{3.137}$$

and the incident intensity

$$I_i = |\mathbf{S}_i| = \frac{1}{2}\Re\{\mathcal{E}_i\times\mathcal{H}_i^*\} = \frac{1}{2}\Re\left\{\sqrt{\frac{\varepsilon}{\mu}}\right\}|\mathcal{E}_0|^2 \tag{3.138}$$

Eqs. 3.135–3.136 gives the magnitude of the respective cross sections. For scattering processes the direction in which the light is scattered is also of great importance. Defining an asymmetry parameter g as the average of the cosine of the scattering angle

$$g = <\cos\theta> \tag{3.139}$$

one gets after lengthy calculations (Bohren and Huffmann, 1983)

$$g = \frac{4}{x^2 Q_{sca}}\left[\sum_{n=1}^{\infty}\frac{n(n+2)}{n+1}\Re\{a_n a_{n+1}^* + b_n b_{n+1}^*\} + \sum_{n=1}^{\infty}\frac{2n+1}{n(n+1)}\Re\{a_n b_n^*\}\right] \tag{3.140}$$

where the scattering efficiency $Q_{sca} = \sigma_{sca}/\pi a^2$, a is the radius of the particle. For isotropic scattering $g = 0$, for complete forward scattering $g = 1$ and for full backward scattering $g = -1$.

The above are for one specific radius of the particles. In the atmosphere a variety of sizes are found. If the particles have a size distribution $\mathbf{p}(a)$ normalized to unity the effective cross section becomes

$$\sigma = \int_0^{\infty}\sigma(a)p(a)da. \tag{3.141}$$

Hence to calculate absorption and scattering properties of particles, one needs to be able to calculate the cross sections for different particles sizes and next integrate over all sizes, weighting with a suitable particle size distribution.

3.2.5 An approximate scheme for Mie theory calculations for water clouds

For water clouds the extinction and scattering coefficients may be written as

$$\beta_{ext} = \frac{\pi}{k^3}\int_0^\infty n(r)r^2 Q_{ext}(r)dr \tag{3.142}$$

$$\beta_{sca} = \frac{\pi}{k^3}\int_0^\infty n(r)r^2 Q_{sca}(r)dr \tag{3.143}$$

where $n(r)$ is the cloud droplet size distribution, r the droplet radius and $k = 2\pi/\lambda$. The extinction and scattering coefficients are needed to specify the environment in which the radiative transfer equation is to be solved. In principle one must calculate β_{ext} and β_{sca} for each different droplet size distribution and wavelength. Due to the slow convergence of the sum in Eq. 3.135, so called Mie calculations (evaluation of Q_{ext} and Q_{sca}) are impractical for many applications and hence parameterizations are invoked. In this work a recent parameterization scheme developed by Hu and Stamnes (1992) will be used. Defining an equivalent droplet radius

$$r_e = \frac{\int_0^\infty n(r)r^3 dr}{\int_0^\infty n(r)r^2 dr} \tag{3.144}$$

they find that the extinction coefficient β_{ext}, the asymmetry factor g and the single scattering albedo ω may be reproduced to great accuracy by the following expressions

$$\frac{\beta_{ext}}{LWC} = a_1 r_e^{b_1} + c_1 \tag{3.145}$$

$$\omega = a_2 r_e^{b_2} + c_2 \tag{3.146}$$

$$g = a_3 r_e^{b_3} + c_3. \tag{3.147}$$

Here LWC is the liquid water content of the cloud, and the coefficients a_i, b_i and c_i $(i = 1, 2, 3)$ are constants for a given wavelength. They were found by fitting Eq. 3.145–3.147 to exact Mie calculations using the least square method. The coefficients for equivalent drop radi from 2.5 to 60 μm and wavelengths between 290–3690 nm are given in Hu and Stamnes (1992).

3.2.6 Rayleigh scattering

For scattering of UV and visible radiation by spherical particles it is noted that $mx = m2\pi Na/\lambda \ll 1$. Expanding the various functions in the scattering coefficients a_n and b_n in Eqs. 3.123–3.124 in power series and retaining enough terms so that the scattering coefficients are accurate to terms

of order x^6, it may be shown that (Bohren and Huffmann, 1983)

$$I_s = \frac{8\pi^4 N a^6}{\lambda^4 r^2} \left| \frac{m^2 - 1}{m^2 + 2} \right|^2 (1 + \cos^2\theta) I_i \tag{3.148}$$

where I_i is the intensity of incident unpolarized light and I_s is the scattered intensity. Hence, the familiar Rayleigh scattering cross section is

$$\sigma_{Ray}(\lambda, \mu) = \frac{(2\pi)^5 N a^6}{3\lambda^4} \left| \frac{m^2 - 1}{m^2 + 2} \right|^2 P_{Ray}(\cos\theta) \tag{3.149}$$

where the normalised Rayleigh phase function is

$$P_{Ray}(\cos\theta) = \frac{3}{4}(1 + \cos^2\theta). \tag{3.150}$$

Thus, if the relative refractive index m varies weakly with wavelength, the radiation scattered by any particle small compared with the wavelength is proportional to $1/\lambda^4$. In air, the refractive index depends upon wavelength varying from $m - 1 = 3.4187 * 10^{-4}$ at $\lambda = 0.2\mu m$ and $0°C$ to $m - 1 = 2.8757 * 10^{-4}$ at $\lambda = 20\mu m$ and $0°C$. Hence there is a slight departure from the inverse fourth power law wavelength dependence. In this work the empirical formula due to Nicolet (1984) is used,

$$\sigma_{Ray}(\lambda) = \frac{4.02 * 10^{-28}}{\lambda^{4+x}}. \tag{3.151}$$

Here, λ is in μm and $x = 0.389\lambda + 0.09426/\lambda - 0.3228$ for the spectral region $0.2\mu m < \lambda < 0.55\mu m$ and $x = 0.04$ for $0.55 < \lambda < 1\mu m$. Eq. 3.151 also includes the effect of depolarization caused by the nonspherical shape of air molecules, i.e. nonspherical molecules do not have scalar polarizability (Goody 1964), and the effect that they are not identical, i.e. the air consists of different molecular species.

3.3 Summary

Starting from first principles the absorption cross sections for air molecules have been derived using semi-classical theory. An approximate scheme, the correlated–k distribution method, for radiative transfer calculations with erratically and strongly varying cross sections has been outlined.

In the last section the absorption and scattering properties of particulates in the atmosphere have been derived under the assumption that the particulates are spheres, i.e. Mie–theory.

Chapter 4

Photodissociation rates

The photochemistry of the atmosphere is driven by sunlight that dissociates certain key molecules which are often highly reactive. In models of the chemistry of the atmosphere, it is necessary to have detailed information about the photodissociation rates under different atmospheric conditions. In this chapter it is described how photodissociation rates may accurately and efficiently be calculated in realistic atmospheres. After deriving an expression for the photodissociation rate the photochemically active molecules for middle atmosphere ozone chemistry included in the present model aer listed. Next, the radiation model developed in this work including appropriate cross-sections, is compared with measurements. Finally, the accuracy of the numerical scheme to calculate photodissociation rates is investigated, and examples given for different atmospheric conditions, e.g. low sun.

4.1 The continuity equation and photochemical processes

The density $n_i(z)$ of an atmospheric constituent i is governed by a continuity–transport equation (e.g. Brasseur and Solomon 1986)

$$\frac{\partial n_i}{\partial t} + \nabla \cdot (n_i \mathbf{v}) = P(n_i) - n_i L(n_i) \tag{4.1}$$

where P and L denote chemical and photodissociative production and loss terms, and $\mathbf{v}$ the wind velocity. Depending on the constituent in question, either chemistry, including photochemistry, or dynamics or both may be important in determining its distributions. Letting τ_{chem} and τ_{dyn}

denote chemical and dynamical lifetimes[1] respectively, it may be distinguished between three cases (Brasseur and Solomon 1986, Andrews, Holton and Leovy 1987)

- $\tau_{chem} \ll \tau_{dyn}$. In this case the constituents will be in local photochemical equilibrium and transport effects will not enter directly into the conservation equations. However, dynamics may still be important in an indirect fashion by changing the local temperature and hence the rate at which chemical processes proceed and by affecting the concentration of other species that photochemically participate in production and loss of the constituent in question. An example of the latter is the very short lived HO_x ($= H + OH + HO_2$) which can be produced and destroyed by the transport depended H_2O.

- $\tau_{chem} \gg \tau_{dyn}$. When the chemical timescales are much longer than the dynamical timescales, the species will be well–mixed by passive advection, e.g. N_2 and O_2 are well–mixed in the middle atmosphere due to their very long chemical lifetimes. However in the thermosphere this is not the case due to their much shorter chemical lifetimes in that region of the atmosphere. CFC–gases are well–mixed in the troposphere, but are relatively rapidly photodissociated once entering the stratosphere (Fig. 4.7).

- $\tau_{chem} \sim \tau_{dyn}$. In this case both dynamical and chemical processes determine the concentration of a species, e.g. the meridional distribution of CH_4 and N_2O depend equally on transport and chemistry in the upper stratosphere.

Generally, the Navier–Stokes equations must be solved in order to obtain an estimate of the vertical, zonal and meridional dynamical timescales. Brasseur and Solomon (1986) give examples of middle latitude transport lifetimes in the stratosphere, mesosphere and lower thermosphere. Typical zonal lifetimes in this region are of the order of a day, while meridional lifetimes vary from several months in the lower stratosphere to a couple of weeks at the mesopause and above. Vertical lifetimes are from several months (lower stratosphere) to a month (mesosphere). At other latitudes the dynamical lifetimes may be different.

The chemical lifetime of a species is generally a function of both chemical rate coefficients and concentration of other species with which it reacts. For certain species and altitude regions, analytic expressions may be written down for the chemical lifetimes. However, generally Eq. 4.1, without transport, must be solved for all species i involved. Photochemical processes play a very

[1] Advective processes (mean motion plus eddies) determine the dynamical lifetime, which is the time required to transport a tracer through a scale height vertically or meridionally from equator to pole.

important role in determining the composition of the atmosphere. The photochemical lifetime, given by the inverse of the photodissociation rate, may be calculated by radiation models such as the one described in preceeding chapters. Below, the photodissociation rate will be defined, it will be discussed how it is calculated and examples of various photodissociation rates given.

4.1.1 Definition of the photodissociation rate.

Depending on the constituent in question, photodissociative processes, i.e. $XY + h\nu \rightarrow X + Y$, may result in either a loss or production of the constituent. The net rate of change in the number density of species i due to photodissociative processes is

$$\frac{dn_i}{dt} = -n_i J(n_i) + \sum_{j \neq i} n_j J(n_j \tag{4.2}$$

Here $J(n_i)$ is the photodissociation rate, typically in units $1/s$. Table 4.1 lists the most important photodissociative processes pertinent to middle atmosphere ozone chemistry, which are included in the present model.

The photodissociation rate J $(1/s)$ is defined by the rate equation (Madronich 1987)

$$-\frac{dn}{dt} = J\, n \tag{4.3}$$

where n is the number density of a particular dissociating molecular species. The number of photodissociations per time unit depends on the available light, the probability for the molecule to absorb the incident photon (the absorption cross section $\sigma(\lambda)$), and the probability for dissociation after photon absorption (the quantum yield $q(\lambda)$). In a thin atmospheric layer dz, the number of photons absorbed when crossing this layer is

$$n\, \sigma(\lambda) \frac{dz}{\cos\theta} dE \tag{4.4}$$

where θ is the polar angle of the incident light with the normal to the incident surface. The radiant energy dE in a wavelength interval $d\lambda$ transported across a particular surface dS and in directions confined to an element of solid angle $d\omega$ (which is at an angle θ to the surface normal) in time dt is given by (Chandrasekhar 1960)

$$dE = I(z, \theta, \phi, \lambda) \cos\theta\, d\lambda\, dS\, d\omega\, dt \tag{4.5}$$

where the intensity $I(z, \theta, \phi, \lambda)$ is in units of photons $nm^{-1}cm^{-2}s^{-1}sr^{-1}$. The total number of dissociation events in a volume element $dV = dzdS$ is found by multiplying Eq. 4.4 by the

Coefficient	Name	Reaction			Uncertainty
$J(O_2)$		$O_2 + h\nu$	$\rightarrow$	$O + O$	1.4
$J(O_3)$		$O_3 + h\nu$	$\rightarrow$	$O(^3P) + O_2$	1.1
$J(O_3^*)$		$O_3 + h\nu$	$\rightarrow$	$O(^1D) + O_2$	1.4
$J(H_2O)$		$H_2O + h\nu$	$\rightarrow$	$OH + H$	
$J(CO_2)$		$CO_2 + h\nu$	$\rightarrow$	$CO + O$	
$J(CH_4)$		$CH_4 + h\nu$	$\rightarrow$	products	
$J(NO)$		$NO + h\nu$	$\rightarrow$	$N + O$	
$J(N_2O)$		$N_2O + h\nu$	$\rightarrow$	$N_2 + O(^1D)$	1.2
$J(NO_2)$		$NO_2 + h\nu$	$\rightarrow$	$NO + O(^3P)$	1.3
$J_a(NO_3)$		$NO_3 + h\nu$	$\rightarrow$	$NO_2 + O$	1.3
$J_b(NO_3)$		$NO_3 + h\nu$	$\rightarrow$	$NO + O_2$	1.3
$J(HNO_3)$		$HNO_3 + h\nu$	$\rightarrow$	$NO_2 + OH$	1.3
$J_a(HNO_4)$		$HNO_4 + h\nu$	$\rightarrow$	$OH + NO_3$	2.0
$J_b(HNO_4)$		$HNO_4 + h\nu$	$\rightarrow$	$HO_2 + NO_2$	2.0
$J_a(H_2CO)$		$H_2CO + h\nu$	$\rightarrow$	$H_2 + CO$	
$J_b(H_2CO)$		$H_2CO + h\nu$	$\rightarrow$	$H + HCO$	
$J(HOCl)$		$HOCl + h\nu$	$\rightarrow$	$OH + Cl$	1.4
$J(HCl)$		$HCl + h\nu$	$\rightarrow$	$H + Cl$	1.1
$J(ClONO_2)$		$ClONO_2 + h\nu$	$\rightarrow$	$NO_3 + Cl$	1.3
$J(N_2O_5)$		$N_2O_5 + h\nu$	$\rightarrow$	$NO_2 + NO_3$	2.0
$J(H_2O_2)$		$H_2O_2 + h\nu$	$\rightarrow$	$OH + OH$	1.4
$J(CCl_4)$		$CCl_4 + h\nu$	$\rightarrow$	$CCl_3 + Cl$	1.1
$J(CH_3Cl)$		$CH_3Cl + h\nu$	$\rightarrow$	$CH_3 + Cl$	1.1
$J(CH_3CCl_3)$		$CH_3CCl_3 + h\nu$	$\rightarrow$	$CH_3CCl_2 + Cl$	
$J(CF_2ClCFCl_2)$	CFC-113	$CF_2ClCFCl_2 + h\nu$	$\rightarrow$	products	
$J(CF_2ClCF_2Cl)$	CFC-114	$CF_2ClCF_2Cl + h\nu$	$\rightarrow$	products	
$J(CF_3CF_2Cl)$	CFC-115	$CF_3CF_2Cl + h\nu$	$\rightarrow$	products	
$J(CHClF_2)$	HCFC-22	$CHClF_2 + h\nu$	$\rightarrow$	products	
$J(CCl_2F_2)$	CFC-12	$CCl_2F_2 + h\nu$	$\rightarrow$	$CF_2Cl + Cl$	1.1
$J(CF_2O)$		$CF_2O + h\nu$	$\rightarrow$	products	2.0
$J(CBrClF_2)$	Halon-1211	$CBrClF_2 + h\nu$	$\rightarrow$	products	3.0
$J(CBrF_3)$	Halon-1301	$CBrF_3 + h\nu$	$\rightarrow$	products	2.0
$J(BrONO_2)$		$BrONO_2 + h\nu$	$\rightarrow$	products	1.4
$J(HOBr)$		$HOBr + h\nu$	$\rightarrow$	$HO + Br$	
$J(CH_3Br)$		$CH_3Br + h\nu$	$\rightarrow$	$CH_3 + Br$	
$J(OClO)$		$OClO + h\nu$	$\rightarrow$	$O + ClO$	
$J(ClOO)$		$ClOO + h\nu$	$\rightarrow$	$O + ClO$	
$J(OCS)$		$OCS + h\nu$	$\rightarrow$	$CO + S$	
$J(Cl_2O_2)$		$Cl_2O_2 + h\nu$	$\rightarrow$	products	
$J(CCl_3F)$	CFC-11	$CCl_3F + h\nu$	$\rightarrow$	$CFCl_2 + Cl$	1.1
$J(CClFO)$		$CClFO + h\nu$	$\rightarrow$	products	
$J(CCl_2O)$		$CCl_2O + h\nu$	$\rightarrow$	products	

Table 4.1: Photochemical reactions of stratospheric interest that are included in the present model. The relevant cross sections (Fig. 4.1) and quantum yields are from DeMore et al. (1990) and the references therein. For the O_2 Schumann–Runge bands and for NO the parameterization of Allen and Frederick (1982) was used. The uncertainty is the combined uncertainty for cross sections and quantum yields. Examples of the different photodissociation rates are given in Fig. 4.7

probability for dissociation, $q(\lambda)$, and integrating over all solid angles and over all wavelengths λ

$$dN = -dVn\,dt \int_0^\infty q(\lambda)\sigma(\lambda) \int_0^{2\pi} \int_{-1}^{1} I(z,\theta,\phi,\lambda) \sin\theta \, d\theta \, d\phi \, d\lambda \tag{4.6}$$

where $dn = dN/dV$, hence

$$\frac{dn}{dt} = -n \int_0^\infty q(\lambda)\sigma(\lambda) \int_0^{2\pi} \int_{-1}^{1} I(z,\theta,\phi,\lambda) \sin\theta \, d\theta \, d\phi \, d\lambda \tag{4.7}$$

Comparison with Eq. 4.3 gives

$$J(z) = \int_0^\infty q(\lambda)\sigma(\lambda) \int_0^{2\pi} \int_{-1}^{1} I(z,\theta,\phi,\lambda) \sin\theta \, d\theta \, d\phi \, d\lambda = 4\pi \int_0^\infty q(\lambda)\sigma(\lambda)\overline{I(z,\lambda)} \, d\lambda \tag{4.8}$$

The absorption cross sections $\sigma(\lambda)$ and the quantum yields $q(\lambda)$ are known for the most important photochemically active molecules (DeMore et al. 1990), see section 4.2. Given the solar flux at the top of the atmosphere the mean intensity $\overline{I(z,\lambda)}$ may readily be computed by the scheme outlined in Chapter 2. The integral over wavelength in Eq. 4.8 must be treated with some care, as the cross sections, quantum yields and the intensity vary rapidly with wavelength, see section 4.4.

4.2 The solar spectrum, cross sections and quantum yields

When computing the integral in Eq. 4.8, only those wavelengths for which the product of the mean intensity, the cross section and quantum yield is sufficiently large to contribute significantly to the integral need to be included. Thus for the calculation of photodissociation rates important in the middle atmosphere, the wavelength region from 120–700 *nm* suffices (Brasseur and Solomon 1986). The intensity at any wavelength and altitude is a function of the incoming solar flux at the top of the atmosphere and the optical properties of the atmosphere. The solar flux in the wavelength region 116.3–735. *nm* is shown in Fig. 4.1a. The accuracy below 175.0 *nm* is rather poor (±50.%), but improves with increasing wavelength. Furthermore, the solar spectrum varies with the solar cycle and with solar activity. However, the accuracy of the computed photodissociation rates depends more on the uncertainty in the adopted solar flux then on possible solar activity effects (Nicolet 1989).

The absorption cross sections for the different photochemical active species in Table 4.1 are shown in Fig. 4.1b–h. The accuracy of the cross sections varies, the combined uncertainty for cross sections and quantum yields are given in Table 4.1 for some of the species considered. The absorption cross sections and quantum yields are all obtained by laboratory measurements. Theoretical

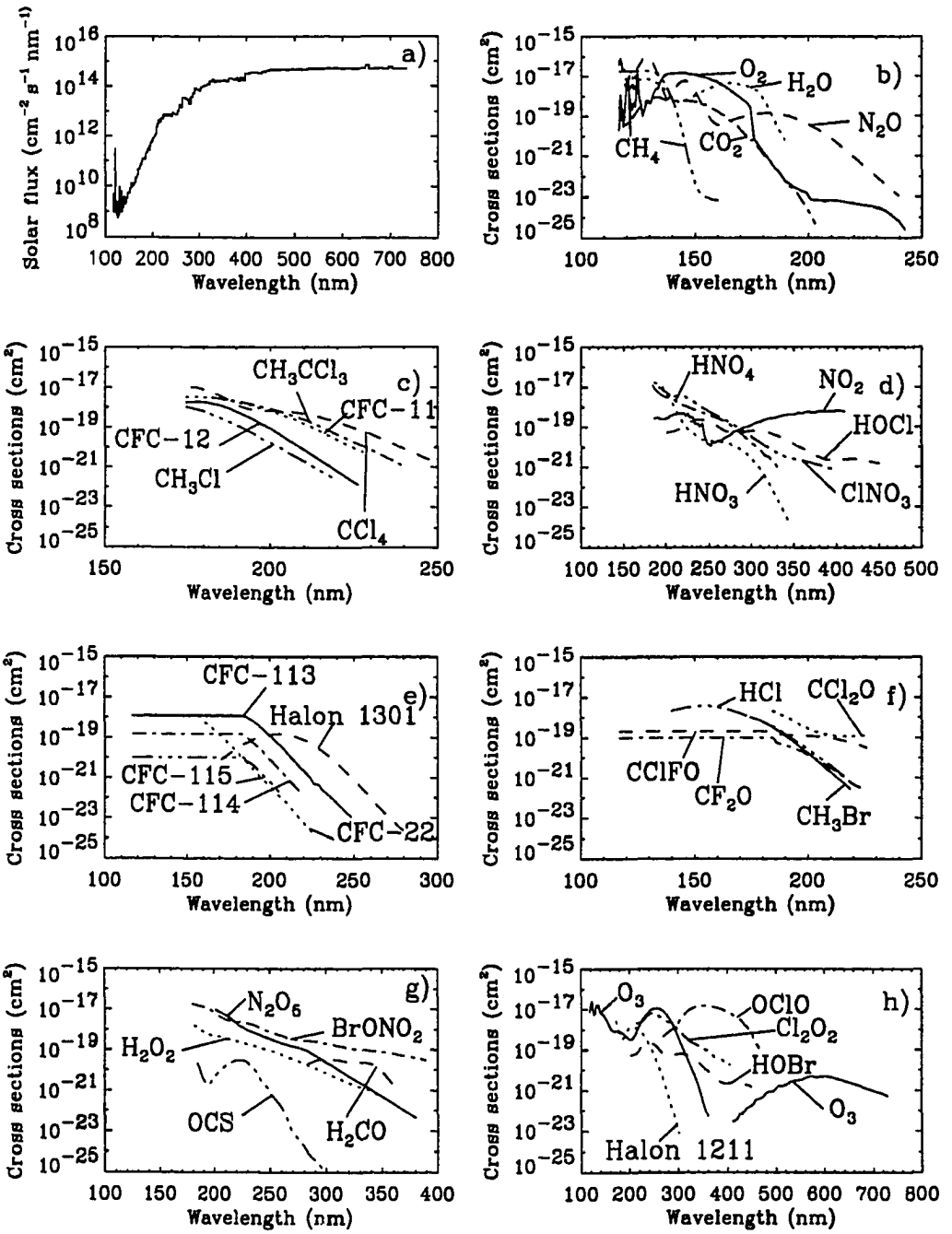

Figure 4.1: The solar flux at the top of the atmosphere is shown in a). The feature at 121.6 *nm* is the Lyman-α line (the data are from Nicolet (1989)). Figs. b)-h) show the absorption cross sections for O_3, O_2, H_2O, CO_2, CH_4, N_2O, NO_2, N_2O_5, CCl_4, HNO_3, HNO_4, HCl, HOCl, H_2O_2, OCS, H_2CO, OClO, Cl_2O_2, HOBr, $BrONO_2$, $ClNO_3$, CH_3Br, CCl_2O, CClFO, CF_2O, CH_3Cl, CH_3CCl_3, CFC-11, CFC-12, CFC-22, CFC-113, CFC-114, CFC-115, Halon 1211 and Halon 1301. The data are from DeMore et al. (1990) and the references therein.

calculations of the cross section for photodissociation of ozone have recently been made possible due to the development of new computer hardware and new algorithms that take advantage of this modern architecture (Le Quéré and Leforestier 1990, 1991 and Neto and Linderberg 1991). These theoretical calculations agree well with the measured cross sections.

Many of the molecules considered exhibit both rotational and vibrational modes. The excitation of these modes depends on the temperature of the molecule. The larger the temperature, the higher the excited states that are occupied and hence the apparent area (or cross section) of the molecule grows. This 'temperature' dependence in the cross sections has been measured for some molecules and, where data are available (DeMore et al. 1990), it has been implemented in the present model.

4.3 Comparison of the radiation transport model with experiment

To compute the integral over wavelength in Eq. 4.8 the integration is replaced by a sum. While the quantum yields and cross sections are deduced from measurement, and are therefore known within experimental errors, the mean intensity is normally calculated using a radiative transfer model.

The direct flux is relatively easy to calculate, even for a spherical geometry. The diffuse flux is more difficult to compute. Thus, experiments to measure both the direct and scattered flux or intensity over large wavelength regions for a variety of atmospheric conditions, would be of great value for validating radiative transfer models including multiple scattering.

Remarkably, there are few such measurements. An attempt to remedy this situation was made by Herman and Mentall (1982, hereafter referred to as HM). They observed the direct, attenuated solar ultraviolet radiation between 190 and 320 *nm* from both a rocket and a balloon, as well as the component of the radiation field produced by atmospheric scattering. The latter was measured for six directions in the sky from a balloon at 40 km. In general, models of the radiance were able to reproduce the observations (see Figure 8 of HM), although discrepancies were seen for certain directions (compare their Figures 5 and 6). Since multiple scattering can enhance the total radiation field substantially in the photochemically active region around 300 *nm* and at longer wavelengths, it is critical to be certain that the radiation field is properly characterized by radiation schemes used in photochemical models.

In order to compute the radiation field in the stratosphere, both the direct, attenuated solar ra-

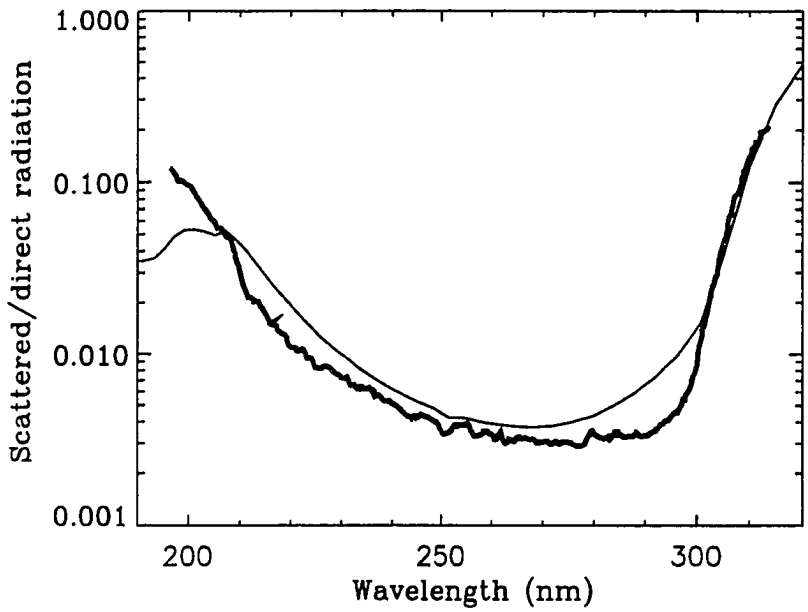

Figure 4.2: The ratio of the scattered to the direct radiation at 40 km altitude. The thick solid line is the empirical curve of HM, their Figure 11, while the thin line represents results of our model calculations.

diation and the multiply-scattered radiation must be known. HM obtained the latter by integrating the observed intensity over the sky, using an interpolation scheme for directions other than those of the measurements. The ratio of the scattered radiation to the direct, attenuated solar radiation provides a measure of the importance of multiple scattering. The 'direct attenuated radiation' is incident on a plane perpendicular to the direction of the sun (i.e. not the vertical), whereas the term 'scattered radiation' is used to denote the diffuse sky radiation integrated over 4π steradians. Figure 11 of HM shows the observed ratio between 200 and 310 *nm* (also reproduced in Figure 4.2). The multiply–scattered radiation is less than 1 % of the direct radiation near 250 *nm*, but approaches 10 % near both 200 and 300 *nm*. Comparison of the observed ratio to a theoretical ratio was not shown by HM, but with regard to the O_2 absorption cross sections they concluded that "on the basis of the measurements of the scattered flux within the Schumann–Runge band region of O_2, the effective cross sections used in current calculations need to be modified to allow greater penetration of the solar radiation into the atmosphere where scattering occurs." HM estimate the

experimental error in the ratio curve to be ±10%. They do not give an error estimate of their data reduction method, i.e. the error made in computing the mean intensity using information from only six directions. However, they estimate that their interpolation scheme gives a ratio equal to or lower then the actual ratio.

In the present work, HM observations are used to test the accuracy of the radiation model developed here to compute the radiation field throughout the earth's atmosphere. Discrepancies are found betweeen theory and observation and possible reasons for these differences are discussed.

4.3.1 Model description

The scattered radiation measured by HM is 4π times the mean intensity

$$\overline{I(\tau)} = \frac{1}{4\pi}\int_0^{2\pi} d\phi \int_0^{\pi} I(\tau,\theta,\phi)\sin\theta\, d\theta = \frac{1}{2}\int_{-1}^{1} I(\tau,\mu)d\mu. \tag{4.9}$$

The direct radiation is described by the Lambert–Beer law, whereas the azimuthally averaged diffuse intensity is governed by the radiative transfer equation 2.31. The radiative transfer equation 2.31 was solved using the discrete ordinate algorithm of Stamnes et al. (1988).

Atmospheric ozone and temperature profiles were taken from Herman and Mentall (1982), see Table 4.2 and discussion below. The ozone absorption cross sections were taken from Molina and Molina (1986) and for the Rayleigh scattering cross section the formula provided by Nicolet (1984) was used, see Eq. 3.151. For molecular oxygen the parameterization due to Allen and Frederick (1982) was used in the Schumann–Runge band whereas in the Herzberg continuum values given by Shardanad and Rao (1977) and corrected as suggested by Frederick and Mentall (1982) were adopted. The solar flux is as in HM, but with a coarser resolution, see Figure 4.3. All calculations were carried out with the wavelength resolution used in most photochemical models (WMO 1986). For the spectral region 190–320 *nm*, there are 42 wavelength intervals with bin sizes varying from 2 to 5 *nm*.

4.3.2 Model results and discussion

The aim is to compute the ratio of the scattered radiation to the direct attenuated solar radiation and compare it to the ratio measured by the HM. As a model atmosphere the profiles in Figure 10 of HM were adopted, they are reproduced in Table 4.2. First the direct downward flux at 40 km is calculated and compared with the results of HM; see Figures 4.3 and 4.4. The direct beam radiation is very sensitive to ozone content where ozone absorbs most strongly, i.e. around 255 *nm*,

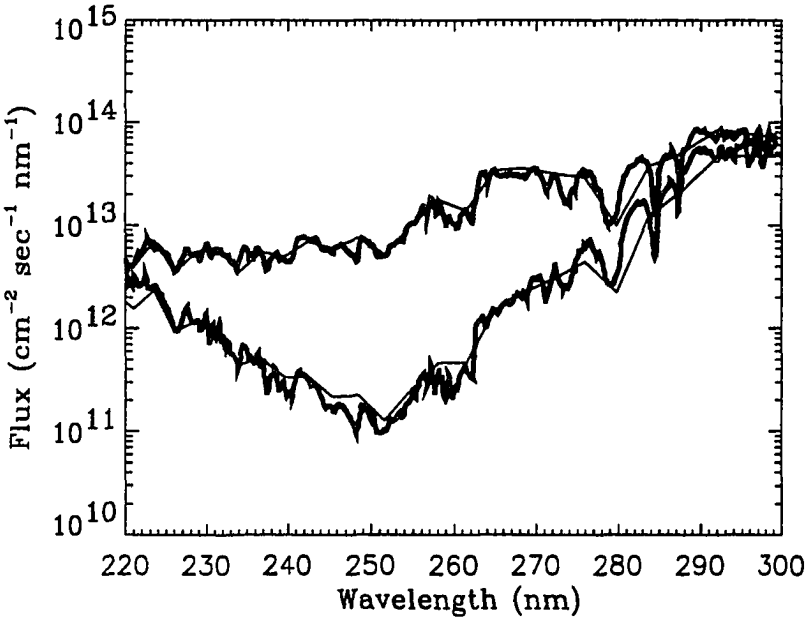

Figure 4.3: The direct flux above the atmosphere and at 40 km altitude. The thin lines are the calculated fluxes while the thick solid lines are experimental data taken from Figure 1 of HM.

whereas in regions where the ozone absorption is small, changes in ozone content have little effect, as discussed by HM. Since interest here is in the ratio of the scattered to the direct radiation, it is obviously important to calculate the direct radiation correctly. To reproduce the measured direct flux at 40 km an altitude resolution of 1 km was required in the model atmosphere just above 40 km. The coarser resolution of 2.5 km used initially, underestimated the direct flux regardless of whether it was assumed that the ozone density varied linearly or exponentially across a single layer. The cause of this was an overestimation of the optical depth by the coarse resolution. In all our calculations the ozone was assumed to vary linearly within each layer. The atmospheric profile that was used in the calculations is given in Table 4.2, unless otherwise noted.

The calculation of the ratio of the scattered to the direct radiation reproduces the main features of the measured ratio, as shown in Figure 4.2. However, there are significant discrepancies. Between 210 and 300 *nm* the model predicts more scattering than the experiment. In particular, between 280 and 300 *nm* the model gives more scattering, up to a factor of two, than inferred from the observations. Between 210–230 *nm* (part of the Herzberg continuum) the model also predicts more

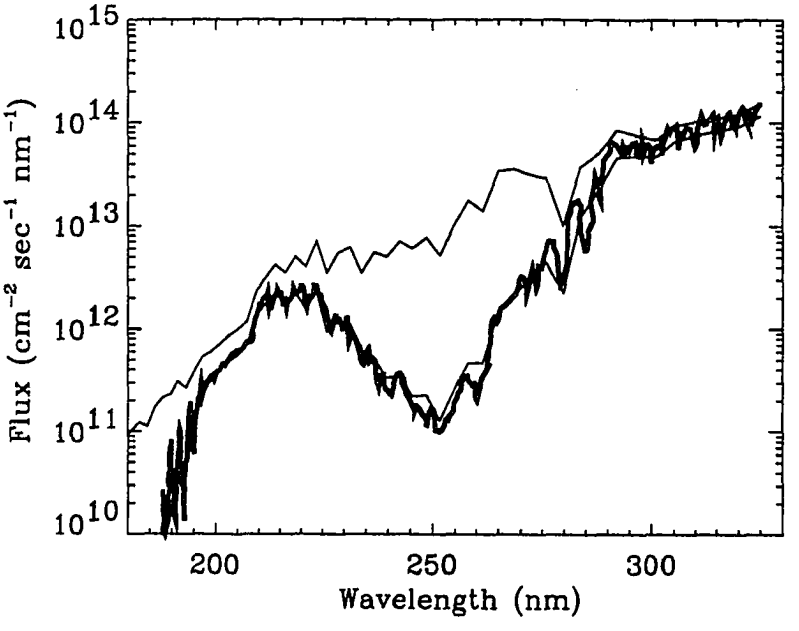

Figure 4.4: The direct flux above the atmosphere and at 40 km altitude. The thin lines are the calculated fluxes while the thick solid line are experimental data taken from Figure 12 of HM.

scattering than is measured, whereas below 210 *nm* (Schumann–Runge bands) the measurements show more scattering. It is noted that there is a certain degree of symmetry in the differences around the wavelength of maximum ozone absorption, 255 *nm*. Lary and Pyle (1991) have also computed the ratio of the scattered to the direct radiation and compared with HM. They conclude that their model agrees well with the measurements, even though they see a difference of more than a factor 3 below 200 *nm*. From our experience with different ozone profiles in calculating the scattered to direct ratio, it seems that the shape of their modelled ratio is caused by their ozone profile, which was 'a standard atmospheric ozone profile', and not representative of the conditions encountered during the experiment of HM. Below is discussed possible sources for the discrepancies between the experimental results and the present model.

Temperature effects: The temperature dependence of the ozone cross section is important above 280 *nm* (Molina and Molina 1986). Thus, a different temperature profile will give a different curve for the ratio of the scattered to direct radiation. Between 280 and 300 *nm* the ozone

absorption cross section varies roughly $\pm 5\%$ from $T = 226K$ to $T = 298K$ around its value at $T = 263K$. Radiation calculations were performed in which the temperature profile was shifted ± 10 K. Such temperature changes do indeed produce different results for the direct and scattered radiation. However, as the scattered radiation is driven by the direct beam radiation, increasing the latter will increase the former and their ratio will not change much as our calculations showed. Thus, for a realistic temperature profile, the temperature dependence measured by laboratory experiments in this wavelength region is too small to explain the discrepancy between the observed and computed radiation ratio.

Albedo effects: For the atmospheric model given in Table 4.2, the radiation above 292 *nm* penetrates to the ground, but not until one reaches 300 *nm* does enough radiation reach the surface to make albedo effects important. The same albedo of 0.2 as assumed by HM, was used. Calculations were also performed with an albedo of 1.0. Although no significant change below 300 *nm* is seen for the latter case, the curves for the experimental and theoretical ratios are in better agreement above 300 *nm*. Experimental data beyond 320 *nm* would be of great value for studying albedo effects.

Polarization: Another possible source of error can be traced to polarization of the Rayleigh scattered light. Although the models do not take polarization into account, the effect is expected to be small for computing sky-integrated intensities (e.g. less than 0.1 % according to Lacis and Hansen (1974)). However, the degree of polarization of the scattered intensities, which depends on the amount of multiple scattering, may result in an important effect. Below 300 *nm*, pure absorption prevents strong multiple scattering, so that intensities in specific directions may be significantly polarized. The observations of HM were made with spectrometers, whose throughput may be dependent on the polarization of the incident light (J. E. Mentall, private communication, 1983). Measurements of the polarization dependence of an 1/8 *m* Ebert-Fastie spectrometer by R. P. McCoy (private communication, 1991) have shown a response varying from 25 to 75 % $(= (I_\perp - I_\parallel)/(I_\perp + I_\parallel))$ across the 200-300 *nm* range. The effects of neglecting polarization by HM are not clear. Good agreement between computed and observed intensities was found for certain directions (see Figure 8 of HM), but not for others (compare curves '5' of Figures 5 and 6 of HM).

Aerosols: Aerosols may significantly alter the optical properties of the atmosphere. It is generally believed that the scattering and absorption properties of aerosols vary slowly with wavelength.

Thus, plausible aerosol loadings do not provide an easy explanation of the strongly wavelength dependent difference between the measured and modelled ratio of the scattered to the direct radiation.

Schumann–Runge bands: The largest discrepancy between the measurement and the model is seen in the region of the Schumann–Runge bands. At 200 nm the ozone absorption cross section has a minimum. Less absorption above and below 40 km means more radiation available for scattering. At both sides of the minimum one would expect the ratio of the scattered to the direct radiation to behave similarly. Hence more absorption means a lower ratio, especially so below 200 nm where both ozone and the Schumann–Runge bands contribute to the absorption. This behaviour of the ratio is seen in the results from the present model, but is absent in the empirical ratio curve of HM. The direct beam radiation displayed in Figure 4.4 of the present paper and Figure 12 of HM both exhibit this behaviour due to increased absorption below $200nm$, as do the modelled scattered radiation field shown in Figure 4.5. However, the scattered radiation field measured by HM and shown in their Figure 5 does not have this behaviour. Since the scattered radiation field is driven by the direct beam radiation, one would expect the direct and scattered radiation fields to have a similar spectral shape, at least for clear sky conditions. It is noted that calculations by Luther and Gelinas (1976) for a similar situation, show very little contribution from the scattered component to the total radiation in this wavelength region (their Figure 3a). HM suggest that the discrepancy seen in the highly structured Schumann-Runge bands may be due to the use of 'bin–averaged' cross sections corresponding to the coarse wavelength resolution of the solar flux used as input. This hypothesis may be tested by turning off all oxygen absorption in the model. This brings the modelled ratio curve closer to the measured one, but one are no longer able to reproduce the direct radiation curve given in Figure 12 of HM and Figure 4.4 of the present paper.

Solar flux data: The radiative transfer equation used in this work is linear in F_0. Both the scattered and the direct radiation are proportional to F_0, hence, when taking the ratio between thw two, the magnitude of the source cancels, and only the optical properties of the medium matter. Thus, the solar flux at the top of the atmosphere has no effect on the calculated and measured ratios.

Table 4.2: Atmospheric profile used in the radiation calculations.

z(km)	p(mb)	T(K)	$O_3(cm^{-3})$	z(km)	p(mb)	T(K)	$O_3(cm^{-3})$
100.0	0.00032	190.0	5.00E+07	24.0	29.72000	218.0	3.84E+12
95.0	0.00076	180.0	9.90E+07	23.0	34.67000	216.0	3.48E+12
90.0	0.00184	173.0	1.50E+08	22.0	40.47000	214.0	3.12E+12
85.0	0.00446	180.0	2.00E+08	21.0	47.29000	212.0	2.76E+12
80.0	0.01050	190.0	2.20E+08	20.0	55.29000	210.0	2.40E+12
75.0	0.02400	205.0	4.70E+08	19.0	64.67000	209.0	1.97E+12
70.0	0.05220	220.0	1.30E+09	18.0	75.65000	207.7	1.54E+12
65.0	0.10900	235.0	3.30E+09	17.0	88.50000	205.0	1.11E+12
60.0	0.21900	250.0	7.07E+09	16.0	103.50000	206.0	6.88E+11
55.0	0.42500	255.0	2.13E+10	15.0	121.10000	210.0	2.60E+11
50.0	0.79780	257.0	6.62E+10	14.0	141.70000	216.0	2.36E+11
47.5	1.09000	255.0	1.20E+11	13.0	165.80000	222.0	2.12E+11
45.0	1.49100	253.0	2.15E+11	12.0	194.00000	228.0	1.88E+11
44.0	1.69681	251.0	2.64E+11	11.0	227.00000	234.0	1.64E+11
43.0	1.93103	250.6	3.24E+11	10.0	265.00000	240.0	1.40E+11
42.0	2.20141	249.0	4.00E+11	9.0	308.00000	246.0	2.72E+11
41.0	2.51401	247.0	4.92E+11	8.0	356.50000	252.0	4.04E+11
40.0	2.87100	245.0	6.07E+11	7.0	411.10001	258.0	5.36E+11
39.0	3.32690	243.0	7.31E+11	6.0	472.20001	264.0	6.68E+11
38.0	3.85518	241.0	8.80E+11	5.0	540.50000	270.0	8.00E+11
37.5	4.15000	240.0	9.65E+11	4.0	616.59998	276.0	8.20E+11
35.0	5.74600	235.0	1.38E+12	3.0	701.20001	282.0	8.40E+11
32.5	8.01000	232.0	1.86E+12	2.0	795.00000	288.0	8.60E+11
30.0	11.97000	230.0	3.00E+12	1.0	898.79999	294.0	8.80E+11
27.5	17.43000	225.0	3.60E+12	0.0	1013.00000	300.0	9.00E+11
25.0	25.49000	220.0	4.20E+12				

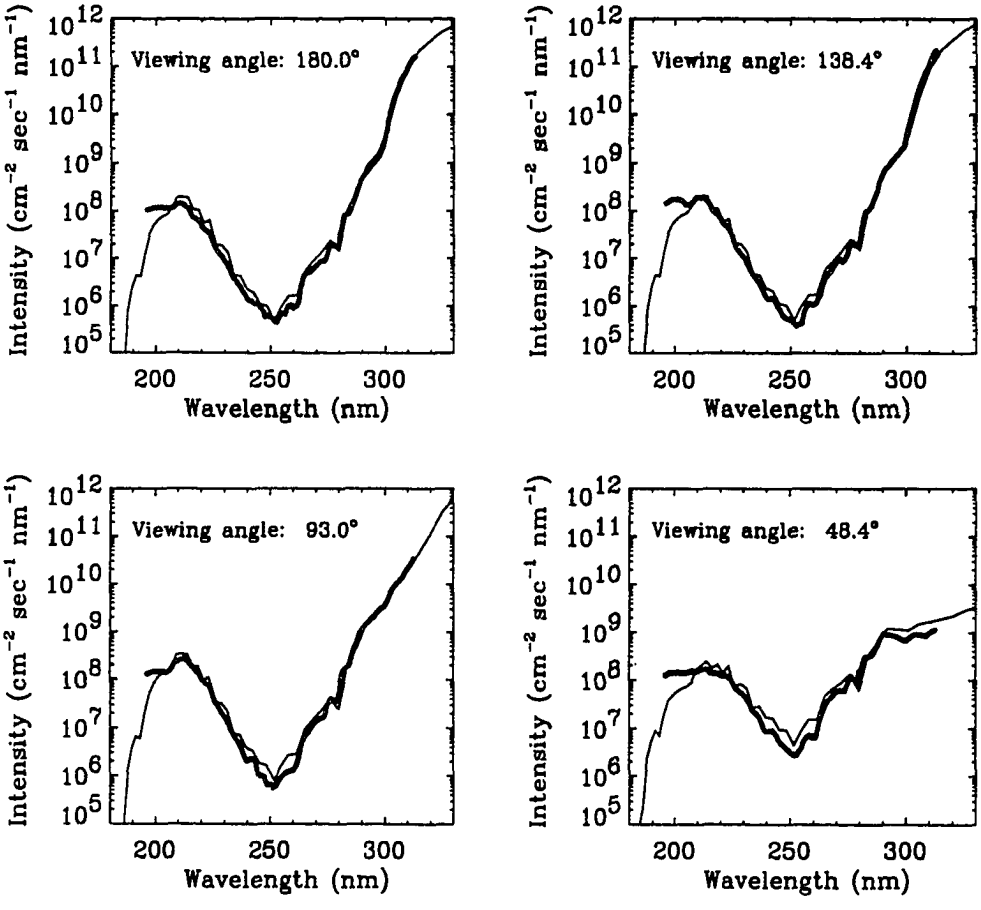

Figure 4.5: The scattered solar flux for four ($\theta = 180.0°$, $\theta = 138.4°$, $\theta = 93.0°$ and $\theta = 48.4°$) of the six viewing directions of the experiment by HM (shown as thick lines). The modelled data (thin lines) have been corrected to take into account the instrument aperture of 0.0474 steradians. This figure should be compared with Figure 5 of HM.

Number of streams: To solve the radiative transfer equation (2.31) for the diffuse intensity, the discrete ordinate method is used. The accuracy of the method depends on the number of quadrature points (or streams) used to approximate the integral in Eq. (2.31). All calculations by the present model used in the comparison with the experimental results of HM, were performed with a 16 stream model for which numerical errors are negligible.

Altering the ozone column: The uniformity in the difference between the modelled and measured ratio of the scattered to the direct radiation suggests that a change in the ozone content may alter the result. Above 40 km the ozone profile is constrained by the requirement that one must be able to reproduce the direct radiation at 40 km. A decrease in ozone below 40 km decreases absorption of radiation and leads to a higher scattered–to–direct radiation ratio, thus increasing the difference between the observed and calculated ratios. An increase in ozone below 40 km will increase the absorption and may thus lead to a lower ratio of the scattered to the direct radiation. Calculations were performed where the ozone column below 40 km was increased by factors of 1.5 and 2.0, but the best agreement was obtained using the the original model atmosphere as given in Table 4.2.

Angular averaging: HM assumed that the scattered radiation changes monotonically with θ between the measurement directions. To find the intensities at intermediate angles they used logarithmic interpolation and then integrated over 4π to obtain the total scattered radiation at 40 km. In Figure 5 of HM the scattered radiation is shown for four of the six viewing directions. In Figure 4.5 of the present work similar modelled intensities are shown. Figure 4.6 shows the variation of the scattered intensity with wavelength and polar angle. For certain wavelength regions, in particular those where multiple scattering is weak, the scattered intensity may vary by several orders of magnitude with the viewing direction. For all of the four viewing directions displayed in Figure 4.5 there is good agreement between measurement and theory, except for the Schumann–Runge bands. It is noted that the largest discrepancies between the modelled and the measured ratio of the scattered to the direct beam radiation are found in the regions of the spectrum (210–230 nm and 280–300 nm) where the intensities vary the least among the different viewing directions. This is somewhat surprising because one would expect the interpolation between the different viewing directions to be more reliable when the variation among them is the smallest.

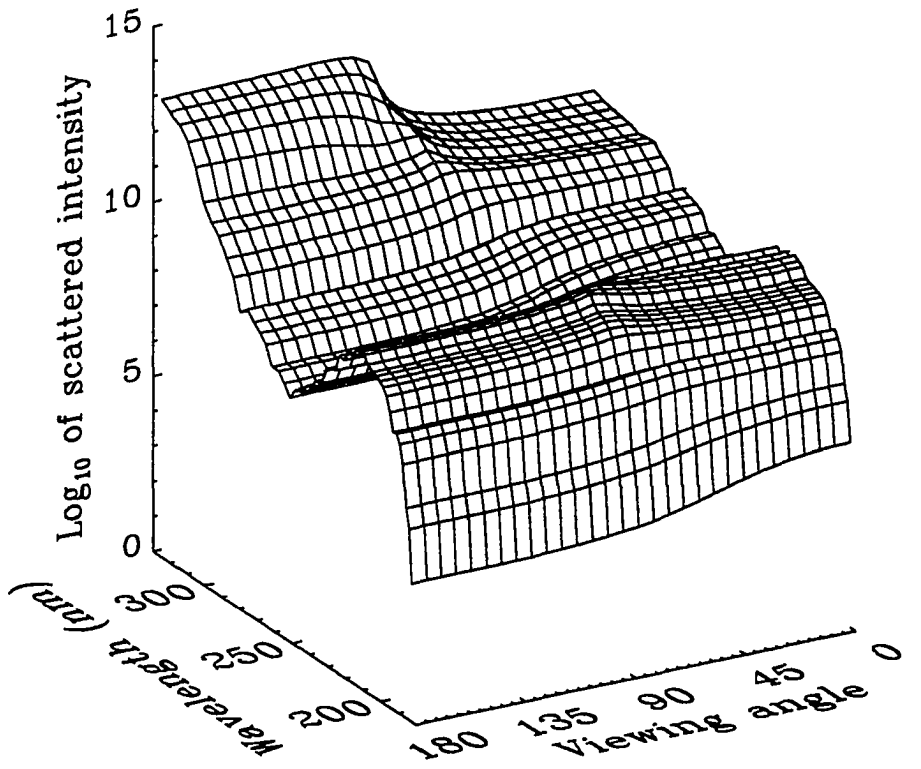

Figure 4.6: The modelled scattered solar flux as a function of wavelength and polar angle. The wavelength resolution is as in WMO (1986) and the angular resolution is 6°.

4.3.3 Summary of comparison of radiation model with experiment

A comparison have been performed between the ratio of the scattered to the direct radiation at 40 km as measured by HM with results of the present state of the art radiative transfer model. Between 210–300 *nm* the model predicts more scattering than observed by measurement. No plausible explanation for this disagreement is found. Furthermore, in the Schumann–Runge bands the model predicts too little scattering. Comparison of Figures 5 and 12 of HM shows that the measured direct radiation and scattered radiation have different spectral shapes in the Schumann–Runge region. The discrepancies are too large to be within the experimental errors.

To help validate radiative transfer models for a Rayleigh scattering atmosphere and to increase

our confidence in radiation schemes used in photochemical models, additional measurements of both the direct and the scattered radiation at several altitudes and zenith angles for clear sky conditions are desirable.

4.4 Calculation of photodissociation rates

To compute the integral over wavelength in Eq. 4.8, it is replaced by a sum of many terms. For each term a monochromatic radiative transfer problem must be solved, as in chapter 2. Furthermore, the wavelength intervals chosen must be selected with care such that all important features in the solar flux, the cross sections and quantum yields are included. Thus, in addition to uncertainties in the solar flux, cross sections and quantum yields, numerical errors also contribute computations of photodissociation rates. The numerical errors arise because either too few 'streams'[2] are used when solving the monochromatic radiative transfer equation, or because the sum over wavelength in Eq. 4.8 is not properly treated. To obtain a fast computer code one wants to use as few streams as possible and solve as few monochromatic radiation problems as possible, by replacing the integral in Eq. 4.8 with the sum of the smallest possible number of terms.

For intensity calculations pertinent to estimating photodissociation rates, only O_2, O_3 and NO_2 are considered[3] as they are the main molecular absorbers in the wavelength region of interest. Hence, only $n(O_2)$, $n(O_3)$ and $n(NO_2)$ enter in the sum for the absorption coefficient β_{abs} in Eq. 2.22. The total air density is used when estimating the scattering coefficient β_{sca} in Eq. 2.23 for Rayleigh scattering. The Rayleigh scattering cross section was calculated using the formula given by Nicolet (1984). For scattering by water clouds the effective radius of the particles and the liquid water content are needed to calculate β_{sca}, see section 3.2.5.

To get a feeling for the behaviour and magnitude of the different photodissociation processes listed in Table 4.1, they are shown in Fig. 4.7 for typical clear sky conditions. The shape of the different photodissociation rate profiles reflects the wavelength dependence of the absorption cross sections and quantum yields entering into Eq. 4.8, and the variation with altitude and wavelength of the mean intensity. For a discussion and explanation of the shapes of the photodissociation rate profiles, see Brasseur and Solomon (1986).

[2] number of streams $= 2N$, where $2N$ is the total number of quadrature points, see Eq. 2.33.

[3] Although NO_2 is indeed a minor species, it absorbs relatively strongly in the region between 357.5 and 407.5 *nm* where O_3 absorption is negligible, and should thus be included, especially for twilight conditions when long pathlengths are encountered.

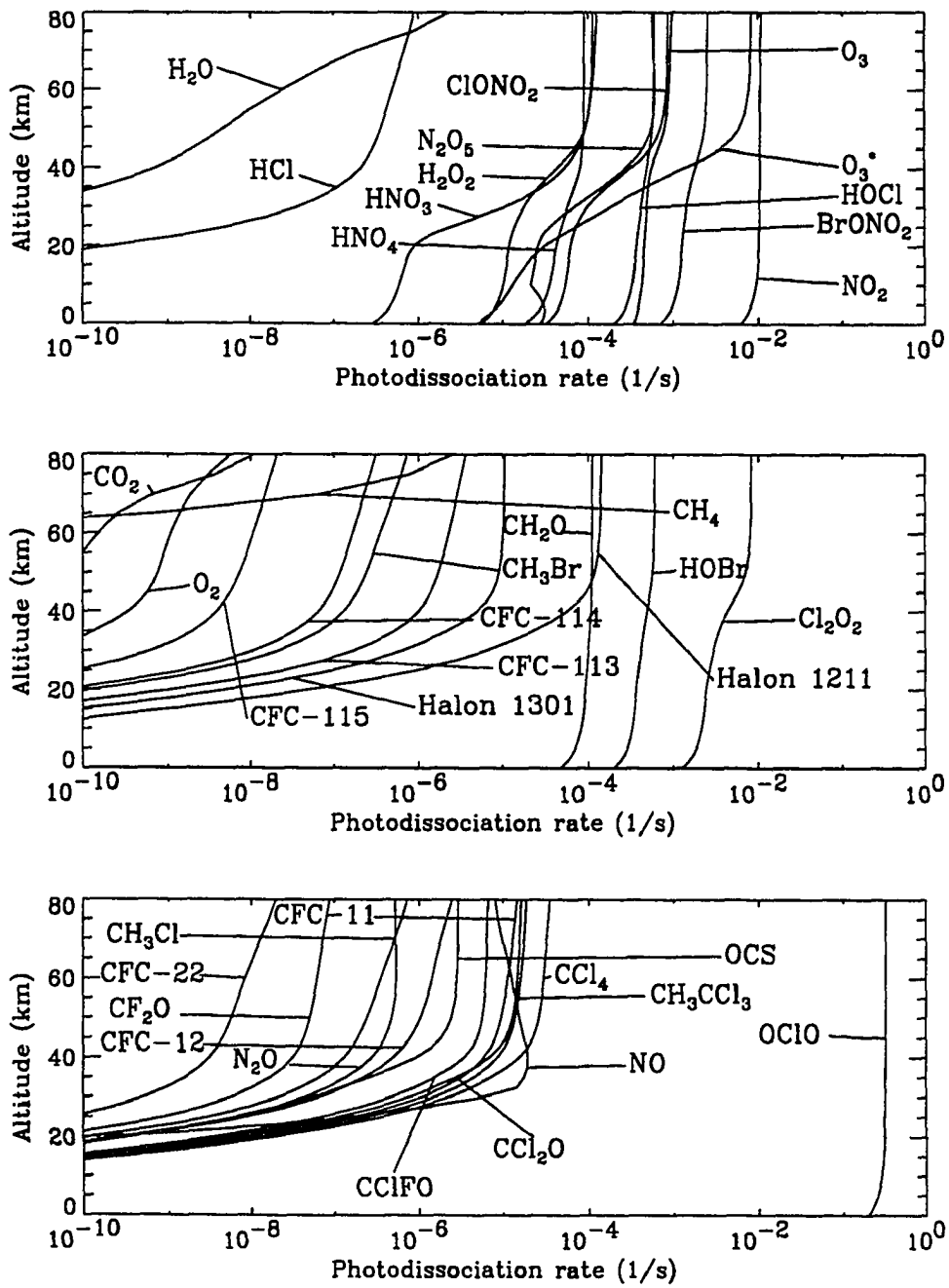

Figure 4.7: Figs. a)-c) show different photodissociation rates for a clear, Rayleigh scattering atmosphere with a solar zenith angle $\theta = 40°$. The density and temperature profiles are taken from the subarctic summer model atmosphere (Anderson et al. 1987) and the ground albedo $A_g = 0.0$.

4.4.1 The accuracy of photodissociation rates with number of streams

From Eq. 4.8 it is seen that the photodissociation rate is given by the integral over wavelength of the product of the the mean intensity and the appropriate cross section and quantum yield. Since as few 'streams' as possible is preferable, the error made by using the smallest possible number of streams, $N = 1$; the two–stream approximation, is investigated. In Fig. 4.8 is presented the mean intensity calculated by the two–stream approximation as a function of wavelength at different altitudes and the relative error as compared with a 16–stream calculation using the DISORT algorithm (Stamnes et al. 1988). The error is largest when the single scattering albedo is close to one throughout the atmosphere, as shown in Fig. 4.9, and at low altitudes where multiple scattering is relatively more important. When integrated over wavelength the error becomes smaller, and due to the product of the cross section and quantum yield, it will be different for each photodissociation process considered. In Fig. 4.10 is shown results for the photodissociation rates $O_3 + h\nu \rightarrow O_2 + O(^3P)$, mostly $\lambda > 310nm$, and $O_3 + h\nu \rightarrow O_2 + O(^1D)$, mostly $\lambda > 310nm$. For the middle atmosphere, errors are less than 3 %, while attaining a maximum of 8 % in the troposphere. The errors will vary with solar zenith angle and ozone concentrations. It is noted, however, that for the example considered here, the error made by the two–stream approximation is less than the combined uncertainty in the cross section and quantum yields, cf. Table 4.1.

Thus, since the two–stream approximation is fastest and the error made when calculating the angle–averaged intensity needed for the photodissociation rates is small, all results below and in the following chapters will be calculated using the two–stream approximation.

4.4.2 The importance of spherical geometry in twilight conditions

For a low sun the effect of the spherical shape of the atmosphere becomes important. For zenith angles less than 75° the atmosphere may be assumed to be plane–parallel. For larger zenith angles the curvature of the earth and its surrounding atmosphere decreases the pathlength that a photon travels as compared with a corresponding plane–parallel atmosphere. This is so because in plane-parallel geometry a $1/\cos\theta$ factor (θ is the zenith angle) is used instead of the Chapman function in Eqs. 2.28 and 2.30. Plane parallel calculations thus overestimates the optical depth of the medium and underestimates the photodissociation rates. Fig. 4.11 exemplifies this effect by showing photodissociation rates for certain molecules; O_2, O_3, O_3^*, NO_2 and CCl_4, calculated in plane–parallel and spherical geometry for twilight conditions. The rightmost column also shows how the rates behave when the sun is below the horizon.

4.5 Summary

An expression has been derived for the photodissociation rate. To calculate photodissociation rates the local intensity is needed. The radiation algorithm developed in this work have been compared with experimental values for the case of Rayleigh scattering. Further measurements are needed of both the direct and the scattered radiation to understand the differences between theory and experiment.

Computational speed and accuracy are important when calculating photodissociation rates. A comparison between 16–stream and 2–stream calculations shows that 2 streams are sufficient for most applications. Finally the importance of including spherical geometry for large solar zenith angles have been demonstrated.

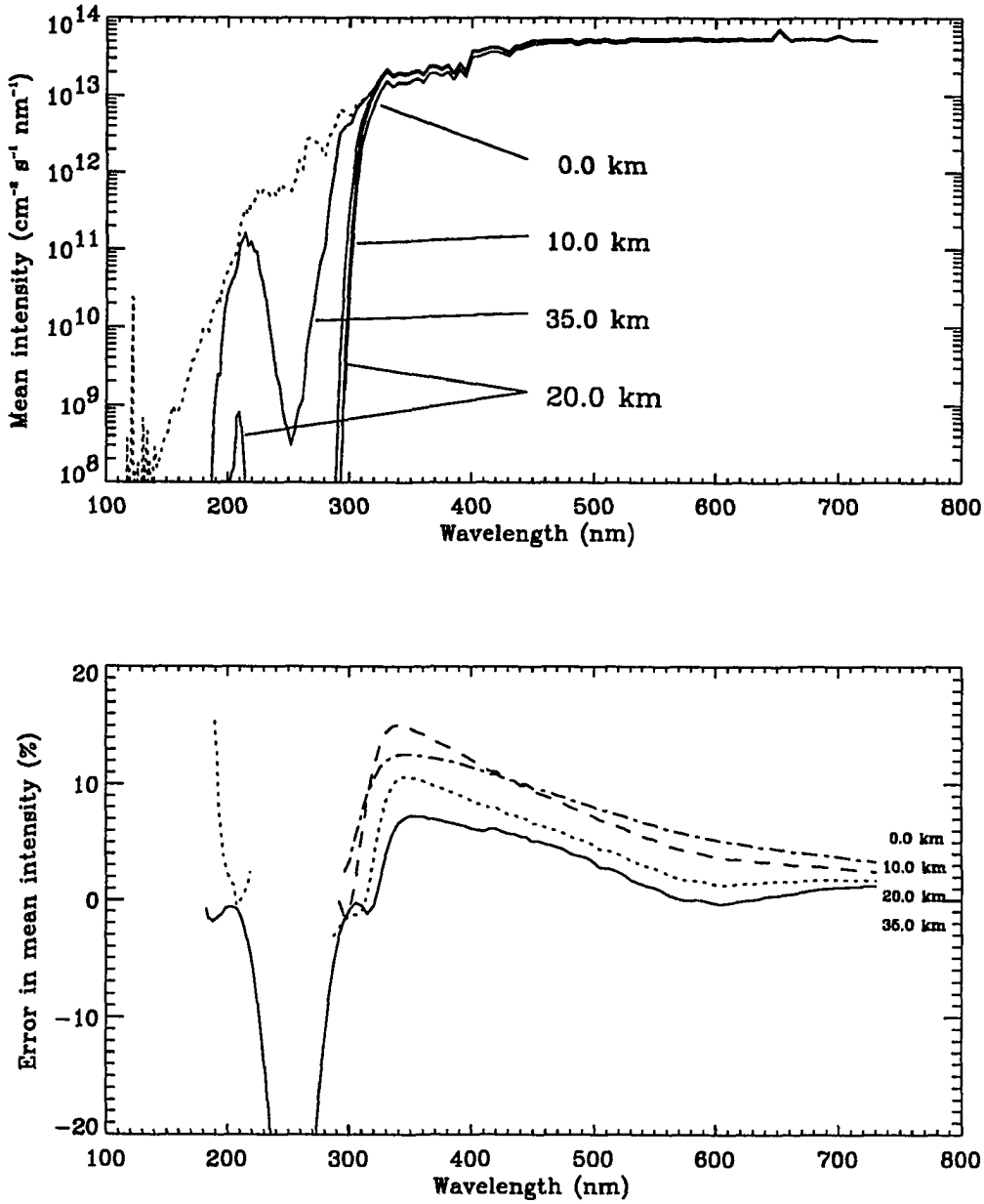

Figure 4.8: The mean intensity at different altitudes and the relative error between the two–stream algorithm and a 16–stream calculation. The dotted line in the top panel is the solar flux incident on the earth's atmosphere. The sub–arctic summer atmosphere (Anderson et al. 1987) was used with a solar zenith angle of 40° and a ground albedo of $A_g = 0.0$.

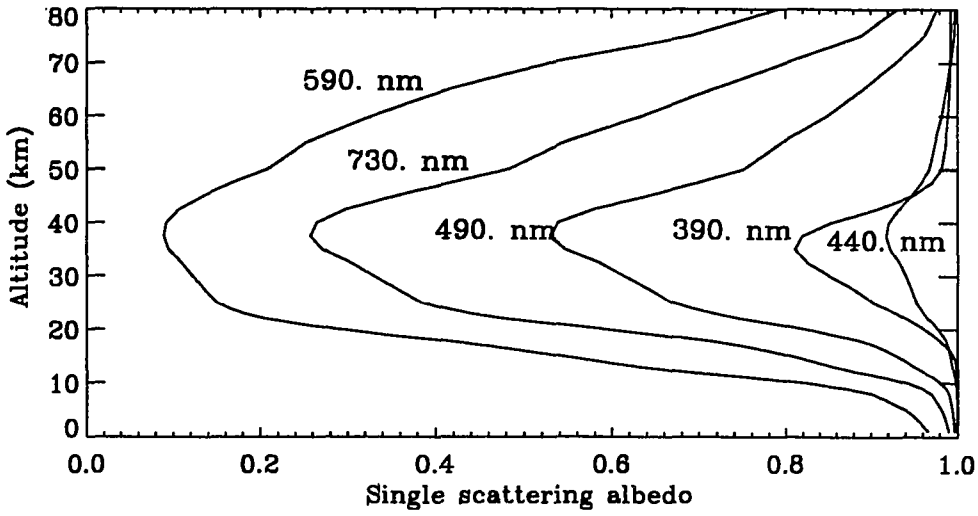

Figure 4.9: The single scattering albedo as a function of altitude for different wavelengths. Same atmospheric conditions as in Fig. 4.8.

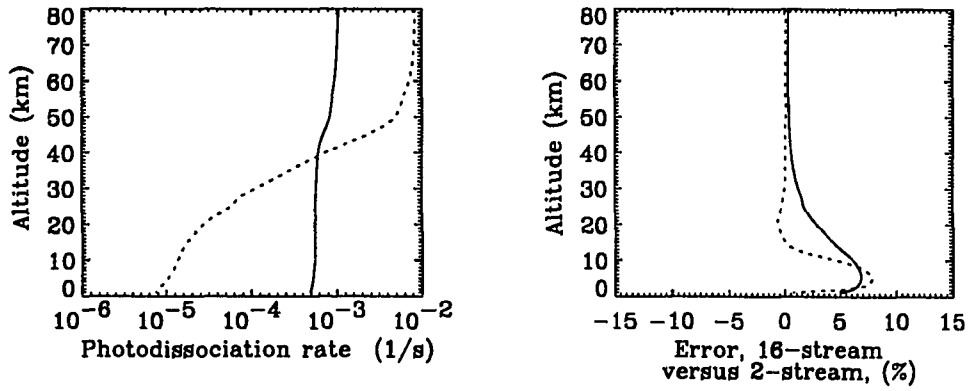

Figure 4.10: Rate coefficients for the processes $O_3 + h\nu \rightarrow O_2 + O(^3P)$ (solid line) and $O_3 + h\nu \rightarrow O_2 + O(^1D)$ (dotted line) as calculated by the 2-stream method together with the error in the rates relative to a 16-stream calculation. The atmospheric conditions are the same as in Fig. 4.8.

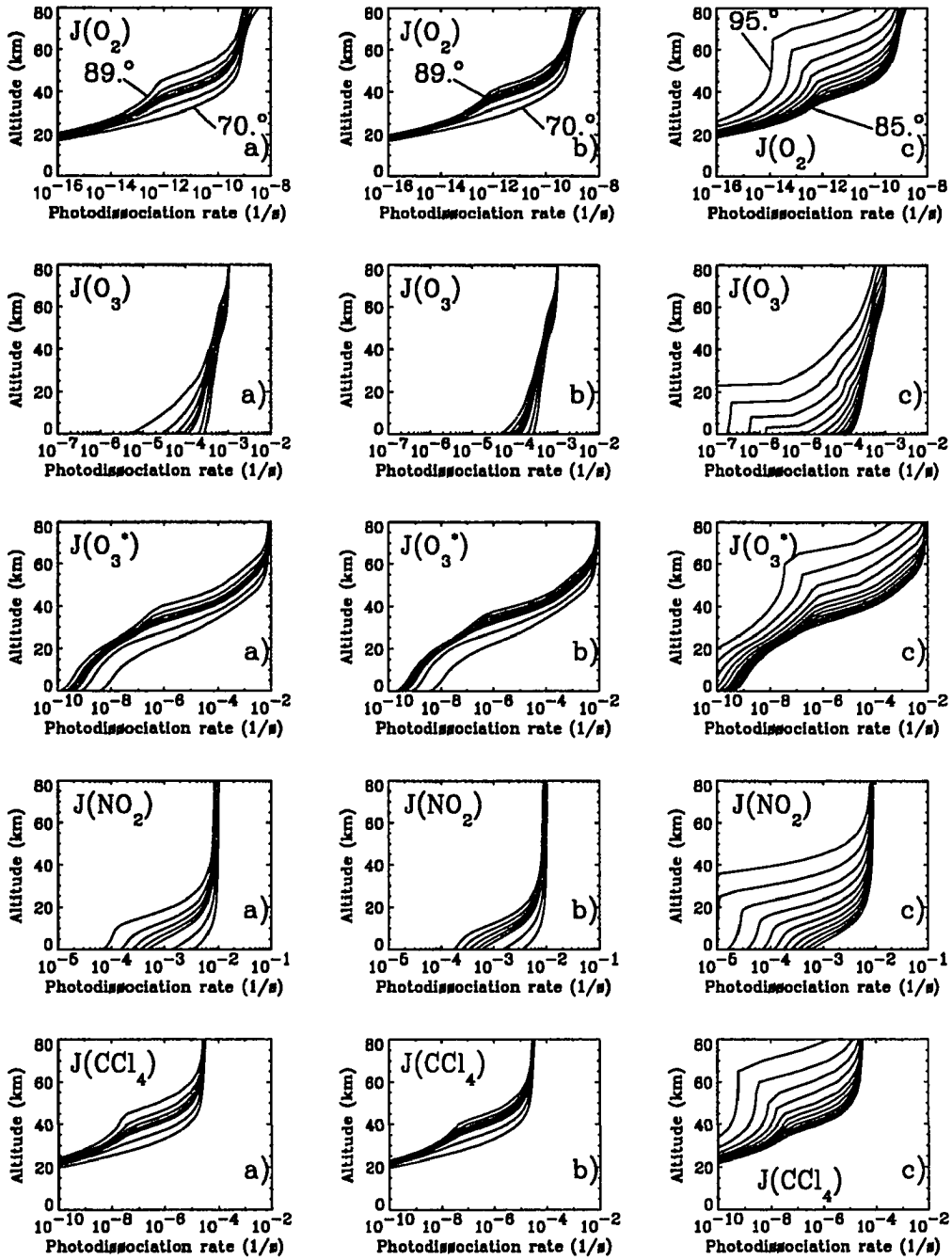

Figure 4.11: a) Photodissociation rates calculated in plane-parallel geometry for solar zenith angles of 70, 80, 85, 86, 87, 88 and 89 degrees. b) shows the same rates in spherical geometry. Finally c) shows results for angles between 85° and 95 ° in 1° steps using spherical geometry. The sub-arctic summer atmosphere (Anderson et al. 1987) was used and the ground albedo is $A_g = 0.0$.

Chapter 5

Biologically active radiation, water cloud effects

The radiation from the sun reaching the earth's surface controls the photosynthetic activity of plants and thus the productivity of all living organisms on land, in the air and the sea. The biological effect of the radiation varies with wavelength, and the intensity at the different wavelengths reaching the ground is determined chiefly by atmospheric processes. Ozone plays a critical role in filtering out most of the harmful UV–radiation incident on the earth's atmosphere. Changes in ozone abundance may therefore influence life on earth due to the associated changes in UV–radiation exposure. Below will first a brief introduction to UV–radiation and its biological effects be given. Next the radiation model developed in preceeding chapters will be used to look at the diurnal variation in biologically effective radiation for different times of the year at high and low latitudes under different atmospheric conditions.

5.1 Introduction

Photosynthetic activity is controlled primarly by visible radiation between 400–700 nm, also called PAR-radiation (Photosynthetic Active Radiation). Radiation of shorter wavelengths, UV–radiation, is of importance because it 1) heats the ground and the middle atmosphere, 2) drives the chemistry of the middle atmosphere and 3) endangers living organisms exposed to high doses, e.g. human skin cancer. UV–radiation is customarily divided into three groups:

- UV–A from 320–400 *nm*. Most of the radiation in this region penetrates to the ground and is normally assumed to be of little harm.

- UV–B labels the region 280–320 *nm*. Some of the radiation in this region reaches the ground and may be harmful. The amount of radiation between 280–320 *nm* that gets to the ground is very sensitive to the total ozone column abundance. In this region the various action spectra, describing relative sensitivity of living organisms to damage by radiation, increase by several orders of magnitude and reach their maximum.

- UV–C is radiation of short wavelengths; 200-280 *nm*. It is lethal for most organisms; however it is entirely absorbed in the atmosphere by ozone and oxygen. UV–C radiation is of great importance for the photochemistry in the middle atmosphere.

The amount of UV–radiation reaching the ground is controlled by atmospheric conditions; ozone absorbs a significant part of it. A decrease in ozone may increase the biologically effective UV–radiation, and hence be harmful to life on earth. The recent ozone loss in Antarctica reported by Farman et al. (1985) gave a new impetus to all kinds of research involving the effects of UV–radiation. For a recent update on research studying the effects of ozone decrease on terrestrial life, the reader is referred to Urbach (1989).

Recent field studies (e.g. Tevini and Teramura (1989) and Bidigare (1989) and references therein), have been performed to learn more about UV–damage. These studies are limited to a few species, and generally no simple conclusions can be drawn as a number of real–life factors tend to destroy 'the ideal experiment' of the reductionist. To quote Smith (1989): 'predictions remain uncertain and estimated effects on natural populations range from insignificant to catastrophic'. However, a stratospheric ozone depletion may not necessarily lead to increased UV–radiation. Brühl and Crutzen (1989) demonstrated that an increase in tropospheric ozone due to industrial NO_x emissions can overcompensate for a stratospheric ozone reduction caused by chlorine catalyzed reactions. It is probably worth noting that increased tropospheric ozone is strongest close to industrial areas, and though it decreases UV–radiation for high sun, it also is most harmful to trees and other living organisms.

A worldwide atmospheric phenomenon that certainly alters the radiation budget at the surface is the presence of clouds. Frederick and Lubin (1988) studied UV–B and UV–A radiation using ozone column measurements from the Nimbus 7 solar backscattered ultraviolet instrument in combination with a two–stream radiation model. They state that 'clouds make the radiation

beneath their bases more isotropic, leading to enhanced absorption by tropospheric ozone.' Tsay and Stamnes (1992) have studied the effect of clouds and aerosols on UV–A and UV–B radiation concluding that, generally, clouds and aerosols provide a shield against UV–radiation, except for low solar zenith angles where both an increase (stratospheric aerosols) and a decrease (arctic haze) may be the result.

Below, the diurnal variation in UV–B, UV–A and PAR for a few selected days for latitudes 26° (e.g. Miami, Florida) and 78° (e.g. Spitsbergen) is studied. Both a clear sky and the presence of water clouds will be investigated for different cloud albedos.

5.2 Model description

To calculate the radiation field at the ground the equation for radiation transport in an atmosphere must be solved. The solution was presented in Chapter 2. Using solar flux data and absorption and scattering properties of atmospheric constituents, as described in Chapters 3 and 4, the biologically active radiation field at the earth's surface for different atmospheric conditions is calculated.

It would be of great interest to also follow the radiation into the ocean and calculate the spectrum at various depths. The air–water interface however, is tricky to model due to the abrupt change in the refractive index across the surface. Efficient and accurate models coupling the radiation field in the air with that in the ocean and including multiple scattering are needed in order to aid the analysis of recent high–resolution underwater spectra (G. A. Hansen 1992). Furthermore, radiation models coupled with biological information will make it possible to assess the influence of UV–radiation on algae production.

The biologically efective dose rate is defined by

$$\frac{dD}{dt} = \int A(\lambda)F(\lambda)d\lambda \tag{5.1}$$

and the dose by

$$D = \int\int A(\lambda)F(\lambda,t)d\lambda dt \tag{5.2}$$

where $F(\lambda,t)$ is the flux at ground level at wavelength λ. The biological action spectrum is denoted by $A(\lambda)$. Examples of typical action spectra (e.g. erythema, plant and DNA) are given by e.g. Setlow (1974), Caldwell et al. (1986), McKinley and Diffey (1987) and reproduced in Tsay and Stamnes (1992). The action spectra increase by several orders of magnitude from 340 *nm* to 280 *nm*. This includes UV–B radiation which is detrimental to plant life (Urbach, 1989).

Each living species has its specific action spectrum. Only action spectra for a few organisms and biological molecules are known, and the uncertainties in the action spectra are not clear (Smith 1989). Thus, instead of calculating biologically effective dose rates as given by Eq. 5.1, UV–A, UV–B radiation and PAR are calculated and the influence of ozone depletion and water clouds on these integrated quantities investigated. Unweighted quantities also have the advantage that they may be directly compared with results of experiments (e.g. these three integrated quantities will be routinely measured at Longyearbyen, Svalbard, in the summer of 1992 [Svenøe, 1992, private communication]).

5.3 Results and discussion

In Figs. 5.1–5.7 diurnal UV–B, UV–A and PAR fluxes, as well as UV–B/PAR, UV–A/PAR and UV–B/UV–A ratios and time–integrated daily UV–B, UV–A and PAR irradiances, for two latitudes, 26°N (e.g. Miami, Florida) and 78° (e.g. Longyearbyen, Svalbard), for the 1st of May, June, July, August and September are presented. The subarctic summer atmosphere (Anderson et al. 1987) was used for the 78° calculations and the midlatitude summer atmosphere for 26°. The water cloud was taken to be 100 m thick starting at 1.9 km, with a constant water content of 0.33 g/m^3 and an effective drop radius of 10 μm. The optical properties of the water cloud were calculated by the parameterization scheme of Hu and Stamnes (1992).

5.3.1 UV–B, UV–A and PAR fluxes

In Figs. 5.1–5.2 is shown the wavelength integrated irradiance Eq. 5.1 with $A(\lambda) = 1$, for the UV–B, UV–A and PAR regions in the case of a 'normal' ozone concentration, 350 DU (Dobson units), and a depleted column of 262.5 DU (25 % depletion). Results for 26° and 78° with a ground albedo of $A_g = 0.2$ are displayed in Fig. 5.1 and with $A_g = 0.95$ in Fig. 5.2. A ground albedo of 0.95, is appropriate for snow cover.

In the low albedo case the UV–B flux at the surface is largest for the clear, ozone depleted atmosphere, Fig. 5.1a, d, g, j, m, in agreement with the conclusions (quoted above) of Frederick and Lubin (1988) and Tsay and Stamnes (1992). The ozone depletion has no effect on the UV–A and PAR regions, as expected from the ozone cross section, Fig. 4.1h. Water clouds are seen to diminish the flux at the ground for low surface albedo. For the high albedo case, $A_g = 0.95$, not considered by Frederick and Lubin (1988) and Tsay and Stamnes (1992), the ozone depleted

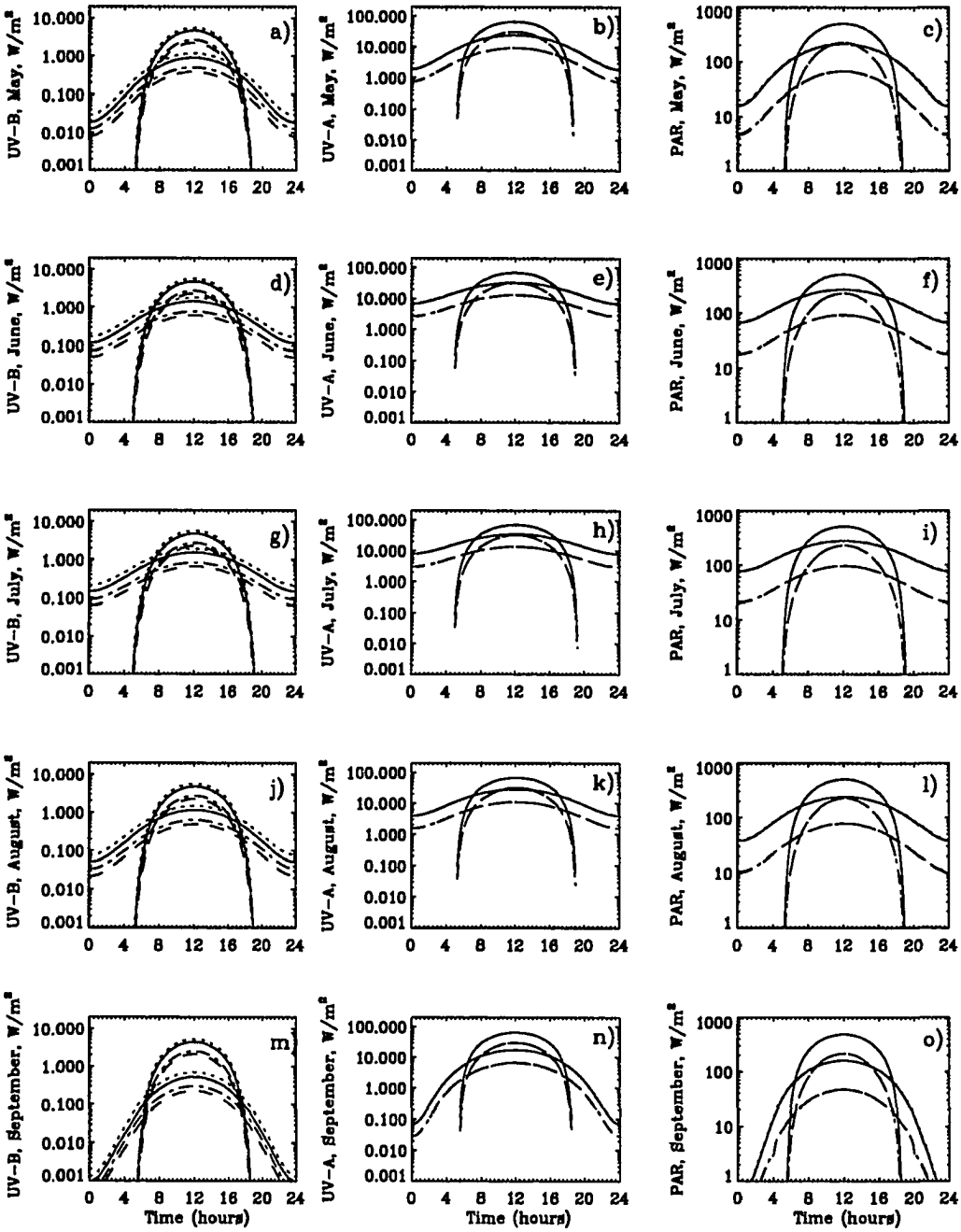

Figure 5.1: UV–B (a, d, g, j, m), UV–A (b, e, h, k, n) and PAR (c, f, i, l, o) for a clear sky with 350.0 DU (solid line), clear sky with 262.5 DU (dotted line), water cloud with 350.0 DU (dashed line) and water cloud with 262.5 DU (dash-dotted line). Results for the 1st of May (a, b, c), June (d, e, f), July (g, h, i), August (j, k, l) and September (m, n, o) are displayed for 26° N and 78° N. The ground albedo is $A_g = 0.2$.

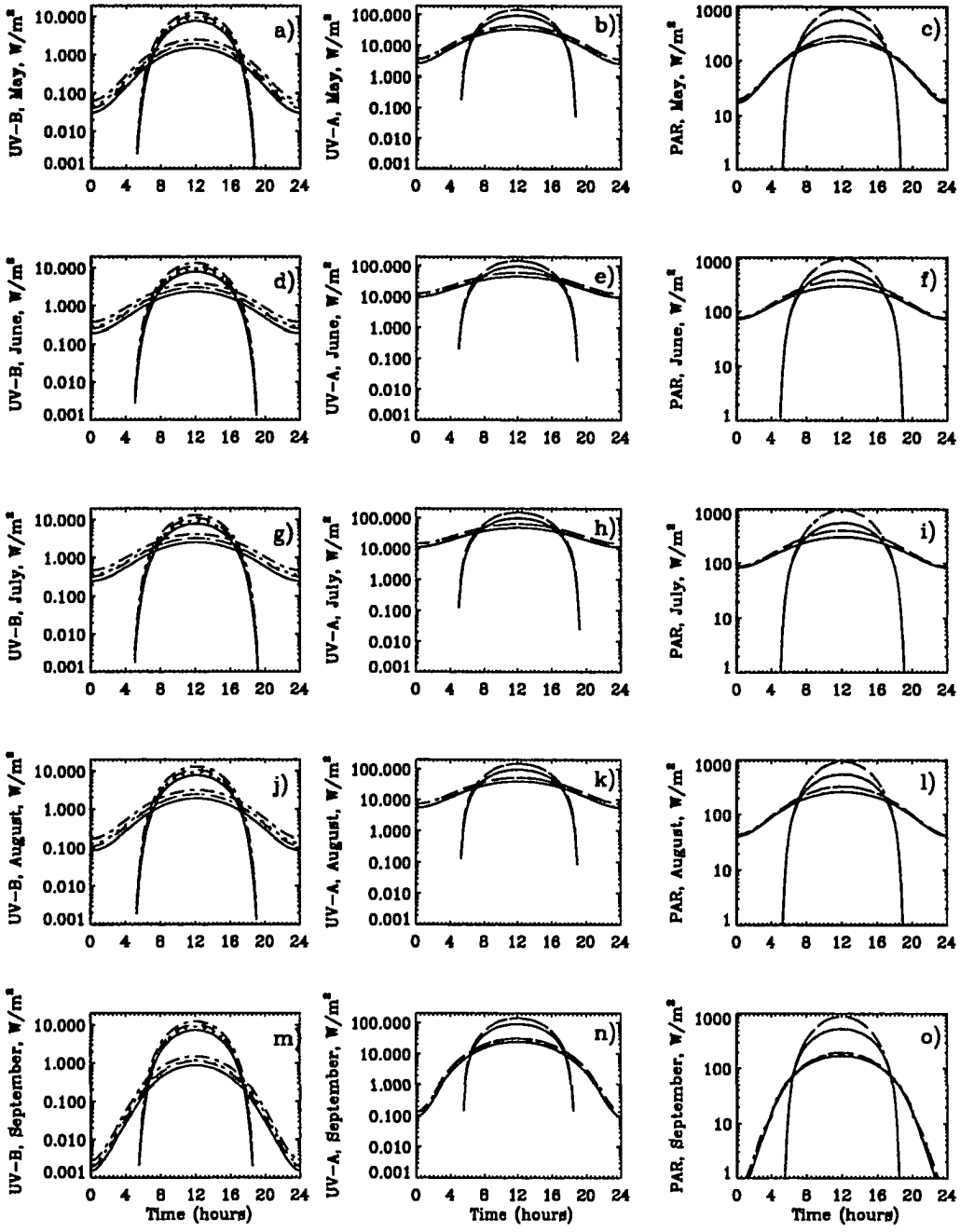

Figure 5.2: UV–B (a, d, g, j, m), UV–A (b, e, h, k, n) and PAR (c, f, i, l, o) for a clear sky with 350.0 DU (solid line), clear sky with 262.5 DU (dotted line), water cloud with 350.0 DU (dashed line) and water cloud with 262.5 DU (dash-dotted line). Results for the 1st of May (a, b, c), June (d, e, f), July (g, h, i), August (j, k, l) and September (m, n, o) are displayed for 26° N and 78° N. The ground albedo is $A_g = 0.95$.

atmosphere including a water cloud gives the highest flux for all radiation regions considered. This is due to multiple reflections of radiation between the ground and the cloud.

Dahlback et al. (1989) looked at the effective UV–dose rate as a function of time during the day for 40° N and 60° N for June 22 and August 22. They concluded that 'the dose rate differences with latitude disappear and even become reversed early in the morning and late in the afternoon.' A similar behaviour is seen in the modelled data for 26° where the sun goes below the horizon, Figs. 5.1–5.2. For latitudes where the sun sets, the solar zenith angle will attain the same values around sunrise and sunset, but at different times of the day. Hence, for otherwise identical conditions, a local zenith angle of e.g. 85 degrees, will at 40° and 60° N give the same radiation dose rates. Obviously, as concluded by Dahlback et al. (1989) and as seen in Figs. 5.1–5.2, for high latitudes with longer days, the radiation dose rates will be higher than at lower latitudes for similar times of the day. The reason is that in the summer season the sun rises earlier and sets later at higher latitudes.

5.3.2 UV–B/PAR, UV–A/PAR and UV–B/UV–A ratios

Figs. 5.3–5.6 display the UV–B/PAR, UV–A/PAR and UV–B/UV–A ratios. 'These ratios provide a measure of the energy available for UV–B damage to that available for photorepair and/or photosynthesis', Smith and Baker (1989). Results for 26° N are shown in Figs. 5.3–5.4 with albedos of $A_g = 0.2$ and $A_g = 0.95$, respectively, and for 78° N in Figs. 5.5–5.6 with albedos $A_g = 0.2$ and $A_g = 0.95$.

It is first noted that the UV–A/PAR ratio is not affected by ozone variations as expected. Furthermore the UV–A/PAR ratio shows a very rapid decrease (increase) around sunrise, just before 6 hours Figs. 5.3–5.4, (sunset) for 26° N. This is due to the long pathlengths encountered under twilight conditions and the corresponding relative increase in the UV–A radiation due to Rayleigh scattering. Similar behaviour is seen in experimental data from Tromsø, Norway, 69° N, around sunset and sunrise (T. Svenøe 1992, private communication). For 78° N the sun is above the horizon 24 hours a day for the dates considered here. The UV–A/PAR ratio is largest for low solar elevations in the presence of water clouds whereas the clear sky ratio has a maximum at midday at solstice. The variations are less pronounced at 78° than at 26° N.

Secondly it is noted that the water cloud gives a higher UV–A/PAR ratio than the clear sky for all situations except the unrealistic case of a ground albedo of 0.95 at 26° N, Fig. 5.4. This is due to multiple scattering of the cloud and the wavelength dependence of the Rayleigh scattering cross

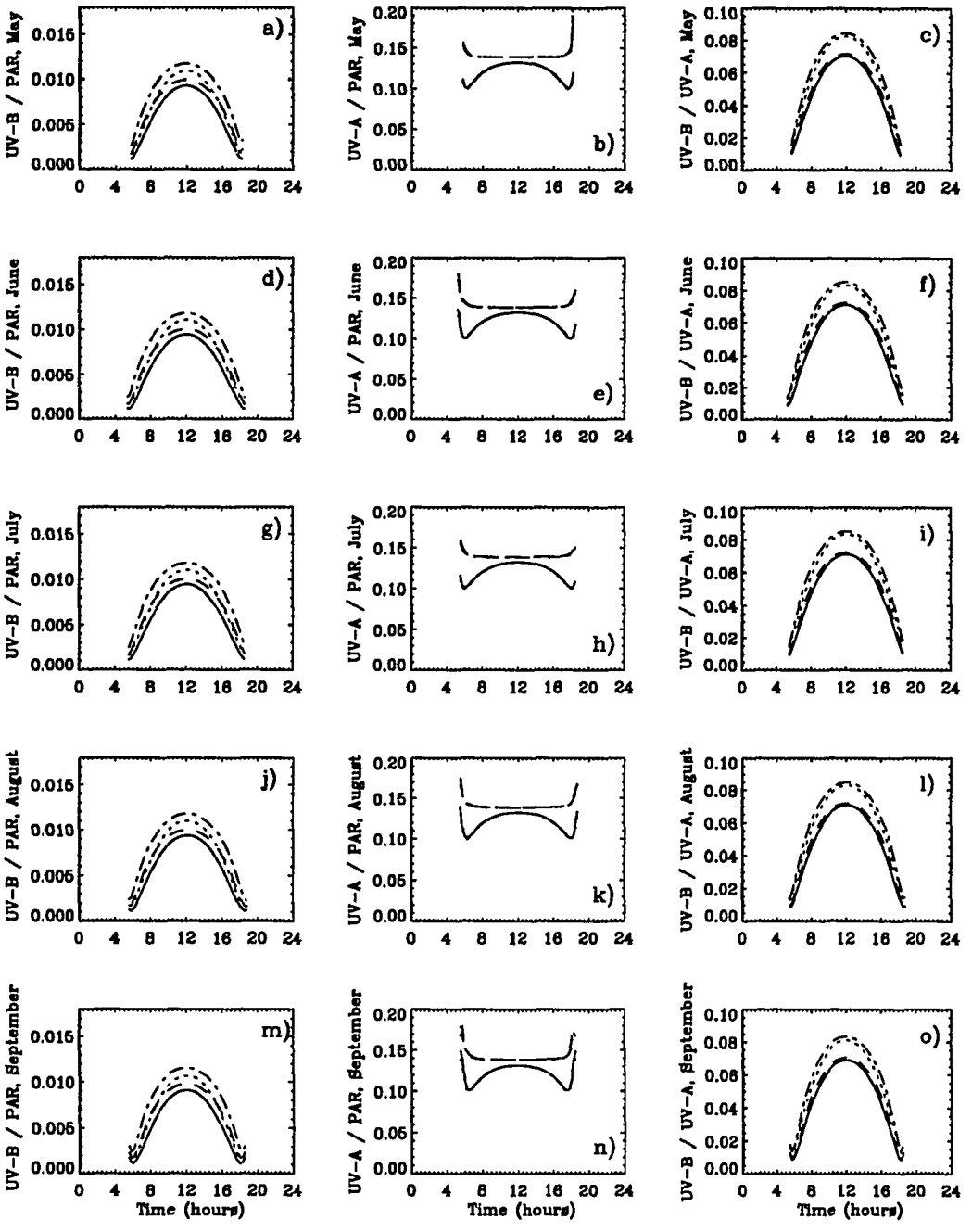

Figure 5.3: UV-B/PAR (a, d, g, j, m), UV-A/PAR (b, e, h, k, n) and UV-B/UV-A (c, f, i, l, o) for a clear sky with 350.0 DU (solid line), clear sky with 262.5 DU (dotted line), water cloud with 350.0 DU (dashed line) and water cloud with 262.5 DU (dash-dotted line). Results for the 1st of May (a, b, c), June (d, e, f), July (g, h, i), August (j, k, l) and September (m, n, o) are displayed for 26° N. The ground albedo is $A_g = 0.2$.

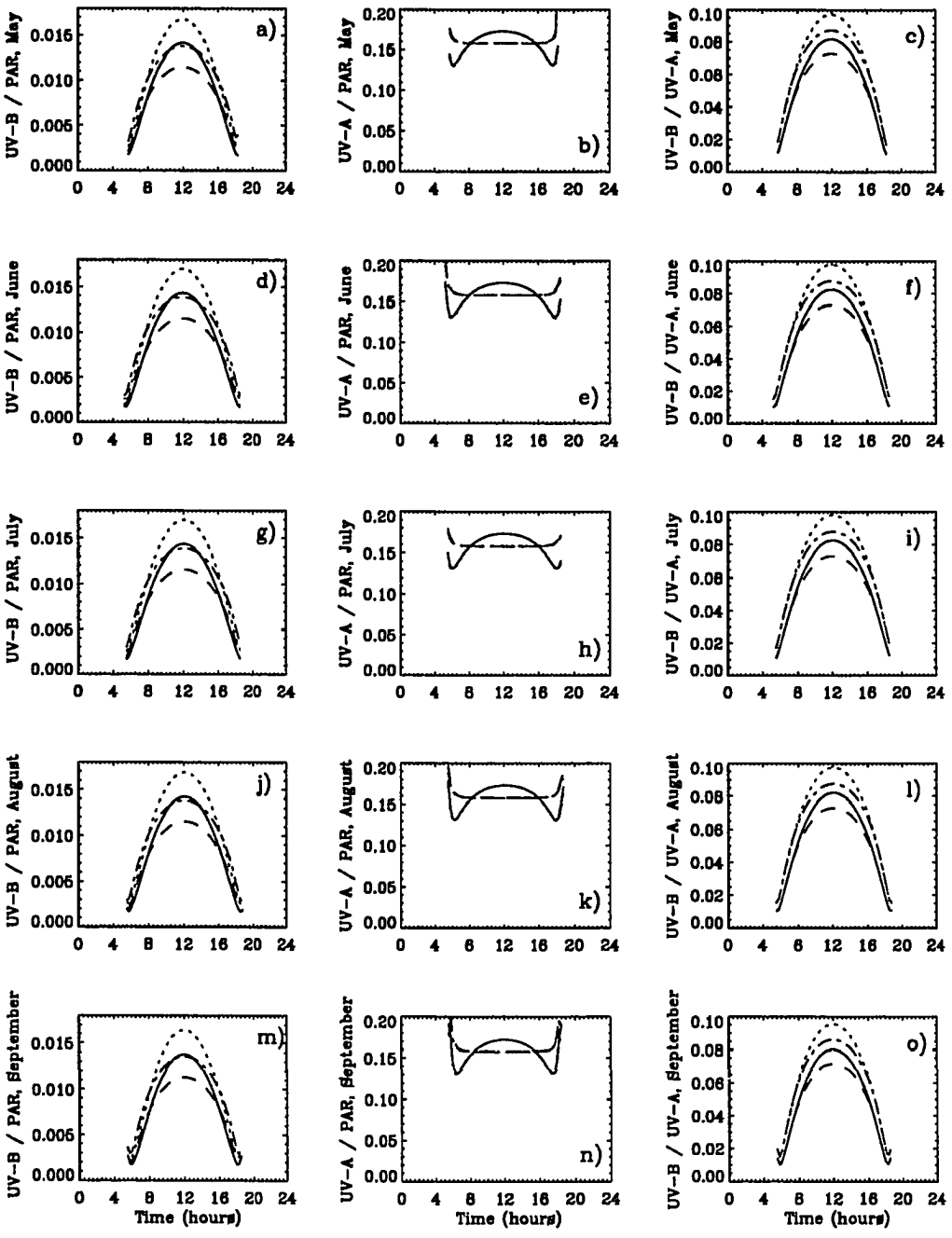

Figure 5.4: UV–B/PAR (a, d, g, j, m), UV–A/PAR (b, e, h, k, n) and UV–B/UV–A (c, f, i, l, o) for a clear sky with 350.0 DU (solid line), clear sky with 262.5 DU (dotted line), water cloud with 350.0 DU (dashed line) and water cloud with 262.5 DU (dash-dotted line). Results for the 1st of May (a, b, c), June (d, e, f), July (g, h, i), August (j, k, l) and September (m, n, o) are displayed for 26° N. The ground albedo is $A_g = 0.95$.

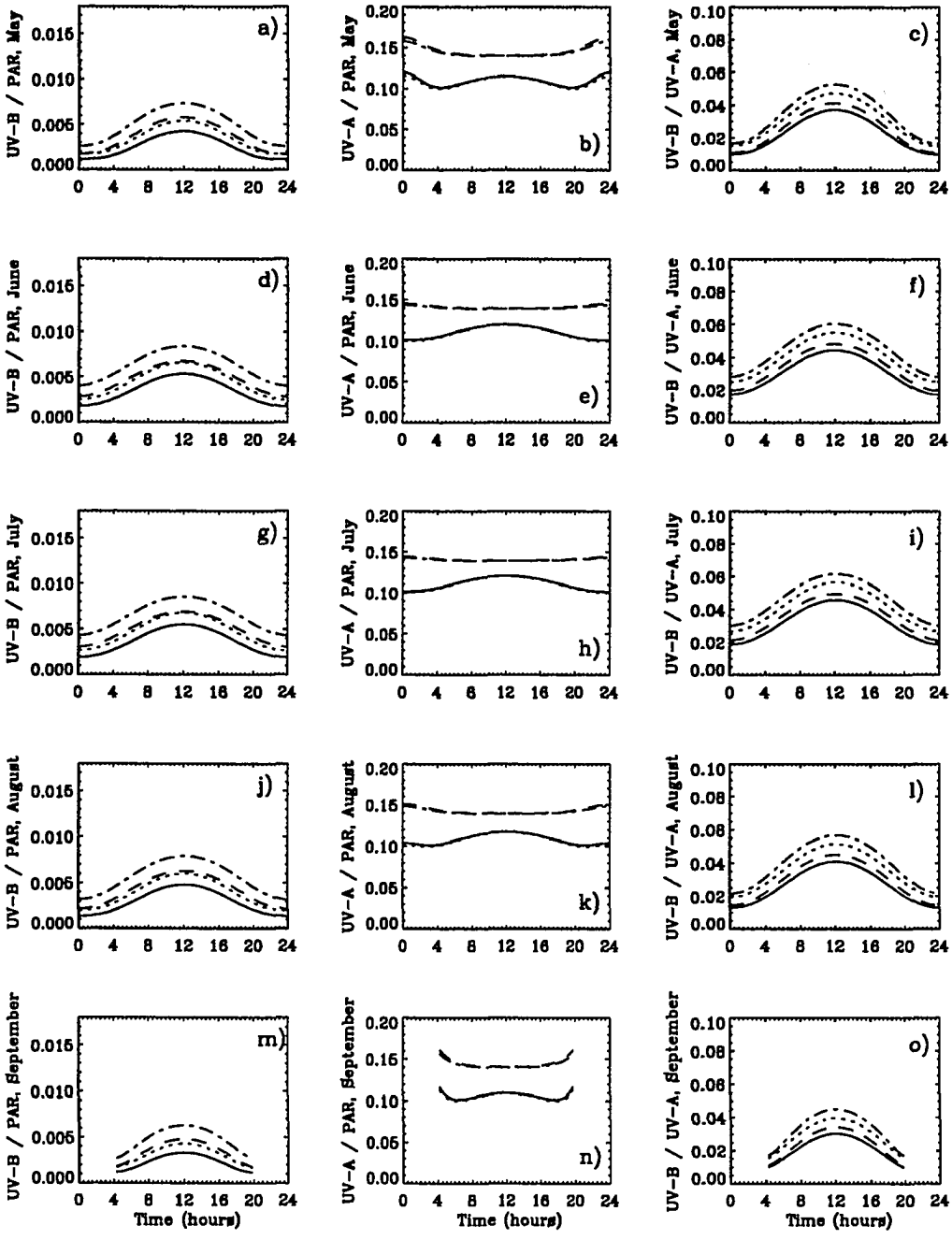

Figure 5.5: UV–B/PAR (a, d, g, j, m), UV–A/PAR (b, e, h, k, n) and UV–B/UV–A (c, f, i, l, o) for a clear sky with 350.0 DU (solid line), clear sky with 262.5 DU (dotted line), water cloud with 350.0 DU (dashed line) and water cloud with 262.5 DU (dash-dotted line). Results for the 1st of May (a, b, c), June (d, e, f), July (g, h, i), August (j, k, l) and September (m, n, o) are displayed for 78° N. The ground albedo is $A_g = 0.2$.

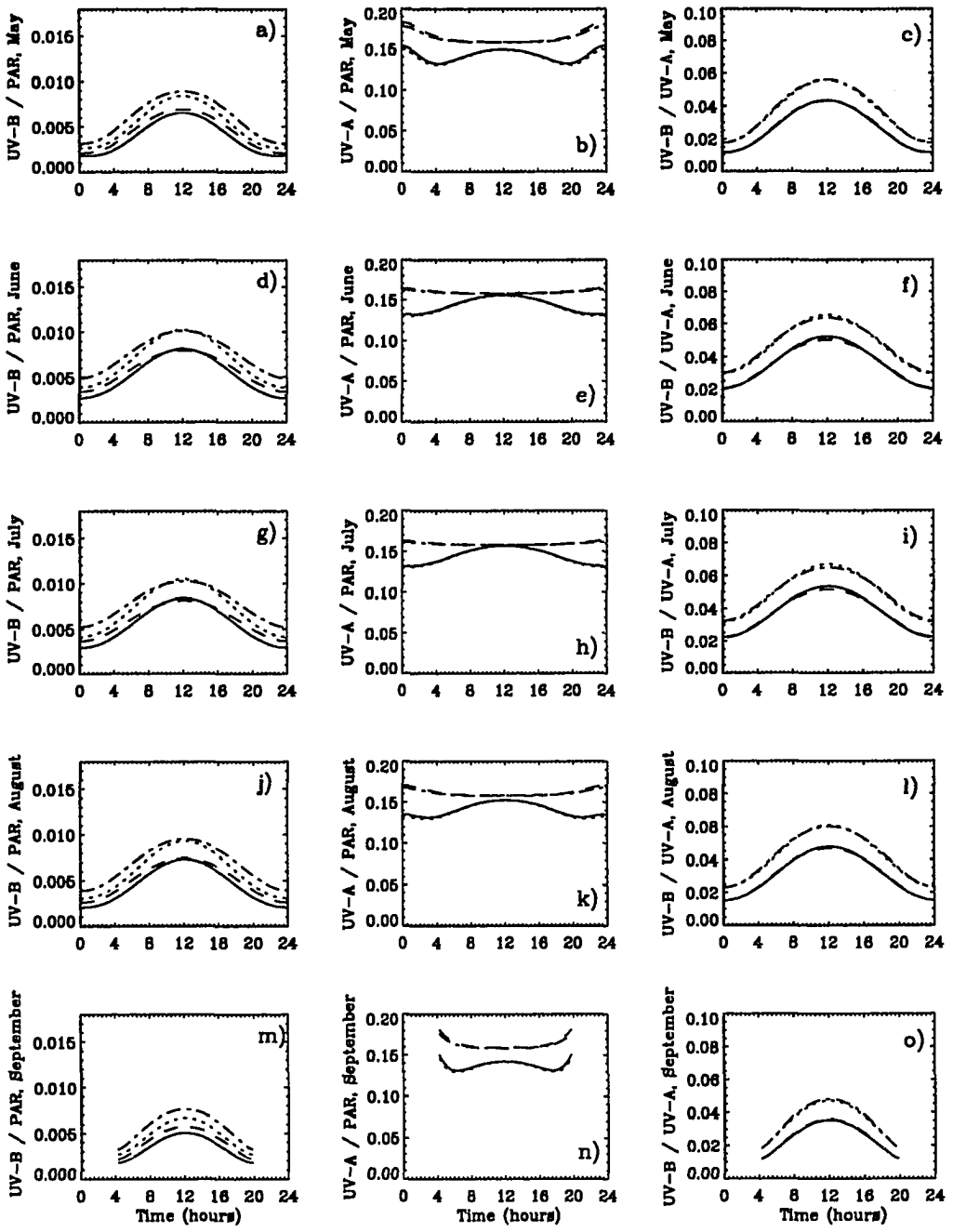

Figure 5.6: UV–B/PAR (a, d, g, j, m), UV–A/PAR (b, e, h, k, n) and UV–B/UV–A (c, f, i, l, o) for a clear sky with 350.0 DU (solid line), clear sky with 262.5 DU (dotted line), water cloud with 350.0 DU (dashed line) and water cloud with 262.5 DU (dash-dotted line). Results for the 1st of May (a, b, c), June (d, e, f), July (g, h, i), August (j, k, l) and September (m, n, o) are displayed for 78° N. The ground albedo is $A_g = 0.95$.

section. The shapes of the water cloud and clear sky UV–A/PAR ratios are markedly different and may be used as an aid to determine cloud conditions.

The effect of ozone depletion is readily seen in the UV–B/PAR ratio. For the situations in Fig. 5.3–5.6, the UV–B/PAR ratio is largest for the ozone depleted case due to the fact that more UV–B radiation reaches the ground for lower ozone concentrations. For 26° N and a ground albedo $A_g = 0.2$, the UV–B/PAR ratio is largest for the ozone depleted overcast sky, Fig 5.3. The same behaviour is seen at 78° for both high and low albedos, Figs. 5.5–5.6. An exception occurs for the high albedos at 78° N where the UV–B/PAR ratio for the overcast sky is lower than the ozone depleted clear sky in the middle of the day around solstice, Fig. 5.6g. For a high albedo and middle latitude the ozone depleted clear sky gives the highest UV–B/PAR ratio, Fig. 5.4. PAR is larger for the water cloud case than the clear sky case when the albedo is high, compare Figs. 5.1 and 5.2. This is due to multiple reflections between the surface and the cloud. The increase in PAR varies with solar zenith angle and is largest for high albedos and low latitudes. A similar behaviour is seen for UV–A and UV–B radiation, but it is smaller in magnitude, due to ozone absorption of UV–A and UV–B, thus decreasing the effect of multiple reflections between the ground and the cloud. Hence the UV–B/PAR ratio for the water cloud case is lower than the clear sky results for low latitudes and high albedos.

The UV–B/UV–A ratio is also sensitive to ozone concentration since UV–B is strongly absorbed by ozone while UV–A is relatively little affected by ozone. For a high albedo the clear sky UV–B/UV–A ratio is largest, Figs. 5.4 and 5.6, while for a low albedo the overcast sky yields the highest UV–B/UV–A ratio. It is noted that a high albedo yields higher UV–B/PAR, UV–A /PAR and UV–B/UV–A ratios than a low albedo.

It may thus be summarized that ozone depletion will increase the amount of harmful UV–B relative to UV–A and PAR for photorepair and/or photosynthesis. Water clouds may further increase the relative amount of UV–B at the surface.

For the different ratios at 26° N little if any variation from month to month is seen for the time period covered. At 78° N there is a distinct difference in the magnitude and shape of the ratio curves.

5.3.3 Daily UV–B, UV–A and PAR irradiances

In Figs. 5.7 a–f and Figs. 5.7 g–l is displayed the daily integrated UV–B, UV–A and PAR irradiances. It is seen that around solstice the radiation exposure, i.e. the time integral of the

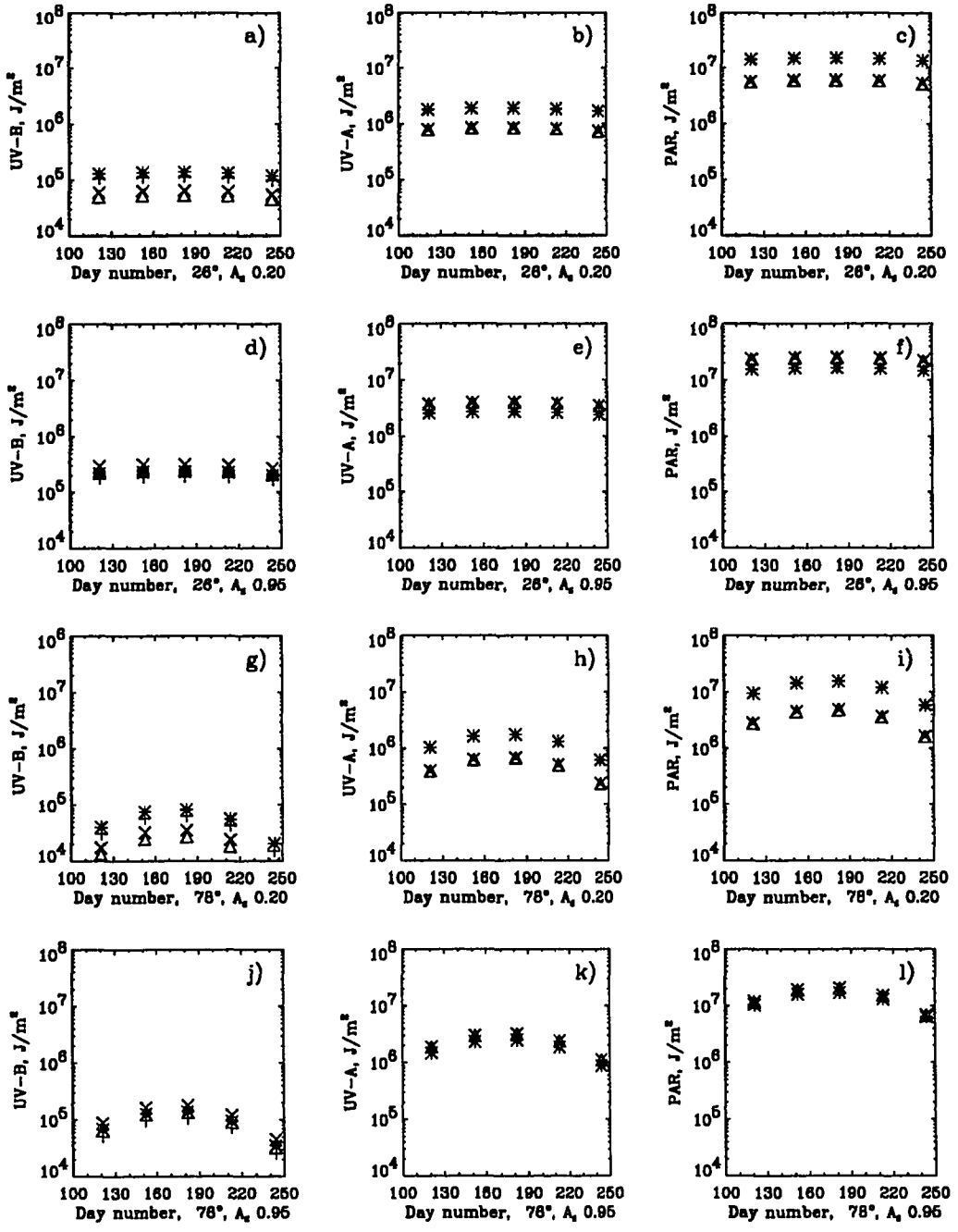

Figure 5.7: UV–B (a, d, g, j), UV–A (b, e, h, k) and PAR (c, f, i, l) doses for a clear sky with 350.0 DU (plus), clear sky with 262.5 DU (asterisk), water cloud with 350.0 DU (triangle) and water cloud with 262.5 DU (×). Results at latitudes 26° N (a–f) and 78° N (g–l) with ground albedos 0.20 (a–c, g–i) and 0.95 (d–f, j–l) are displayed.

irradiances, Eq. 5.2 with $A(\lambda) = 1$, at the ground is only slightly less at high latitudes than at low latitudes. This suggests that living organisms at high latitudes are able to cope with radiation exposure, including UV, comparable to those experienced at low latitudes. However, at low latitudes a relatively short exposure with high intensity is present, whereas in the polar regions the intensity is significantly lower and the exposure time longer (e.g. 24 hours a day around solstice). Thus, even if radiation doses are comparable in magnitude, this does not necessarily imply that polar organisms could cope with the radiation levels at noon at lower latitudes.

While the daily radiation dose varies little at low latitudes from month to month, it may vary by more than a factor of 3 at high latitudes. Calkins and Thordardottir (1980) suggest that the current levels of damaging UV–B radiation are an already occurring natural stress for phytoplankton communities. Protection against UV–radiation requires energy and thus reduces the resources available for other purposes. While the stress to organisms at low latitudes is fairly constant, the stress at high latitudes varies dramatically over the year. Thus plankton in the polar regions need less UV–protection in the spring than summer unless there is an ozone hole. Since protective mechanisms require energy it is possible that the ability of plankton in the polar regions to protect itself varies throughout the growing season, contrary to plankton at low latitudes which experiences similar radiation levels all year long. Generally speaking, an increase in harmful UV–B radiation may cause increased damage to exposed organisms. Protective mechanisms need time to build up, thus, for organisms living in an environment where the UV–B dose changes rapidly from day to day, such as around the breakup of the polar vortex during the Antarctic spring, ozone depletions may be harmful. Also, the 'life–time' for evolution ('growth') of an organism and its tolerance to UV exposure at different stages in its evolution is important, e.g. increased UV exposure during an ice–edge bloom could be detrimental.

Finally, it is noted that 'the extreme change in ozone associated with an ozone hole, produces a sharp gradient which creates a UV–B front analogous to an oceanic front. Comparative studies of UV–B effects across this front may provide a natural laboratory for direct observation of the impact of UV–B on natural phytoplantkon communitites', Smith and Baker (1989).

5.4 Summary

UV–B, UV–A and PAR have been calculated for high and low latitudes for different ground albedos and atmospheric conditions. An ozone depletion will increase the amount of UV–B radiation

detrimental to life. Water clouds will diminish UV–B, UV–A and PAR for low albedos, while for high albedos water clouds increase the amount of radiation reaching the ground. The relative amount of harmful UV–B is increased on an overcast day, the increase being largest at high latitudes and for small ground albedos. The daily radiation doses vary little at low latitudes from month to month, but by more than a factor of 3 at high latitudes due to the change in the length of the day at high latitudes.

Chapter 6

Warming/cooling rates

The solar warming and terrestrial cooling of the atmosphere are directly and indirectly responsible for the atmospheric temperature structure. Accurate knowledge of the temperature structure is important since many chemical reactions occur at temperature dependent rates and since the temperature structure, in part, determines the dynamical behavior of the atmosphere. Thus, in realistic chemistry/transport/radiation models of the atmosphere, accurate and fast computation of warming/cooling rates are required. In this chapter the warming/cooling rate is defined first and next it is discussed how it can be accurately and efficiently calculated for a realistic inhomogenous atmosphere. Finally the warming and cooling rates due to the major absorbing species are discussed.

6.1 Definition of warming/cooling rates

The rate h_λ at which heat (energy) is gained by matter from radiation at wavelength λ equals the negative of the divergence of the energy flux through a volume of the matter

$$h_\lambda = -\nabla \cdot F_\lambda. \tag{6.1}$$

For a layered atmosphere

$$\nabla \cdot F_\lambda = \frac{\partial F_\lambda}{\partial z} = \frac{\partial \tau_\lambda}{\partial z}\frac{\partial F_\lambda}{\partial \tau_\lambda} = 4\pi(1-\omega)(\overline{I_\lambda} - B_\lambda)\frac{\partial \tau_\lambda}{\partial z} \tag{6.2}$$

by Eq. 2.95. Assuming that the atmosphere behaves like an ideal gas the first law of thermodynamics (Wallace and Hobbs, 1977) may be written as

$$h_\lambda dt = \rho_m c_p dT - dp \tag{6.3}$$

where c_p is the specific heat of air at constant pressure and dt an infinitesimal time interval. The air density ρ_m has been given the subscript m to emphasize that it is the mass density that is to be used when calculating warming/cooling rates. Dividing by dt and expanding the total derivative

$$\frac{d}{dt} = \frac{\partial}{\partial t} + \mathbf{v} \cdot \nabla \tag{6.4}$$

Eq. 6.3 may be written as

$$\frac{\partial T}{\partial t} = \frac{h_\lambda}{c_p \rho_m} + d \tag{6.5}$$

where the dynamic warming/cooling rate is

$$d = \frac{1}{c_p \rho_m} \left(\frac{\partial p}{\partial t} + \mathbf{v} \cdot \nabla p \right) - \mathbf{v} \cdot \nabla T. \tag{6.6}$$

In view of Eqs. 6.1, 6.2 and 6.5 the monochromatic warming/cooling rate due to radiation may thus be written as

$$\frac{\partial T}{\partial t} = \frac{h_\lambda}{c_p \rho_m} = -\frac{4\pi}{c_p \rho_m}(1-\omega)(\overline{I_\lambda} - B_\lambda)\frac{\partial \tau_\lambda}{\partial z}. \tag{6.7}$$

The mean intensity $\overline{I_\lambda}$ in Eq. 6.7 is given by (see also chapter 2)

$$\overline{I(\tau,\lambda)} = \frac{1}{4\pi} \int_0^\pi \int_{-1}^1 I(\tau,\mu,\phi,\lambda) d\mu d\phi \tag{6.8}$$

The total (integrated) heating rate h is obtained by integration of h_λ over all wavelengths

$$h = \int_0^\infty h_\lambda d\lambda. \tag{6.9}$$

Since h is in energy units it is called a heating rate, and the term warming/cooling rates is reserved to quantities with temperature units, i.e. $\partial T/\partial t$ (Stamnes and Tsay 1990).

Depending on the problem, either the dynamic or the radiative or both warming/cooling rates must be accounted for in climatic and photochemical models of the atmosphere. The magnitude of the radiative warming/cooling rate may be calculated from radiation models as the one presented in this work. The dynamic warming/cooling rate is calculated by solving the Navier–Stokes equation. The dynamic warming/cooling rate or the radiative warming/cooling rate or both determine the temperature structure of the atmosphere. Letting let[1] $\tau_{dyn,Q}$ denote the $1/e$ response time of the atmosphere to a change in the dynamical warming/cooling and τ_{rad} a corresponding radiative timescale, one may distinguish between three cases:

[1]The subscript Q on $\tau_{dyn,Q}$, is used to distinguish the response time of the atmosphere to changes in the dynamical heating from the transport lifetime, τ_{dyn}, introduced in Chapter 4. Thus $\tau_{dyn,Q}$ is an indicator of the dynamical forcing of atmospheric motions while τ_{dyn} describes the lifetimes of the motions.

- $\tau_{rad} \ll \tau_{dyn,Q}$. In this case the atmosphere will be in radiative equilibrium. Regions that are in near radiative equilibrium in the atmosphere are the tropical and subtropical stratosphere. It is also noted that one dimensional radiative–convective models (e.g. Ramanathan 1976) assume that the stratosphere is in radiative equilibrium.

- $\tau_{rad} \gg \tau_{dyn,Q}$. Dynamical processes will in this case dominate the warming/cooling. Examples are the upper mesosphere where gravity wave breaking provides dynamical forcing, and the lower troposphere where radiation plays an insignificant role in short term weather patterns.

- $\tau_{rad} \sim \tau_{dyn,Q}$. In this case both dynamical and radiative forcing is of importance. Problems involving general circulation in the atmosphere should include both dynamical and radiative warming /cooling. Depending on latitude, longitude, altitude and season either one or the other or both influence the circulation.

In the lower stratosphere and below, the radiative timescale is 80–100 days or more (Kiehl and Solomon 1986, Ramanathan et al. 1983). The timescale varies with latitude in the lower stratosphere, with a maximum at the equator. The poleward decrease in the radiative timescale is due to the temperature dependent absorption coefficients of CO_2, O_3 and H_2O. The radiative timescale has a minimum at the mesopause, $\tau_{rad} \sim 5 - 10$ days, and then increases at higher altitudes. The dynamical timescale in the stratosphere is of the order of weeks and decreases in the upper mesosphere to a day or so due to gravity wave breaking (Brasseur and Solomon 1986, Andrews, Holton and Leovy 1987). Further discussions on the dynamical and radiative warming/cooling rates and their relative importance for different applications may be found in Goody and Yung (1989), Brasseur and Solomon (1986) and Andrews, Holton and Leovy (1987).

Typically, warming/cooling rates exhibit a Chapman layer structure. For monochromatic radiation in an isothermal, well–mixed gas, i.e the gas is in hydrostatic equilibrium, this may be demonstrated by noting that for radiation from the sun at $\theta_0 = \cos^{-1}\mu_0$ (the argument for thermal radiation is similar)

$$\frac{\partial F}{\partial \tau}\frac{\partial \tau}{\partial z} \propto e^{-\tau(z)/\mu_0} e^{-z/H}. \tag{6.10}$$

Here $H = kT/mg$, g is the gravitational acceleration and m the air mass. The total optical depth is $\tau_0 = \sigma n_0 H/\mu_0$ and hence $\tau(z) = \tau_0 \exp(-z/H)$ since $n(z) = n_0 \exp(-z/H)$. The warming rate

is thus proportional to

$$\frac{\partial T}{\partial t} \propto e^{-(\tau_0 e^{-z/H}+z/H)} \tag{6.11}$$

which has a maximum at

$$z_m = H \ln \tau_0 = H \ln(H\sigma n_0/\mu_0). \tag{6.12}$$

Eq. 6.11 describes the Chapman layer structure (Chapman 1931).

6.2 Cooling rates

In chapter 2 the monochromatic mean intensity $\overline{I(\tau,\lambda)}$ in an absorbing, emitting and scattering layered atmosphere was derived. The integration over wavelength in Eq. 6.9 poses another problem. For the UV and visible part of the spectrum averaged cross sections are available (WMO 1986) for the principal absorbers, O_3, NO_2 and O_2, and the integral over wavelength in Eq. 6.8 may be replaced by a sum with not too many terms, see chapter 4 and below. For the solar near infrared and the terrestrial infrared, the absorption cross sections vary rapidly, erratically and by several orders of magnitude with wavelength, see e.g. Fig. 3.1 and Park et al. (1987). To resolve the finest Doppler broadened absorption lines in the middle atmosphere[2], a resolution of 0.0005 cm^{-1} is used. Over such a small wavenumber interval the absorption coefficient may be taken to be constant, hence the Lambert absorption law is obeyed. 'Exact' line–by–line calculations at this high resolution, may be made to perform the integration over wavelength in Eq. 6.8. However, they are extremely time consuming and are usually performed to provide a benchmark for the validation of approximate methods. Several different approximate methods have been developed, see e.g. Goody and Yung (1989) for a recent review. They typically perform spectral averages over many lines, e.g. narrow band models (over spectral ranges that are small compared to a band contour, i.e. 5 cm^{-1}), wide–band models (over complete bands) and emissivity models (over the entire thermal spectrum). However, these band models have some drawbacks that limit their use. They may not be used for scattering problems, e.g. scattering of clouds and aerosols. Further, most of them assume that each spectral region is statistically homogeneous as to the placement of lines with respect to wavenumber. Also, to account for the pressure and temperature dependence

[2]The Doppler width is a function of wavenumber and temperature (Eq. 3.82. For $T = 250K$ and a wavenumber $\omega_{fi} = 475.0cm^{-1}$, the Doppler width is 0.0005 cm^{-1}. For a higher temperature and/or a larger wavenumber a coarser resolution may be used.

of the absorption lines, various scaling approximations are invoked. Scaling approximations seek to represent the absorption of an atmospheric path in which the temperature and pressure varies, by a scaled absorption path with constant temperature and pressure. Generally, scaling approximations work well for uniformly mixed gases such as CO_2, but not so well for nonhomogenous gases, e.g. O_3. With the exponential–sum fitting of transmissions (ESFT) method multiple scattering may be included. The ESFT method approximates the transmission of a given spectral region by a finite sum of exponential terms, see e.g. Wiscombe and Evans (1977), Tsay et al. (1990). However, scaling approximations must be used to account for the pressure and temperature dependence. Lacis and Oinas (1991) introduced the correlated–k distribution method which largely overcame all these problems. It may be described as a wide–band model where the absorption cross sections are grouped by strength over a given spectral range. The method is described in section 3.1.10. Scattering problems may be studied with the correlated–k distribution method without any further approximations. Further, the line placements in a spectral region need not be statistically homogeneous. Finally the correlated–k distribution method overcomes the problems with the scaling approximations, and it offers substantial savings in computer time compared with line–by–line calculations. Thus the correlated–k distribution method yields a fast and accurate scheme for calculating the radiation field in an inhomogeneous, scattering, absorbing and emitting atmosphere.

To demonstrate the correlated–k distribution method for the calculation of cooling rates, a sample calculation will be given for the case of absorption by CO_2 in the region 5000–5050 cm^{-1}. Next, results will be presented for realistic cooling rates by CO_2, H_2O and O_3. Other gases, e.g. CH_4, N_2O and CFC's, may also add minor contributions to the total cooling rate (Ramanathan et al. 1985). They have been ignored in this work, but may easily be included in the present model although it would take some appreciable additional time.

6.2.1 Sample calculation, CO_2 in the 5000–5050 cm^{-1} region

As a first example the thermal cooling rate due to CO_2 in the interval 5000–5050 cm^{-1} is calculated. Goody et al. (1989) studied this region to assess the accuracy of the correlated-k distribution method because of its 'inattractiveness for any band model that seeks to treat it as a single interval.' In this narrow region the absorption cross section for CO_2 varies with 3–6 orders of magnitude depending on the local pressure and temperature, see Fig. 3.1. In this work a a calculation of the cooling rate up to 20 km was performed for the midlatitude summer atmosphere, see Fig.

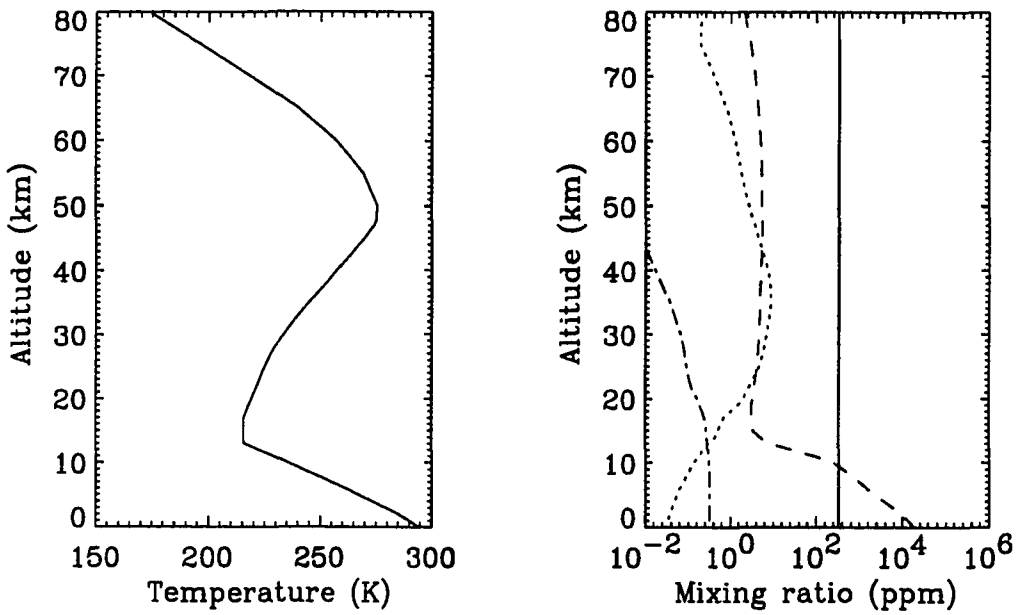

Figure 6.1: The temperature profile and profiles of CO_2 (solid line), O_3 (dotted line), H_2O (dashed line) and NO_2 (dashed–dotted line) for the midlatitude summer atmosphere (Anderson et al. 1987), used in the calculation of warming/cooling rates.

6.1 (Anderson et al. 1987). The model atmosphere was divided into 1 km layers and the surface temperature was set equal to the temperature of the bottom layer. No scattering was included.

First a line–by–line calculation with resolution of 0.004 cm^{-1} was performed. The resolution required varies with altitude and wavelength. It was set to resolve the finest lines at the highest altitude (lowest pressure). A resolution of 0.004 cm^{-1} means that the monochromatic radiative transfer equation has to be solved 12,500 times for the 5000–5050 cm^{-1} region. The correlated–k calculations were performed next.

The absorption cross sections were calculated with the GENLN2 program (Edwards 1988, 1992), see left column Fig. 3.1. These cross sections were sorted in ascending order layer by layer, right column Fig. 3.1. As mentioned in chapter 3 the smooth behavior of the sorted cross section makes it much easier to integrate numerically. A Gaussian quadrature rule (Press et al. 1985, Vetterling et al. 1985) was used to decide which g–values should be sampled depending on the number of points utilized. Quadrature points for a 10–point Gaussian quadrature rule are shown

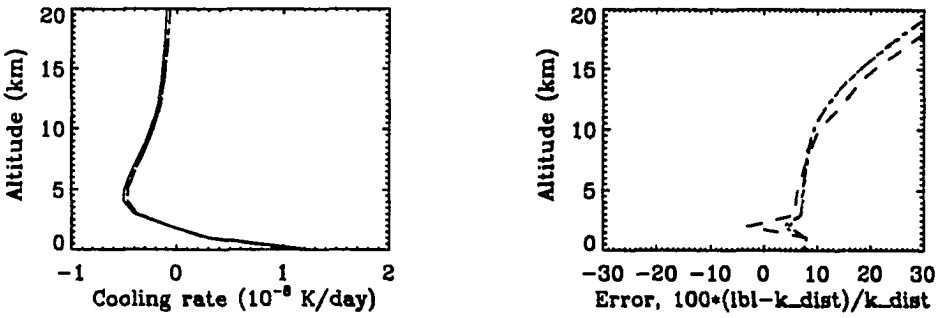

Figure 6.2: In the left panel is shown the cooling rate in the 5000–5050 cm^{-1} interval for the midlatitude summer atmosphere (Anderson et al. 1987), thermal radiation only. The solid line represents the line–by–line calculation. Results are also shown for a 50–points (dotted line), 36–points (dashed line) and 10–points Gaussian approximation (dashed–dotted line). In the right panel the errors of the different approximations are displayed.

in Fig. 3.1. Different correlated–k distributions were made by sampling the sorted absorption cross sections at different numbers of g–value points.

Results for the CO_2 cooling rate in the 5000–5050 cm^{-1} are shown in Fig. 6.2. The different correlated–k distribution approximations, using 50 Gaussian quadrature points (dotted line), 36 points (dashed line) and 10–points (dashed–dotted line), fairly well reproduce the line–by–line results (solid line). A 10–points quadrature rule requires 10 monochromatic solutions of the radiative transfer equation as opposed to 12,500 for the 'exact' line–by–line results. A large savings in computer time results.

The different correlated–k approximations in this example typically result in an error of 10–15 %. Calculations were performed with more quadrature points, e.g. 100 and 500. However only minor changes were seen in the accuracy. Thus the error made must be due to the failure of the correlation assumption, e.g. Fig. 3.2, and/or numerical precision problems. All calculations presented in this work were done on single precision 32 bit computers. The error displayed in Fig. 6.2 is largest where the cooling rate is smallest, i.e. above 10 km, indicating that part of the error is due to precision problems. Due to the complexity of the problem, e.g. seven FORTRAN programs consisting of approximately 30,000 lines of code were used to produce the present line–by–line and correlated–k distribution results, double precision calculations were not carried out. It should be noted that the results displayed in Fig. 6.2 may not be directly compared with the results of

Goody et al. (1989). Only thermal radiation is considered here, the adopted model atmosphere is different and no scattering is included. Goody et al. (1989) give the error in the net flux at different atmospheric levels. Typically the error is less then 1 %, but may be as large as 10–20 % for some levels. In Fig. 6.2 the error in the cooling rate is given, i.e. the combined error of the flux divergence and the divergence of the optical depth, given by Eq. 6.7.

An error of 10–15 % is too large to be acceptable in climatic model calculations[3]. Thus the above results may not be very encouraging to individuals interested in applying the method to warming/cooling rate calculations of the entire solar and terrestrial infrared spectrum. A way of improving the accuaracy of the correlated–k distribution method has been suggested by West et al. (1990). Unfortunately it is computationally more expensive. Also, as pointed out by Lacis and Oinas (1991), the CO_2 5000–5050cm^{-1} region is a rather 'pathological' case since this is a part of the spectrum where both terrestrial and solar radiation is weak. Hence the contribution from CO_2 absorption in the 5000–5050 cm^{-1} interval is negligible when computing warming/cooling rates for the entire terrestrial and solar spectrum. For realistic applications, e.g. absorption by the major bands of CO_2, H_2O and O_3, smaller errors are obtained as demonstrated below.

6.2.2 H_2O cooling rate

Water vapor or H_2O is the main absorber in the troposphere. The H_2O molecule is nonlinear and asymmetric and hence has a rather complex spectrum. In the ground state it has a dipole moment and a strong rotational band between 0–700 cm^{-1} (or, from approx. 15 μm toward longer wavelengths), which is the most important band for thermal radiative exchange in the troposphere. The 6.3 μm vibration–rotation band influences the radiative budget of the middle atmosphere at relatively high temperatures, while a number of higher–overtone bands in the near infrared and the subvisible contributes to the warming rate (see below). In the stratosphere and mesosphere H_2O has relatively minor influence on thermal infrared exchange due to its low concentration, approximately 5 ppm (see Fig. 6.1).

In Fig. 6.3 the water vapor cooling rates from both line–by–line (solid line) and correlated–k (dotted, dashed and dashed-dotted lines) calculations are shown. As stated above, the cooling rate due to H_2O is strongest in the troposphere due to its high abundance there, Fig. 6.1. The maximum at 50 km (approx. 1 mb) may be explained by the Chapman layer structure.

[3] In the middle and lower stratosphere the net heating rates rarely exceed 20 % of the solar heating or thermal cooling components. A 10% error in the solar heating or thermal cooling may thus potentially produce a 50 % error in the net heating rates and the diabatic circulation.

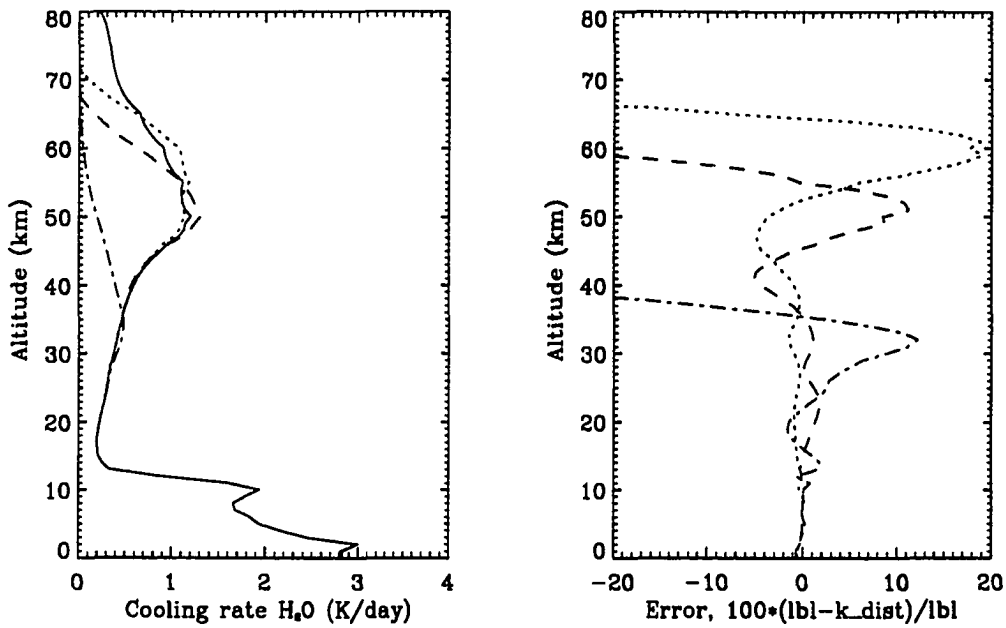

Figure 6.3: The H_2O cooling rate from line–by–line calculations (solid line) together with correlated–k distribution results with 50 point quadrature rule (dotted line), 36 points quadrature rule (dashed line) and 10 points quadrature rule (dashed–dotted line). The right panel shows the error made by the different correlated–k distribution approximations.

The wavenumber region 0–2000 cm^{-1} is included in the results displayed in Fig. 6.3, see Table 6.1. A resolution of 0.0005 cm^{-1} was considered good enough to resolve the finest lines at low pressures (Lacis and Oinas 1991). The model atmosphere extended up to 100 km and was divided into 1 km layers. To account for the pressure and temperature dependence the absorption cross sections were calculated at each altitude for each wavenumber point using the GENLN2 program (Edwards, 1988, 1992). Next these absorption cross sections, together with the mid–latitude summer atmosphere (Anderson et al. 1987), were used to generate input for the monochromatic radiative transfer program described in chapter 2. For the wavenumber resolution adopted here, 0.0005 cm^{-1}, the radiative transfer equation had to be solved 4 million times to cover the 0–2000 cm^{-1} region. For the correlated–k distribution calculations, the 0–2000 cm^{-1} region was divided into 10 cm^{-1} intervals. For each 10 cm^{-1} interval correlated–k distributions were made. For the results displayed in Fig. 6.3, 10, 36 and 50–point Gaussian quadrature rules were used. As can

Terrestrial radiation			
Molecule	Spectral intervals included		Method
H_2O	0–2000 cm^{-1}	∞–5 μm	Correlated-k distribution
CO_2	440–1100 cm^{-1}	2.27–9.09 μm	Correlated-k distribution
	1200–1430 cm^{-1}	8.33–6.99 μm	
	1800–2000 cm^{-1}	5.56–5.0 μm	
O_3	0–200 cm^{-1}	∞–50.0 μm	Correlated-k distribution
	560–1280 cm^{-1}	17.85–7.81 μm	
	1650–2000 cm^{-1}	6.06–5.0 μm	

Solar radiation			
Molecule	Spectral intervals included		Method
H_2O	2500–12940 cm^{-1}	4.0–0.077 μm	Correlated-k distribution
	13270–14500 cm^{-1}	0.075–0.069 μm	
O_2	116.5–243 nm		Allen and Frederick (1982)
NO_2	185–410 nm		DeMore et al. (1990)
O_3	116.5–360 nm		Molina and Molina (1986)
	450–730 nm		

Table 6.1: The different molecules included in the radiation model, the spectral interval included for each molecule and the sources for the cross sections used to calculate their optical properties.

be seen the 50–point Gaussian quadrature rule gives sufficient accuracy for the altitude region of most interest in this study, namely the troposphere–stratosphere. The 10–, 36– and 50–points Gaussian quadrature rules give a factor of 2000, 555 and 400, respectively, in savings of computer time compared with the 'exact' line–by–line results. Thus, substantial savings in computer time with little loss of accuracy is achieved. A discussion of the discrepancy between the different correlated–k distribution results is given in section 6.2.5.

The calculated values for the cooling rate for H_2O in both the troposphere and the middle atmosphere agree well with results from other investigators, NASA (1988) and Lacis and Oinas (1991).

6.2.3 CO_2 cooling rate

The carbon dioxide molecule is linear with three vibrational modes in its ground state: symmetric stretching (ν_1), bending (ν_2) and asymmetric stretching (ν_3) (Andrews, Holton and Leovy 1987). Linear, symmetric molecules have no electric dipole moment in the ground vibrational state and hence no electric dipole rotational spectra. The ν_2 fundamental band at 15 μm, together with the highly temperature–dependent excited bands, are of great importance for the energy budget of the Earth's atmosphere since they are located in a part of the spectrum where terrestrial emission of radiation is strong. Furthermore, there is little else except CO_2 that absorbs in this 'window' region. A change in CO_2 concentration is thus likely to alter the temperature distribution in the atmosphere[4]. The very strong ν_3 band at 4.3 μm has a rather marginal influence because it is situated at a wavelength where both terrestrial and solar radiation are weak. It has not been included in the present calculations, see Table 6.1. Contributions from different CO_2 isotopes ($^{13}C^{16}O_2$, $^{12}C^{16}O^{18}O$, $^{12}C^{16}O^{17}O$) are also included. Even if they are few in number, they efficiently emit radiation to space due to their small optical depths even in strong line centers.

As shown in Fig. 6.1 carbon dioxide is well mixed (a mixing ratio of 330 ppm is used in the calculations presented here) and its cooling rate exhibits a clear Chapman layer structure, see Fig. 6.4. The CO_2 cooling has its maximum at the stratopause. Good agreement is found throughout the atmosphere between the 'exact' line–by–line result and the correlated–k distribution approximations. The 'spike' in the error at 14 km is where the cooling rate is smallest. It may be attributed to precision problems similar to those encountered above for the cooling rate of CO_2 in the 5000–5050 cm^{-1} region. The resolution for the line–by–line calculation was the same as for the water vapor case, i.e. 0.0005 cm^{-1}. The CO_2 cooling rate calculated here is in good agreement with previous investigations, e.g. Lacis and Oinas (1991), NASA (1988), Dickinson (1973), Chou, Kratz and Ridgway (1991). The results of Lacis and Oinas (1991) are marked as stars at 5 km intervals in Fig. 6.4. The differences above 50 km between the present results may be attributed to differences in the temperature profiles used. Above 50 km the temperature values adopted by Lacis and Oinas (1991) are substantially lower than the ones used in the present study. CO_2 has a large number of transitions, corresponding to absorption by excited bands. These excited bands are very temperature sensitive, since their absorption strength depends on the population

[4]Doubling the amount of CO_2 is a popular exercise in climate models, yielding typically a 4 degree warming of the earth's 'average' surface temperature. However, "most of the so called 'CO_2 effect' is , in fact, an 'H_2O effect' brought into play by the climate modeler's assumption that planetary average temperature dictates water–vapor concentration (following Clapeyron–Clausius)" (Twomey 1991).

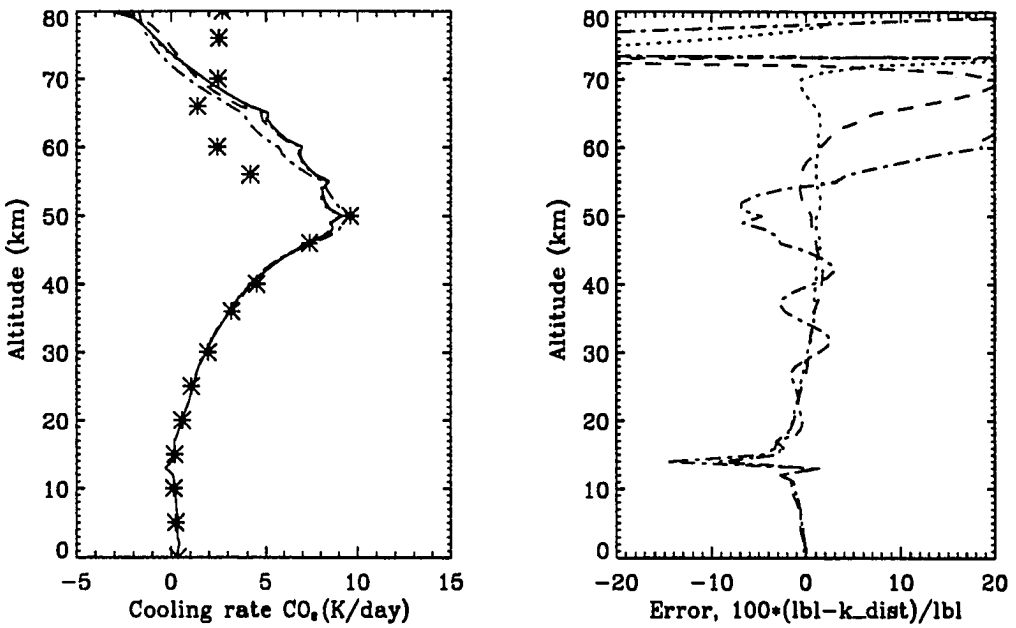

Figure 6.4: The CO_2 cooling rate from line–by–line calculations (solid line), together with correlated–k distribution results with 50 points quadrature rule (dotted line), 36 points quadrature rule (dashed line) and 10 points quadrature rule (dashed–dotted line). The stars are the results of Lacis and Oinas (1991) given at 5 km intervals. The right panel shows the error made by the different correlated–k distribution approximations.

of excited molecular states. Thus, a different temperature profile will yield substantially different results for cooling by CO_2.

As noted earlier, the atmosphere is assumed to be in local thermodynamic equilibrium (LTE). It has been common to include non–LTE effects above approximately 80 km for the main coolant in this region, namely CO_2. However, recent results show that the rotational and vibrational temperature profiles of the CO_2 ν_2 level are nearly identical up to 110 km. Thus the dominant atmospheric emission process is in LTE or very nearly so, up to 110 km (Rodgers et al. 1992). The method employed here for calculating CO_2 cooling rates may thus readily be extended to higher altitudes.

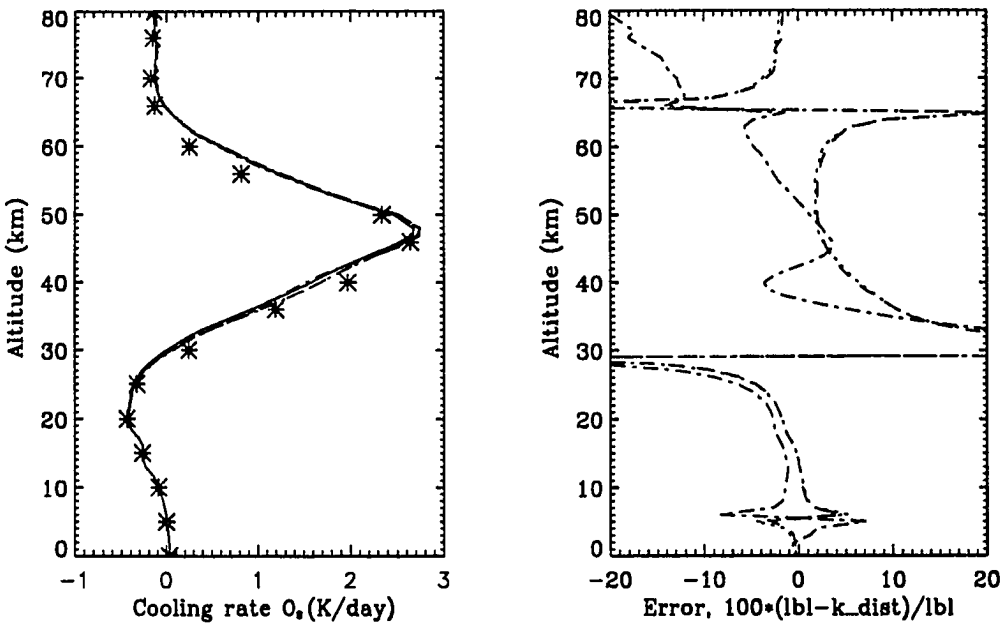

Figure 6.5: The O_3 cooling rate from line–by–line calculations (solid line) together with correlated–k distribution results with 50 points quadrature rule (dotted line), 36 points quadrature rule (dashed line) and 10 points quadrature rule (dashed–dotted line). The stars are the results of Lacis and Oinas (1991) given at 5 km intervals. The right panel shows the error made by the different correlated–k distribution approximations. An explanation for the rather large errors around 5, 30 and 66 km is given in the text.

6.2.4 O_3 cooling rate

Like the water vapor molecule, ozone is non–linear and asymmetric with a dipole moment in the ground state. It has three fundamental vibration–rotation bands, ν_1, ν_2 and ν_3, as well as a pure rotational spectrum. The 9.6 μm band with the strong ν_1 (1110 cm^{-1}) and ν_3 (1045 cm^{-1}) fundamentals together with excited bands and minor isotopic bands in the same region, are the most important for thermal radiative exchange. The ν_2 (701 cm^{-1}) fundamental is masked by the CO_2 15 μm band and is of minor significance.

The radiative cooling rate by ozone is displayed in Fig. 6.5 and the spectral intervals included in the calculations are given in Table 6.1. The non–uniform distribution of ozone, see Fig 6.1, has long been regarded as difficult to handle by frequently used radiative transfer methods such as the Curtis–Godson approximation where pressure and temperature scaling of the absorber amount

is utilized in an attempt to account for pressure broadening (Goody and Yung 1989). As stated earlier, the correlated–k distribution method largely overcomes this problem, see Fig. 6.5. The line–by–line results were calculated with a resolution of 0.0005 cm^{-1}, as for CO_2 and H_2O.

The rather large errors made by the correlated–k distribution approximations around 5, 30 and 60 km, are in regions where the cooling due to O_3 is negligible, and they may thus be ignored. The errors at these altitudes are due to numerical precision problems as explained above. In these regions, the upper troposphere and the lower stratosphere, the absorption of upwelling radiation by ozone dominates self emission, resulting in warming between 5–30 km as well as above 66 km. The maximum cooling by ozone is found at the stratopause. In magnitude the cooling due to ozone is roughly one–third compared to the cooling by carbon dioxide in the middle atmosphere. The results obtained for O_3 are in agreement with results from other studies, e.g. Lacis and Oinas (1991) and NASA (1988). The results of Lacis and Oinas (1991) are marked as stars at 5 km intervals in Fig. 6.4. As opposed to the results for CO_2 the present results for O_3 are in much better agreement with the results of Lacis and Oinas above 50 km, thus indicating that for O_3 the fundamental bands are relatively much stronger than the excited bands.

Fig. 6.6 shows the total cooling rate due to H_2O, CO_2 and O_3 together with cooling rates calculated for each gas in the absence of the other gases. Due to overlapping absorption the total cooling rate is less then the sum of the individual cooling rates. It is noted that overlapping absorption between lines and different gases may be accurately treated by the correlated–k distribution method (Lacis and Oinas 1991). To handle overlapping absorption it is common to assume that the absorption line positions of one gas relative to the other are randomly distributed. Hence the optical depth for the correlated–k interval Δg_i for gases a and b may be written $\tau_i = \tau_i^a + \tau_i^b$. Here $i = 1, \ldots, N$, where N is the number of quadrature points over the wavenumber region of interest. However, as noted by Lacis and Oinas (1991), this is not generally valid in a multilayered atmosphere where there is strong correlation of overlapping spectra in neighbouring atmospheric layers. Hence, the optical depth for an interval is given by $\tau = \tau_i^a + \tau_j^b$, where $i = 1, \ldots, N$ and $j = 1, \ldots, N$, giving N^2 monochromatic radiative transfer calculations to be performed as compared to N for nonoverlapping gases. The radiation field in the overlapping case is given by summing over the N^2 monochromoatic components. For the gases and wavenumber regions considered here, the effect of overlapping absorption is small and has not been included. For other gases and wavenumber regions, e.g. CH_4 and N_2O in the 1100–1350 cm^{-1} region, it is of importance, e.g. Lacis and Oinas (1991).

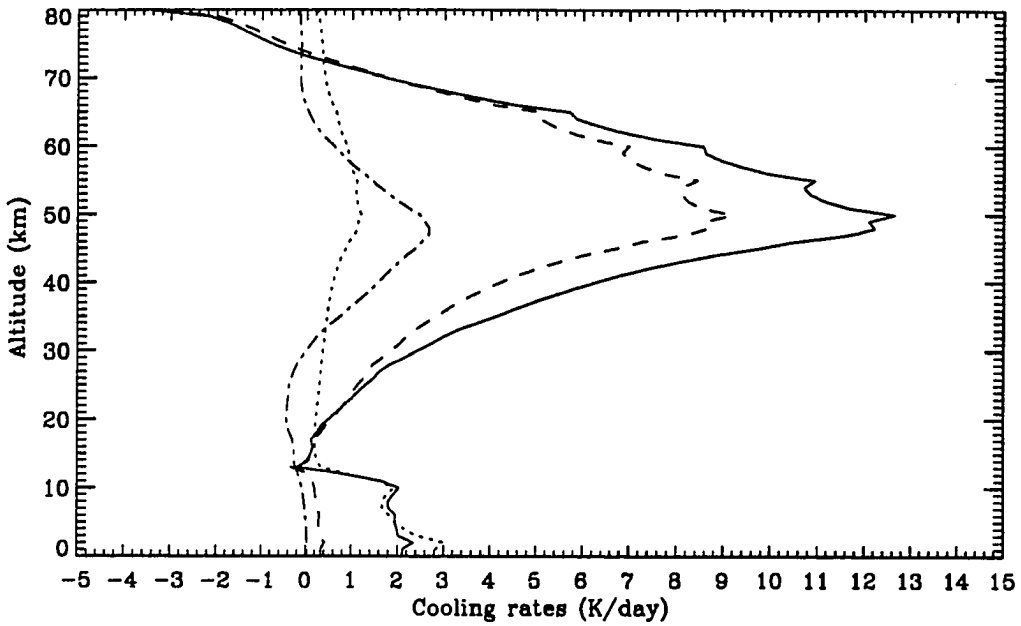

Figure 6.6: Individual cooling rates for H_2O (dotted line), CO_2 (dashed line) and O_3 (dashed–dotted line) together with the total cooling rate (solid line) for all three absorbers.

6.2.5 Note on the correlated–k distribution method

As mentioned in chapter 3, Lacis and Oinas (1991) fitted correlated–k distributions to the Malkmus band model whereas Goody et al. (1989) performed the integration of the correlated–k distribution by a Gaussian quadrature rule. The latter approach was adopted in the present study. The number of monochromatic computations required across a given wavelength interval equals the number of terms adopted in the Gaussian quadrature. In Figs. 6.3–6.5, line–by–line results are shown together with correlated–k distribution results with 10, 36 and 50 points Gaussian quadrature rules for H_2O, CO_2 and O_3. The more points that are used for the quadrature, to a higher altitude (lower pressure) will the correlated–k approximation give accurate results. This is due to the narrowing of the absorption lines and the related peaking of the k distribution, see Fig. 3.1 and Lacis and Oinas (1991). With too few quadrature points the peak in the k distribution will not be accounted for. Too many quadrature points will however make the radiation model rather expensive to execute. An integration rule with unequal spacing and closely spaced intervals near

$g = 0$ and around the strong absorption end ($g = 1$) (Lacis and Hansen 1991), gives good accuracy with fewer integration points. Such a quadrature should be adopted, if fast radiation models are required.

6.3 Warming rates

Unlike the cooling rate which is driven by terrestrial radiation and thus has only minor diurnal variations, the warming rate, driven by the sun, exhibits strong diurnal variations. Furthermore, for terrestrial radiation most molecular scattering cross sections are small and may be ignored to a first approximation in the absence of clouds and aerosols. However, molecular scattering must be included for solar radiation calculations. Rayleigh scattering is important in the ultraviolet and in the visible, and ground reflection must be included. In the ultraviolet and the visible part of the spectrum cross sections averaged over narrow wavelength intervals may be defined, yielding sufficient accuracy for photochemical applications and climate studies (WMO 1986). In the solar near-infrared the highly structured absorption features of the key absorbers in this region, H_2O, O_2 and CO_2, requires a more careful treatment. As for the terrestrial case different band models have also been developed for the solar near-infrared, see Kratz and Cess (1985) for a review. As pointed out above, these models do not include scattering, hence in this work the correlated-k distribution method will be adopted as was done for the terrestrial infrared. To the author's knowledge, this is the first time the correlated-k distribution method has been used in the solar part of the spectrum.

To give an example of atmospheric warming rates the midlatitude summer atmosphere (Anderson et al. 1987) will be used together with a solar zenith angle $\theta_0 = 0$ (i.e. overhead sun) and a ground albedo $A_g = 0$ to eliminate albedo effects. In the UV and visible part of the spectrum, O_3, O_2 and NO_2 cross sections averaged over narrow wavelength intervals are used to calculate warming rates, see Fig. 4.1. For tropospheric H_2O the correlated-k distribution is used in the near infrared. Bands of O_2 centered at 7882, 13121 and 14526 cm^{-1}, and CO_2, 3715, 4978 and 6973 cm^{-1}, also give minor contributions to the warming in the lower stratosphere. They are not included in the present work. For a midlatitude summer atmosphere, absorption by O_2 and CO_2 in these spectral bands contributes less then 5 % of the total atmospheric absorption (Fouquart et al. 1991).

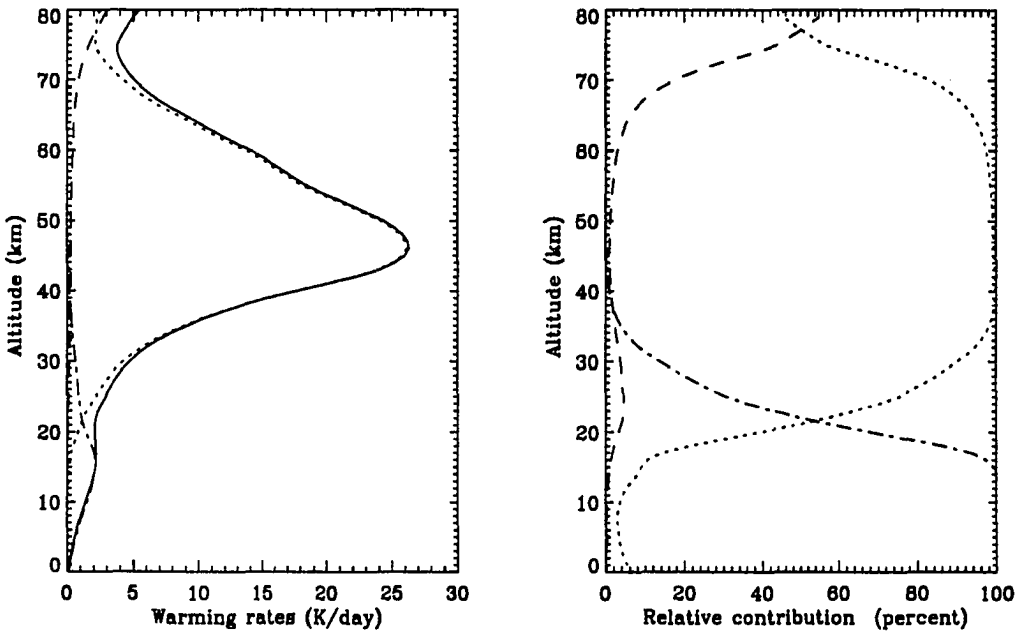

Figure 6.7: The O_3 (dotted line), O_2 (dashed line) and NO_2 (dashed–dotted line) warming rates and their total (solid line). Also shown is the relative contribution of each gas with altitude. Note that due to overlapping absorption, the total warming rate is less than the sum of the individual warming rates.

6.3.1 O_3, O_2 and NO_2 warming rates

Whereas CO_2 is the main coolant of the middle atmosphere, O_3 is responsible for most of the warming, see Fig. 6.7, dotted line. Ozone has a very large cross section between 200 and 330 *nm* (the Hartley and Huggins bands), and it also absorbs in the Chappuis band between 550 and 800 *nm*, see Fig. 4.1. The warming due to ozone determines the temperature profile in the middle atmosphere. It is noted that the present results for warming by ozone in the upper mesosphere may be overestimated by as much as 50 %. This is due to spontaneous emission from metastable oxygen species which are products of ozone photolysis (Mlynczak and Solomon 1991).

The oxygen molecule absorbs strongly in the Schumann–Runge bands (170–200 *nm*) and somewhat less in the Herzberg continuum (200–250 *nm*). Due to the short wavelengths involved, the absorption of UV–radiation by O_2 only contributes to the warming of the mesosphere and upwards, see Fig. 6.7 dashed line.

The nitrogen dioxide concentration varies throughout the day with a maximum at night. In this work a profile from Anderson et al. (1987) have been used, see Fig. 6.1. NO_2 absorbs in the visible where little else absorbs, see Fig. Fig. 4.1. The relative warming due to NO_2 is substantial below 25 km, Fig. 6.7 dashed–dotted line.

For the results shown in Fig. 6.7 for O_2, O_3 and NO_2, cross sections averaged over narrow wavelength intervals as recommended by WMO (1986) were used. The temperature dependence of the O_3 cross section was treated as by Molina and Molina (1986). The parameterization due to Allen and Frederick (1982) was used for O_2. With the resolution recommended by WMO (1986) a total of 171 monochromatic radiative transfer problems had to be solved for the ultra–violet and the visible part of the spectrum. Stamnes and Tsay (1990) devised a scheme in which the simple sum over monochromatic calculations was replaced by a solar flux weighted average with far fewer terms. They presented results for warming and photodissociation rates due to ozone. Attempts were made to implement this scheme for the calculation of photodissociation and warming rates in the ultra violet and the visible part of the spectrum. Due to the complex spectral behavior of the various cross sections (see Fig. 4.1), the quantum yields and the solar flux, the attempt to define suitable solar flux weighted averages was unsuccessful. Thus, while the method of Stamnes and Tsay (1990) works very well for a single species, it remains to be demonstrated that it may be utilized in calculations involving more than one species.

The warming rates shown in Fig. 6.7 are instantaneous warming rates and not diurnal averages. They are calculated for noon conditions, solar zenith angle $\theta_0 = 0.0$ and with a ground albedo $A_g = 0.0$. In the following chapter the method of Cogley and Borucki (1976) will be used to compute daily averaged solar heating rates. Their method gives the daily average as a multiplication factor times the instantaneous rate, evaluated at an appropriate solar zenith angle.

6.3.2 H_2O warming rate

Not only is water vapor the main coolant of the troposphere, it is also the main source of warming. Water vapor absorbs in a number of bands in the near infrared, centered at 0.72, 0.81, 0.94, 1.14, 1.38, 1.87, 2.7 and 3.4 μm. To account for the warming due to the nearly 24,000 water vapor lines in this wavelength region (HITRAN data base, 1986 version, Rothman et al. 1987), line–by–line calculations were performed with a resolution of 0.01 cm^{-1} which is sufficient up to the lower stratosphere. The wavenumber intervals that are included are given in Table 6.1. For each 200 cm^{-1} interval correlated-k distributions were made. The line–by–line and correlated-k distribution

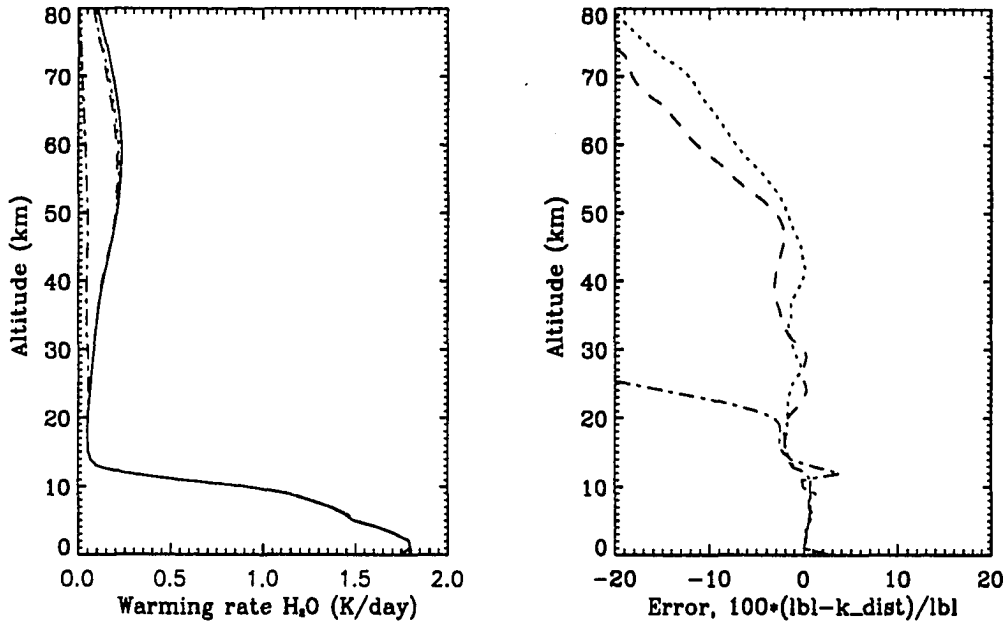

Figure 6.8: The H_2O near-infrared warming rate from line–by–line calculations (solid line) together with correlated–k distribution results with 50 point quadrature rule (dotted line), 36 point quadrature rule (dashed line) and 10 point quadrature rule (dashed–dotted line). The right panel shows the error associated with the different correlated–k distribution approximations.

results are shown in Fig. 6.8. Only solar radiation was used as input to the radiation model with an incident solar zenith angle $\theta_0 = 0.0$ and ground albedo $A_g = 0.0$. The solar spectrum was taken from the MODTRAN model (Beck, Bernstein and Robertson 1989). As for the warming rate results presented above for O_3, O_2 and NO_2, the results in Fig. 6.8 for H_2O are instantaneous warming rates.

The different correlated–k approximations all agree well with the 'exact' line–by–line results in the troposphere and the lower stratosphere. Above this level the results should be judged with some care, as the resolution of the line–by–line calculation is too low to resolve the finest lines at the low pressures encountered.

Ramaswamy and Freidenreich (1991) provided benchmark results for water vapor absorption and water cloud extinction in inhomogenous atmospheres to be used in the Intercomparison of Radiation Codes in Climate Models (Ellingson and Fouquart 1991). They gave line–by-line results

for the region 0–33,333 cm^{-1}. In the solar near–infrared calculations, the region 2500–14,500 cm^{-1} is covered, see Table 6.1. There are no water vapor lines between 12,940 and 13,270 cm^{-1}, Park et al. (1987). For solar radiative transfer the contributions from the 0–2500 and 14,500–18,000 cm^{-1} intervals are small; therefore, they have been ignored in this work (see Fig. 5, Ramaswamy and Freidenreich 1991). Ramaswamy and Freidenreich (1991) gave results for solar zenith angles of 30° and 75° with a ground albedo of 0.2. Their results may thus not be directly compared with the present results, but qualitatively they are similar in shape and magnitude.

As pointed out by Ramaswamy and Fredenreich (1991), line–by–line calculations 'consume an exorbitant amount of computational resources'. Their model atmosphere had 50 layers, which is half the number of layers used in the present study. Furthermore, because of the computational burden, they included scattering in one single layer using a doubling–adding method. The present method allows for scattering to be included in all layers without any increase in computer time over the scattering in the one layer case. Ramaswamy and Freidenreich (1991) also gave approximate methods for calculating the warming due to water vapor. Typically these methods decreased computer time by a factor of 30 over line–by–line calculations. It is noted that the correlated–k distribution adopted in the present study decreases computer time by factors between 400-2000, depending on the number of Gaussian quadrature points chosen. Thus, it provides a fast and yet accurate way of studying the effects of scattering from clouds and aerosols which may not be treated by most traditional band models.

6.4 Summary

An expression for the warming/cooling rate has been derived. Using results for the mean intensity and absorption cross sections from previous chapters, 'exact' and approximate warming/cooling rates were calculated. For the ultra–violet and the visible (120–700 nm) averaged cross sections were used, while in the near–infrared and infrared line–by–line calculations served as a basis for developing correlated–k distribution approximations. The warming effects of O_3, O_2, NO_2 and H_2O were included for the solar part of the spectrum, while O_3, H_2O and CO_2 were included in the calculation of cooling rates in the terrestrial part of the spectrum.

The correlated–k distribution method was found to substantially reduce the required number of monochromatic radiative transfer problems, while still giving accurate results both for well–mixed, e.g. CO_2, and non–uniformly distributed gases, e.g. O_3. Factors of 400–2000 in savings

of computer time over line–by–line calculations may easily be achieved, depending on the specific application, i.e. at which altitude accurate warming/cooling rates are needed. The correlated–k distribution method used in this work is fast enough to be applied to 1–D radiative–convective models. However, as mentioned by Lacis and Oinas (1991), further approximations are needed for it to be applicable to 3–D calculations.

As opposed to band models with one– or two–parameter pressure and temperature scaling approximations, the correlated–k distribution method includes the pressure and temperature dependence of the absorption cross section, thus allowing the troposphere and the stratosphere to be treated in a unified manner.

Finally, the correlated–k distribution method makes it possible to include multiple scattering which is not possible to treat with most other band models, except the ESFT method and the (non–correlated) k–distribution method. These latter two methods, however, utilize scaling approximations to account for the pressure and temperature dependence of the absorption cross sections. Thus, the correlated–k distribution method in connection with a multiple scattering radiative transfer model as the one described in chapter 2, is well suited to study the effects of clouds and aerosols on the radiation field in the terrestrial atmosphere. The radiative effects of clouds and aerosols will be the topic of the next chapter.

Chapter 7

The radiative effects of clouds and aerosols

In the previous chapters tools have been developed for calculating the earth's atmospheric radiation field in an inhomogenous atmosphere. In chapter 2 the equation for radiative transfer was developed, cast into a form amenable to solution and solved. Chapter 3 was devoted to the description of the absorption and scattering mechanisms of light by molecules and particulate matter and their respective cross sections. In chapter 4 and 6 it was shown how photodissociation and warming/cooling rates may be accurately and efficiently computed in inhomogeneous atmospheres. In this chapter the question raised in the introduction is addressed: how do clouds and aerosols affect the tropospheric and stratospheric photodissociation and warming/cooling rates. First, the different aerosol and cloud models used will be described and next the radiative effects of surface albedo, aerosols and clouds on photodissociation and warming/cooling rates are investigated. Finally, the radiative effects of clouds and aerosols on chemistry and dynamics are discussed.

7.1 Cloud and aerosol models

Aerosols and clouds may perturb the atmosphere in a number of ways. Obviously, it is impractical to discuss every conceivable atmospheric condition. Rather than attempting to consider all possible atmospheric conditions, only a few selected examples will be presented. Judiciously chosen, these examples might nevertheless encompass a wide range of conditions occurring in nature. It will be focused on the effects of water clouds, cirrus clouds and different aerosol situations. The effect of

clouds on the radiation field above and below the cloud will be investigated. Detailed studies of the radiation field inside the cloud require a much higher vertical resolution than the one adopted here (1 km thick layers), and preferably a three dimensional radiation model.

7.1.1 Water cloud model

Clouds cover 50–60% of the Earth's surface at any time and as such they greatly influence the Earth's climate by increasing the planetary albedo and by trapping longwave terrestrial radiation. A large part of the incoming solar radiation is reflected by clouds, while longwave terrestrial radiation is absorbed and emitted at the colder cloud tops, causing a reduction in the longwave radiation emitted to space. This is the greenhouse effect. The net effect of these two competing processes was investigated by the Earth Radiation Budget Experiment (ERBE) (Ramanathan et al. 1989). They concluded that in the present atmosphere clouds cool the troposphere. In this work the influence of tropospheric clouds on the stratospheric radiation budget will be studied. The optical properties of the water cloud adopted here, were calculated by the parameterization scheme of Hu and Stamnes (1992). Assuming that the water droplets are spherical, they used results of detailed Mie theory calculations as a basis for developing an accurate and fast parameterization scheme. The variable parameters are the liquid water content and the effective droplet radius. These two parameters were found to be the only ones necessary to characterize the cloud radiative properties accurately (Hu and Stamnes 1992).

For the calculations presented below, the effective droplet radius was taken to be 10.0 μm and the liquid water content 0.15 g/m^3. The cloud base is at 1 km and the cloud thickness is 1 km.

7.1.2 Cirrus cloud model

The optical properties of cirrus clouds used in the present study are shown in Fig. 7.2. Shettle and Fenn (1976) used standard Mie theory to calculate the optical properties, i.e. they assumed the cirrus (ice) particles to be spherical. According to Shettle (1989), this should not affect the major spectral characteristics of the cloud. However the detailed values will be affected.

As seen from Fig. 7.2, the single scattering albedo of cirrus clouds is $\sim$ 0.5 in the terrestrial infrared part of the spectrum. The absorption coefficient is also much larger in the terrestrial infrared then in the ultraviolet and visible part of the spectrum. Hence, although they are optically relatively thin, cirrus clouds may have an appreciable effect on the thermal radiation budget. The cirrus clouds adopted for the calculations shown below, have a base altitude at 11 km, which is

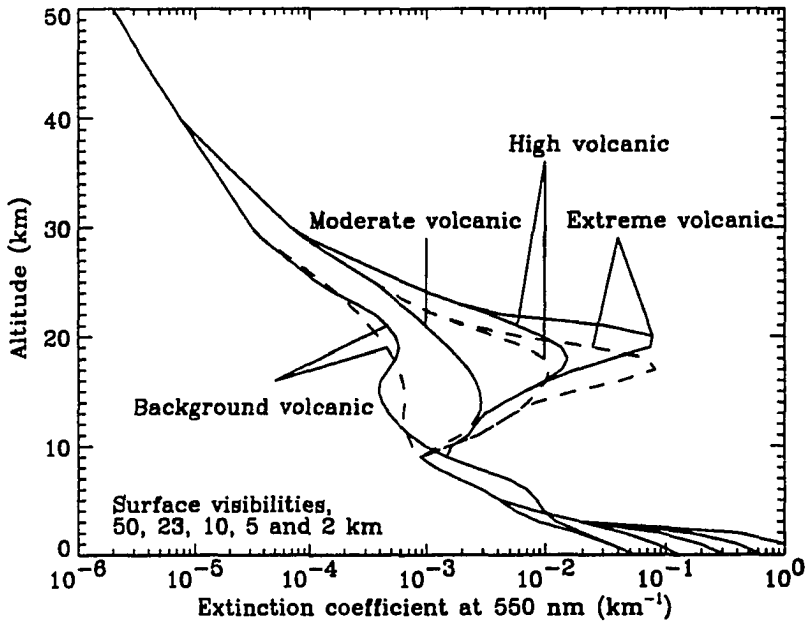

Figure 7.1: The aerosol extinction at 550 *nm* from the Shettle and Fenn (1976) aerosol models. The solid line represents spring–summer conditions and the dashed line fall–winter conditions.

a realistic altitude at latitude 30°N. The cloud thickness is 1 km, and a plane–parallel layer is assumed for all types of clouds in this study.

7.1.3 Aerosol models

The stratospheric aerosol layer is situated between 15 and 25 km and is composed primarily of sulfuric acid (Turco et al. 1982). Being mainly of volcanic origin the stratospheric aerosol layer has a high degree of natural variability. A typical profile of the extinction coefficient for background aerosol conditions is shown in Fig. 7.1. Also shown, are extinction coefficient profiles for moderate, high and extreme volcanic aerosol loading situations. The wavelength dependence of the extinction and absorption coefficients, the asymmetry factor and the single scattering albedo are displayed in Fig. 7.2.

The extreme volcanic aerosol model is representative for aerosol conditions associated with major volcanic eruptions, such as Mt. Agung (1963), El Chichon (1982) and Mount Pinatubo (1991). The optical properties of the aerosol layer change with time due to removal of aerosols

and due to changes in the composition of the aerosols caused by photochemical and chemical processes. The different aerosol models shown in Fig. 7.1 represent various stages in the evolution of the stratospheric aerosol layer after a volcanic eruption. The time evolution will vary with the magnitude, location and time of the eruption. For Mount Pinatubo, Hansen et al. (1992) assumed that initially the aerosols spread zonally and latitudinally for $\sim$ 10 months. Afterwards, the optical depth decays exponentially with a 12 month time constant. Below photodissociation and warming/cooling rates for the different aerosol models are calculated. For the troposphere, the model with a surface visibility of 50 km is used. The globally averaged optical depth of tropospheric aerosols has been estimated to be $\tau \sim 0.1$ (Hansen and Lacis 1990), which is somewhat higher than the value adopted here.

7.2 Photodissociation rates

Photodissociation rates depend directly on the atmospheric radiation field (cf. Eq. 4.8). Hence, varying atmospheric conditions influencing the radiation field will also affect the amount of light available for photolysis. Relatively little work has been done to assess how photodissociaton rates behave for different surface albedos, aerosol loadings and cloud situations. Luther and Gelinas (1976) emphasized the importance of molecular (Rayleigh) scattering and surface albedo. Meier et al. (1982) studied in detail the effects of ground albedo and multiple scattering due to Rayleigh scattering on photodissociation rates. Using the radiation model of Meier et al. (1982), Nicolet et al. (1982) calculated enhancement factors due to multiple scattering as a function of height, solar zenith angle and wavelength. The enhancement factors were meant to be directly applicable to photochemical models. Madronich (1987) pointed out that due to the use of wrong radiative quantities: a fraction of the current photochemical literature contains improperly calculated photodissociation rates. Furthermore, he discussed the importance of properly calculating photodissociation rates within clouds. The effect of an aerosol layer on the ultraviolet and visible radiation field was investigated by Michelangeli et al. (1992). They concluded that the actinic flux increases below a stratospheric aerosol layer for small solar zenith angles. Finally Tsay and Stamnes (1992) have looked at the effects of clouds and haze on photodissociation rates under arctic conditions.

In this work the variation of photodissociation rates with surface albedo and solar zenith angle is examined. Furthermore, it is investigated how aerosols and water and cirrus clouds affect

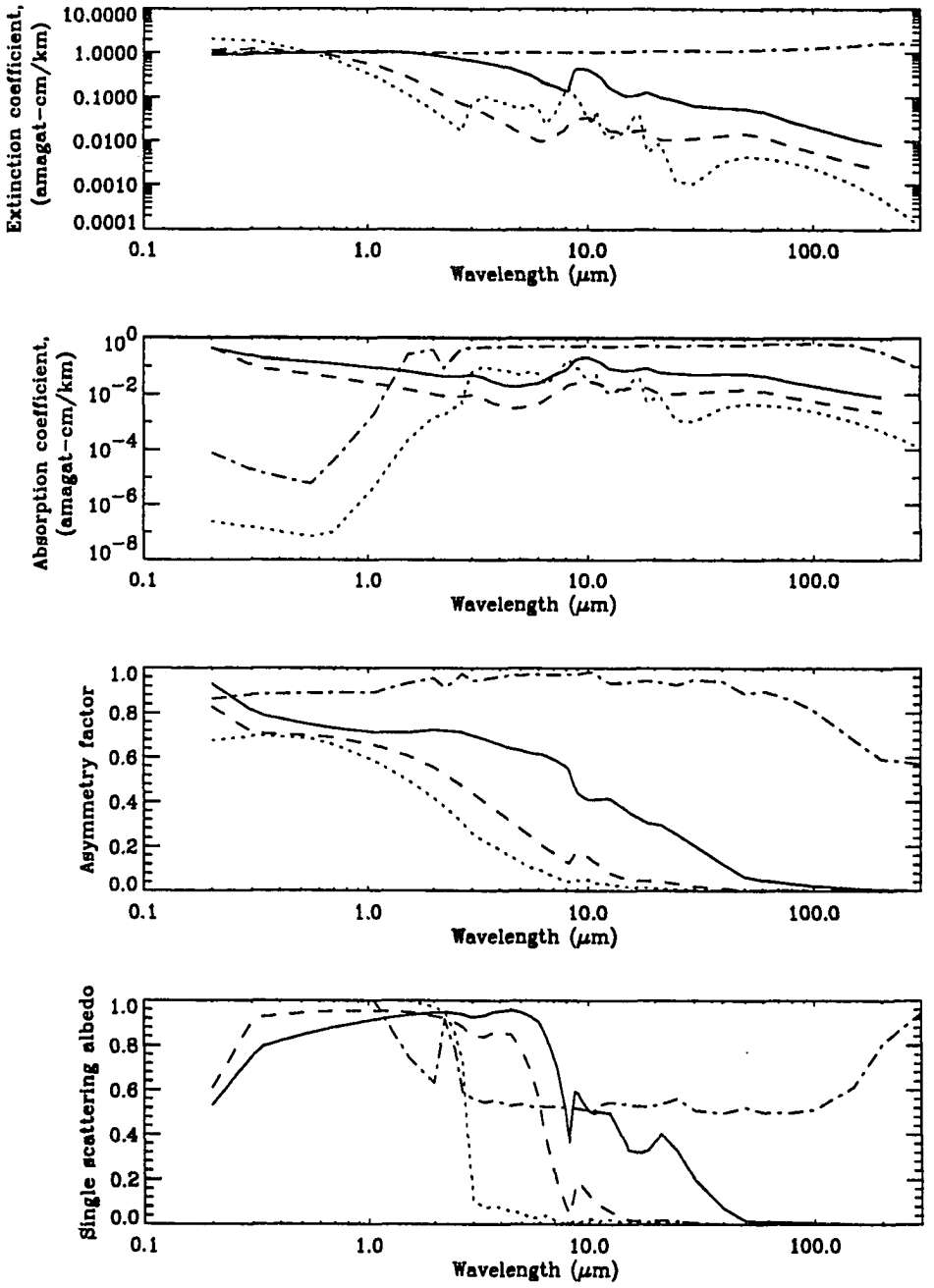

Figure 7.2: The wavelength dependence of the extinction and absorption coefficients, the asymmetry factor and the single scattering albedo used in the region 10–30 km for fresh volcanic (solid line), background (dotted line) and aged volcanic (dashed line) conditions. Also shown are the optical properties of the cirrus cloud model used (dashed–dotted line). From the Shettle and Fenn (1976) models. (1 amagat = 1 atm at STP)

photodissociation rates.

7.2.1 Surface albedo effects

To study the effects of surface albedo on photodissociation rates, photodissociation rates of O_3 ($O_3 + h\nu \rightarrow O(^3P)+O_2$) and O_3^* ($O_3 + h\nu \rightarrow O(^1D)+O_2$) were computed for three solar zenith angles $\theta = 30°, 60°, 85°$, and five surface albedos, A_g=0.0, 0.25, 0.50, 0.75, 1.0. The two reactions $O_3 + h\nu \rightarrow O(^3P)+O_2$ and $O_3 + h\nu \rightarrow O(^1D)+O_2$ are studied because of their different spectral dependence. Photolysis of O_3 to the $O(^3P)$ channel takes place for $310 < \lambda < 730$ *nm*, while $O(^1D)$ is produced for $\lambda \leq 310$ *nm*. For a non-scattering atmosphere the atmosphere is more or less transparent at all altitudes in the spectral region 310–730 *nm* . Between 290 and 310 *nm* there is partial transmission of radiation to low altitudes (cf. the O_3 cross section in Fig. 4.1h). Shortward of 290 *nm* no radiation reaches the Earth's surface for normal ozone concentrations. For molecules dissociated by radiation at wavelengths shorther than 290 *nm* (e.g. O_2 and CCl_4) albedo effects are negligible as shown in Fig 4.7.

In Figs. 7.3–7.4 the effects of different ground albedos and zenith angles on O_3 and O_3^* photodissociation rates are demonstrated. As opposed to the $O(^1D)$ channel, the $O(^3P)$ channel exhibit relatively little variation with altitude. This is due to the different spectral response of the two channels, as explained below. The atmosphere is transparent in the spectral region for photodissociation of O_3 to the $O(^3P)$ channel. Hence, changing the surface albedo from $A_g = 0.0$ to $A_g = 1.0$, can cause a 50% or more increase in the O_3 photodissociation rate throughout the atmosphere for small to moderate ($\sim 30°$) solar zenith angles. With increasing solar zenith angle the effect due to changes in the surface albedo decreases. This is because the absorption of incoming radiation increases due to the longer pathlengths encountered for low solar elevations.

While increasing the solar zenith angle from 30° to 85° decreased the O_3 photodissociation rate by less than one order of magnitude, a four order of magnitude decrease results in the photodissociation rate of O_3^* in the troposphere (Fig. 7.4). This is due to the large ozone absorption cross section for $\lambda \leq 310nm$. Surface albedo effects for the O_3^* channel are seen up to 8 km for the case studied here. Hence surface albedo effects do not affect O_3^* photolysis in the stratosphere. This result differs from that reported by Luther and Gelinas (1976). They found differences in the O_3^* photodissociation rate due to different surface albedos up to 25 km. Also, a slight increase is seen in the O_3^* photodissociation rate close to the ground for large surface albedos which is not

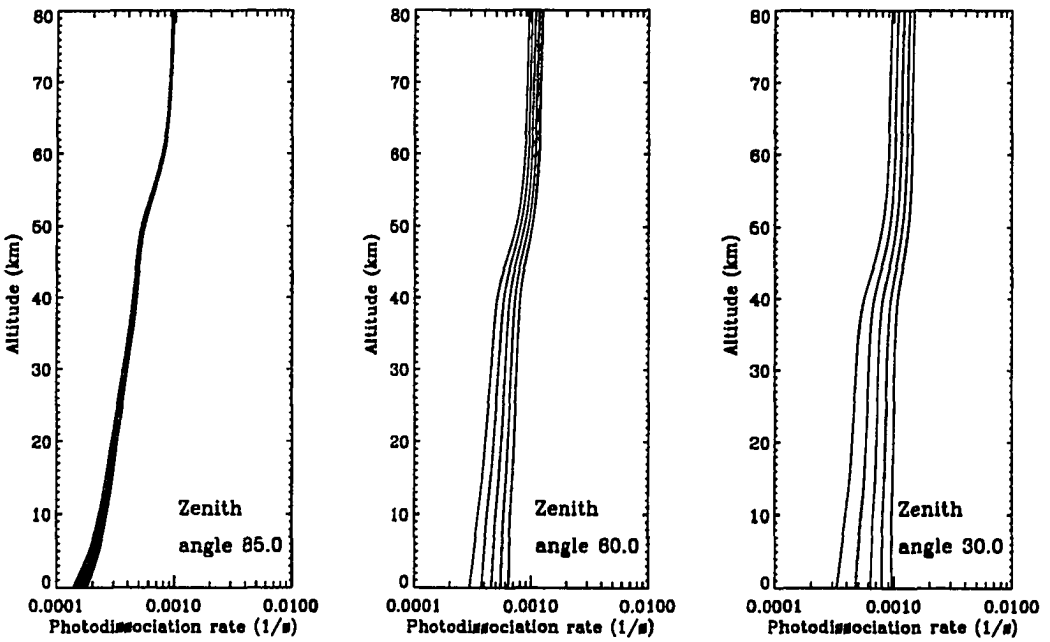

Figure 7.3: The $O_3 + h\nu \rightarrow O(^3P) + O_2$ photodissociation rate for different solar zenith angles and surface albedos. The rightmost curve in each figure is for $A_g = 1.0$, the next to the left for $A_g = 0.75$ and so on in steps of 0.25 to $A_g = 0.0$. A midlatitude summer atmosphere (Anderson et al. 1987) was used in the calculation.

present in the calculations of Luther and Gelinas (1976). The discrepancies have two plausible explanations; the use of different model atmospheres; and improved values for the relevant cross sections and quantum yields.

The combined uncertainties due to cross sections and quantum yields for O_3 photodissociating to the $O(^3P)$ and $O(^1D)$ channels are 1.1 and 1.4, respectively (cf. Table 4.1). For the $O(^1D)$ channel reflection from the surface has little influence in the stratosphere and may be neglected there. For the $O(^3P)$ channel the effect of varying the surface albedo is larger than the uncertainty in the relevant cross section and quantum yield. Latitudinal and zonal variations in surface albedo should, therefore, be included in photochemical models.

Finally, it is noted that the results presented here for the $O(^3P)$ channel are representative of photodissociation of molecules with similar spectral behaviour of their combined absorption cross section and quantum yield, such as NO, NO_2, HOCl, OClO (cf. Figs. 4.1 and 4.7).

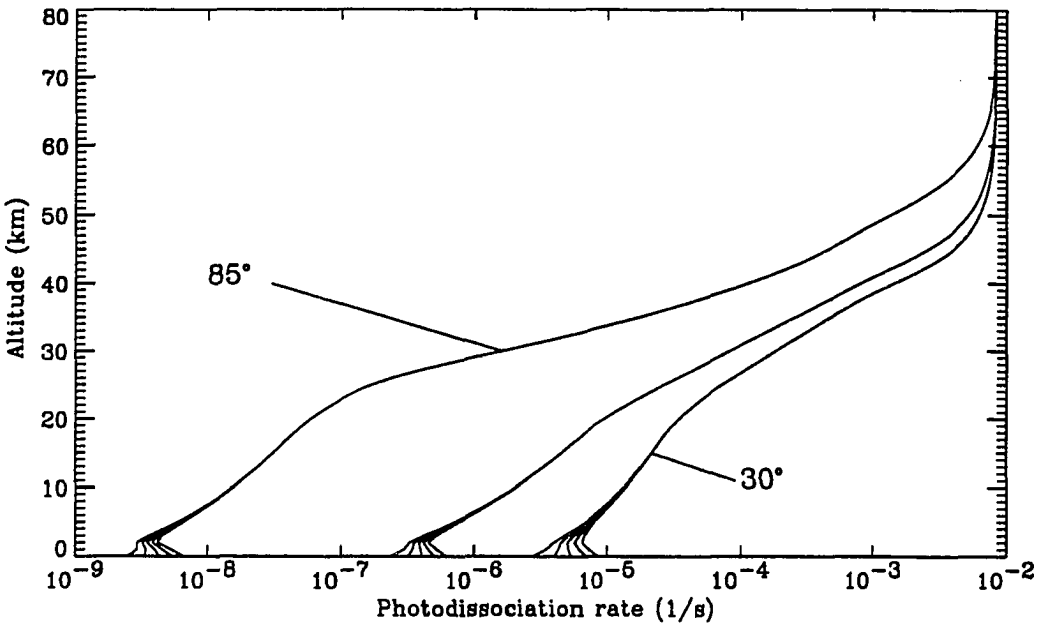

Figure 7.4: The $O_3 + h\nu \rightarrow O(^1D) + O_2$ photodissociation rate for solar zenith angles $\theta_0 = 30°, 60°$ and 85° and different surface albedos. The rightmost curve for each solar zenith angle is for $A_g = 1.0$, the next to the left for $A_g = 0.75$ and so on in steps of 0.25 to $A_g = 0.0$. A midlatitude summer atmosphere (Anderson et al. 1987) was used in the calculation.

7.2.2 The effects of clouds and aerosols

In Figs. 7.5–7.6 is shown O_2, O_3, O_3^*, NO_2 and CCl_4 photodissociation rates for a clear sky, for an aerosol loaded atmosphere and for an atmosphere with cirrus and water clouds. The selection of the O_2, O_3, O_3^*, NO_2 and CCl_4 photodissociation rates are partly due to the different spectral behavior of the O_2, O_3, NO_2 and CCl_4 absorption cross sections and quantum yields, and partly because of their respective importance for ozone chemistry.

The oxygen molecule, O_2, is photodissociated for wavelengths shorter than than 242 nm. Thus the O_2 photodissociation rate drops off rapidly when the atmosphere becomes optically thick for these short wavelengths as shown in Figs. 4.7 and 7.6. Photolysis of O_2 is the principal production mechanism for O_3 in the stratosphere through the reactions

$$O_2 + h\nu \rightarrow O + O \tag{7.1}$$

$$O + O_2 + M \rightarrow O_3 + M. \tag{7.2}$$

Here M represents a third body, typically N_2 or O_2, the main constituents of the Earth's atmosphere. A change in the O_2 photodissociation rate may alter the rate of production of O_3. The top row in Fig. 7.6 shows the O_2 photodissociation rate for various aerosol loaded atmospheres. Below 20 km a decrease in the O_2 photodissociation rate results when aerosols are introduced into the atmosphere. However, this decrease is well below the altitude of maximum O_3 production (approximately 40 km) due to reactions 7.1–7.2. Hence, the effect of aerosols on O_2 photodissociation rates, while present below 20 km, is expected to have little impact on the chemistry of the stratosphere. The shortwave radiation responsible for O_2 photolysis never penetrates to the cirrus and water clouds, hence they have no effect on the O_2 photodissociation rate.

As discussed above, O_3 has two photodissociation channels. Their respective response to different aerosol loadings is shown in the second and third row of Fig. 7.6, and the response to the presence of cirrus and water clouds in the two upper rows of Fig. 7.5. For the aerosol loaded atmospheres the $O_3 + h\nu \rightarrow O(^3P)+O_2$ channel is found to increase from 8% (background volcanic) to 22% (extreme volcanic) around the maximum aerosol concentration. The extreme volcanic model gives a decrease in the actinic flux below the aerosol layer, whereas the other aerosol loadings increase the actinic flux in the upper and middle troposphere and the lower stratosphere, at least for this particular solar elevation (30°). The different aerosol models have different absorption and scattering properties. This is the reason for their different influence on the O_3 photodissociation rate. The older the aerosol layer gets, the more effectively it scatters in the wavelength region of importance for photolysis rate calculations, cf. Fig. 7.2. This is also seen in the O_3^* photodissociation rates. A small increase in the O_3^* channel is observed above the aerosol layer for the extreme volcanic model, whereas below the rate is decreased for all aerosol models except the background aerosol model. The background aerosol model gives a small increase in the O_3^* photodissociation rate below the maximum aerosol concentration. This is due to increased scattering of radiation caused by the aerosols.

The changes in the O_3 and O_3^* photodissociation rates are rather small when introducing aerosols in the atmosphere. The same is true if a cirrus cloud is introduced, as evidenced by the dotted line in the first and second rows of Fig. 7.5. Cirrus clouds have an optical thickness of about $\tau \sim 1.0$, and their single scattering albedo is large for the wavelengths of importance for photodissocciation (Fig. 7.2). A 10% increase in the O_3 photodissociation rate above the cirrus cloud is due to reflection from the cloud. The surface albedo was taken to be $A_g = 0.0$. Assigning

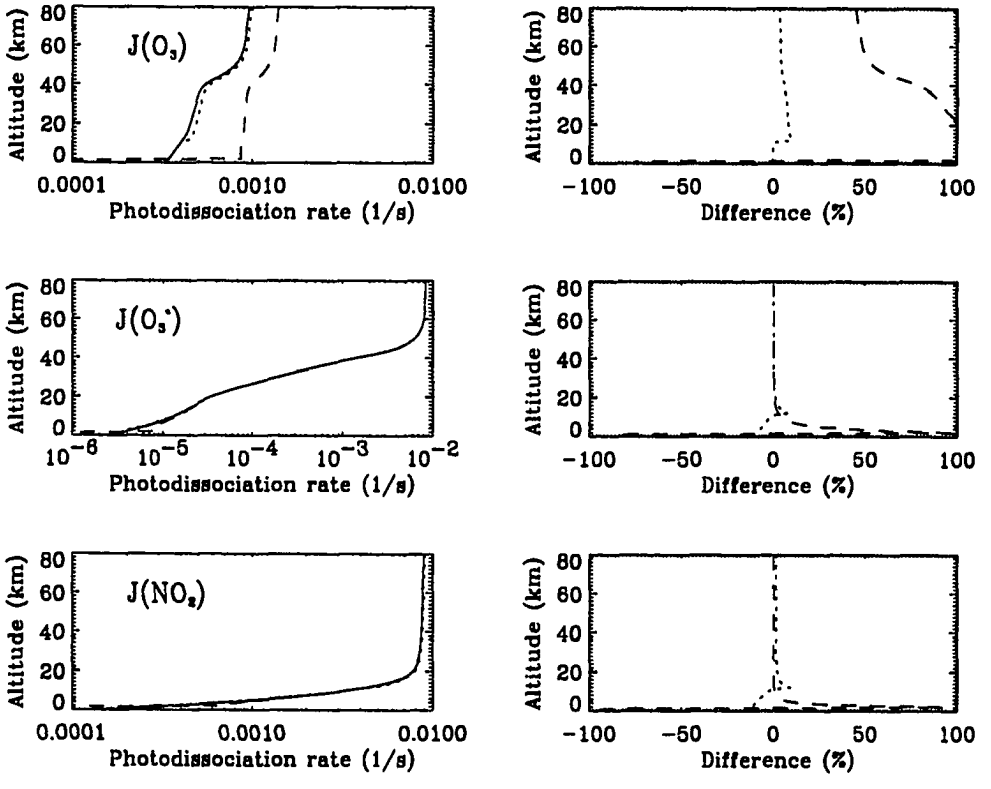

Figure 7.5: The left column shows O_3, O_3^* and NO_2 photodissociation rates for a clear sky (solid line) and an atmosphere with a cirrus cloud (dotted line) and a water cloud (dashed line). The right column shows the % difference between the clear sky situation and the different cloud cases. As a model atmosphere, the midlatitude summer atmosphere (Anderson et al. 1987) was adopted. The surface albedo $A_g = 0.0$ and the solar zenith angle $\theta_0 = 30.0$.

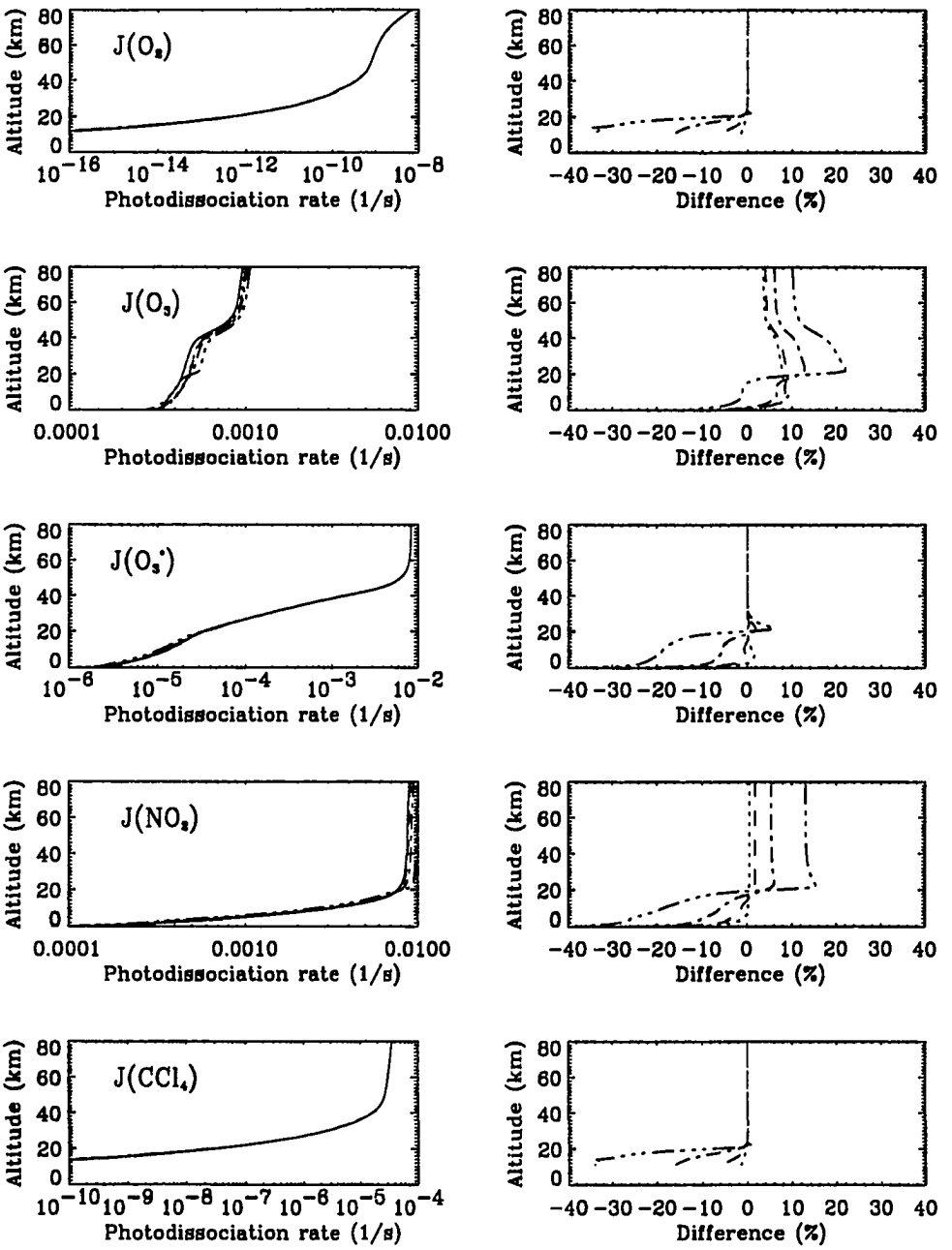

Figure 7.6: The left column shows O_2, O_3, O_3^*, NO_2 and CCl_4 photodissociation rates for a clear sky (solid line) and different aerosol loadings; background volcanic (dotted line), moderate volcanic (dashed line), high volcanic (dashed–dotted line) and extreme volcanic (dot–dot–dot–dashed line). The right column shows the % difference between the clear sky and the different aerosol loadings. The model atmosphere, solar zenith angle and surface albedo are as in Fig. 7.5. Summer conditions were used for the aerosol loadings.

a non–zero value to the surface albedo will allow the radiation to be reflected between the cloud and the surface, increasing the photodissocation rate further.

Water clouds are optically thick and efficiently scatter visible radiation. This is clearly seen in the upper row of Fig. 7.5. The effect of the low water cloud is similar to an increase in the surface albedo; this may be noted by comparison with Fig. 7.3. For the $O(^1D)$ channel the water cloud also will give an increased rate just above the cloud. The cloud effect rapidly falls off above the cloud for the same reasons, as explained above for surface albedo effects on O_3^* photolysis. Below the water cloud the O_3 and O_3^* photodissociation rates are reduced.

While photolysis of O_3 destroys ozone

$$O_3 + h\nu \rightarrow O(^3P \quad \text{or} \quad ^1D) + O_2 \tag{7.3}$$

there may be no net loss of ozone, since the oxygen atom rapidly recombines with O_2 to form O_3. Thus to understand fully the radiative effects of aerosols, cirrus, and water clouds on ozone chemistry, a photochemical model must be utilized.

Nitrogen dioxide, NO_2, plays a crucial role in the destruction of ozone in the stratosphere through the catalytic reaction cycle

$$NO + O_3 \rightarrow NO_2 + O_2 \tag{7.4}$$

$$NO_2 + O \rightarrow NO + O_2. \tag{7.5}$$

Photolysis of NO_2

$$NO_2 + h\nu \rightarrow NO + O(^3P) \tag{7.6}$$

produces NO and plays an important role in ozone chemistry. NO_2 photodissociates for $\lambda < 405$ *nm*. The different aerosol models affect the NO_2 photodissociation in much the same way as for O_3 photolysis (Fig. 7.6, fourth row). The discussion of the O_3 photolysis rate therefore pertains to NO_2 as well. The response of the NO_2 photolysis rate to cirrus and water clouds is similar to that of the O_3^* photolysis rate.

In the bottom row of Fig. 7.6 is shown the effect of aerosols on the CCl_4 photolysis rate. As for O_2 photolysis, the photolysis of CCl_4 takes place at wavelengths so short that the radiation never penetrates below the troposphere. Hence cirrus and water clouds have no effect on the CCl_4 photodissociation rate. The absorption cross section and consequently the photodissociation rate of CCl_4 are similar to those for the CFC–gases (Figs. 4.1 and 4.7). Hence the present discussion

for CCl_4 is valid for the CFC–gases as well. The CFC–gases are highly stable in the troposphere. However, once transported to the stratosphere they are exposed to ultraviolet radiation which dissociates them. One of the photodissociation products is chlorine atoms that participate in catalytic reaction cycles that destroy ozone,

$$Cl + O_3 \rightarrow ClO + O_2 \tag{7.7}$$

$$ClO + O \rightarrow Cl + O_2. \tag{7.8}$$

Hence, a change in the photolysis rate of the CFC–gases will change the number of chlorine atoms available for ozone destruction. From the fifth row of Fig. 7.6 it is seen that for the extreme volcanic model the CCl_4 photodissociation rate is decreased by more than 30% in the lower stratosphere, < 20 km. However, this is below the altitude where ozone destruction due to chlorine is strongest (25–35 km).

The results presented here are all for a solar zenith angle of 30°. For larger solar zenith angles the effect of the aerosols will be stronger due to the larger pathlengths encountered.

7.3 Warming/cooling rates

As with the photodissociation rates, the atmospheric warming/cooling rates depend directly on the atmospheric radiation field, through Eq. 6.7. Solar radiation warms the atmosphere while thermal terrestrial radiation mostly cools it. The solar radiation enters the atmosphere as a collimated beam and its magnitude varies with the solar zenith angle. Terrestrial radiation is diffuse in nature and varies with the temperature of the atmosphere and the surface. The importance of scattering has long been acknowledged in the solar part of the spectrum. The clear sky is blue due to Rayleigh scattering, which is included in many photochemical models. The effects of scattering of aerosols in the ultraviolet and visible part of the spectrum, have been included in models investigating the climatic impact of major volcanic events (e.g. Pollack et al. 1976, Pollack and Ackerman 1983, Hansen et al. 1992). Scattering of radiation in the solar infrared and the terrestrial part of the spectrum has largely been neglected, partly because it is believed to be of little importance, and partly because the radiation models employed in the terrestrial part of the spectrum have not been able to handle scattering (e.g. Goody and Yung 1989).

In this section the effect of different surface albedos, aerosol models and clouds on solar warming and terrestrial cooling rates will be studied. The radiation model developed earlier in this work will be used to include scattering throughout the spectrum.

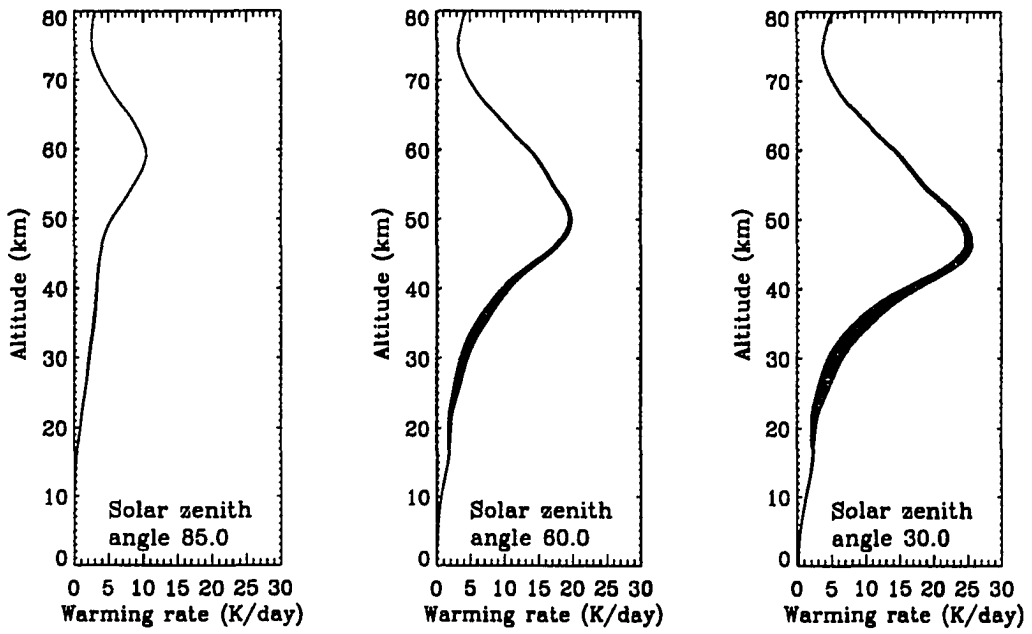

Figure 7.7: Instantaneous warming rates in the ultra–violet and the visible part of the spectrum, 116.3–730.0 *nm*, for different surface albedos. The rightmost curve in each figure is for $A_g = 1.0$, the next to the left for $A_g = 0.75$, and so on in steps of 0.25 to $A_g = 0.0$ for the leftmost curve. The midlatitude summer atmosphere (Anderson et al. 1987) was used in the calculations.

7.3.1 Surface albedo effects

In Fig. 7.7 instantaneous[1] warming rates for the ultra–violet and visible part of the spectrum, 116.3–730.0 *nm*, for different surface albedos are presented. Surface albedos of 0.0, 0.25, 0.5, 0.75 and 1.0 were considered. For zenith angles up to at least 60°, an enhancement of the surface albedo leads to an increase in the warming rate between 20 and 50 km. For a surface with an albedo equal to zero, no radiation is reflected back to the atmosphere. For a non–zero surface albedo, some of the reflected radiation will be absorbed when it traverses the ozone layer for the second time. This 'additional' radiation is responsible for the increase in the warming rate between 20 and 50 km. The Chapman layer structure of the warming rate due to radiation reflected from the surface is

[1]The warming/cooling rates are usually given in units of K/day. However, this does not imply that the warming/cooling rates have been averaged over the day. Unless noted, the warming/cooling rates displayed in this work are instantaneous rates. For terrestrial cooling rates the difference between instantaneous and diurnally averaged rates is rather small due to the large heat capacity of the oceans. The solar warming rate varies strongly with the solar zenith angle (Fig. 7.7).

different from that due to radiation incident at the top of the atmosphere.

For relatively small solar zenith angles (e.g. 30°), the difference in the warming rate for a low, $A_g = 0.0$, and large albedo, $A_g = 1.0$, may be as much as 50% at 33 km. The difference decreases with increasing solar zenith angle. This is due to the increased absorption of the incident radiation since larger optical paths are encountered for large solar zenith angles.

Most 2– and 3– dimensional chemical dynamical radiative models of the stratosphere set the surface albedo equal to 0.2 (see e.g. Brasseur et al. 1990). As shown above, the warming rate in the stratosphere varies substantially for different surface albedos. Hence, the dynamics of this region will be different for different surface albedos. Therefore 2– and 3– dimensional dynamical chemical radiative models should include information on both temporal and spatial variations of the earth's albedo.

As the solar zenith angle increases, the warming rate decreases, and the altitude of its maximum increases. In long term climatic model calculations one needs diurnally averaged warming rates. The diurnal average can be done in a variety of different ways, from 'brute force' integration (e.g. hour by hour), to simple averaging of warming rates calculated at two 'representative' solar zenith angles, or the somewhat more sophisticated scheme of Cogley and Borucki (1976). They compute the diurnal average of the radiation field, given by Beer's law in their work, by approximating the integral over the solar day by an exponential integral function. The effects of multiple scattering are not included in their diurnal averaging method. The variation of the warming rate with solar zenith angle, as shown in Fig. 7.7, suggests that great care should be excersized when performing diurnal averaging, especially for obtaining a recipe that is valid at all latitudes year–round. The topic of diurnal averaging warrants further study.

The different surface albedos considered here were kept constant throughout the spectrum. It would be desirable to include the wavelength dependence of the surface albedo. Most surface materials are non–reflecting (unit emissivity) for thermal infrared wavelengths ($\lambda \geq 4\mu m$). One important exception is a desert, which has an emissivity ~ 0.75, or albedo ~ 0.25 (Prabhakara and Dalu 1976). Other land surfaces have an emissivity ~ 0.95. In this work albedo effects for terrestrial radiation are not considered. The present calculations are thus representative for oceans which have unit emissivity. It is noted that the formalism allows albedo effects to be included for thermal radiation without any extra effort. The surface albedo has also benn set equal to zero in the solar infrared part of the spectrum ($0.8 < \lambda < 4\mu m$).

7.3.2 The effects of clouds and aerosols

The instantaneous solar and terrestrial warming rates for clear skies (solid line), and aerosol loaded and cloudy atmospheres are shown in the left columns of Figs. 7.8–7.9 . The extreme volcanic aerosol model may increase the solar warming by up to 10 K/day within the maximum of the aerosol layer (~ 20 km). This is due to increased absorption by the thick (optically) aerosol layer (Fig. 7.1). Backscattering of radiation leads to a further warming of ~0.3 K/day throughout the stratosphere above the aerosol layer. Below the aerosol layer less radiation is available, leading to a cooling compared with the clear sky situation. The response of the warming rate to the introduction of the high, moderate and background aerosol models, is similar to that for the extreme volcanic aerosol model, albeit much smaller in magnitude. This is due to the smaller optical depth of the high, moderate and background aerosol models.

As can be seen from Fig. 7.2, fresh volcanic aerosols (solid line in Fig. 7.2) have a significant single scattering albedo well into the terrestrial infrared part of the spectrum. For background aerosols and also for aged volcanic aerosols, the effect of scattering is negligible. This behaviour of the optical properties of the different aerosol models is reflected in the response of the terrestrial warming rate. The background, moderate and high aerosol models have a small effect on the terrestrial warming rate (Fig. 7.8). The extreme volcanic aerosol model on the other hand, gives a warming (less cooling) below the aerosol layer. This is due to upcoming terrestrial radiation being backscattered by the aerosol layer and absorbed by the underlying atmosphere. Above the aerosol layer a cooling is observed due to the decrease in available terrestrial radiation.

The summer aerosol models were used for calculating the solar and terrestrial warming rates. Calculations for the winter aerosol models were also performed. They exhibit similar behaviour, but the altitude of maximum response is shifted downwards due to the lower altitude of the aerosol layer (Fig. 7.1).

The net effect of introducing an aerosol layer is one of cooling below the aerosol layer and warming within and above the aerosol layer. This behaviour is supported by measurements of tropospheric and stratospheric temperatures and other model calculations (cf. e.g. Hansen et al. 1978). The magnitude of the cooling in the troposphere depends on the magnitude of the volcanic perturbation. The recent Mount Pinatubo eruption provided a unique opportunity for the climate modelling community to test its model predictions and sensitivities to aerosol perturbations. The cooling effect of Mount Pinatubo is expected to be larger than the warming due to increases in anthropogenic trace gases, CO_2, CFC's etc. (Hansen et al. 1992). Careful observations of

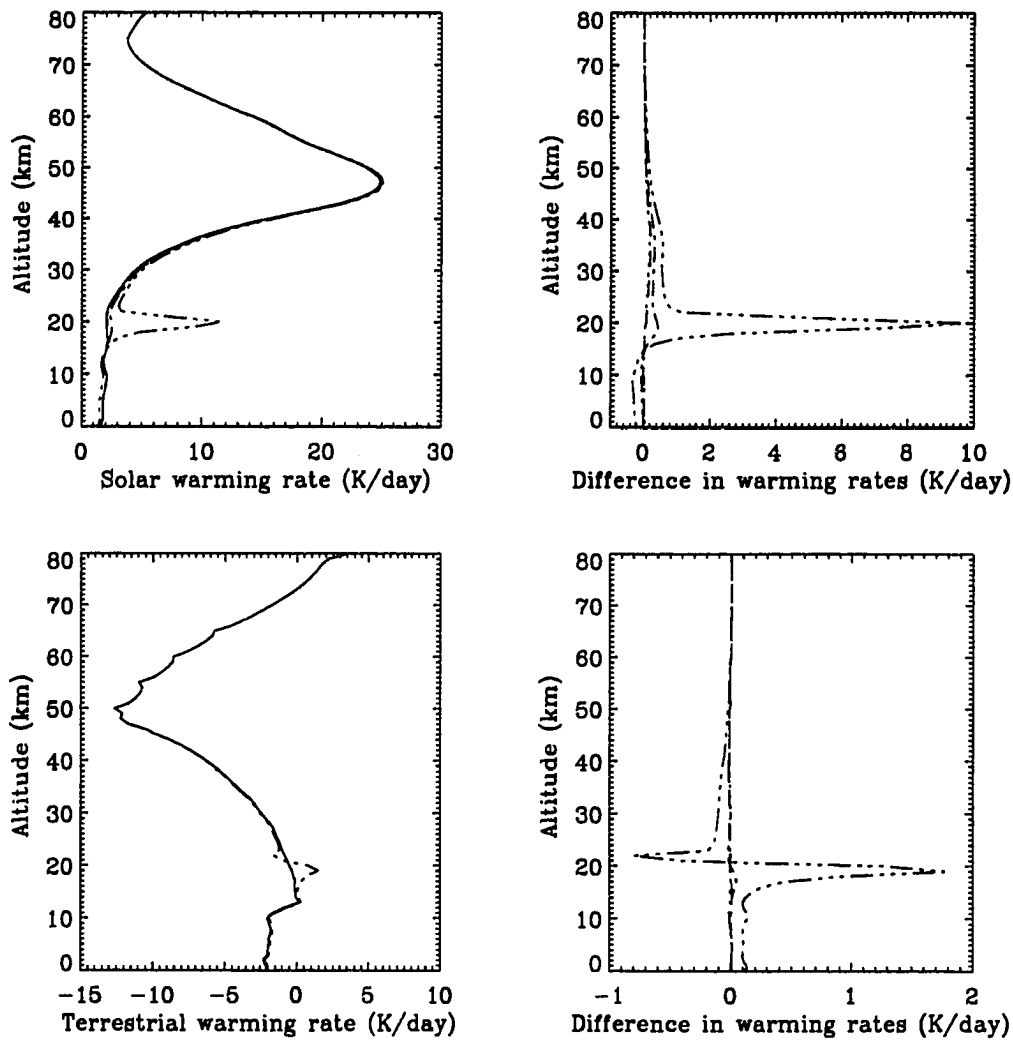

Figure 7.8: In the left column is shown the instantaneous solar and terrestrial warming rate for a clear sky (solid line), an atmosphere with background (dotted line), moderate volcanic (dashed line), high volcanic (dashed–dotted line) and extreme volcanic (dot–dot–dot–dashed line) aerosol content. The right column shows the difference between the clear sky and the different aerosol loaded atmospheres. The solar zenith angle was 30°, the surface albedo $A_g = 0.0$ and the midlatitude summer atmosphere was used (Anderson et al. 1987).

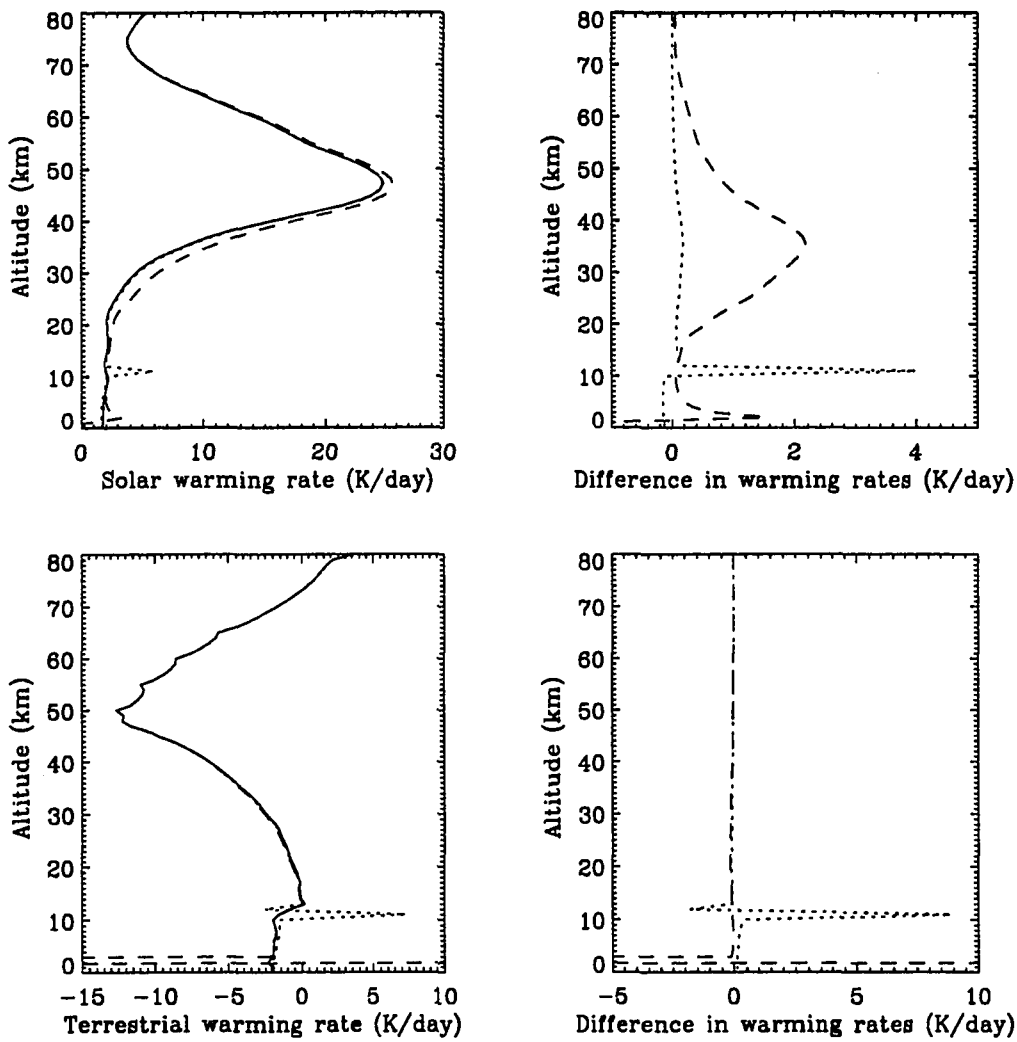

Figure 7.9: In the left column is shown the instantaneous solar and terrestrial warming rate for a clear sky (solid line), and atmosphere with a cirrus cloud (dotted line) and a water cloud (dashed line). The right column gives the difference between the clear sky warming rate and the cloudy sky warming rates. The surface albedo was $A_g = 0.0$, the solar zenith angle 30°, and the midlatitude summer atmosphere was used (Anderson et al. 1987).

atmospheric temperatures in the coming years will tell if the models are predicting observed temperature trends, assuming that the models correctly simulate changes in atmospheric states, such as changes in cloud effects.

The effects of cirrus and water clouds on solar and terrestrial warming rates are displayed in Fig. 7.9. The cirrus cloud very efficiently scatters solar radiation (cf. Fig. 7.2). This leads to an increase in the solar warming above the cloud due to backscattering of radiation. Below the cirrus cloud the solar warming rate decreases since less radiation is available for warming. The terrestrial warming rate reacts similarly to the cirrus cloud as it did to the extreme volcanic aerosol model, albeit the magnitude of the perturbation is larger for the cirrus cloud. A decrease in the terrestrial cooling is observed below the cirrus cloud. The net effect of cirrus clouds is one of warming the atmosphere.

Water clouds are seen to have no immediate effect on the terrestrial warming rate except inside and below the cloud. For the solar warming rate in the stratosphere the effect of water clouds is much the same as that resulting from an increase in the surface albedo, Fig. 7.7.

After a volcanic eruption aerosols will slowly spread over the whole Earth. Hence, being a global phenomenon, the effect of aerosols should be studied from a global perspective. In Fig. 7.10 is shown the global clear sky warming rate due to ultraviolet and visible radiation (116.3–730.0 nm). The rates are for mid–July and diurnally averaged by the method of Cogley and Borucki (1976). To produce Fig. 7.10 warming rates were calculated for latitudes 85°S, 60°S, 45°S, 15°S, 15°N, 45°N, 60°N and 85°N. The surface albedos at the different latitudes were selected to be 0.9, 0.8, 0.3, 0.05, 0.05, 0.3, 0.5 and 0.9 respectively. These surface albedo values were chosen to reflect winter and summer conditions in the southern and northern hemispheres. The model atmospheres of Anderson et al. (1987) were used. The seasonal and latitudinal characteristics of the model atmospheres are summarized in Table 7.1, dictating the choice of latitudes at which warming rates were calculated. The winter atmosphere model was used in the southern hemisphere, and the summer model was used in the northern hemisphere. For latitudes 85°S and 85°N the subartic winter and subarctic summer atmospheres were used respectively.

A detailed discussion of the warming rates shown in Fig. 7.10, and their influence on the general circulation is beyond the scope of this work (see however Brasseur and Solomon 1986 and Andrews, Holton and Leovy 1987). Introducing background aerosols in the atmosphere causes differences in the warming rate displayed in Fig. 7.11. A warming 'peak' is observed in the middle stratosphere at low latitudes and in the summer troposphere at high latitudes. For an extreme

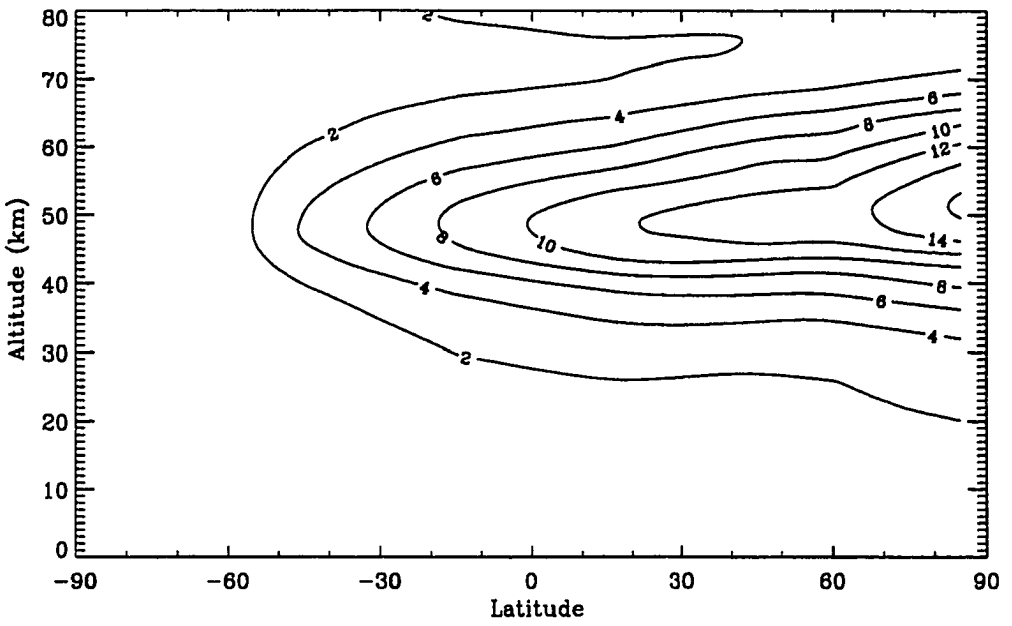

Figure 7.10: Mid-july diurnally averaged warming rates (K/day) for solar ultraviolet and visible radiation (116.3–730.0 nm) for a clear Rayleigh scattering atmosphere.

volcanic aerosol loading the picture is different (Fig. 7.12) with a large warming taking place within the aerosol layer. Furthermore there is a small, but significant cooling below the aerosol layer in the summer hemisphere. Computations for high and moderate volcanic aerosol loadings give differences in warming rates that lie between the two examples provided here representing extreme and background conditions.

From a single volcanic eruption it is unrealistic to get an extreme aerosol loading of global extent. However comparison of Figs. 7.11 and 7.12 gives an indication of the possible consequenses following a major volcanic eruption at high latitudes, either during the summer or winter season. A summer eruption will immediately lead to a cooling of the troposphere (cf. Fig. 7.12, 60°N). Six months later (Fig. 7.11, 60°S) the volcanic aerosols have little or no influence on the solar radiation. This is due to the decrease or absence of sunlight at high latitudes in the winter and the much smaller optical depth of the aerosol layer six months after the eruption. A winter eruption (Fig. 7.12, 60°S) will give a small warming of the stratosphere and no effect in the troposphere. Six months later (Fig. 7.11, 60°N) a warming of the troposphere is expected. Hence, a summer

Model	Latitude	Season
Tropic	15°N	Annual average
Midlatitude summer	45°N	July
Midlatitude winter	45°N	January
Subarctic summer	60°N	July
Subarctic winter	60°N	January

Table 7.1: The seasonal and latitudinal characteristics of the AFGL model atmospheres, Anderson et al. (1987).

eruption gives a tropospheric summer cooling and little or no changes in the subsequent winter temperatures, while a winter eruption will cause a small warming within the aerosol layer and a tropospheric warming the subsequent summer. This result is somewhat different from Pollack et al. (1976) who argued that 'an explosion during polar summer might lead to large particle warming in the summer and small particle warming in the winter. A winter eruption might lead to winter warming and summer cooling'. They did not however, present calculations to support their view. The terrestrial radiation has not been considered here. It is assumed to have little effect on the high, moderate and background aerosol models (Fig. 7.8) while the extreme model leads to a warming of the troposphere, but smaller than the cooling due to reduced incoming solar radiation. Finally it is noted that this problem should be studied in further detail by applying a radiative convective model.

7.4 The radiative effects of clouds and aerosols on chemistry and dynamics

So far the effects of clouds and aerosols on photodissociation and warming/cooling rates have been discussed. Changes in the photodissociation and warming/cooling rates will affect the chemistry and the dynamics of the atmosphere. The three major mechanisms that describe tropospheric and stratospheric chemistry are shown in Fig. 7.13. The continuity equation for an atmospheric specie n_i is given by

$$\frac{\partial n_i}{\partial t} + \nabla \cdot (n_i \mathbf{v}) = P(n_i) - n_i L(n_i). \tag{7.9}$$

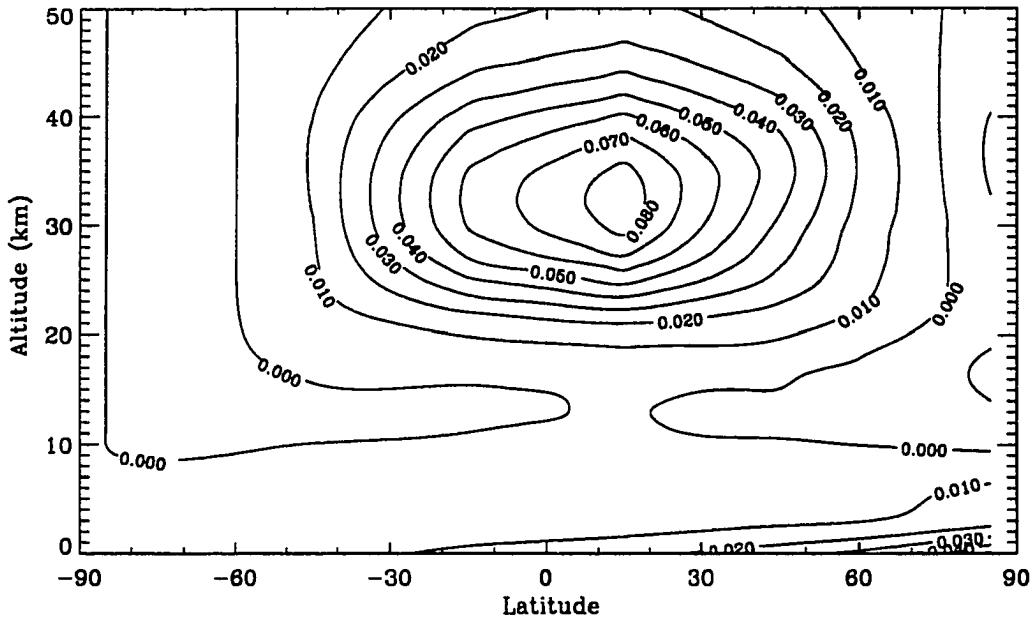

Figure 7.11: The difference in the solar diurnal warming rate after introducing the background aerosol model.

The production (P) and loss (L) terms include photochemical processes, cf. Table 4.1. Hence, as pointed out in Fig. 7.13, radiation may directly change the concentration of atmospheric species. Also, radiation warms and cools the atmosphere, thereby changing the temperature. Chemical reactions, $k_{reaction}$, are temperature sensitive, e.g. for bimolecular reactions

$$k_{reaction} = A\, e^{-B/T}. \tag{7.10}$$

Here A and B are reaction constants (DeMore et al. 1990). Radiatively induced temperature changes may thus influence the rate at which chemical processes proceed. Chemical processes may, in turn, change the concentration of radiatively important species like ozone, and hence cause changes in the radiation field.

The temperature field is related to the radiation field by the first law of thermodynamics, conservation of energy,

$$\frac{dT}{dt} - \frac{1}{c_p \rho_m}\frac{dp}{dt} = \frac{Q}{c_p}. \tag{7.11}$$

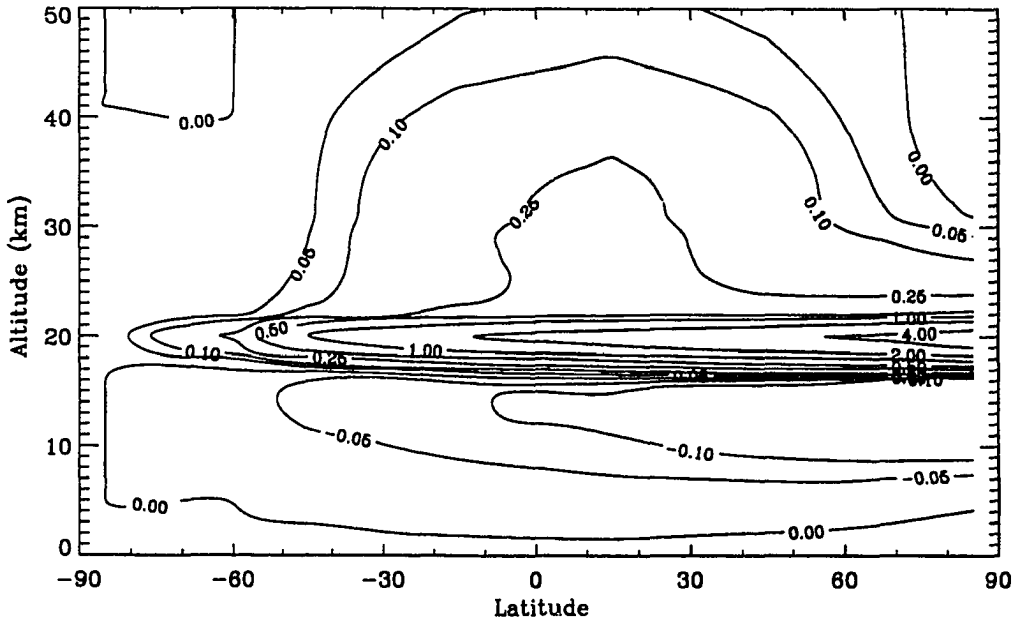

Figure 7.12: The difference in the solar diurnal warming rate after introducing the extreme volcanic aerosol model.

Here Q is the net diabatic heating, including radiative warming and cooling. All other quantities entering Eq. 7.11 are defined in chapter 6. The temperature field is connected to the wind field, v, by the momentum conservation equation

$$\frac{d\mathbf{v}}{dt} + \frac{1}{\rho_m}\nabla p + 2\boldsymbol{\Omega} \times \mathbf{v} = \mathbf{g} + \mathbf{F}, \tag{7.12}$$

where g is the gravitational acceleration, $\boldsymbol{\Omega}$ the angular rotation rate of the Earth and F the frictional force due to viscosity. The pressure p is related to the temperature by the ideal gas law. Together with the equation for conservation of mass

$$\frac{d\rho_m}{dt} + \rho_m \nabla \cdot \mathbf{v} = 0, \tag{7.13}$$

Eqs. 7.11–7.12, subject to appropriate boundary conditions, may be solved to yield the pressure, temperature and wind fields. These quantities may next be used in Eq. 7.9 to obtain concentrations of chemically active gases.

As indicated out in Fig. 7.13, dynamics may change the concentrations of atmospheric gases and hence affect the chemistry through the transport term $\nabla \cdot (n_i \mathbf{v})$ in Eq. 7.9. Dynamical effects

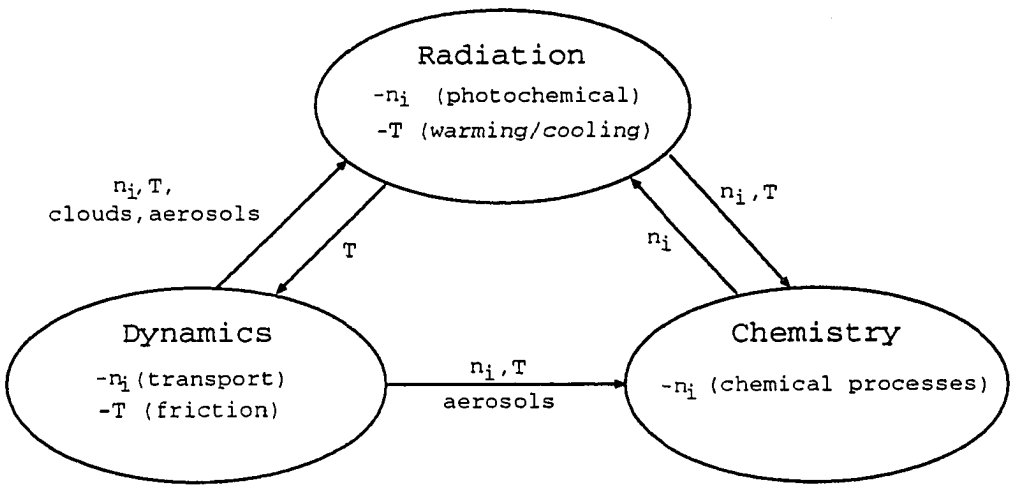

Figure 7.13: The coupling between the three major mechanisms necessary to describe stratospheric and tropospheric chemistry. The mechanisms directly change the atmospheric properties inside the circles and they interact through changes in the atmospheric properties indicated by arrows. For further details, see the text.

like gravity wave breaking, may change the temperature field and hence chemical reaction rates. Winds also play a vital role in distributing aerosols after volcanic eruptions. Aerosols take part in the chemistry in regions where they reside, both by changing the radiation field and through heterogeneous chemical processes. As well as affecting the distribution of aerosols, winds also directly participate in creating and moving clouds. Aerosols and clouds may greatly change the radiation field, as discussed above. Dynamics also affects the radiation field by changing trace gas concentrations, e.g. ozone, and the temperature field (absorption cross sections are temperature dependent, cf. chapter 3).

Radiation, dynamics and chemistry are all important when trying to understand the composition and behaviour of the atmosphere. In this work the effects of clouds and aerosols on radiative quantities, namely photodissociation and warming/cooling rates have been investigated. Below a simple estimate will be given of how changes in photodissociation and warming/cooling rates due to the presence of clouds and aerosols, affect dynamics and chemistry.

The radiation may affect the chemistry via changes in photodissociation rates and by causing changes in the local temperature. A complete picture of ozone chemistry involves reactions with hydrogen, nitrogen, carbon, chlorine and bromine compounds. For simplicity only oxygen

chemistry will be considered

$$(J_{O_2}) \quad O_2 + h\nu \rightarrow 2O \tag{7.14}$$

$$(k_2) \quad O + O_2 + M \rightarrow O_3 + M \tag{7.15}$$

$$(J_{O_3}) \quad O_3 + h\nu \rightarrow O_2 + O \tag{7.16}$$

$$(k_3) \quad O + O_3 \rightarrow 2O_2. \tag{7.17}$$

Eqs. 7.14–7.17 provide a zeroth order approximation to stratospheric ozone chemistry and allow an analytic expression to be written for the ozone concentration. Ignoring transport, the coupled continuity equations 7.9 for O_3 and O become

$$\frac{\partial[O_3]}{\partial t} = k_2(T)[O][O_2][M] - k_3(T)[O][O_3] - J_{O_3}[O_3] \tag{7.18}$$

$$\frac{\partial[O]}{\partial t} = J_{O_2}[O_2] + J_{O_3}[O_3] - k_2(T)[O][O_2][M] - k_3(T)[O][O_3]. \tag{7.19}$$

Here $[O_3]$, $[O_2]$, $[O]$ and $[M]$ denote O_3, O_2, O and air number densities respectively. The chemical reaction coefficients are $k_2(T) = 6.0 \times 10^{-34}(300/T)^{2.3}$ and $k_3(T) = 8.0 \times 10^{-12}\exp(-2060/T)$ (Brasseur and Solomon 1986). In the upper stratosphere and lower mesosphere O and O_3 are short lived (< 2 min.) and in approximate photochemical equilibrium. Setting $\partial[O_3]/\partial t = \partial[O]/\partial t = 0$ in Eqs. 7.18–7.19, eliminating $[O]$ in the resulting equations and noting that $k_2[O_2][M] \gg k_2[O_3]$ gives

$$[O_3]_{eq} = \sqrt{\frac{k_2(T)}{k_3(T)}[M][O_2]^2\frac{J_{O_2}}{J_{O_3}}}. \tag{7.20}$$

Hence, a 10% increase in J_{O_3} due to e.g. the presence of a cirrus cloud (Fig. 7.5) or an aerosol layer (Fig. 7.6), will lead to a $\sim$ 5% decrease in the ozone abundance in this simplified model. The presence of water clouds may increase J_{O_3} by as much as 100%, Fig 7.5, resulting in a 30% ozone decrease in the upper stratosphere and lower mesosphere by Eq. 7.20. It is noted that temperature feedback processes due to decreased ozone concentrations and reactions with other chemical compounds will modify these simple zeroth order results.

By changing the temperature field, radiative processes will also influence the speed of chemical reactions. The connection between temperature changes and ozone changes for oxygen chemistry is given by

$$\frac{\Delta[O_3]}{[O_3]} = \frac{1}{2}\frac{\Delta(k_2(T)/k_3(T))}{k_2(T)/k_3(T)} \tag{7.21}$$

from Eq. 7.20. Insertion of the above expressions for k_2 and k_3 gives

$$\frac{\Delta[O_3]}{[O_3]} = -\left(\frac{1.15}{T} + \frac{1030}{T^2}\right)\Delta T. \tag{7.22}$$

At the stratopause a typical value for the temperature is T=270 K. A temperature increase of 5 K will, by Eq. 7.22, results in a 19% decrease in ozone. A 5 K stratospheric temperature increase is not unrealistic e.g. 15–30 days after a major volcanic eruption (Fig. 7.8 and Labitzke and McCormick 1992). Ozone decreased by 7% at 24 km altitude following the El Chichon eruption (Michelangeli et al. 1989). It is noted that an increase in CO_2 will lead to increased cooling of the upper stratosphere and lower mesosphere. This cooling will increase the ozone abundance, hence increase solar warming of this region. Thus, at least in this simplified picture, an increase in CO_2 abundance will stabilize the temperature of this region.

As indicated in Fig. 7.13, radiation induced temperature changes will affect the dynamics. In general, the full set of energy, momentum and mass conservation equations, 7.11–7.13, must be solved to investigate this effect. The situation is simplified here by ignoring horizontal motion. The vertical velocity $w = dz/dt$, may be estimated by noting that in log–pressure coordinates

$$z = -H\ln(p/p_s) \tag{7.23}$$

where p_s is a standard reference pressure[2]. Using Eq. 7.23 and the relationship $dT/T = (R/c_p)(dp/p)$, the vertical velocity becomes (positive velocity upwards)

$$w = H\frac{c_p}{R}\frac{1}{T}\frac{dT}{dt}. \tag{7.24}$$

A much used value for H in the middle atmosphere is 7000 m. For dry air $R/c_p = 0.286$. In the lower midlatitude stratosphere the net diabatic warming rate is $\sim$ 1 K/day and the temperature 220 K, giving $w = 111$ m/day. Hence, an air parcel will take $\tau_w = 63$ days to traverse a vertical scale height H. An increase in the warming/cooling rate of 0.3 K/day following e.g. a volcanic eruption, gives $w = 144$ m/day and $\tau_w = 49$ days. Decreasing the warming/cooling rate by 0.3 K/day results in $w = 77$ m/day and $\tau_w = 90$ days. Hence, changes in the warming/cooling rate induced by the presence of tropospheric clouds and stratospheric aerosols may significantly alter the dynamics of the atmosphere.

As noted above, a full understanding of the impact of the radiative effects of clouds and aerosols on dynamics and chemistry requires the complete solution of Eqs. 7.9 and 7.11–7.13. Such a

[2]The z defined here will generally be different from the geometric vertical height used previously. However, the difference is generally insignificant, except near the ground (Andrews, Holton and Leovy 1987)

Change in variable	Variable	Effect of change		
		Photodissociation rate	Solar warming rate	Terrestrial cooling rate
↓	O_3 concentration	↑	↓	↓
↓	NO_2 concentration	↑	↓	–
↓	H_2O concentration	–	↓	↓
↓	Solar zenith angle	↑	↑	–
↑	Albedo	↑	↑	↓
↑	Temperature	↓	↑	↑
+	Water cloud	↑↓	↑↓	–↓
+	Cirrus cloud	↑↓	↑↓	↓↑
+	Stratospheric aerosols	↑↕	↑↓	↓↑

Table 7.2: The response of photodissociation, solar warming and terrestrial cooling rates to increases (↑), decreases (↓) or introduction (+) of some atmospheric properties. An increase in the rates is indicated by ↑ and a decrease by ↓. If two symbols appear in the same column then the first symbol refers to the region above the cloud or aerosol layer and the second to the region below. The magnitude and sign of the changes may be different for atmospheric conditions not considered in this work.

solution is beyound the scope of the present work. However, from the above examples it should be evident that clouds and aerosols should be included in realistic radiative chemical transport models of the atmosphere.

7.5 Summary

The effects of surface albedos, aerosols and cirrus and water clouds on photodissociation and warming/cooling rates have been investigated and are symbolically summarized in Table 7.2. After a major volcanic eruption (extreme volcanic aerosol model) aerosols may cause changes in O_3 and NO_2 photodissociation rates of 20%, which is comparable to the combined uncertainty in the respective absorption and quantum yields (Table 4.1). Aged aerosols (background model) have little (< 5%) effect on photodissociation rates. The effect of cirrus clouds is relatively small (< 10% for photodissociation of O_3). For water clouds large increases in the $O_3 + h\nu \rightarrow O(^3P)+O_2$ rate are found, comparable to increasing the surface albedo from $A_g = 0.0$ to $A_g = 1.0$. Thus photochemical models should include variations in surface albedo and cloud cover. To be consistent,

they should also include the radiative effects of aerosols, although the chemical effects of aerosols may be of larger significance.

Solar warming rates may vary up to 50% in the stratosphere due to changing surface albedo. Water clouds have a similar effect. The net effect of cirrus clouds is a warming of the troposphere and the stratosphere. Only an extreme volcanic aerosol loading affects the terrestrial warming rate, causing a warming below the layer and a cooling above it. Existing aerosols models give increased solar warming above the aerosol layer and a cooling below the aerosol layer. The net effect of aerosols is to cool the atmosphere below the aerosol layer and to warm it above the layer. While the warming/cooling effect of aerosols and cirrus clouds may seem to be small, typically some tenths K/day, or less, the cumulative effects over long time periods may be substantial. Hence they should not be ignored in terrestrial climate predictions.

Chapter 8

Summary and suggestions for further work

The primary goal of this work has been to develop a radiation model to study the effect of aerosols and clouds on atmospheric photodissociation and warming/cooling rates. In Chapter 2 the equation pertinent to radiation transport in the Earth's atmosphere was derived from the Boltzmann equation. Assuming a stratified spherical atmosphere, the radiative transfer equation was cast in a form amenable to solution and solved using the discrete ordinate method. Based on the general discrete ordinate solution, a new computationally efficient and stable two–stream algorithm, which accounts for spherical geometry was developed.

Chapter 3 was devoted to the calculation of the absorption and scattering properties of atmospheric molecules and particulate matter. Starting from first principles, the absorption cross sections for air molecules were derived using semi-classical theory. The absorption cross sections of the principal absorbers in the atmosphere, H_2O, CO_2 and O_3, vary erratically and rapidly with wavelength. Thus, calculations of atmospheric warming/cooling rates for which an integration over wavelength is required are computationally very expensive. An approximate method, the correlated–k distribution method, was employed to simplify the integration over wavelength. The major advantages of the correlated–k distribution method over other approximate methods is that it allows scattering processes to be included, and it naturally takes into account the change in the broadening of line widths with temperature and pressure. To describe the scattering processes of molecular and particulate matter, Mie theory pertinent for spherical particles was utilized.

In Chapter 4 an expression for the photodissociation rate was derived. To calculate photodissociation rates the intensity of the radiation field is needed. The radiation algorithm developed here was compared for the case of Rayleigh scattering with experimental values from a balloon flight. Further measurements are needed of both the direct and the scattered radiation to understand the differences between theory and experiment.

Computational speed and accuracy are important when calculating photodissociation rates for use in atmospheric chemistry models. A comparison between 16–stream and 2–stream computations shows that 2 streams are sufficient for most applications. Finally, the importance of including spherical geometry for large solar zenith angles was demonstrated.

Using the radiation model developed and described in preceeding chapters, ultraviolet (UV) and photosynthetic active radiation (PAR) for high and low latitudes for different ground albedos and atmospheric conditions were calculated in Chapter 5 . UV radiation is divided into UV–C (200–280 nm), UV–B (280–320 nm) and UV–A (320–400 nm) , PAR covers the wavelength region 400–700 nm. It was found that ozone depletion will increase the amount of UV–B radiation detrimental to life. Water clouds will diminish UV–B, UV–A and PAR for low albedos, while for high surface albedos water clouds increase the amount of radiation reaching the ground. The relative amount of harmful UV–B increases on an overcast day, the increase being largest at high latitudes for small ground albedos. The daily radiation doses vary little at low latitudes from month to month, but vary by more than a factor of 3 at high latitudes due to the change in the length of the day.

In Chapter 6 the warming/cooling rates were derived. Using results for the mean intensity and absorption cross sections from previous chapters, 'exact' and approximate warming/cooling rates were calculated. For the ultra–violet and the visible (116.3–730.0 nm) averaged cross sections were used, while in the solar near–infrared and terrestrial infrared line–by–line calculations served as a basis for developing correlated–k distribution approximations. The warming effects of O_3, O_2, NO_2 and H_2O were included for the solar part of the spectrum including the solar near–infrared. O_3, H_2O and CO_2 were included in the calculation of cooling rates in the terrestrial part of the spectrum.

The correlated–k distribution method was found to reduce substantially the number of monochromatic radiative transfer problems required to integrate across a given spectral interval, while still giving accurate results both for well–mixed, e.g. CO_2, and non–uniformly distributed gases, e.g. O_3. Factors of 400–2000 in savings of computer time over line–by–line calculations may be achieved, depending on the specific application, i.e. at which altitude accurate warming/cooling

rates are needed. The correlated–k distribution method used in this work is fast enough to find its applications in 1–D radiative–convective models. However, further approximations are needed for it to be applied in 3–D models.

As opposed to band models with one– or two–parameter pressure and temperature scaling approximations, the correlated–k distribution method includes the pressure and temperature dependence of the absorption cross section, thus allowing the troposphere and the stratosphere to be treated in a unified manner. Finally, the correlated–k distribution method allows multiple scattering to be included. Thus, the correlated–k distribution method in connection with a multiple scattering radiative transfer model, such as the one described in chapter 2, is well suited to study the effects of clouds and aerosols on the radiation field in the Earth's atmosphere.

In Chapter 7 the effects of surface reflection, aerosols, cirrus and water clouds on photodissociation and warming/cooling rates were investigated. After a major volcanic eruption, aerosols may cause changes in O_3 and NO_2 photodissociation rates of 20%, which is comparable to the combined uncertainty in the respective absorption and quantum yields. Aged aerosols have little ($< 5\%$) effect on photodissociation rates. The effect of cirrus clouds is relatively small ($< 10\%$ for photodissociation of O_3). For water clouds large variations are found in the photodissociation rates that are sensitive to visible radiation., e.g. $O_3 + h\nu \rightarrow O(^3P)+O_2$. These variations are comparable to increasing the surface albedo from $A_g = 0.0$ to $A_g = 1.0$. Photochemical models should account for variations in surface albedo and cloud cover. To be consistent, they should also include the radiative effects of aerosols, although the chemical effects of aerosols may be of greater significance.

Solar warming rates may vary up to 50% in the stratosphere due to changing surface albedo. Water clouds have a similar effect. The net effect of cirrus clouds is a warming of the troposphere and the stratosphere. Only extreme volcanic aerosol loading affects the terrestrial warming rate, causing a warming below the layer and a cooling above it. Aerosols give increased solar warming above the aerosol layer and cooling below the aerosol layer. The net effect of aerosols is to cool the atmosphere below the aerosol layer and to warm it above the layer. While the warming/cooling effect of aerosols and cirrus clouds may seem small, typically a tenths or less K/day, the cumulative effect over long time periods may be substantial. Hence they should not be ignored in terrestrial climate predictions.

The results of this thesis suggest several avenues of further research:

- Further development of the correlated–k distribution method is desirable to (1) include the

effect of overlapping lines from different gases, (2) improve the integration over wavelength, and (3) include the absorption bands of O_2 and CO_2 in the solar infrared and absorption bands of CH_4, N_2O and CFC–gases in the terrestrial infrared.

- With the new results reported by Rodgers et al. (1992) of carbon dioxide being in local thermodynamic equilibrium in the upper atmosphere, the radiation model could be extended into the thermosphere, i.e. 100–115 km.

- Inclusion of the present radiation model in 1– and 2–dimensional photochemical models of the troposphere and stratosphere would allow one to study both the chemical and radiative effects of clouds and aerosols.

- A surface albedo climatology should be compiled for inclusion in climate models. Experiments measuring surface albedos throughout the solar and terrestrial spectrum should be conducted.

- To aid in our understanding of recent underwater high resolution radiation measurements, the radiation model should be extended into the sea, i.e. refraction must be included.

- Radiation experiments measuring specific intensities and integrated radiative quantities, such as fluxes and mean intensities as a function of altitude and for different atmospheric conditions are needed, even for the 'simple' case of pure Rayleigh scattering. The present or similar radiation models may be used to aid in the design of radiation experiments. The experimental results should subsequently be used to test the validity of existing radiation models including that of the present study.

Appendix A

The existence of the α coefficient for thermal radiation

The α coefficient will always exist if

$$\frac{B_1^2}{B_2^2} - \frac{B_0}{B_2} > 0 \tag{A.1}$$

or, since $B_2 > 0$ for the Planck function,

$$B_1^2 - B_0 B_2 > 0 \tag{A.2}$$

where

$$B_i = B(T_i) = \int_{\nu_1}^{\nu_2} \frac{2h\nu^3}{c^2} \frac{d\nu}{exp(\frac{h\nu}{kT_i}) - 1} \tag{A.3}$$

and

$$T_1 = \frac{T_0 + T_2}{2} \tag{A.4}$$

Using eq. (A.3) it is found that the inequality (A.2) is fulfilled if

$$(exp(\frac{h\nu}{kT_2}) - 1)(exp(\frac{h\nu'}{kT_0}) - 1) - (exp(\frac{h\nu}{kT_1}) - 1)(exp(\frac{h\nu'}{kT_1}) - 1) > 0 \tag{A.5}$$

since $e^{h\nu/kT} > 1$ for $\nu > 0$ and $T > 0$. Using the relation:

$$e^x - 1 = \sum_{n=1}^{\infty} \frac{x^n}{n!} \tag{A.6}$$

the left hand side of eq. (A.5) may be written as

$$\sum_{n=1}^{\infty}\frac{(\frac{h\nu}{kT_2})^n}{n!}\sum_{m=1}^{\infty}\frac{(\frac{h\nu'}{kT_0})^m}{m!}-\sum_{n=1}^{\infty}\frac{(\frac{h\nu}{kT_1})^n}{n!}\sum_{m=1}^{\infty}\frac{(\frac{h\nu'}{kT_1})^m}{m!}=$$
$$\sum_{n=1}^{\infty}\sum_{m=1}^{\infty}\frac{h}{k}^{n+m}\left\{\frac{\nu^n\nu'^m}{n!m!}\left(\frac{1}{T_2^n}\frac{1}{T_0^m}-\frac{1}{T_1^{n+m}}\right)\right\} \tag{A.7}$$

In general $T_2^n T_0^m$ is not less than $T_1^{n+m}=(\frac{T_0+T_2}{2})^{n+m}$. However, for terms with $n=m$

$$\frac{1}{T_2^n}\frac{1}{T_0^n}-\frac{1}{T_1^{2n}}=\left(\frac{1}{T_2T_0}\right)^n-\left(\frac{1}{T_1^2}\right)^n>0 \tag{A.8}$$

since $T_1^2=\left(\frac{T_0+T_2}{2}\right)^2=\frac{1}{4}(T_0-T_2)^2+T_0T_2>T_0T_2$. For terms with $n>m$ n is set equal to $m+l$, $l>0$ and

$$\frac{1}{T_2^n}\frac{1}{T_0^m}-\frac{1}{T_1^{m+n}}=\frac{1}{T_2^l}\left(\frac{1}{T_2T_0}\right)^m-\frac{1}{T_1^l}\left(\frac{1}{T_1^2}\right)^m, \tag{A.9}$$

and for terms with $n<m$ n is set equal to $m-l$, $l>0$ which gives

$$\frac{1}{T_2^n}\frac{1}{T_0^m}-\frac{1}{T_1^{m+n}}=T_2^l\left(\frac{1}{T_2T_0}\right)^m-T_1^l\left(\frac{1}{T_1^2}\right)^m \tag{A.10}$$

For $T_2>T_1>T_0\gg 1$ the terms given by (A.9) may be ignored while (A.10) is always positive. For $T_2<T_1\ll 1$ the term (A.10) may be ignored and (A.9) is then always positive. A similar argument may be used for the case $T_0>T_1>T_2\gg 1$ and $T_0<T_1\ll 1$, by rewriting eq. (A.9)-(A.10) (set $m=n-l$ in (A.9) and $m=n+l$ in (A.10)).

For typical terrestrial and stellar temperatures ($T_i>100K$) one thus have that eq. (A.7) is always positive implying that the condition given in relation (A.2) is always fulfilled for the Planck function integrated over an arbitrary frequency interval. This shows that the α coefficient exists for most realistic applications.

Bibliography

Aida, M. (1977). 'Scattering of solar radiation as a function of cloud dimensions and orientation', *J. Quant. Spectrosc. Radiat. Transfer*, **17**, 303.

Allen, M. and J. E. Frederick (1982). 'Effective photodissociation cross sections for molecular oxygen and nitric oxide in the Schumann–Runge bands', *J. Atmos. Sci.*, **39**, 2066.

Anderson, G. P., S. A. Clough, F. X. Kneizys, J. H. Chetwynd and E. P. Shettle (1987). 'AFGL Atmospheric Constituent Profiles (0–120 km)', AFGL–TR–86–0110, AFGL (OPI), Hanscom AFB, MA 01736.

Anderson, P. W. (1949), 'Pressure broadening in the microwave and infra–red regions', *Phys. Rev.*, **76**, 647–661.

Andrews, D. G., J. R. Holton and C. B. Leovy (1987). *Middle atmosphere Dynamics*, (Academic Press).

Baranger, M. (1958a). 'Simplified Quantum–Mechanical Theory of Pressure Broadening', *Phys. Rev.*, **111**, 481.

Baranger, M. (1958b). 'Problem of Overlapping Lines in the Theory of Pressure Broadening', *Phys. Rev.*, **111**, 494.

Baranger, M. (1958c). 'General Impact Theory of Pressure Broadening', *Phys. Rev.*, **112**, 855.

Baym, G. (1969). *Lectures on Quantum Mechanics* (W. A. Benjamin, Inc., New York/Amsterdam).

Beck, A., L. S. Bernstein and D. C. Robertson (1989). 'MODTRAN: a moderate resolution model for LOWTRAN 7', Report GL–TR–89–0122, , Geophysics Laboratory, Air Force Systems Command, United States Air Force Base, MA 01731–5000, USA.

Bidigare, R. R. (1989). 'Potential effects of UV–B radiation on marine organisms of the southern ocean: distributions of phytoplankton and krill during austral spring', *Photochemistry and Photobiology*, **50**, 469–477.

Bohren, C. F. and D. R. Huffmann (1983). *Absorption and scattering of light by small particles* (Wiley & Sons, New York).

Bradley, S. G. (1982). 'Transient Radiative Influences of Cumulus Clouds on Surface Temperature and Fluxes', *J. Geophys. Res.*, **87**, 3135.

Brasseur, G. and S. Solomon (1986). *Aeronomy of the middle atmosphere*, (D. Reidel Publishing Company).

Brasseur, G. et al. (1990). 'An interactive chemical dynamical radiative two–dimensional model of the middle atmosphere', *J. Geophys. Res.*, **95**, 5639–5655.

Brühl, C. and P. J. Crutzen (1989). 'On the disproportionate role of tropospheric ozone as a filter against solar UB–B radiation', *Geophys. Res. Letters*, **16**, 703–706.

Calkins, J. and T. Thordardottir (1980). 'The ecological significance of solar UV radiation on aquatic organisms', *Nature*, **283**, 563–566.

Caldwell, M. M., L. B. Camp, C. W. Warner, and S. D. Flint (1986). 'Action spectra and their key role in assessing biological consequences of solar UV–B radiation change', In *Stratospheric ozone reduction, solar ultraviolet radiation and plant life*, R. C. Worrest and M. M. Caldwell, (Eds.), 87–111, (Springer Verlag, Berlin).

Cannon, C. J. (1984). 'Nonlocal perturbation techniques in radiative transfer', p. 157–172, in *Methods in Radiative Transfer Problems*, Kalkofen, W. (Ed.), (Cambridge University Press, New York).

Cercignani, C. (1975). *Theory and application of the Boltzmann equation* (Scottish Academic Press, Edinburgh and London).

Chapman, S. (1931). 'The absorption and dissociative or inonizing effect of monochromatic radiations in an atmosphere on a rotating Earth', *Proc. Phys. Soc., London*, **43**, 26–45.

Chandrasekhar, S. (1960). *Radiative Transfer* (Dover, New York).

Chou, M.–D., D. P. Kratz and W. Ridgway (1991). 'Infrared radiation parameterizations in numerical climate models', *J. of Climate*, 4, 424–437.

Clough, S. A., F. X. Kneizys, L. S. Rothman and W. O. Gallery (1981). 'Atmospheric spectral transmission and radiance: FASCOD1B', SPIE 277 *Atmospheric Transmission*, 152–166.

Cogley, A. C. and W. J. Borucki (1976). 'Exponential approximation for daily average solar heating or photolysis', *J. Atmos. Sci.*, **33**, 1347–1356.

Cooper, J. (1967). 'Broadening of Isolated Lines in the Impact Approximation Using a Density Matrix Formulation', *Rev. Mod. Phys.*, **39**, 167.

Cooper, J. (1969). 'Line Broadening', in *Lectures in Theoretical Physics*, Vol XI–C, *Atomic collision processes*, Eds. Geltman, Mahanthappa and Brittin, Gordon and Breach Science Publishers, New York.

Dahlback, A., T. Henriksen, S. H. H. Larsen and K. Stamnes. (1989). 'Biological UV–doses and the effect of an ozone layer depletion', *Photochemistry and Photobiology*, **49**, 621–625.

Dahlback, A. and K. Stamnes. (1990). 'A new spherical model for computing the radiation field available for photolysis and heating at twilight', *Planet. Space Sci.*, **39**, 671–683.

Davies, R. (1978). 'The Effect of Finite Geometry on the Three–Dimensional Transfer of Solar Irradiance in Clouds', *J. Atmos. Sci.*, **35**, 1712.

Davis, A., P. Gabriel, S. Lovejoy, D. Schertzer and G. L. Austin (1990). 'Discrete angle radiative transfer – part III: Numerical results and applications', *J. Geophys. Res.*, **95**, 11729.

DeMore, W. B. et al. (1990). 'Chemical kinetics and photochemical data for use in stratospheric modeling', Evaluation number 9, JPL publ. 90–1. Jet Propul. Lab., Pasadena, Calif.

Dickinson, R. E. (1973), 'Method of parameterization for infrared cooling between altitudes of 30 and 70 kilometers', *J. Geophys. Res.*, **78**, 4451–4457.

Dirac, P. A. M. (1958). *The Principles of Quantum Mechanics* (Oxford University Press, New York/London).

Edwards, D. P. (1988). 'Atmospheric transmittance and radiance calculations using line–by–line computer models', SPIE **298** *Modelling of the Atmosphere.*

Edwards, D. P. (1992). 'A general line–by–line atmospheric transmittance and radiance model', NCAR Technical note, NCAR/TN-367+STR. NCAR, Boulder, Colorado.

Ellingson, R. G. (1982). 'On the Effects of Cumulus Dimensions on Longwave Irradiance and Heating Rate Calculations', *J. Atmos. Sci.*, **39**, 886.

Ellingson, R. G., and Y. Fouquart (1991). 'The Intercomparison of Radiation Codes in Climate Models: an Overview', *J. Geophys. Res.*, **96**, 8925–8927.

Farman, J. C., B. G. Gardiner and J. D. Shanklin (1985). 'Large losses of total ozone in Antarctic reveal seasonal ClO_x/NO_x interaction', *Nature*, **315**, 207–210.

Feynman, R. P. (1949). 'The Theory of Positrons', *Phys. Rev.*, **76**, 749.

Fouquart, Y., B. Bonnel and V. Ramaswamy (1991). 'Intercomparing shortwave radiation codes for climate studies', *J. Geophys. Res.*, **96**, 8955–8968.

Frederick, J. E. and D. Lubin (1988). 'The budget of biologically active ultraviolet radiation in the earth–atmosphere system', *J. Geophys. Res.*, **93**, 3825–3832.

Frederick, J. E., and J. E. Mentall (1982), 'Solar irradiance in the stratosphere: implications for the Herzberg continuum absorption of O_2', *Geophys. Res. Lett.*, **9**, 461–464.

Gabriel, P., S. Lovejoy, A. Davis, G. L. Austin and D. Schertzer (1990). 'Discrete angle radiative transfer – part II: Renormalization approach for homogeneous and fractal clouds', *J. Geophys. Res.*, **95**, 11717.

Goldstein, H. (1980). *Classical Mechanics*, second edition, (Addison–Wesley).

Goody, R. M. (1964). *Atmospheric Radiation: Theoretical basis* (Oxford University Press, New York).

Goody, R. M. and Y. L. Yung (1989). *Atmospheric Radiation: Theoretical basis* (Oxford University Press, New York).

Goody, R., R. West, L. Chen and D. Crisp (1990). 'The correlated–k method for radiation calculations in nonhomogeneous atmospheres', *J. Quant. Spectrosc. Radiat. Transfer*, **42**, 539–550.

Hansen, G. A. (1992). 'Submersible Monochromator Instrumentation and Measurements', Cand. Scient. thesis, Institute of Mathematical and Physical Sciences, Departement of Physics, University of Tromsø, Norway.

Hansen, J., W.–C. Wang and A.A. Lacis (1978), 'Mount Agung eruption provides test of a global climatic perturbation', *Science*, **199**, 1065–1068.

Hansen, J., and A.A. Lacis (1990), 'Sun and dust versus greenhouse gases: an assessment of their relative roles in global climate change', *Nature*, **346**, 713–719.

Hansen, J., A. Lacis, R. Ruedy and M. Sato (1992), 'Potential climate impact of Mount Pinatubo eruption', *Geophys. Res. Lett.*, **19**, 215–218.

Harshvardhan, J. A. Weinman and R. Davies (1981). 'Transport of Infrared Radiation in Cuboidal Clouds', *J. Atmos. Sci.*, **38**, 2500.

Herman, J. R. and J. E. Mentall (1982). 'The direct and scattered solar flux within the stratosphere', *J. Geophys. Res.*, **87**, 1319–1330.

Hu, Y. X. and K. Stamnes (1992). 'An accurate parameterization of the radiative properties of water clouds suitable for use in climate models', *J. Climate*, in press.

Huber, D. L. and J. H. Van Vleck (1966). 'The role of Boltzmann factors in line shape', *Rev. Mod. Phys.*, **38**, 187.

Isaksen, I. S. A., K. H. Midtbø, J. Sunde and P. J. Crutzen (1977). 'A simplified method to include molecular scattering and reflection in calculations of photon fluxes and photodissociation rates', *Geophys. Norv.*, **31**, 11-26.

Jackson, J. D. (1975). *Classical Electrodynamics*, second edition, (John Wiley & Sons Inc.).

Kiehl, J. T., and S. Solomon (1986). 'On the radiative balance of the stratosphere', *J. Atmos. Sci.* **43**, 1525–1534.

Kratz, D. P. and R. D. Cess (1985). 'Solar absorption by atmospheric water vapor: a comparison of radiation models' *Tellus*, **37 B**, 53–63.

Kylling, A. (1991). 'Discrete ordinate solution of the radiative transfer equation in the 'polarization normal wave representation", *Astrophys. J.*, **383**, 243–249.

Kylling, A. and K. Stamnes (1992). 'Efficient yet accurate solution of the linear transport equation in the presence of internal sources: the exponential–linear approximation', *J. Comp. Phys.*, **102**, 265–276.

Kylling, A., K. Stamnes and S.-C. Tsay (1992). 'A new, numerically stable algorithm for two–stream–method radiative transfer and particle transport in planetary atmospheres', in preparation.

Labitzke, K., and M. P. McCormick (1992). 'Stratospheric temperature increases due to Pinatubo aerosols', *Geophys. Res. Letters*, **19**, 207–210.

Lacis, A., A. and J. E. Hansen (1974), 'A parameterization for the absorption of solar radiation in the Earth's atmosphere', *J. Atmos. Sci.*, **31**, 118–133.

Lacis, A., A. and V. Oinas (1991), 'A description of the correlated k distribution method for modeling nongray gaseous absorption, thermal emission, and multiple scattering in vertically inhomogenous atmospheres', *J. Geophys. Res.*, **96**, 9027–9063.

Lary, D. J., and J. A. Pyle (1991a), 'Diffuse radiation, twilight, and photochemistry – I', *J. Atmospheric. Chem.*, **13**, 373–392.

Lary, D. J., and J. A. Pyle (1991b), 'Diffuse radiation, twilight, and photochemistry – II', *J. Atmospheric. Chem.*, **13**, 393–406.

Lee, J. A. H. (1989). 'The relationship between malignant melanoma of skin and exposure to sunlight', *Photochemistry and Photobiology*, **50**, 493–496.

Lenoble, J. (Ed.) (1985). *Radiative Transfer in Scattering and Absorbing Atmospheres: Standard Computation Procedures* (C. A. Deepak, Hampton, VA).

Le Quéré, F., and C. Leforestier (1990), 'Quantum exact three–dimensional study of the photodissociation of the ozone molecule', *J. Chem. Phys.*, **92**, 247–253.

Le Quéré, F., and C. Leforestier (1991), 'Hyperspherical formulation of the photodissociation of ozone', *J. Chem. Phys.*, **94**, 1118–1126.

Lovejoy, S., A. Davis, P. Gabriel, G. L. Austin and D. Schertzer (1990). 'Discrete angle radiative transfer – part I: Scaling and similarity, universality and diffusion', *J. Geophys. Res.*, **95**, 11699.

Lovelock, J. E. (1979). *Gaia, a new look at life on earth* (Oxford University Press).

Luther, F. M. and R. J. Gelinas (1976), 'Effect of Molecular Multiple Scattering and Surface Albedo on Atmospheric Photodissociation Rates', *Journ. of Geophys. Res.*, **81**, 1125–1132.

Madronich, S. (1987). 'Photodissociation in the atmosphere: 1. Actinic flux and the effects of ground albedo and clouds', *J. Geophys. Res.*, **92**, 9740-9752.

McKee, T. B. and S. K. Cox. (1976). 'Scattering of Visible Radiation by Finite Clouds', *J. Atmos. Sci.*, **31**, 1885.

McKellar, B. H. J. and M. A. Box. (1981). 'The Scaling Group of the Radiative Transfer Equation', *J. Atmos. Sci.*, **38**, 1063.

McKinley, A. F., B. L. Diffey, (1987). 'A reference action spectrum for ultra–violet induced erythema in human skin', In *Human exposure to ultraviolet radiation: risk and regulations*, W. F. Passchier and B. F. M. Bosnjakovic, (Eds.), (*Excerpta Medica*, International Congress Series 744, Amsterdam).

Meador, W. E., and W. R. Weaver (1980). 'Two–stream approximation to radiative transfer in planetary atmospheres: A unified description of existing methods and a new improvement,' *J. Atmos. Sci.*, **37**, 630.

Meier, R. R., D. E. Anderson, Jr., and M. Nicolet (1982), 'Radiation transfer in the troposphere and stratosphere from 240–1000 nm, I. General Analysis.' *Planet. Space Sci.*, **33**, 923–933.

Michelangeli, D. V., M. Allen and Y. L. Yung (1989), 'El Chichon volcanic aerosols: Impact of radiative, thermal, and chemical perturbations, *Journ. of Geophys. Res.*,**94**, 18,429–18,443.

Michelangeli, D. V., M. Allen, Y. L. Yung, R.–L. Shia, D. Crisp and J. Eluszkiewicz (1992), 'Enhancement of atmospheric radiation by an aerosol layer', *Journ. of Geophys. Res.*,**97**, 865–874.

Mihalas, D. (1978). *Stellar Atmospheres* (W. H. Freeman and Company, New York).

Mlynczak, M. G., and S. Solomon (1991). 'On the efficiency of solar heating in the middle atmosphere', *Geophys. Res. Letters*, **18**, 1201–1204.

Molina, L. T. and M. J. Molina (1986), 'Absolute Absorption Cross Sections of Ozone in the 185- to 350–nm Wavelength Range', *Journ. of Geophys. Res.*, **91**, 14,501–14,508.

NASA Conference Publication 3042, (1988) 'Two–dimensional intercomparison of stratospheric models', Proceedings of workshop held at Virgina Beach, Virgina, September 11–16, 1988.

Neto, J. J. Soares, and J. Linderberg (1991), 'Photodissociation of triatomic molecules: Formulation of the three–dimensional problem', *J. Chem. Phys.*, **95**, 8022–8028.

M. Nicolet, R. R. Meier and D. E. Anderson, Jr. (1982), 'Radiation transfer in the troposphere and stratosphere from 240–1000 nm, II. Numerical Analysis.' *Planet. Space Sci.*, **33**, 935–983.

Nicolet, M. (1984). 'On the molecular scattering in the terrestrial atmosphere: an empirical formula for its calculation in the homosphere'. *Planet. Space Sci.*, **32**, 1467–1468.

Nicolet, M. (1989). 'Solar spectral irradiances with their diversity between 120 and 900 *nm*', *Planet. Space Sci.*, **37**, 1249–1289.

Park, J. H., L. S. Rothman, C. P. Rinsland, H. M. Pickett, D. J. Richardson and J. S. Namkung (1987). 'Atlas of absorption lines from 0 to 17900 cm^{-1}', NASA Reference Publication 1188.

Pollack, J. B., O. B. Toon, C. Sagan, A. Summers, B. Baldwin and W. van Camp (1976). 'Volcanic explosions and climatic change: a theoretical assessment', *J. Geophys. Res.*, **81**, 1071–1083.

Pollack, J. B., and T. P. Ackerman (1983), 'Possible effects of the El Chichon volcanic cloud on the radiation budget of the northern tropics', *Geophys. Res. Lett.*, **10**, 1057–1060.

Prabhakara, C., and G. Dalu (1976). 'Remote sensing of the surface at 9 μm over the globe', *J. Geophys. Res.*, **81**, 3719–3724.

Press, W. H., B. P. Flannery, S. A. Teukolsky and W. T. Vetterling (1985). *Numerical Recipes: The Art of Scientific Computing*, (Cambridge University Press).

Ramanathan, V., E. J. Pitcher, R. C. Malone and M. L. Blackman (1976). 'Radiative transfer within the Earth's troposphere and stratosphere: a simplified radiative–convective model', *J. Atmos. Sci.* **33**, 1330–1346.

Ramanathan, V., E. J. Pitcher, R. C. Malone and M. L. Blackman (1983). 'The response of a spectral general circulation model to refinements in radiative processes', *J. Atmos. Sci.* **40**, 605–630.

Ramanathan, V., R. J. Cicerone, H. B. Singh and J. T. Kiehl (1985). 'Trace gas trends and their potential role in climate change', *J. Geophys. Res.*, **90**, 5547–5566.

Ramanathan, V., R. D. Cess, E. F. Harrison, P. Minnis, B. R. Barkstrom, E. Ahmad and D. Hartmann, (1989), 'Cloud–radiative forcing and climate: results from the earth radiation budget experiment', *Science*, **243**, 57–63.

Ramaswamy, V., and S. M. Freidenreich (1991). 'Solar radiative line–by–line determination of water vapor absorption and water cloud extinction in inhomogeneous atmospheres', *J. Geophys. Res.*, **96**, 9133–9157.

Rees, M. H. (1989). *Physics and chemistry of the upper atmosphere*, (Cambridge University Press).

Reif, F. (1965). *Fundamentals of Statistical and Thermal Physics*, (McGraw–Hill Book).

Rodgers, C. D., F. W. Taylor, A. H. Muggeridge, M. López–Puertas and M. A. López–Valverde (1992). 'Local thermodynamic equilibrium of carbon dioxide in the upper atmosphere', *Geophys. Res. Letters*, **19**, 589–592.

Rothman, L. S. et al. (1987). 'The HITRAN database: 1986 edition', *Applied Optics*, **26**, 4058-4097.

Rottmann, K. (1960). *Mathematische Formelsammlung*, (Bibliographisches Institut Mannheim/Wien/Zürich).

Setlow, R. B.,(1974). 'The wavelenghts in sunlight effective in producing skin cancer: a theoretical analysis', *Proceedings of the National Academy of Science*, **71**, 3363–3366.

Shardanand and A. D. Pradad Rao (1977), 'Collision–induced absorption of O_2 in the Herzberg continuum', *J. Quant. Spectrosc. Radiat. Transfer*, **17**, 433–439.

Shettle E. P., and R. W. Fenn (1976), 'Models of atmospheric aerosols and their optical properties', in AGARD Conference Proceedings No. 183, *Optical Propagation in the Atmosphere*, AGARD–CP–183, (NTIS, ADA 028615).

Shettle E. P. (1989), 'Models of aerosols, clouds and precipitation for atmospheric propagation studies', in AGARD Conference Proceedings No. 454, *Atmospheric propagation in the uv, visible, ir and mm-region and related system aspects.*

Smith, R. C., and K. S. Baker (1989). 'Stratospheric ozone, middle ultravioloet radiation and phytoplankton productivity', *Oceanography*, Nov., 4–10.

Stamnes, K. and R. A. Swanson. (1981). 'A new look at the discrete ordinate method for radiative transfer calculations in anisotropically scattering atmospheres', *J. Atmos. Sci.*, 38, 387-399.

Stamnes, K. and P. Conklin. (1984). 'A New Multi–Layer Discrete Ordinate Approach to Radiative Transfer in Vertically Inhomogeneous Atmospheres', *J. Quant. Spectrosc. Radiat. Transfer*, 31, 273.

Stamnes, K. (1986). 'The theory of multiple scattering of radiation in plane parallel atmospheres', *Rev. Geophys.*, 24, 299-310.

Stamnes, K., S.-C. Tsay, W. Wiscombe and K. Jayaweera. (1988). 'Numerically stable algorithm for discrete-ordinate-method radiative transfer in multiple scattering and emitting layered media'. *Applied Optics*, 27, 2502-2509.

Stamnes, K. and S.-C. Tsay (1990). 'Optimum spectral resolution for computing atmospheric heating and photodissociation rates', *Planet. Space. Sci.*, 38, 807-820.

Stephens, G. L. (1988a). 'Radiative transfer through arbitrarily shaped optical media. Part I: A general method of solution', *J. Atmos. Sci.*, 45, 1818.

Stephens, G. L. (1988b). 'Radiative transfer through arbitrarily shaped optical media. Part II: Group theory and simple closures', *J. Atmos. Sci.*, 45, 1837.

Tevini, M. and A. H. Teramura (1989). 'UV–B effects on terrestrial plants', *Photochemistry and Photobiology*, 50, 479–487.

Tsay, S.-C., K. Stamnes and K. Jayaweera. (1990). 'Radiative transfer in stratified atmospheres: Development and verification of a unified model', *J. Quant. Spectrosc. Radiat. Transfer*, 43, 133-148.

Tsay, S.-C., and K. Stamnes (1992). 'Ultraviolet radition in the Arctic: The impact of potential ozone depletions and cloud effects', *J. Geophys. Res.*, **97**, 7829–7840.

Turco, R. P., (1975). 'Photodissociation rates in the atmosphere below 100 km', *Geophys. Sur.*, **2**, 153–192.

Turco, R. P., R. C. Whitten and O. B. Toon (1982). 'Stratospheric aerosols: observation and theory', *Rev. Geophys. and Space Phys.*, **20**, 233–279.

Twomey, S., (1991). 'Aerosols, clouds and radiation', *Atmospheric Environment*, **25**, 2435–2442.

Urbach, F. (1989). 'The biological effects of increased ultraviolet radiation: an update' *Photochemistry and Photobiology*, **50**, 439–441.

Van Vleck, J. H. and D. L. Huber (1977). 'Absorption, emission and linebreadths: A semihistorical perspective', *Rev. Mod. Phys.*, **49**, 939.

Vetterling, W. T., S. A. Teukolsky Press, W. H. and B. P. Flannery, (1985). *Numerical Recipes: Example Book (FORTRAN)*, (Cambridge University Press).

Wallace, J. M. and P. V. Hobbs (1977), *Atmospheric Science, An Introductory Survey*, (Academic Press, New York).

Welch, R. and W. Zdunkowski (1981a). 'Radiative characteristics of noninteracting cumulus cloud fields. I: Parameterizations for finite clouds', *Contrib. Atmos. Phys.*, **54**, 258–272.

Welch, R. and W. Zdunkowski (1981b). 'Radiative characteristics of noninteracting cumulus cloud fields. I: Calculations for cloud fields', *Contrib. Atmos. Phys.*, **54**, 273–285.

Wendling, P. (1977). 'Albedo and Reflected Radiance of Horizontally Inhomogeneous Clouds', *J. Atmos. Sci.*, **34**, 642.

Weng, F. (1992a). 'A multi-layer discrete-ordinate method for vector radiative transfer in a vertically-inhomogeneous, emitting and scattering atmosphere–I. Theory', *J. Quant. Spectrosc. Radiat. Transfer*, **47**, 19–33.

Weng, F. (1992b). 'A multi-layer discrete-ordinate method for vector radiative transfer in a vertically-inhomogeneous, emitting and scattering atmosphere–II. Application', *J. Quant. Spectrosc. Radiat. Transfer*, **47**, 35–42.

West, R., D. Crisp and L. Chen (1990). 'Mapping transformations for broadband atmospheric radiation calculations', *J. Quant. Spectrosc. Radiat. Transfer*, **43**, 191–199.

Wiscombe, W. J. (1976). 'Extension of the doubling method to inhomogeneous sources', *J. Quant. Spectrosc. Radiat. Transfer*, **16**, 477-489.

Wiscombe, W. J. (1977). 'The Delta–M Method: Rapid Yet Accurate Flux Calculations for Strongly Asymmetric Phase Functions', *J. Atmos. Sci.*, **34**, 1408.

Wiscombe, W. J. and J. W. Evans (1977). 'Exponential–sum fitting of radiative transmission functions', *J. Comp. Phys.*, **24**, 416–444.

Wiscombe, W. J. (1983). 'Atmospheric Radiation: 1975–1983', *Rev. of Geophysics and Space Physics*, **21**, 997–1021.

World Meteorological Organization, Atmospheric Ozone 1985, Assessment of Our Understanding of the Processes Controlling its Present Distribution and Changes, *Rep. 16*, Global Ozone Res. and Monit. Proj., Geneva, Switzerland, 1986.